Karlsruher Institut für Technologie

GENERALIZED TRANSITION MATRIX METHODS FOR THE ANALYSIS OF LINEAR NANOPHOTONIC SYSTEMS

Zur Erlangung des akademischen Grades eines

Doktors der Naturwissenschaften (Dr. rer. nat.)

von der KIT-Fakultät für Physik des
Karlsruher Instituts für Technologie (KIT)

genehmigte

DISSERTATION

von

M. Eng. Aristeidis G. Lamprianidis

am Institut für Theoretische Festkörperphysik

Tag der mündlichen Prüfung: 16. June 2023

Referent:	Prof. Dr. Carsten Rockstuhl
Korreferent:	Prof. Dr. Brian Stout

Abstract

Lately, the rapid advancement of nanofabrication technologies has paved the way for the flourishing of nanophotonics. The latter attempt to mold the flow of light in ever more sophisticated ways. Today they find many technological applications in various fields, from biochemistry, till communications, and information technology, just to name a few.

As a result, there is an ever growing need to study, model, and design ever more complicated nanophotonic systems. Semi-analytical methods in nanophotonics can provide rather efficient ways to obtain unique insights into the systems. Nevertheless, they are typically characterized by severe limitations regarding their scope of applicability and are rarely preferred against computationally expensive, yet versatile, full-wave numerical methods. Arguably, abolishing the existing boundaries of applicability of semi-analytical methods can provide valuable agency to the further development of nanophotonics.

The T-matrix method belongs to such a class of semi-analytical methods in electromagnetic scattering theory. It is based on a matrix representation of the linear scattering system connecting the incident and scattered fields, which are expanded upon a finite basis set of elementary waves. The method excels in dealing with complex multi-scattering phenomena involving large ensembles of scatterers. The present thesis aims to enrich the available toolkit of semi-analytical methods in light-scattering by pushing against the existing limitations of the T-matrix method and stretching its scope of applicability. Specifically, we present three cases of generalized T-matrix methods tailored to the particular characteristics of the nanophotonic systems that they model.

First, we develop a T-matrix-based Floquet-Mie theory to semi-analytically model light scattering from spheres made of time-varying materials. Time-varying systems in nanophotonics recently attract lots of attention. Recent experiments of all-optical modulation in transparent conducting oxides, as well as other semiconductors, have demonstrated rather fast and considerably strong modulation of the material properties of such media. Temporal modulation provides an extra degree of freedom in nanophotonic systems and allows for the observation of several novel phenomena. We demonstrate that the T-matrix of a time-modulated sphere is characterized by inelastic scattering processes. Moreover, we drive time-modulated spheres into lasing states by means of parametric Mie resonances and discuss the breaking of electromagnetic reciprocity in such time-varying systems.

Next, we introduce the topological skeleton method to overcome a fundamental limitation of the conventional T-matrix method known as the problem of the Rayleigh Hypothesis. The problem is related with the inherently invalid representation of the near-fields of non-spherical scatterers and constitutes a major impediment that has been plaguing the applicability of the T-matrix method for multi-scattering calculations with strong near-field coupling among the scatterers. We develop a distributed T-matrix formalism that transcends the problem of the Rayleigh Hypothesis.

Finally, motivated by recent experimental observations, we study the directional coupling of emitters into waveguides by employing a generalized T-matrix description of the system and studying its properties. We decompose the general emissions into a set of chiral multipolar eigenstates and we study the directionality of each eigenstate independently. We conduct a symmetry analysis of the T-matrix of the system and we study the evanescent part of the transverse angular spectrum of the emissions, where we identify the prominent role of the transverse angular momentum of the emissions in governing the directionality of the coupling.

Contents

List of publications

Published peer-review scientific publications

1. A. G. Lamprianidis, C. Rockstuhl, and I. Fernandez-Corbaton, "Transcending the Rayleigh Hypothesis with multipolar sources distributed across the topological skeleton of a scatterer", *Journal of Quantitative Spectroscopy and Radiative Transfer*, **296**, 108455 (2023)

2. G. Ptitcyn, A. G. Lamprianidis, T. Karamanos, V. S. Asadchy, R. Alaee, M. M. Müller, M. Albooyeh, M. S. Mirmoosa, S. Fan, S. A. Tretyakov, and C. Rockstuhl, "Floquet-Mie Theory for Time-Varying Dispersive Spheres", *Laser & Photonics Reviews*, **17** (3), 2100683 (2023)

3. P. Garg, A. G. Lamprianidis, D. Beutel, T. Karamanos, B. Verfürth, and C. Rockstuhl, "Modeling four-dimensional metamaterials: a T-matrix approach to describe time-varying metasurfaces", *Optics Express*, **30** (25), 45832–45847 (2022)

4. V. S. Asadchy, A. G. Lamprianidis, G. Ptitcyn, M. Albooyeh, M. Rituraj, T. Karamanos, R. Alaee, S. A. Tretyakov, C. Rockstuhl, and S. Fan, "Parametric Mie Resonances and Directional Amplification in Time-Modulated Scatterers", *Physical Review Applied*, **18** (5), 054065 (2022)

5. A. Rahimzadegan, T. Karamanos, R. Alaee, A. G. Lamprianidis, D. Beutel, R.W. Boyd, and C. Rockstuhl, "A Comprehensive Multipolar Theory for Periodic Metasurfaces", *Advanced Optical Materials*, **10** (10), 2102059 (2022)

6. A. G. Lamprianidis, X. Zambrana-Puyalto, C. Rockstuhl, and I. Fernandez-Corbaton, "Directional Coupling of Emitters into Waveguides: A Symmetry Perspective", *Laser & Photonics Reviews*, **16** (1), 2000516 (2022)

7. M. R. Whittam, A. G. Lamprianidis, Y. Augenstein, and C. Rockstuhl, "Identifying regions of minimal back-scattering by a relativistically-moving sphere", *Physical Review A*, **108**, 043510 (2023)

Conference contributions

1. V. Asadchy, A. G. Lamprianidis, G. Ptitcyn, M. Albooyeh, M. Rituraj, T. Karamanos, R. Alaee, S. A. Tretyakov, C. Rockstuhl, and S. Fan, "Mie Resonances and Kerker Effects in Parametric Time-Modulated Spheres", *The Sixteenth International Congress on Artificial Materials for Novel Wave Phenomena – Metamaterials 2022*, (Siena, Italy, 09-2022)

2. A. G. Lamprianidis, G. Ptitcyn, T. Karamanos, V. S. Asadchy, R. Alaee, M. M. Müller, M. Albooyeh, M. S. Mirmoosa, S. Fan, S. A. Tretyakov, and C. Rockstuhl, "Electromagnetic scattering from homogeneous, time-varying and dispersive spheres", *Conference on Mathematics of Wave Phenomena 2022, KIT*, (online, 02-2022)

3. G. Ptitcyn, A. G. Lamprianidis, T. Karamanos, V. S. Asadchy, R. Alaee, M. M. Müller, M. Albooyeh, M. S. Mirmoosa, S. Fan, S. A. Tretyakov, and C. Rockstuhl, "Scattering of light by spheres made from a time-modulated and dispersive material", *The Fifteenth International Congress on Artificial Materials for Novel Wave Phenomena – Metamaterials 2021*, (online, 09-2021)

4. A. G. Lamprianidis, C. Rockstuhl, and I. Fernandez-Corbaton, "Overcoming the Rayleigh Hypothesis with sources distributed on the topological skeleton of the scatterer: a numerical demonstration of the method", *Bremen Zoom Workshop on Light Scattering 2021*, (online, 03-2021)

5. I. Fernandez-Corbaton, A. G. Lamprianidis, X. Zambrana-Puyalto, and C. Rockstuhl, "Directional coupling of emitters into waveguides: Symmetry mechanisms and the roles of angular momentum and handedness", *Metanano 2020*, (online, 09-2020)

1 — Introduction

Between 1885 and 1889 Heinrich Hertz, as a professor at the University of Karlsruhe, has been conducting a series of experiments attempting to verify Maxwell's newly developed electromagnetic theory [1]. In those experiments, Hertz transmitted and received radio waves in his laboratory, proving experimentally that light consisted of electromagnetic waves of short wavelength, as Maxwell's theory had already predicted. By 1901, Guglielmo Marconi would be already transmitting the first transatlantic Morse code radio signal, opening the doors to the commercialization of radio communications [2].

A couple of years after Hertz's departure from Karlsruhe, Gustav Mie arrived in Karlsruhe to work as an assistant in Hertz's lab with his former equipment. About a decade after Mie completed his habilitation there, he published his seminal paper on the theoretical study of plasmon resonance absorption of gold colloid nanoparticles [3, 4]. Mie theory treated analytically the problem of light scattering by spherical objects and provided a reference solution to a canonical problem of light interaction with matter. It constitutes today the archetype of electromagnetic scattering theory [5].

Since then, science has been endeavoring to master electromagnetic waves, and capitalize with ever more sophisticated ways on their fundamental ability to interact with matter, transfer energy, and carry information. Arguably, the last decades the use of electromagnetic waves had a tremendous impact on addressing human needs, and transforming, modernizing and expanding our productive forces. Today, we have several prominent examples of the significance of this scientific quest to tame light. It is telling that the first two of the six priorities of the EU Commission for the period 2019-2024 are titled as "A European Green Deal", and "A Europe fit for the digital age" [6].

On the one hand, harnessing solar energy with optimal efficiency is paramount for the strategic decarbonization of energy production, and the optimized manipulation of solar electromagnetic waves has been instrumental in modernizing the technology of solar cells [7–14].

On the other hand, artificial intelligence, cloud computing, and the internet of things are major drivers of the digital transformation of our economy. Faster communication of large amount of information is becoming increasingly important. It requires, though, communication in high frequencies where larger bandwidths are available and, to that end, significant advances in the technology of optical communications are taking place [15–23].

Simultaneously, with the rise of artificial intelligence the processing of large amounts of data leads to an ever increasing demand in computational power. Meanwhile, the significance of mastering the most modern lithographic processes in a "chip war" era cannot be overstated [24]. The development of high-precision optical elements is a cardinal point of the high-end extreme ultraviolet lithography technology [25–27].

Besides this, the maturation of nanofabrication technologies has paved the way to various other applications of nanophotonics in fields such as data storage [28, 29], light emitting diodes [30–32], flat lenses for smartphone cameras [33, 34], optical sensing for biomedical applications [35–38], and quantum technologies [39, 40], just to name a few.

As a result, novel numerical methods for nanophotonics that are capable to address the modern challenges are required [41]. On the one hand, the necessity for the analysis and modeling of phenomena involving ever more complicated ways of light interacting

with matter at the nanoscale arises. For this, the unveiling of the internal dynamics of a nanophotonic system is often required to shed light on the actual physical mechanisms that give birth to the observed phenomena. On the other hand, the simulation and design of ever more complicated devices to manipulate electromagnetic waves becomes also a necessity. Quite often, the fully-numerical simulation of modern nanophotonic systems, which are frequently characterized by a disparity of the involved optical length scales, can be expensive, if possible at all. The main problem that arises here is the "gray zone" that exists between the regime of applicability of ray optics solvers and that of conventional full-wave solvers. While the former require that the geometrical features of the system are much larger than the wavelength of light, the latter are only able to treat systems that are usually not larger than a few dozens of cubic wavelengths. Computational inverse design for nanophotonic devices has evolved considerably the last years, with a few approaches standing out: 1) free-form shape optimization [42, 43], 2) topology optimization with the adjoint method [44, 45], and 3) deep learning with artificial neural networks [46, 47]. However, regardless of the approach, its further development requires access to fast, large-scale numerical simulations of nanophotonic systems. Only recently, GPU-optimized FDTD solvers that are able to efficiently simulate, e.g., a quite large metasurface of dimensions of 100 square wavelengths have been reported [48–50].

In various cases, the Transition Matrix (T-matrix) method can offer solutions to such challenges that arise in the field of numerical methods in nanophotonics. The T-matrix method belongs to a class of semi-analytical methods that deal with problems of scattering of electromagnetic waves [51–60]. The method is based on matrix descriptions of the linear nanophotonic system. Two finite dimensional Hilbert spaces are constructed: one for the incident field and another for the scattered field. Then, the T-matrix that constitutes a compact representation of the nanophotonic system within the considered Hilbert spaces can be calculated [61–65]. Each element of the T-matrix represents the strength of the transition from an input (i.e., incident) to an output (i.e., scattered) state. Consequently, the T-matrix is generally able to provide the response of the nanophotonic system upon an arbitrary excitation, and, in that sense, it can fully describe the inner dynamics of the system.

A major advantage of the T-matrix method is that it can solve complex multiple-scattering problems rather efficiently in an hierarchical way. Once the T-matrix of each individual scatterer is known, then the T-matrix of the full system of an aggregate of scatterers can be obtained semi-analytically without much computational effort, and, furthermore, even get coupled straightforwardly to some planar interface [54–56, 66]. This is because, in such semi-analytical methods, the propagation of the fields in the free background medium to account for multi-scattering interactions is cheaply performed semi-analytically. Moreover, note that, by virtue of the fully analytical Mie theory, the T-matrix method excels for spherical scatterers, but can, generally, still be used for the case of arbitrary scatterers. Recently, the method has been employed to model efficiently large-area metasurfaces [58, 67]. Moreover, an interesting technique has been recently proposed to drastically increase the computational efficiency of the T-matrix method, although it still remains unexplored [68].

This thesis attempts to push against the traditional boundaries of the applicability range of the T-matrix method by proposing three exemplary generalizations of the method tailored to the particular characteristics of some modern nanophotonic systems.

First, we generalize the T-matrix method for the case of light scattering from time-varying scatterers, i.e., from scatterers whose electromagnetic material properties vary in time. In what follows, let us briefly introduce the underlying physics of time-varying nanophotonic systems.

Tunable nanophotonic systems for the dynamic control of light have been recently

gaining significant attention. Several methods to modulate the response of the tunable systems have been reported. The first method is electrical modulation. Here, the case of electrostatic gating of graphene stands out [69, 70], but we also have the case of electrical tuning of microwave metamaterials with varactor diodes [71, 72], and the case of electrical tuning of metamaterials with liquid crystal that is forced to change from an isotropic to a nematic phase through an externally applied voltage bias, which changes its optical properties [73]. Similarly, the optical properties of liquid crystal can be modulated thermally: there is a threshold temperature that changes the liquid crystal from the isotropic to the nematic phase [74]. Thermal modulation with other phase change materials or, also, with silicon has been reported as well [75]. However, those modulation methods can only provide rather slow tunability with respect to optical frequencies. The modulation frequency of thermal tuning can vary from a couple of KHz till around 0.1 MHz, whereas the modulation frequency of electrical tuning can reach up to several GHz. Moreover, while the thermal modulation strength is typically rather small, well below 1%, a quite large modulation strength can be achieved with the electrical tuning of 2D materials like graphene [76].

Therefore, at this point we would like to differentiate between "tunable" and "time-varying" nanophotonic systems. With the latter term, we refer to systems whose material properties vary fast enough with respect to the frequency of light, being characterized, also, by a considerable modulation strength.

Recent experiments have been proposing rather fast all-optical modulation in infrared frequencies for transparent conductive oxides, such as Aluminium-Doped Zinc Oxide and Tin-Doped Indium Oxide, operated in their Epsilon-Near-Zero spectral regime [77–80]. In all-optical modulation we have a pump laser that boosts electrons from the valence to the conduction band of such doped semiconductors that are characterized by strong nonlinear properties, which are mediated through the existence of real electron states. Transition through those states is realized by photocarrier excitation which has as a result the redistribution of electrons between the valence and the conduction band. This induced mobility of the electrons is what finally modulates the material properties of the medium [81]. The pulse duration of the pump, together with the rate of photon-absorption by the electrons, as well as the recombination time of the photocarriers are factors that limit the speed of the all-optical modulation of the medium [82, 83]. For Aluminium-Doped Zinc Oxide, the recombination time of the photocarriers was measured to be below 100fs, whereas the average induced carriers concentration was measured to be around 5% of the intrinsic carrier concentration of the medium [79]. Note, though, that the modulation strength strongly depends on the intensity of the pump, which is typically required to be quite high. Finally, let us also mention that transitions through virtual states in nonlinear processes (such as four-wave-mixing and sum-frequency-generation) are also possible and even are much faster. However, they typically exhibit quite lower modulation strengths. Gallium Arsenide, having a direct band gap, demonstrates stronger modulation strengths in comparison to, e.g., Silicon which has an indirect band gap [84–87].

A plethora of novel interesting phenomena has been already observed in time-varying nanophotonic systems, which, therefore, recently attract lots of attention. Arguably, the temporal variation of material properties unlocks a new dimension of control in electromagnetic systems [88, 89]. Recently, a wide range of novel optical effects has been observed for periodically time-varying media, known as photonic time crystals (PTCs). Phenomena such as magnetless nonreciprocity [90–96], frequency conversion and Doppler shift [97–99], amplification, [100–102], and others [103–109]. Furthermore, there has been several studies of time-varying meta-atoms [110–114]. Generalizing the T-matrix method for the analysis of time-varying scatterers, opens new doors to the study of such exotic phenomena.

Next, in our second considered exemplary case of genaralization of the T-matrix method, we move on to address a rather fundamental problem that typically plagues the conventional T-matrix method. It is famous as the problem of the "Rayleigh Hypothesis". In what follows, let us briefly introduce the problem.

In 1907, Lord Rayleigh studied the diffraction of waves from gratings [115]. His famous hypothesis back then was that the reflected field by the grating could be represented everywhere above the grating -*even inside the region of the corrugations*- as a superposition of a discrete set of plane waves propagating/decaying along the diffraction orders of the grating. Rayleigh used this hypothesis to enforce the interface conditions at the surface of the grating and, finally, solve the diffraction problem. Since then, the problem of the Rayleigh Hypothesis has been imbued with a more generalized content that concerns the *region of validity of analytical representations of fields*. In that sense, the problem of the Rayleigh Hypothesis becomes relevant for all semi-analytical methods in nanophotonics that employ such analytical representations of the fields. Initially constituting a topic of scientific dispute, the Rayleigh Hypothesis has been revisited multiple times from a mathematical, physical, or engineering point of view. Still today, more than a century later, it surprisingly remains an active topic of scientific research [116–138].

A year after the seminal work of Lord Rayleigh, Gustav Mie solved the canonical problem of light scattering by a sphere. As a representation of the scattered field, he employed a multipolar series where the origin was the center of the sphere. Indeed, that constituted a natural representation for his case due to the spherical geometry of the scatterer. However, the strength of the paradigm of Mie's representation was such that it still resonates today: we commonly keep employing the same representation Mie used to treat scatterers of non-spherical geometry [55, 66]. Unfortunately, though, here comes the devil of the Rayleigh Hypothesis indoors; it is known that such a representation is guaranteed to be valid only outside a sphere that circumscribes the scatterer. Using spherical waves to represent the scattered field from non-spherical scatterers is the three-dimensional analogue of Rayleigh's problematic usage of plane waves to represent the reflected field by a non-planar grating, even inside its corrugations.

The first major mathematical treatment of the problem of the Rayleigh Hypothesis came several decades later when Millar highlighted the critical role of the analytic properties of the fields, i.e., the properties of the analytic continuation of the scattered fields within the domain of the scatterer [116]. Since then, physicists and engineers have struggled to capitalize on the insights that the state-of-the-art mathematical understanding of the problem provided. Besides this, they have been also working to develop alternative practical methods to semi-analytically solve wave scattering problems that are not plagued with spurious effects related to the problem of the Rayleigh Hypothesis, which the existing conventional methods typically face.

Importantly, representations of the fields that unlock access to the near-fields of the scatterers are essential for the semi-analytical modeling of multi-scattering phenomena involving scatterers placed in proximity, inside that problematic near-field region of each other. Modeling the electromagnetic coupling of nanoemitters such as molecules/quantum dots with nanoantennas, or modeling the electromagnetic coupling of an array of tightly packed nanoparticles whose circumscribing spheres intersect with each other, are two indicative examples where semi-analytical modeling methods, employing Mie's conventional representation, typically fail to address the Rayleigh Hypothesis issue. As a result, this ends up posing as a fundamental challenge to the applicability of the method itself. Evidently, the problem of the Rayleigh Hypothesis, being exactly related to the region of validity of the analytical representations of the fields, plays a pivotal role in all such semi-analytical methods, since it directly affects their major advantage as a method: that of the cheap semi-analytical propagation of the fields in the background medium to account

for the multi-scattering interactions.

To deal with this problem, a plethora of methods employing alternative representations, usually based on a scheme with a spatial distribution of discrete sources, has been reported in the literature, including the Discrete Sources Method, the Null Field Method with Discrete Sources, the Multiple Multipole Method, the Method of Auxilliary Sources, the Global Polarizability Matrix Method [57, 139–144]. Those alternative methods provided improved representation schemes for the fields that practically helped to model with greater accuracy the scattering from particles with extreme geometries. They had their respective limitations, but, arguably, their most important problem was the lack of much evidence, maybe apart from intuition or some empirical rules [144], for the optimal placement of the discrete sources representing the scattered fields from a particle of arbitrary geometry. In this thesis, we will be introducing a novel discrete-sources-based representation scheme for the fields that generalizes the T-matrix method in a way that transcends the problem of the Rayleigh Hypothesis, allowing for the practical use of the method for scatterers of arbitrary geometry.

Finally, in the third considered exemplary case of generalization of the T-matrix method, we construct a T-matrix representation of a waveguiding system excited by nearby emitters. This generalization case of the T-matrix argues for T-matrix representations of linear nanophotonic systems beyond the conventional ones that treat a finite scatterer as a "black box" and only focus on its interaction with the outer environment. In our case, we use the constructed generalized T-matrix to study the directionality of the coupling of the emissions to the waveguide. In what follows, let us briefly introduce the underlying physics of this problem.

Recently, there have been several experiments demonstrating directional coupling of light radiated by emitters into waveguide modes. For example, pronounced directionality has been shown in the collection of atomic emissions by optical fibers [145] and quantum dot emissions by waveguides [146–152]. Furthermore, other experiments have shown pronounced directional coupling of focused light beams into waveguides, either directly [153], or mediated by a scatterer [154, 155]. The directionality effect demonstrated by those experiments highlights the potential to route light and classify emissions according to the electromagnetic properties that actually determine the preferential coupling direction.

Different theoretical approaches have been developed to analyse the underlying physics and understand the effect of observed directionality [156–169]. In particular, the concepts of transverse spin and spin-momentum locking in evanescent waves have been put forward as the origin of the directionality. However, the use of the photonic spin introduces an ambiguity: In the context of the common separation of the optical angular momentum into orbital and spin parts [170], the spin of the photon is often simultaneously connected to both angular momentum and helicity/handedness [165, 171–173]. This ambiguity may cause confusion and raises the question of which of the two generally distinct properties actually dictates the directional coupling. The answer to this question may imply fundamentally different characteristics and applications of the directional coupling effect. Importantly, while on the one hand, the angular momentum of the emissions is related with the rotational properties of the emissions, on the other hand, the helicity/handedness of the emissions is related with their chiral properties.

Apart from the ambiguity between the angular momentum and the helicity of the emissions, there is another point of ambiguity that characterize the experimental observations, and is related with the selected quantization axis of the emissions, i.e., the axis with respect to which the emissions are characterized by a well-defined angular momentum. Note that, in general, there are two common ways to experimentally select the quantization axis of the emissions. One either needs to use an external bias of a static magnetic field (e.g. in [145, 146, 148]), or, otherwise, the axis of propagation of a circularly polarized

incident beam is the one that selects the quantization axis of the emissions (e.g. in [147, 154]). Note that, when a magnetic bias is used for such selection, the signals originating from emissions with opposite angular moment with respect to the selected bias axis are spectrally distinguished due to the occurring Zeeman splitting that lifts their spectral degeneracy. One of three different options of quantization axes, which we call transverse axis [145, 154, 155], vertical axis [146–149, 164], and longitudinal axis [153], is typically selected in the experiments. However, note that the concept of spin-momentum locking only applies naturally to the transverse angular momentum case. Clarifying the qualitative differences between the three different quantization axes is therefore essential to appreciate the underlying physics and to properly design the experiments.

Moreover, the dipolar approximation is routinely made to characterize the emitter. This precludes the theoretical study and prediction of possible directional coupling effects for the light emitted from higher-order multipolar transitions of atoms, molecules, and quantum dots [174–179]. However, note that, while the numerical simulation of systems excited with dipolar emitters is straightforward, this is not really the case for multipolar emissions of higher order which require special technical treatment for their injection inside the numerical simulations.

In this thesis, we are interested to address those issues and unveil the electromagnetic properties of the emissions that actually drive the observed directional phenomena in the experiments by studying the symmetries and the inner dynamics of the generalized T-matrix that represents such nanophotonic systems.

Structure of the thesis

The thesis is divided into six chapters. After introducing the reader to the topics to be studied in this first chapter, in the second chapter, we present the foundational elements of electromagnetic theory on which this thesis is based. We discuss general principles of electromagnetism that govern linear nanophotonic systems such as the electromagnetic properties of the media, causality and stability, energy and photon number conservation, reciprocity. Moreover, we present an eigenmode analysis of infinite, homogeneous, and isotropic media, and we also discuss electromagnetism under the prism of the helicity operator. Finally, we briefly recall the basics of waveguiding systems, and we introduce some basic abstract notions of the T-matrix method.

In the third chapter, we study the scattering of electromagnetic waves from spheres made of time-varying media. First, we discuss the physics of the eigensolutions of the electromagnetic wave equation in bulk time-varying media, and, then, we develop a Floquet-Mie theory that solves the problem of light scattering from time-modulated spheres with a generalized T-matrix method. We verify our results against full-wave simulations. Finally, we demonstrate how such spheres can be driven to lasing states by means of parametric Mie resonances, and we discuss the reciprocity symmetry under the prism of the T-matrix of the system.

The fourth chapter addresses the problem of the Rayleigh Hypothesis in the context of the T-matrix method. First, we present a theoretical analysis of the problem, and, then, we propose a solution to the problem of the Rayleigh Hypothesis by introducing the topological skeleton method to attain novel representations of the fields that transcend the problem. Furthermore, we formulate a distributed T-matrix based on the new representations of the fields, we demonstrate how it can be calculated with full-wave simulations, and we develop the generalization of the conventional multi-scattering theoretical formulation to account for the newly introduced distributed T-matrices.

In the fifth chapter, we study the physics of directional coupling of emitters into waveg-

uides under the prism of the generalized T-matrix of the system. First, we construct a Hilbert space that is suitable to represent chiral emissions as the input of the T-matrix of the waveguiding system, and, then, we present numerical results of the directionality of the T-matrix of an exemplary system. To theoretically interpret our results, we conduct a symmetry analysis of the T-matrix, and we study the transverse angular spectrum of the emissions, which sheds light on our observations and highlights the prominent role of transverse angular momentum of the emissions in governing the directionality of the couplings.

Finally, the thesis concludes with the sixth chapter, in which we briefly summarize our findings and provide an outlook for future research.

2 — Foundational elements of electromagnetic theory

2.1 Introduction

In this chapter, we will introduce the basic theoretical background on which the analysis of the following chapters is based. In the first section, we introduce Maxwell's equations which, together with the general constitutive relations that characterize linear media, comprise the backbone of electromagnetic theory. In the second section, we discuss the notions of causality and stability and the implications that they have for the response of the media. In the third section, we present the generalized Poynting's theorem and we discuss the energy and photon number conservation in optical systems. In the fourth section, we discuss electromagnetic reciprocity, which is a symmetry typically characterizing optical systems. In the fifth section, we present the sets of eigenmodes of homogeneous and isotropic media that we will frequently use in the following chapters of the thesis. In the sixth section, we introduce the helicity operator and briefly discuss how it can assist the analysis of chiral electromagnetic phenomena. In the seventh section, we briefly present the basics of the electromagnetic theory for waveguides. Finally, in the last section of this chapter, we theoretically introduce the T-matrix methods to analyze linear electromagnetic systems.

2.2 Maxwell's equations and constitutive relations

From a *classical*, *microscopic* electromagnetic perspective, every material is spatially inhomogeneous and varies in time; it is constituted by a collection of point charges. The electromagnetic waves inside the media are governed by the microscopic Maxwell equations. However, the spatiotemporal microscopic variations, e.g. nuclear vibrations or electronic orbital motions, typically take place on temporal scales much shorter than the oscillation period of light and on spatial scales that are much shorter than the wavelength of light. Therefore, by introducing spatiotemporal averages of the involved physical quantities, it is convenient to resort to a *macroscopic* description of electromagnetic waves. Maxwell's equations, in their macroscopic form, read as follows:

$$\nabla \times \tilde{\mathbf{H}}(\mathbf{r},t) - \frac{\partial}{\partial t}\left[\varepsilon_0 \tilde{\mathbf{E}}(\mathbf{r},t) + \tilde{\mathbf{P}}_{\mathrm{e}}(\mathbf{r},t)\right] = \tilde{\mathbf{J}}(\mathbf{r},t), \tag{2.1}$$

$$\nabla \times \tilde{\mathbf{E}}(\mathbf{r},t) + \frac{\partial}{\partial t}\left[\mu_0 \tilde{\mathbf{H}}(\mathbf{r},t) + \tilde{\mathbf{P}}_{\mathrm{m}}(\mathbf{r},t)\right] = 0, \tag{2.2}$$

$$\nabla \cdot \left[\varepsilon_0 \tilde{\mathbf{E}}(\mathbf{r},t) + \tilde{\mathbf{P}}_{\mathrm{e}}(\mathbf{r},t)\right] = \tilde{\rho}(\mathbf{r},t), \tag{2.3}$$

$$\nabla \cdot \left[\mu_0 \tilde{\mathbf{H}}(\mathbf{r},t) + \tilde{\mathbf{P}}_{\mathrm{m}}(\mathbf{r},t)\right] = 0. \tag{2.4}$$

$\tilde{\mathbf{E}}(\mathbf{r},t)$ and $\tilde{\mathbf{H}}(\mathbf{r},t)$ correspond to the *macroscopic* electric and magnetic fields respectively, whereas $\tilde{\mathbf{P}}_{\mathrm{e}}(\mathbf{r},t)$ and $\tilde{\mathbf{P}}_{\mathrm{m}}(\mathbf{r},t)$ correspond to the *macroscopic* electric and magnetic

polarization densities, respectively. Note that the magnetic polarization density is related with the macroscopic magnetization of the medium $\tilde{\mathbf{M}}(\mathbf{r},t)$ in the following way: $\tilde{\mathbf{P}}_{\mathrm{m}}(\mathbf{r},t) = \mu_0\tilde{\mathbf{M}}(\mathbf{r},t)$. $\tilde{\rho}(\mathbf{r},t)$ and $\tilde{\mathbf{J}}(\mathbf{r},t)$ denote the *macroscopic* free charge and current densities, respectively, and are related to each othere with the charge continuity equation: $\nabla\cdot\tilde{\mathbf{J}}(\mathbf{r},t) = -\partial\tilde{\rho}(\mathbf{r},t)/\partial t$. ε_0 is the dielectric permittivity of vacuum and μ_0 is the magnetic permeability of vacuum. Note that we use the symbol $\tilde{\cdot}$ to denote a functional dependency on time. All the aforementioned time-dependent quantities are real-valued.

To solve Maxwell's equations, we need to accompany them with the *constitutive relations*. These constitutive relations physically describe the way a medium gets polarized in the presence of electromagnetic fields. In their most general form, the constitutive relations of a *linear* medium read as follows:

$$\begin{bmatrix}\tilde{\mathbf{P}}_{\mathrm{e}}(\mathbf{r},t)\\ \tilde{\mathbf{P}}_{\mathrm{m}}(\mathbf{r},t)\end{bmatrix} = \int_{-\infty}^{+\infty}\int_{\mathbb{R}^3}\tilde{\boldsymbol{\chi}}(\mathbf{r},\mathbf{r}-\mathbf{r}',t,t-t')\cdot\begin{bmatrix}\tilde{\mathbf{E}}(\mathbf{r}',t')\\ \tilde{\mathbf{H}}(\mathbf{r}',t')\end{bmatrix}\mathrm{d}^3\mathbf{r}'\,\mathrm{d}t', \tag{2.5}$$

$$\text{where}\quad \tilde{\boldsymbol{\chi}} = \begin{bmatrix}\varepsilon_0\tilde{\boldsymbol{\chi}}_{\mathrm{ee}} & \sqrt{\varepsilon_0\mu_0}\tilde{\boldsymbol{\chi}}_{\mathrm{em}}\\ \sqrt{\varepsilon_0\mu_0}\tilde{\boldsymbol{\chi}}_{\mathrm{me}} & \mu_0\tilde{\boldsymbol{\chi}}_{\mathrm{mm}}\end{bmatrix}, \tag{2.6}$$

and $\tilde{\boldsymbol{\chi}}_{\mathrm{ee}},\tilde{\boldsymbol{\chi}}_{\mathrm{em}},\tilde{\boldsymbol{\chi}}_{\mathrm{me}},\tilde{\boldsymbol{\chi}}_{\mathrm{mm}}$ are the electric-electric, electric-magnetic, magnetic-electric, and magnetic-magnetic, *susceptibility* dyadic (3x3) tensors, respectively. The spatial integral shall span the whole space that is occupied by the polarized medium. Note that the susceptibility tensor $\tilde{\boldsymbol{\chi}}$ is actually the response function of the medium, which only in frequency domain is typically named as susceptibility. However, since in what follows we will frequently refer to quantities in both time and frequency domain alternately, we will refer to the response function of the medium as the susceptibility tensor as well, for simplicity. Moreover, note that the linearity of the system implies that the induced polarization in the medium is linearly dependent on the electromagnetic fields, i.e., it does not depend on higher powers of them. Nonlinear phenomena are generally weak, and only become prominent once we operate the system in a regime of large field intensities. We will avoid such considerations in this thesis.

Here, let us highlight some specific classes of media:

- For a *homogeneous* medium, i.e., one that possesses continuous translation symmetry in space, $\tilde{\boldsymbol{\chi}}(\mathbf{r},\mathbf{r}-\mathbf{r}',t,t-t')$ is invariant with respect to its first argument. In this case, an arbitrary translation of the electromagnetic field in space, i.e., the transformation $\left[\tilde{\mathbf{E}}(\mathbf{r},t),\tilde{\mathbf{H}}(\mathbf{r},t)\right] \to \left[\tilde{\mathbf{E}}(\mathbf{r}+\mathbf{d},t),\tilde{\mathbf{H}}(\mathbf{r}+\mathbf{d},t)\right]$, always gives equally displaced induced polarizations in space, i.e., $\left[\tilde{\mathbf{P}}_{\mathrm{e}}(\mathbf{r},t),\tilde{\mathbf{P}}_{\mathrm{m}}(\mathbf{r},t)\right] \to \left[\tilde{\mathbf{P}}_{\mathrm{e}}(\mathbf{r}+\mathbf{d},t),\tilde{\mathbf{P}}_{\mathrm{m}}(\mathbf{r}+\mathbf{d},t)\right]$, for arbitrary spatial translations $\mathbf{d}$.

- For a *stationary* medium, i.e., one that possesses continuous translation symmetry in time, $\tilde{\boldsymbol{\chi}}(\mathbf{r},\mathbf{r}-\mathbf{r}',t,t-t')$ is invariant with respect to its third argument. In this case, an arbitrary translation of the electromagnetic field in time, i.e., the transformation $\left[\tilde{\mathbf{E}}(\mathbf{r},t),\tilde{\mathbf{H}}(\mathbf{r},t)\right] \to \left[\tilde{\mathbf{E}}(\mathbf{r},t+t_0),\tilde{\mathbf{H}}(\mathbf{r},t+t_0)\right]$, always gives equally displaced induced polarizations in time, i.e., $\left[\tilde{\mathbf{P}}_{\mathrm{e}}(\mathbf{r},t),\tilde{\mathbf{P}}_{\mathrm{m}}(\mathbf{r},t)\right] \to \left[\tilde{\mathbf{P}}_{\mathrm{e}}(\mathbf{r},t+t_0),\tilde{\mathbf{P}}_{\mathrm{m}}(\mathbf{r},t+t_0)\right]$, for arbitrary temporal translations t_0.

- For a medium with *local* response, we have that $\tilde{\boldsymbol{\chi}}(\mathbf{r},\mathbf{r}-\mathbf{r}',t,t-t') = \delta(\mathbf{r}-\mathbf{r}')\tilde{\boldsymbol{\chi}}_{\mathrm{local}}(\mathbf{r},t,t-t')$, where $\delta(\mathbf{r}-\mathbf{r}')$ is the Dirac delta distribution. Typically, non-local effects can be neglected since the characteristic length scale of the medium is much shorter than the wavelength of light. However, non-local effects become more

pronounced in artificial metamaterials. There, non-locality gives rise to *spatial dispersion*, i.e., a spatial spreading of the response of the medium. The polarization induced at some point in space depends on the fields at the vicinity of that point.

➢ For a medium with *instantaneous* response, we have that $\tilde{\boldsymbol{\chi}}(\mathbf{r}, \mathbf{r}-\mathbf{r}', t, t-t') = \delta(t-t')\tilde{\boldsymbol{\chi}}_{\text{instant}}(\mathbf{r}, \mathbf{r}-\mathbf{r}', t)$. In contrast to *spatial dispersion*, *temporal dispersion*, i.e., a non-instantaneous response of the medium, cannot be easily ignored, especially at high temporal frequencies where the media typically possess resonances. Temporal dispersion effects correspond to a temporal spreading of the response of the medium. In the next section, we will discuss the effect of causality, which constraisn that temporal spreading of the response of the medium to be one-directional, specifically only allowing for memory effects.

➢ In general, when the tensor $\tilde{\boldsymbol{\chi}}(\mathbf{r}, \mathbf{r}-\mathbf{r}', t, t-t')$ is a full 6x6 tensor, the medium is called *bi-anisotropic*, whereas, when the tensors $\tilde{\boldsymbol{\chi}}_{\text{ee}}, \tilde{\boldsymbol{\chi}}_{\text{em}}, \tilde{\boldsymbol{\chi}}_{\text{me}}, \tilde{\boldsymbol{\chi}}_{\text{mm}}$ become a scalar multiple of the 3x3 identity matrix, the medium is called *bi-isotropic*. When $\tilde{\boldsymbol{\chi}}_{\text{em}} = \tilde{\boldsymbol{\chi}}_{\text{me}} = \mathbf{0}$, the medium is called *anisotropic*, and when, furthermore, the tensors $\tilde{\boldsymbol{\chi}}_{\text{ee}}, \tilde{\boldsymbol{\chi}}_{\text{mm}}$ become a scalar multiple of the 3x3 identity matrix the medium is called *isotropic*. Moreover, if $\tilde{\boldsymbol{\chi}}_{\text{mm}} = \mathbf{0}$, the medium is called *non-magnetic*.

By making use of the following Fourier-transform pair:

$$\tilde{X}(t) = \frac{1}{\sqrt{2\pi}} \int_{-\infty}^{+\infty} X(\omega) e^{-\mathrm{i}\omega t} \mathrm{d}\omega \quad \longleftrightarrow \quad X(\omega) = \frac{1}{\sqrt{2\pi}} \int_{-\infty}^{+\infty} \tilde{X}(t) e^{\mathrm{i}\omega t} \mathrm{d}\omega, \tag{2.7}$$

the macroscopic Maxwell equations take the following form in the frequency domain:

$$\begin{aligned}
\nabla \times \mathbf{H}(\mathbf{r}, \omega) + \mathrm{i}\omega \left[\varepsilon_0 \mathbf{E}(\mathbf{r}, \omega) + \mathbf{P}_{\text{e}}(\mathbf{r}, \omega)\right] &= \mathbf{J}(\mathbf{r}, \omega), && (2.8)\\
\nabla \times \mathbf{E}(\mathbf{r}, \omega) - \mathrm{i}\omega \left[\mu_0 \mathbf{H}(\mathbf{r}, \omega) + \mathbf{P}_{\text{m}}(\mathbf{r}, \omega)\right] &= 0, && (2.9)\\
\nabla \cdot \left[\varepsilon_0 \mathbf{E}(\mathbf{r}, \omega) + \mathbf{P}_{\text{e}}(\mathbf{r}, \omega)\right] &= \rho(\mathbf{r}, \omega), && (2.10)\\
\nabla \cdot \left[\mu_0 \mathbf{H}(\mathbf{r}, \omega) + \mathbf{P}_{\text{m}}(\mathbf{r}, \omega)\right] &= 0, && (2.11)
\end{aligned}$$

whereas the constitutive relations take the following form in the frequency domain:

$$\begin{bmatrix} \mathbf{P}_{\text{e}}(\mathbf{r}, \omega) \\ \mathbf{P}_{\text{m}}(\mathbf{r}, \omega) \end{bmatrix} = \int_{-\infty}^{+\infty} \int_{\mathbb{R}^3} \boldsymbol{\chi}(\mathbf{r}, \mathbf{r}-\mathbf{r}', \omega-\omega', \omega') \cdot \begin{bmatrix} \mathbf{E}(\mathbf{r}', \omega') \\ \mathbf{H}(\mathbf{r}', \omega') \end{bmatrix} \mathrm{d}^3\mathbf{r}' \, \mathrm{d}\omega', \tag{2.12}$$

$$\text{where} \quad \boldsymbol{\chi} = \begin{bmatrix} \varepsilon_0 \boldsymbol{\chi}_{\text{ee}} & \sqrt{\varepsilon_0 \mu_0} \boldsymbol{\chi}_{\text{em}} \\ \sqrt{\varepsilon_0 \mu_0} \boldsymbol{\chi}_{\text{me}} & \mu_0 \boldsymbol{\chi}_{\text{mm}} \end{bmatrix}. \tag{2.13}$$

Let us highlight that, since $\tilde{\boldsymbol{\chi}}(\mathbf{r}, \mathbf{r}-\mathbf{r}', t, t-t')$ is a *real-valued* function, we have that

$$\boldsymbol{\chi}(\mathbf{r}, \mathbf{r}-\mathbf{r}', \omega-\omega', \omega') = \boldsymbol{\chi}^*(\mathbf{r}, \mathbf{r}-\mathbf{r}', -\omega+\omega', -\omega'), \tag{2.14}$$

where we use the symbol $(*)$ to denote complex conjugation.

Importantly, note that for a *stationary* medium whose susceptibility tensor in time domain is invariant with respect to its third argument, we have that $\boldsymbol{\chi}(\mathbf{r}, \mathbf{r}-\mathbf{r}', \omega-\omega', \omega') = \delta(\omega-\omega')\boldsymbol{\chi}_{\text{stationary}}(\mathbf{r}, \mathbf{r}-\mathbf{r}', \omega)$. It implies that the constitutive relations of the medium do

not introduce coupling between the fields of different frequencies ω, which is otherwise the case. Spectral coupling, i.e., violation of the conservation of frequency, is an important property of systems without continuous translation symmetry in time.

Finally, let us also note, that *non-local* but *homogeneous* media are conveniently analyzed in momentum instead of real coordinate space, i.e., when an extra Fourier transform is performed to shift in the domain of spatial frequencies. That is because the continuous translation symmetry in space of such media (in analogy with that in time discussed in the previous paragraph) conserves spatial frequencies, i.e., linear momentum. However, non-local effects go beyond the scope of this thesis and we refrain from introducing such a further step in our analysis here. We will keep considering, though, non-locality in the next sections of this chapter just for reasons of completeness of the presented theoretical analysis of the linear electromagnetic systems under study. Note, also, that throughout this thesis, we will only focus on electrodynamics and avoid considerations of electrostatics, i.e., we will consider only electromagnetic fields with vanishing spectral content at zero frequency.

2.3 Causality and stability: two fundamental properties of electromagnetic media, and their consequences on how to phenomologically model material properties

In this section, we will discuss the implications of two fundamental properties that characterize electromagnetic media: *causality* and *stability*. It will be important especially in the context of time-varying media, as we can derive based on these two principles a mathematical framework concerning how to phenomenologically express the materials properties of dispersive and time-varying media.

The principle of *causality* states that there cannot be any response of the electromagnetic system before it gets excited, i.e., the medium is polarized only *after* its excitation by the electromagnetic fields; the past reflects on the present, but the future does not. Moreover, no non-local response of the system can occur faster than the vacuum speed of light, c_0. Algebraically, this physical requirement translates into the following property of the susceptibility tensor for media:

$$\tilde{\boldsymbol{\chi}}(\mathbf{r}, \mathbf{r}-\mathbf{r}', t, t-t') \;=\; 0, \;\; \text{for} \;\; t-t' \leq \left|\mathbf{r}-\mathbf{r}'\right|/c_0. \tag{2.15}$$

We consider causality a fundamental property of the electromagnetic media studied in this thesis.

Another fundamental property that characterizes the considered electromagnetic media is *stability*. By this, here, we mean that the response function of the medium, $\tilde{\boldsymbol{\chi}}(\mathbf{r}, \mathbf{r}-\mathbf{r}', t, t-t')$, is finite everywhere and, with respect to its last argument, decays at least as fast as $O(1/(t-t')^2)$, as $(t-t') \to \infty$ [180]. This implies that a finite excitation of the medium gives always a finite response that dies out over a long enough period of time.

Therefore, a real-valued function, $\tilde{f}(t)$, which abides with the principles of causality and stability, has the following properties: 1) $\tilde{f}(t) = 0$ for $t \leq 0$, 2)$\tilde{f}(t)$ is finite everywhere, and 3) $\lim_{t\to\infty} \tilde{f}(t)$ decays at least as fast as $O(t^{-2})$. Let us now consider its Fourier transform $f(\omega)$ and study some of its properties.

First of all, as shown in Ref. [180], the above three conditions of $\tilde{f}(t)$ suffice to satisfy the Cauchy-Riemann conditions for the function $f(\omega)$ everywhere in the upper-half space including the real axis, $\mathrm{Im}\{\omega\} \geq 0$, with $\mathrm{Im}\{\cdot\}$ denoting the imaginary part of a quantity.

This means that causality and stability imply the analyticity of $f(\omega)$ in the upper half-plane.

Moreover, following Section 7.10 of Ref. [181], and making use of the same properties of causality and stability, we can derive the following power series expansion of $f(\omega)$:

$$f(\omega) = \sum_{n=1,2,\ldots}^{\infty} \frac{1}{(-\mathrm{i}\omega)^{n+1}} \frac{\partial^n \tilde{f}}{\partial t^n}(0), \tag{2.16}$$

which implies that, for $|\omega| \to \infty$, the absolute value and the real part of $f(\omega)$ decay with a rate of $O(1/|\omega|^2)$, whereas the imaginary part of $f(\omega)$ decays with a rate of $O(1/|\omega|^3)$. In view of this result, and by virtue of Cauchy's integral theorem applied for the complex contour of the circle with infinite radius $|\omega| \to \infty$, we can deduct that $f(\omega)$ *cannot* be an *entire* function, i.e., analytic everywhere in the complex frequency plane, since that would imply that it is zero everywhere. Therefore, the analyticity of $f(\omega)$ has to be broken somewhere in the lower half-plane.

As a next step, based on the above results, let us *assume* that $f(\omega)$ is a *meromorphic* function possessing a countable number of simple poles in the lower half space $\mathrm{Im}\{\omega\} < 0$. Consequently, we can expand $f(\omega)$ in the following Laurent series:

$$f(\omega) = \sum_{i=-1,0,\ldots}^{\infty} a_i(\omega_0)(\omega-\omega_0)^i, \text{ with } a_{-1}(\omega_0) = \sum_n a_{-1,n}\delta(\omega_0-\omega_n), \tag{2.17}$$

where ω_n ($\mathrm{Im}\{\omega_n\} < 0$) denotes the complex frequencies of the poles of $f(\omega)$. We also introduced the coefficients $a_{-1,n}$. By making use of Cauchy's residue theorem, we can finally get the following pole expansion of $f(\omega)$:

$$\begin{aligned}
\oint_{C_\infty} \frac{f(\omega')}{\omega'-\omega}\mathrm{d}\omega' &= \oint_{C_\omega} \frac{f(\omega')}{\omega'-\omega}\mathrm{d}\omega' + \sum_n \oint_{C_{\omega_n}} \frac{f(\omega')}{\omega'-\omega}\mathrm{d}\omega' \quad \Rightarrow \\
0 &= 2\pi\mathrm{i} f(\omega) + 2\pi\mathrm{i}\sum_n \frac{a_{-1,n}}{\omega_n-\omega} \quad \Rightarrow \\
f(\omega) &= \sum_n \frac{a_{-1,n}}{\omega-\omega_n},
\end{aligned} \tag{2.18}$$

where C_∞, C_ω and C_{ω_n} denote integration over closed contours in the complex plane with the first being a circular contour around $|\omega'| \to \infty$, the second being a circular contour around $|\omega'-\omega| \to 0$ and the last being a circular contour around $|\omega'-\omega_n| \to 0$.

Last but not least, the analyticity in the upper half-plane ($\mathrm{Im}\{\omega_n\} \geq 0$) gives the following Kramers-Kronig relation that mutually associates the real with the imaginary part of $f(\omega)$ [182]:

$$f(\omega) = \frac{1}{\pi\mathrm{i}} P.V.\left\{\int_{-\infty}^{+\infty} \frac{f(\omega')}{\omega'-\omega}\mathrm{d}\omega'\right\} \tag{2.19}$$

$$= \frac{2}{\pi} P.V.\left\{\int_0^{+\infty} \frac{\omega'\mathrm{Im}\{f(\omega')\} - \mathrm{i}\omega\mathrm{Re}\{f(\omega')\}}{\omega'^2-\omega^2}\mathrm{d}\omega'\right\}, \tag{2.20}$$

with $P.V.\{\cdot\}$ denotes the Cauchy principal value of the improper integral. Moreover, because, as we've shown above, the imaginary part of $f(\omega)$ decays with a rate of $O(1/|\omega|^3)$

for $|\omega| \to \infty$, we can apply the superconvergence theorem, so that, from the latter Kramers Kronig relation together with Eq. (2.16), we get the following sum rule [182]:

$$\frac{\partial \tilde{f}}{\partial t}(0) = \; - \lim_{\omega \to \infty} \left[\omega^2 \mathrm{Re}\left\{f(\omega)\right\}\right] = \; \frac{2}{\pi} \int_0^{+\infty} \omega \mathrm{Im}\left\{f(\omega)\right\} d\omega. \tag{2.21}$$

Let us now apply the above mathematical results, based on the properties of causality and stability, to the particular case of the generalized susceptibility tensor. To begin with, from Eq. (2.19), we readily get (after performing an extra Fourier transform for the third argument) the following generalized Kramers Kronig relation:

$$\boldsymbol{\chi}(\mathbf{r}, \mathbf{r}-\mathbf{r}', \omega-\omega', \omega') \;\; = \;\; \frac{1}{\pi \mathrm{i}} P.V. \left\{ \int_{-\infty}^{+\infty} \frac{\boldsymbol{\chi}(\mathbf{r}, \mathbf{r}-\mathbf{r}', \omega-\omega'', \omega'')}{\omega''-\omega'} d\omega'' \right\}. \tag{2.22}$$

In order to derive a sum rule for the generalized susceptibility tensor based on Eq. (2.21), we need to further specify its asymptotic behavior for large arguments. This is done on physical grounds, even though the section so far has been dealing with purely algebraic manipulations. Specifically, following Ref. [181], we have the physical requirement that for large enough frequencies all the electrons of the medium, which are constant over time within a given volume, should behave like a *plasma*, i.e., like free, unbound electrons with the electric field acting on them. The equation of motion of such electrons (ignoring the magnetic field contribution in the Lorentz force as comparatively minor in strength, and ignoring also the damping from the ionic collisions and any non-local effects as insignificant) is simple: $m_\mathrm{e}\ddot{\mathbf{r}} = q_\mathrm{e}\mathbf{E}(\mathbf{r}, t)$, and gives the following asymptotic behavior of the generalized susceptibility tensor:

$$\lim_{\omega' \to \infty} \left[\omega'^2 \boldsymbol{\chi}(\mathbf{r}, \mathbf{r}-\mathbf{r}', \omega-\omega'', \omega')\right] = -\delta(\mathbf{r}-\mathbf{r}')\delta(\omega-\omega'') \begin{bmatrix} \mathbf{I} & \mathbf{0} \\ \mathbf{0} & \mathbf{0} \end{bmatrix} \frac{N_\mathrm{e}(\mathbf{r}) q_\mathrm{e}^2}{m_\mathrm{e}}, \tag{2.23}$$

where $\mathbf{I}$ is the 3x3 identity matrix and $\mathbf{0}$ is a 3x3 matrix full of zeros. $N_\mathrm{e}(\mathbf{r})$ is the electron density of the medium, while q_e and m_e are the charge and the mass of the electron, respectively. Using the latter equation together with Eq. (2.21), we readily get the following sum rule for the generalized susceptibility tensor:

$$\delta(\mathbf{r}-\mathbf{r}')\delta(\omega-\omega'') \begin{bmatrix} \mathbf{I} & \mathbf{0} \\ \mathbf{0} & \mathbf{0} \end{bmatrix} \frac{\pi N_\mathrm{e}(\mathbf{r}) q_\mathrm{e}^2}{2 m_\mathrm{e}} = \int_0^{+\infty} \omega' \mathrm{Im}\left\{\boldsymbol{\chi}(\mathbf{r}, \mathbf{r}-\mathbf{r}', \omega-\omega'', \omega')\right\} \mathrm{d}\omega'. \tag{2.24}$$

Moreover, in view of Eq. (2.18), and *assuming* that the function of the generalized susceptibility tensor is separable with respect to its two last arguments, i.e., $\tilde{\boldsymbol{\chi}}(\mathbf{r}, \mathbf{r}-\mathbf{r}', t, t-t') = \tilde{\boldsymbol{\chi}}^{(1)}(\mathbf{r}, \mathbf{r}-\mathbf{r}', t)\tilde{\boldsymbol{\chi}}^{(2)}(\mathbf{r}, \mathbf{r}-\mathbf{r}', t-t')$, and, also, that $\tilde{\boldsymbol{\chi}}^{(2)}(\mathbf{r}, \mathbf{r}-\mathbf{r}', t-t')$ is meromorphic with respect to its last argument in frequency domain, we can perform the following pole expansion of the generalized susceptibility tensor by introducing the tensors $\boldsymbol{\chi}_n(\mathbf{r}, \mathbf{r}-\mathbf{r}', \omega-\omega')$ and the resonance frequencies $\omega_n(\mathbf{r}, \mathbf{r}-\mathbf{r}')$:

$$\boldsymbol{\chi}(\mathbf{r}, \mathbf{r}-\mathbf{r}', \omega-\omega', \omega') \;\; = \;\; \sum_n \frac{\boldsymbol{\chi}_n(\mathbf{r}, \mathbf{r}-\mathbf{r}', \omega-\omega')}{\omega' - \omega_n(\mathbf{r}, \mathbf{r}-\mathbf{r}')}, \tag{2.25}$$

which we can recast into the following form so that it abides with the symmetry $\boldsymbol{\chi}(\mathbf{r}, \mathbf{r}-$

$\mathbf{r}', \omega - \omega', \omega') = \boldsymbol{\chi}^*(\mathbf{r}, \mathbf{r} - \mathbf{r}', -\omega^* + \omega'^*, -\omega'^*)$ that is a generalization of Eq. (2.14) for complex frequencies:

$$\boldsymbol{\chi}(\mathbf{r}, \mathbf{r} - \mathbf{r}', \omega - \omega', \omega') = \sum_n \frac{\boldsymbol{\chi}_n(\mathbf{r}, \mathbf{r} - \mathbf{r}', \omega - \omega')}{\omega' - \omega_n(\mathbf{r}, \mathbf{r} - \mathbf{r}')} - \frac{\boldsymbol{\chi}_n^*(\mathbf{r}, \mathbf{r} - \mathbf{r}', \omega' - \omega)}{\omega' + \omega_n^*(\mathbf{r}, \mathbf{r} - \mathbf{r}')}. \tag{2.26}$$

In the above equation, it is considered, without loss of generality, that $\mathrm{Re}\{\omega_n\}$ is positive, with $\mathrm{Re}\{\cdot\}$ denoting the real part of a quantity. If, furthermore, we impose the physical requirement for the asymptotic behavior of Eq. (2.23), we, first, get that the nominators in the fractions of the above equation are equal. This equality implies a real-valued inverse Fourier transform of $\boldsymbol{\chi}_n(\mathbf{r}, \mathbf{r} - \mathbf{r}', \omega - \omega')$ with respect to its last argument. Moreover, we get the following generalized sum rule:

$$\sum_n -2\mathrm{Re}\left\{\omega_n(\mathbf{r}, \mathbf{r} - \mathbf{r}')\right\} \boldsymbol{\chi}_n(\mathbf{r}, \mathbf{r} - \mathbf{r}', \omega - \omega') = \delta(\mathbf{r} - \mathbf{r}')\delta(\omega - \omega') \begin{bmatrix} \mathbf{I} & \mathbf{0} \\ \mathbf{0} & \mathbf{0} \end{bmatrix} \frac{N_\mathrm{e}(\mathbf{r}) q_\mathrm{e}^2}{m_\mathrm{e}}. \tag{2.27}$$

Finally, the generalized susceptibility tensor gets the following expression:

$$\boldsymbol{\chi}(\mathbf{r}, \mathbf{r} - \mathbf{r}', \omega - \omega', \omega') = \sum_n \frac{-2\mathrm{Re}\left\{\omega_n(\mathbf{r}, \mathbf{r} - \mathbf{r}')\right\} \boldsymbol{\chi}_n(\mathbf{r}, \mathbf{r} - \mathbf{r}', \omega - \omega')}{-\omega'^2 + 2\mathrm{i}\,\mathrm{Im}\left\{\omega_n(\mathbf{r}, \mathbf{r} - \mathbf{r}')\right\} \omega' + \left|\omega_n(\mathbf{r}, \mathbf{r} - \mathbf{r}')\right|^2}. \tag{2.28}$$

The latter equation constitutes a Lorentz-pole expansion of the generalized susceptibility tensor. Its physical content can be elucidated once we study the simple case of homogeneous, local, non-magnetic, and isotropic media, where the generalized susceptibility tensor takes the following simplified form: $\boldsymbol{\chi}(\mathbf{r}, \mathbf{r}-\mathbf{r}', \omega-\omega', \omega') = \varepsilon_0 \delta(\mathbf{r}-\mathbf{r}') \begin{bmatrix} \mathbf{I} & \mathbf{0} \\ \mathbf{0} & \mathbf{0} \end{bmatrix} \chi_{\mathrm{ee}}(\omega-\omega', \omega')$, with $\chi_{\mathrm{ee}}(\omega-\omega', \omega')$ being a scalar function. In that case, we can define the following quantities:

$$\begin{aligned}
\omega_\mathrm{p} &= \sqrt{\frac{N_\mathrm{e} q_\mathrm{e}^2}{m_\mathrm{e} \varepsilon_0}}, && (2.29)\\
f_n(\omega - \omega') &= -2\mathrm{Re}\left\{\omega_n\right\} \chi_{\mathrm{ee},n}(\omega - \omega') \omega_\mathrm{p}^{-2}, && (2.30)\\
\gamma_n &= -2\mathrm{Im}\left\{\omega_n\right\}, && (2.31)\\
\omega_{0,n} &= |\omega_n|, && (2.32)
\end{aligned}$$

with ω_p being the plasma frequency of the medium, $f_n(\omega - \omega')$ being the oscillator strengths, γ_n being the damping coefficient of the oscillator, and $\omega_{0,n}$ being the oscillator's central frequency. Those definitions readily give the following reformulated Lorentz-pole expansion (following from Eq. (2.28)):

$$\chi_{\mathrm{ee}}(\omega - \omega', \omega') = \omega_\mathrm{p}^2 \sum_n \frac{f_n(\omega - \omega')}{-\omega'^2 - \mathrm{i}\gamma_n \omega' + \omega_{0,n}^2}. \tag{2.33}$$

with

$$\sum_n f_n(\omega - \omega') = \delta(\omega - \omega') \tag{2.34}$$

being the f-sum rule of Eq. (2.27) rewritten in the new formalism. Moreover, taking the inverse Fourier transform of the latter expression, we get the following f-sum rule in time domain:

$$\sum_n \tilde{f}_n(t) \quad = \quad 1/\sqrt{2\pi}, \tag{2.35}$$

with $\tilde{f}_n(t)$ required to be a real-valued function, as we discussed above, in order to comply with the asymptotic behavior of Eq. (2.23).

Let us highlight now that Eq. (2.33) corresponds to the superposition of the response functions of Lorentz oscillators with time-varying electron densities $\tilde{N}_{\mathrm{e},n}(t) = \sqrt{2\pi}\tilde{f}_n(t)N_\mathrm{e}$. The physical picture corresponds to the case of having $\tilde{N}_{\mathrm{e},n}(t)$ electrons per unit volume oscillating within the potential of the n-th Lorentz harmonic oscillator. The respective electric dipole moments, $\tilde{\mathbf{p}}_{\mathrm{e},n}(\mathbf{r},t)$, obey the following equation of motion [181]:

$$\left[\frac{\partial^2}{\partial t^2} + \gamma_n \frac{\partial}{\partial t} + \omega_{0,n}^2\right] \tilde{\mathbf{p}}_{\mathrm{e},n}(\mathbf{r},t) \quad = \quad \frac{q_\mathrm{e}^2}{m_\mathrm{e}} \tilde{\mathbf{E}}(\mathbf{r},t), \tag{2.36}$$

and the total electric polarization of that medium is given by

$$\tilde{\mathbf{P}}_\mathrm{e}(\mathbf{r},t) \quad = \quad \sum_n \tilde{\mathbf{P}}_{\mathrm{e},n}(\mathbf{r},t) \quad = \quad \sum_n \tilde{N}_{\mathrm{e},n}(t)\tilde{\mathbf{p}}_{\mathrm{e},n}(\mathbf{r},t). \tag{2.37}$$

With the new formulation, it becomes clear that the f-sum rule of Eq. (2.35) simply states that the sum of the electrons oscillating within the potentials of the different Lorentz oscillators should be always constant and equal to the total electron density of the medium:

$$\sum_n \tilde{N}_{\mathrm{e},n}(t) \quad = \quad N_\mathrm{e}. \tag{2.38}$$

The solution of the differential equation of Eq. (2.36) is known to be:

$$\tilde{\mathbf{p}}_{\mathrm{e},n}(\mathbf{r},t) \quad = \quad \int_{-\infty}^{+\infty} \tilde{\alpha}_{\mathrm{ee},n}(t-t')\tilde{\mathbf{E}}(\mathbf{r},t')\,\mathrm{d}t', \tag{2.39}$$

where

$$\tilde{\alpha}_{\mathrm{ee},n}(t) \quad = \quad \frac{1}{\sqrt{\omega_{0,n}^2 - \frac{\gamma_n^2}{4}}} \frac{q_\mathrm{e}^2}{m_\mathrm{e}} H(t) e^{-\frac{\gamma_n}{2}t} \sin\left(t\sqrt{\omega_{0,n}^2 - \frac{\gamma_n^2}{4}}\right) \tag{2.40}$$

is the electric polarizability kernel of the Lorentz oscillator and $H(t)$ is the Heaviside step function. From the latter equation, together with Eqs. (2.5,2.6,2.37), we readily get the susceptibility of the medium in time domain

$$\tilde{\chi}_\mathrm{ee}(t,t-t') \quad = \quad \frac{1}{\varepsilon_0}\sum_n \tilde{N}_{\mathrm{e},n}(t)\tilde{\alpha}_{\mathrm{ee},n}(t-t'), \tag{2.41}$$

with $\tilde{\chi}_{\mathrm{ee}}(t, t-t')$ being the inverse Fourier transform of $\chi_{\mathrm{ee}}(\omega-\omega', \omega')$.

As we've shown, the above-described model for the susceptibility of a time-varying medium nicely respects the principles of causality and stability, however, it has a significant drawback from another physics point of view. As we see from Eq. (2.37), the electric polarization density of the n-th Lorentz oscillator $\tilde{\mathbf{P}}_{\mathrm{e},n}$ at time t induced by an electric field impulse at time t' is not proportional to the electron density of the n-th Lorentz oscillator at the time of the impulse excitation t', $\tilde{N}_{\mathrm{e},n}(t')$. We can attempt to fix this problem by slightly modifying our model. Specifically, we need to drop the previous assumption that the function of the generalized susceptibility tensor $\tilde{\boldsymbol{\chi}}(\mathbf{r}, \mathbf{r}-\mathbf{r}', t, t-t')$ is separable with respect to its two last arguments and express the susceptibility of the medium as

$$\tilde{\chi}_{\mathrm{ee}}(t, t-t') \;=\; \frac{1}{\varepsilon_0}\sum_n \tilde{N}_{\mathrm{e},n}(t')\tilde{\alpha}_{\mathrm{ee},n}(t-t'). \tag{2.42}$$

Note the slight difference between the last equation and Eq. (2.41). In this way, we managed to correct the old model in a way that only the *available* electrons per unit volume within the potential of each Lorentz oscillator get excited by the electric field at each moment. In this case, it is easy to show that $\tilde{\mathbf{P}}_{\mathrm{e},n}$ obeys the following partial differential equation:

$$\left[\frac{\partial^2}{\partial t^2} + \gamma_n \frac{\partial}{\partial t} + \omega_{0,n}^2\right]\tilde{\mathbf{P}}_{\mathrm{e},n}(\mathbf{r}, t) \;=\; \frac{q_{\mathrm{e}}^2}{m_{\mathrm{e}}}\tilde{N}_{\mathrm{e},n}(t)\tilde{\mathbf{E}}(\mathbf{r}, t), \tag{2.43}$$

and that the corresponding electric susceptibility takes the following form in frequency domain:

$$\chi_{\mathrm{ee}}(\omega-\omega', \omega') \;=\; \omega_{\mathrm{p}}^2 \sum_n \frac{f_n(\omega-\omega')}{-\omega^2 - \mathrm{i}\gamma_n\omega + \omega_{0,n}^2}. \tag{2.44}$$

Note, again, the slight difference between the latter equation and Eq. (2.33). It is important to note that the latter model of the susceptibility also respects the principles of causality and stability, and that it obeys the same f-sum rules as the previous model (see Eqs. (2.34,2.35)). Moreover, note how either of the two above presented models collapse to well-known expressions for the stationary case where $\tilde{N}_{\mathrm{e},n}(t)$ is constant over time and, therefore, $N_{\mathrm{e},n}(\omega-\omega') = \sqrt{2\pi} f_n(\omega-\omega')N_{\mathrm{e}}$ is proportional to $\delta(\omega-\omega')$.

Furthermore, we would like to highlight that the last presented model for the susceptibility is still plagued by an unphysical aspect. In this model, once the electrons get excited by the electric field, they oscillate to infinity according to the damped oscillations described by the electric polarizability kernel of Eq. (2.40), contributing to the polarization of the medium. However, this physical picture fails to account for the temporal variations of the electron density of the medium. Some electrons, after they get excited by the electric field, at a later moment are "removed" from the medium before they manage to "finish" their damped oscillations. In order to account for this problem, a further modification of our phenomenological model for the electric susceptibility of the medium could be the following:

$$\tilde{\chi}_{\mathrm{ee}}(t, t-t') \;=\; \frac{1}{\varepsilon_0}\sum_n \tilde{\alpha}_{\mathrm{ee},n}(t-t') \int_0^{\tilde{N}_{\mathrm{e},n}(t')} H\left(\tau(n', t') - t\right) \mathrm{d}n', \tag{2.45}$$

where $\tau(n', t')$ is equal to the minimum time greater than t' for which we have that $\tilde{N}_{\mathrm{e},n}(\tau(n', t')) < n'$. Here, we integrate over the variable n' to separately account for the excitation of each electron available in the medium at a given time t'. The introduced Heaviside step function accounts for the lifetime of each electron in the medium. According to this model, each electron associated with the variable n' shall obey a Lorentzian differential equation whose damping coefficient, though, goes to infinity during temporal windows where we have $\tilde{N}_{\mathrm{e},n}(t) > n$ in order to account for the "removal" of the electron from the medium during those windows in time. Let us note that such kind of considerations discussed here, could be potentially ignored, though, if we assume that the oscillatory decay of the electrons happens much faster compared to the time scale of the temporal variations of the electron density of the medium.

Finally, we would like to emphasize that the above described models are all phenomenological models that we constructed just based on the principles of causality and stability of the system, together with some extra basic physical considerations that we imposed to improve further the model. For example, let us note that in the above analysis, specifically for the derivation in Eq. (2.18), we have tacitly assumed for simplicity the analyticity of the function $f(\omega)$ all along the real frequency axis. This entails the absence of Drude type of oscillators in the pole expansion of the generalized susceptibility tensor, which correspond to a pole at zero frequency ($\omega_{0,n} = 0$). Such kind of extra terms, can be straightforwardly taken into consideration in the analysis, in order to account for the additional presence of free charge carriers in the medium, which is commonly the case for conductors with available intraband transitions.

It is crucial to highlight that, although such phenomenological mass-spring-damper models of the media (as is the Lorentz oscillator model) may provide a quite simple modeling of the response of the medium upon electromagnetic excitation, behind them there is always the quite more complicated quantum mechanical reality of the dynamics within the medium. Generally, such phenomenological Lorentz-pole-based models for the susceptibility can provide a good description of the response of the media though [183]. In fact, in the sixth chapter of Ref. [184], it is shown that a similar Lorentz-pole expansion of the response of a medium can be reached by following a quantum description of the optical properties of crystals. Specifically, the resonance frequencies of the crystal ($\omega_{0,n}$) in the quantum description are associated with interband transitions of the electrons from the valence to the conduction band that are characterized by non-vanishing dipole matrix elements and a large joint density of states (JDOS) [81]. Large JDOS occurs at critical points of the electronic band structure of the crystal, where the valence and conduction bands have the same slope locally. Photons with energy similar to the energy difference between the valence and conduction band at the critical points are, therefore, efficiently absorbed. On the other hand, in the quantum description, Drude-type of poles in the optical response function of a crystal are associated with intraband transitions and have oscillator strengths related to the curvature of the bands at the positions where they cross the Fermi level.

A non-phenomenological quantum description of non-stationary media, whose optical properties are modulated in time through some external physical mechanism, may be essential in providing physically accurate models (i.e., models that capture properly the physics of the realistic external modulation mechanism) of the linear optical response of such media that is represented by the susceptibility tensor $\boldsymbol{\chi}(\mathbf{r}, \mathbf{r}-\mathbf{r}', \omega-\omega', \omega')$. However, we would like to note that such a quantum description of non-stationary media goes beyond the scope of this thesis and, unfortunately, to the best of our knowledge, is an interesting open research topic that is not yet studied in the relevant literature. For this reason, in this thesis, we will simply adopt the Lorentz-pole-based phenomenological models that we

developed in this section to describe in a more abstract way the optical response function of non-stationary media.

2.4 Generalized Poynting's theorem and conservation of energy and photon number in linear media

In this section, we will discuss the electromagnetic energy balance, as well as the photon number balance within a general non-local, non-homogeneous, bi-anisotropic linear medium with both spatial and temporal dispersion, as introduced in Section 2.2.

The flow of electromagnetic energy inside a medium is dictated by the differential equation of Poynting's theorem, which is a simple algebraic derivation following from the macroscopic Maxwell equations in time domain. It reads as follows:

$$\tilde{\mathbf{E}}\cdot\tilde{\mathbf{J}}+\tilde{\mathbf{E}}\cdot\frac{\partial\tilde{\mathbf{P}}_{\mathrm{e}}}{\partial t}+\tilde{\mathbf{H}}\cdot\frac{\partial\tilde{\mathbf{P}}_{\mathrm{m}}}{\partial t}+\frac{1}{2}\frac{\partial}{\partial t}\left(\varepsilon_0\left|\tilde{\mathbf{E}}\right|^2+\mu_0\left|\tilde{\mathbf{H}}\right|^2\right)+\nabla\cdot\left(\tilde{\mathbf{E}}\times\tilde{\mathbf{H}}\right)=0. \tag{2.46}$$

We can identify the following terms in the above expression:

➢ The first term is the power density provided by the electromagnetic field to the external free sources:

$$\tilde{P}_{\mathrm{source}}(\mathbf{r},t) \;=\; \tilde{\mathbf{E}}\cdot\tilde{\mathbf{J}}. \tag{2.47}$$

This can be shown by calculating the work done by an electromagnetic field on external free moving charges (with speed $\mathbf{v}$) through the macroscopic Lorentz Force law: $\partial W_{\mathrm{source}}=\tilde{\rho}\partial^3\mathbf{r}\left(\tilde{\mathbf{E}}+\mu_0\mathbf{v}\times\tilde{\mathbf{H}}\right)\cdot\mathbf{v}\partial t=\tilde{\mathbf{E}}\cdot\tilde{\mathbf{J}}\partial^3\mathbf{r}\partial t$.

➢ The second term is the power density provided by the electromagnetic field to the bound moving charges of the medium:

$$\tilde{P}_{\mathrm{medium}}(\mathbf{r},t) \;=\; \tilde{\mathbf{E}}\cdot\frac{\partial\tilde{\mathbf{P}}_{\mathrm{e}}}{\partial t}+\tilde{\mathbf{H}}\cdot\frac{\partial\tilde{\mathbf{P}}_{\mathrm{m}}}{\partial t}. \tag{2.48}$$

The two terms can be shown to be the power density provided by the electromagnetic field to the polarization and magnetization of the medium, respectively [185].

➢ The third term is the local gain power density of the electromagnetic field:

$$\tilde{P}_{\mathrm{field}}(\mathbf{r},t) \;=\; \frac{1}{2}\frac{\partial}{\partial t}\left(\varepsilon_0\left|\tilde{\mathbf{E}}\right|^2+\mu_0\left|\tilde{\mathbf{H}}\right|^2\right), \tag{2.49}$$

since the local electromagnetic energy density is equal to $\frac{1}{2}\left(\varepsilon_0\left|\tilde{\mathbf{E}}\right|^2+\mu_0\left|\tilde{\mathbf{H}}\right|^2\right)$.

➢ The last term is the divergence of the Poynting vector $\tilde{\mathbf{S}}(\mathbf{r},t)=\tilde{\mathbf{E}}\times\tilde{\mathbf{H}}$ representing the local outflow power density of the electromagnetic field:

$$\tilde{P}_{\mathrm{outflow}}(\mathbf{r},t) \;=\; \nabla\cdot\tilde{\mathbf{S}}. \tag{2.50}$$

Therefore, Poynting's theorem can be rewritten as the following equation of energy conservation:

$$\tilde{P}_{\text{sources}}(\mathbf{r},t)+\tilde{P}_{\text{medium}}(\mathbf{r},t)+\tilde{P}_{\text{field}}(\mathbf{r},t)+\tilde{P}_{\text{outflow}}(\mathbf{r},t)=0, \tag{2.51}$$

i.e., the outflow of electromagnetic power per unit volume is equal to the power per unit volume provided by the external free sources, the polarized medium, and the electromagnetic field.

The total energy absorbed by the medium is given by the following formula:

$$\begin{aligned} W_{\text{medium}} &= \int_{-\infty}^{+\infty}\int_{\mathbb{R}^3}\tilde{P}_{\text{medium}}(\mathbf{r},t)\mathrm{d}^3\mathbf{r}\mathrm{d}t && (2.52)\\ &= -\int_{-\infty}^{+\infty}\int_{\mathbb{R}^3}\omega\,\mathrm{Im}\left\{\mathbf{E}\cdot\mathbf{P}_{\text{e}}^{*}+\mathbf{H}\cdot\mathbf{P}_{\text{m}}^{*}\right\}\mathrm{d}^3\mathbf{r}\mathrm{d}\omega && (2.53)\\ &= \iint_{-\infty}^{+\infty}\iint_{\mathbb{R}^3}\begin{bmatrix}\mathbf{E}(\mathbf{r},\omega)\\ \mathbf{H}(\mathbf{r},\omega)\end{bmatrix}^{\dagger}\cdot\boldsymbol{\mathcal{W}}(\mathbf{r},\mathbf{r}',\omega,\omega')\cdot\begin{bmatrix}\mathbf{E}(\mathbf{r}',\omega')\\ \mathbf{H}(\mathbf{r}',\omega')\end{bmatrix}\mathrm{d}^3\mathbf{r}\mathrm{d}^3\mathbf{r}'\mathrm{d}\omega\mathrm{d}\omega', && (2.54)\end{aligned}$$

with the 6x6 matrix $\boldsymbol{\mathcal{W}}$ being given by

$$\boldsymbol{\mathcal{W}} = \begin{bmatrix}\boldsymbol{\mathcal{W}}_{\text{ee}} & \boldsymbol{\mathcal{W}}_{\text{em}}\\ \boldsymbol{\mathcal{W}}_{\text{me}} & \boldsymbol{\mathcal{W}}_{\text{mm}}\end{bmatrix}, \tag{2.55}$$

with

$$\begin{aligned} \boldsymbol{\mathcal{W}}_{\text{ee}} &= \tfrac{\omega\varepsilon_0}{2\mathrm{i}}\left[\boldsymbol{\chi}_{\text{ee}}(\mathbf{r},\mathbf{r}-\mathbf{r}',\omega-\omega',\omega')-\tfrac{\omega'}{\omega}\boldsymbol{\chi}_{\text{ee}}^{\dagger}(\mathbf{r}',\mathbf{r}'-\mathbf{r},\omega'-\omega,\omega)\right], && (2.56)\\ \boldsymbol{\mathcal{W}}_{\text{em}} &= \tfrac{\omega\sqrt{\varepsilon_0\mu_0}}{2\mathrm{i}}\left[\boldsymbol{\chi}_{\text{em}}(\mathbf{r},\mathbf{r}-\mathbf{r}',\omega-\omega',\omega')-\tfrac{\omega'}{\omega}\boldsymbol{\chi}_{\text{me}}^{\dagger}(\mathbf{r}',\mathbf{r}'-\mathbf{r},\omega'-\omega,\omega)\right], && (2.57)\\ \boldsymbol{\mathcal{W}}_{\text{me}} &= \tfrac{\omega\sqrt{\varepsilon_0\mu_0}}{2\mathrm{i}}\left[\boldsymbol{\chi}_{\text{me}}(\mathbf{r},\mathbf{r}-\mathbf{r}',\omega-\omega',\omega')-\tfrac{\omega'}{\omega}\boldsymbol{\chi}_{\text{em}}^{\dagger}(\mathbf{r}',\mathbf{r}'-\mathbf{r},\omega'-\omega,\omega)\right], && (2.58)\\ \boldsymbol{\mathcal{W}}_{\text{mm}} &= \tfrac{\omega\mu_0}{2\mathrm{i}}\left[\boldsymbol{\chi}_{\text{mm}}(\mathbf{r},\mathbf{r}-\mathbf{r}',\omega-\omega',\omega')-\tfrac{\omega'}{\omega}\boldsymbol{\chi}_{\text{mm}}^{\dagger}(\mathbf{r}',\mathbf{r}'-\mathbf{r},\omega'-\omega,\omega)\right]. && (2.59)\end{aligned}$$

Here, the symbol (†) denotes the conjugate transpose of a matrix. We got Eq. (2.53) by plugging the Fourier transform of Eq. (2.48) in Eq. (2.52), and then we used Eqs. (2.12,2.13) to get Eq. (2.54).

Importantly, note that the matrix $\boldsymbol{\mathcal{W}}$ has the following symmetry property:

$$\boldsymbol{\mathcal{W}}(\mathbf{r},\mathbf{r}',\omega,\omega') = \boldsymbol{\mathcal{W}}^{\dagger}(\mathbf{r}',\mathbf{r},\omega',\omega). \tag{2.60}$$

Therefore, we can recast Eq. (2.54) into the following Hermitian quadratic form, in Dirac notation, by introducing the self-adjoint operator $\hat{\mathbb{W}}$ (which we assume to be compact):

$$W_{\text{medium}} = \langle \text{EM}_{\text{field}}|\,\hat{\mathbb{W}}\,|\text{EM}_{\text{field}}\rangle\,. \tag{2.61}$$

In view of the latter equation, according to the spectral theorem for a compact self-adjoint operator, we can formulate the following properties of the operator $\hat{\mathbb{W}}$ that reflect on the energy absorption properties of the system for *arbitrary* electromagnetic fields:

- ➢ For $\hat{\mathbb{W}}$ being a *positive semi-definite* operator, i.e., in the case that all its eigenvalues are non-negative, we get that $W_{\text{medium}} \geq 0$, i.e., the system is *passive*.
- ➢ Specifically, for $\hat{\mathbb{W}} = \hat{\mathbf{0}}$, i.e., for $\boldsymbol{\mathcal{W}}(\mathbf{r}, \mathbf{r}', \omega, \omega') = \mathbf{0}$, we get that $W_{\text{medium}} = 0$, i.e., the system is *lossless* and conserves energy. Hence, let us highlight that energy conservation manifests itself as a symmetry condition of the generalized susceptibility tensor given by the equation $\boldsymbol{\mathcal{W}}(\mathbf{r}, \mathbf{r}', \omega, \omega') = \mathbf{0}$. Note that, for the special case of a *stationary* system, the latter condition, $\boldsymbol{\mathcal{W}}(\mathbf{r}, \mathbf{r}', \omega, \omega') = \mathbf{0}$, boils down to well-known expressions characterizing lossless media: $\boldsymbol{\chi}_{\text{ee,stationary}}(\mathbf{r}, \mathbf{r} - \mathbf{r}', \omega) = \boldsymbol{\chi}^{\dagger}_{\text{ee,stationary}}(\mathbf{r}', \mathbf{r}' - \mathbf{r}, \omega)$, $\boldsymbol{\chi}_{\text{em,stationary}}(\mathbf{r}, \mathbf{r} - \mathbf{r}', \omega) = \boldsymbol{\chi}^{\dagger}_{\text{me,stationary}}(\mathbf{r}', \mathbf{r}' - \mathbf{r}, \omega)$ and $\boldsymbol{\chi}_{\text{mm,stationary}}(\mathbf{r}, \mathbf{r} - \mathbf{r}', \omega) = \boldsymbol{\chi}^{\dagger}_{\text{mm,stationary}}(\mathbf{r}', \mathbf{r}' - \mathbf{r}, \omega)$. We would like to highlight that in this case, apart from a global, we also have a local conservation of energy, since the system operator is diagonal with respect to $\mathbf{r}$, For the same reason, i.e., because in that case the system operator is diagonal with respect to ω as well, we also have energy conservation for each individual frequency ω. Moreover, Fourier-transforming the susceptibility tensors from the real $(\mathbf{r}, \omega)$- into the momentum $(\mathbf{k}, \omega)$-space, we can also get similar expressions for the case of *homogeneous* but *non-local*, *stationary* systems. In the last case, apart from globally, energy is also conserved for each individual momentum $\mathbf{k}$, since the system operator is diagonal with respect to it.
- ➢ For $\hat{\mathbb{W}}$ being a *negative definite* operator, i.e., in the case that all its eigenvalues are negative, we get that $W_{\text{medium}} < 0$, i.e., the system is *active*.
- ➢ For $\hat{\mathbb{W}}$ being an *indefinite* operator, i.e., in the more general case that its eigenvalues take both positive and negative values, the system may behave either as *active* or *passive* depending on the particular electromagnetic fields.

Let us now formulate the generalized Poynting theorem in its integral form in frequency domain. For this, we consider an arbitrary finite volume V enclosed by a surface S (whose pointing-outwards normal unit vector we denote with $\hat{\mathbf{n}}$) that shall contain all space that encompasses non-local interactions. By integrating Eq. (2.51) over time and space V, we get that the total energy absorbed by the polarized medium inside V is given by the formula:

$$\begin{aligned} W_{\text{medium},V} &= \int_{-\infty}^{+\infty} \int_V \tilde{P}_{\text{medium}}(\mathbf{r}, t) \mathrm{d}^3\mathbf{r}\mathrm{d}t \\ &= \langle \mathrm{EM}_{\text{field}} | \, \hat{\mathbb{W}}_V \, | \mathrm{EM}_{\text{field}} \rangle \\ &= -W_{\text{sources},V} - W_{\text{outflow},V}, \end{aligned} \tag{2.62}$$

where, in the above energy conservation equation, we have defined the quantities

$$W_{\text{sources},V} = \int_{-\infty}^{+\infty} \int_V \mathrm{Re}\left\{\mathbf{E} \cdot \mathbf{J}^*\right\} \mathrm{d}^3\mathbf{r}\mathrm{d}\omega, \tag{2.63}$$

$$W_{\text{outflow},V} = \int_{-\infty}^{+\infty} \oiint_S \hat{\mathbf{n}} \cdot \mathbf{S} \, \mathrm{d}^2\mathbf{r}\mathrm{d}\omega, \tag{2.64}$$

$$\text{with} \quad \mathbf{S} = \mathrm{Re}\left\{\mathbf{E} \times \mathbf{H}^*\right\} \tag{2.65}$$

being the Poynting vector in frequency domain, representing the electromagnetic power

flux density. The quantity $W_{\text{sources},V}$ denotes the total electromagnetic energy absorbed by the free external sources, whereas the quantity $W_{\text{outflow},V}$ denotes the total electromagnetic energy that flowed outside the surface S enclosing the volume V. With $\hat{\mathbb{W}}_V$ we denote the same operator as in Eq. (2.54), but with the spatial integrals spanning only the volume V. We get Eqs. (2.63-2.65) by integrating over time and space V, and Fourier transforming Eqs. (2.47,2.50), respectively. For the latter term, we also made use of Gauss's theorem to convert the initial volumetric integral of the divergence of the Poynting vector into the final surface integral. The generalized Poynting theorem in its integral form simply states that the total energy absorbed by a medium inside V is equal to the total energy provided by the sources inside V minus the total net energy that flowed outside V.

Importantly, note that, in view of the discussion above and specifically Eqs. (2.56-2.59), a non-stationary medium that does *not* break energy conservation is generally unrealistic. Actually, according to Noether's theorem, energy conservation is directly related with the symmetry of continuous translation over time, which, in our case, is broken by a non-stationary system. In a later chapter, we will make use of this property to drive a sphere made from a non-stationary material into a lasing state by means of parametric oscillations.

We would like to highlight that, while energy conservation in stationary systems is equivalent to photon number conservation, this is not the case for non-stationary systems. Since the energy of a photon of frequency ω is equal to $\hbar\omega$, with $\hbar$ being the reduced Planck constant, we can get the following expression for the total number of photons absorbed inside the medium, N_{medium}, by dividing the integrand of the spectral integral of Eq. (2.53) -recasted into a form involving integration over positive, only, frequencies- with the single photon energy $\hbar\omega$:

$$N_{\text{medium}} = -\frac{2}{\hbar}\int_{0^+}^{+\infty}\int_{\mathbb{R}^3} \text{Im}\left\{\mathbf{E}\cdot\mathbf{P}_{\text{e}}^{*} + \mathbf{H}\cdot\mathbf{P}_{\text{m}}^{*}\right\}\text{d}^3\mathbf{r}\text{d}\omega \tag{2.66}$$

$$= \iint_{-\infty}^{+\infty}\iint_{\mathbb{R}^3}\begin{bmatrix}\mathbf{E}(\mathbf{r},\omega)\\ \mathbf{H}(\mathbf{r},\omega)\end{bmatrix}^{\dagger}\cdot\boldsymbol{\mathcal{N}}(\mathbf{r},\mathbf{r}',\omega,\omega')\cdot\begin{bmatrix}\mathbf{E}(\mathbf{r}',\omega')\\ \mathbf{H}(\mathbf{r}',\omega')\end{bmatrix}\text{d}^3\mathbf{r}\text{d}^3\mathbf{r}'\text{d}\omega\text{d}\omega', \tag{2.67}$$

with the 6x6 matrix $\boldsymbol{\mathcal{N}}$ being given by

$$\boldsymbol{\mathcal{N}} = \begin{bmatrix}\boldsymbol{\mathcal{N}}_{\text{ee}} & \boldsymbol{\mathcal{N}}_{\text{em}}\\ \boldsymbol{\mathcal{N}}_{\text{me}} & \boldsymbol{\mathcal{N}}_{\text{mm}}\end{bmatrix}, \tag{2.68}$$

with

$$\boldsymbol{\mathcal{N}}_{\text{ee}} = \frac{\varepsilon_0}{2\text{i}\hbar}\left[\frac{\omega}{|\omega|}\boldsymbol{\chi}_{\text{ee}}(\mathbf{r},\mathbf{r}-\mathbf{r}',\omega-\omega',\omega') - \frac{\omega'}{|\omega'|}\boldsymbol{\chi}_{\text{ee}}^{\dagger}(\mathbf{r}',\mathbf{r}'-\mathbf{r},\omega'-\omega,\omega)\right], \tag{2.69}$$

$$\boldsymbol{\mathcal{N}}_{\text{em}} = \frac{\sqrt{\varepsilon_0\mu_0}}{2\text{i}\hbar}\left[\frac{\omega}{|\omega|}\boldsymbol{\chi}_{\text{em}}(\mathbf{r},\mathbf{r}-\mathbf{r}',\omega-\omega',\omega') - \frac{\omega'}{|\omega'|}\boldsymbol{\chi}_{\text{me}}^{\dagger}(\mathbf{r}',\mathbf{r}'-\mathbf{r},\omega'-\omega,\omega)\right], \tag{2.70}$$

$$\boldsymbol{\mathcal{N}}_{\text{me}} = \frac{\sqrt{\varepsilon_0\mu_0}}{2\text{i}\hbar}\left[\frac{\omega}{|\omega|}\boldsymbol{\chi}_{\text{me}}(\mathbf{r},\mathbf{r}-\mathbf{r}',\omega-\omega',\omega') - \frac{\omega'}{|\omega'|}\boldsymbol{\chi}_{\text{em}}^{\dagger}(\mathbf{r}',\mathbf{r}'-\mathbf{r},\omega'-\omega,\omega)\right], \tag{2.71}$$

$$\boldsymbol{\mathcal{N}}_{\text{mm}} = \frac{\mu_0}{2\text{i}\hbar}\left[\frac{\omega}{|\omega|}\boldsymbol{\chi}_{\text{mm}}(\mathbf{r},\mathbf{r}-\mathbf{r}',\omega-\omega',\omega') - \frac{\omega'}{|\omega'|}\boldsymbol{\chi}_{\text{mm}}^{\dagger}(\mathbf{r}',\mathbf{r}'-\mathbf{r},\omega'-\omega,\omega)\right]. \tag{2.72}$$

Proceeding in the same way like before, we can recast Eq. (2.67) into the following Hermitian quadratic form, in Dirac notation, by introducing the self-adjoint operator $\hat{\mathbb{N}}$ (which we assume to be compact):

$$N_{\text{medium}} = \langle \text{EM}_{\text{field}} | \, \hat{\mathbb{N}} \, | \text{EM}_{\text{field}} \rangle \, . \tag{2.73}$$

Note that, for $\hat{\mathbb{N}} = \hat{\mathbf{0}}$, i.e., for $\boldsymbol{\mathcal{N}}(\mathbf{r}, \mathbf{r}', \omega, \omega') = \mathbf{0}$, we get that $N_{\text{medium}} = 0$, i.e., the system conserves the number of photons. Moreover, it is evident from the above equations that for stationary systems the condition $\hat{\mathbb{N}} = \hat{\mathbf{0}}$ is equivalent to the condition $\hat{\mathbb{W}} = \hat{\mathbf{0}}$, i.e., for stationary systems energy conservation simultaneously implies photon number conservation, which is not generally the case for non-stationary systems. Importantly, it is also evident from the above equations that a non-stationary system, apart from breaking energy conservation as we discussed before, generally breaks also the photon number conservation. However, we can identify a special class of media that conserves the number of photons as long as they have the following three properties: 1) they are dispersionless, i.e., they are characterized by an instantaneous response, 2) they do *not* couple frequencies of opposite signs and 3) their susceptibility tensors have the following symmetries in time domain:

$$\tilde{\boldsymbol{\chi}}_{\text{ee,instant}}(\mathbf{r}, \mathbf{r} - \mathbf{r}', t) = \tilde{\boldsymbol{\chi}}^{\text{T}}_{\text{ee,instant}}(\mathbf{r}', \mathbf{r}' - \mathbf{r}, t), \tag{2.74}$$

$$\tilde{\boldsymbol{\chi}}_{\text{em,instant}}(\mathbf{r}, \mathbf{r} - \mathbf{r}', t) = \tilde{\boldsymbol{\chi}}^{\text{T}}_{\text{me,instant}}(\mathbf{r}', \mathbf{r}' - \mathbf{r}, t), \tag{2.75}$$

$$\tilde{\boldsymbol{\chi}}_{\text{mm,instant}}(\mathbf{r}, \mathbf{r} - \mathbf{r}', t) = \tilde{\boldsymbol{\chi}}^{\text{T}}_{\text{mm,instant}}(\mathbf{r}', \mathbf{r}' - \mathbf{r}, t). \tag{2.76}$$

The second required property that we just mentioned practically implies though that photon number conservation inside such a class of dispersionless, non-stationary media does *not* hold true for *arbitrary* electromagnetic fields: in order that the number of photons are conserved we need to operate the system in large enough frequencies compared to the bandwidth of the susceptibility tensors, so that we practically avoid the undesired coupling between positive and negative frequencies, which could spoil the photon number conservation.

Furthermore, starting from the following equation, which can be derived directly from Maxwell's equations:

$$\text{Re}\left\{ \text{i}\omega \left(\mathbf{E} \cdot \mathbf{P}^*_{\text{e}} + \mathbf{H} \cdot \mathbf{P}^*_{\text{m}} \right) + \mathbf{E} \cdot \mathbf{J}^* + \nabla \cdot (\mathbf{E} \times \mathbf{H}^*) \right\} = 0, \tag{2.77}$$

we can get the following photon number conservation equation in analogy to the generalized Poynting theorem in its integral form:

$$N_{\text{medium},V} = -N_{\text{sources},V} - N_{\text{outflow},V}, \tag{2.78}$$

with

$$\begin{aligned} N_{\text{medium},V} &= -\frac{2}{\hbar} \int_{0^+}^{+\infty} \int_V \text{Im} \left\{ \mathbf{E} \cdot \mathbf{P}^*_{\text{e}} + \mathbf{H} \cdot \mathbf{P}^*_{\text{m}} \right\} \text{d}^3\mathbf{r} \text{d}\omega \\ &= \langle \text{EM}_{\text{field}} | \, \hat{\mathbb{N}}_V \, | \text{EM}_{\text{field}} \rangle \, , \end{aligned} \tag{2.79}$$

$$N_{\text{sources},V} = \int_{0^+}^{+\infty} \int_V \frac{2\text{Re}\left\{ \mathbf{E} \cdot \mathbf{J}^* \right\}}{\hbar\omega} \text{d}^3\mathbf{r} \text{d}\omega, \tag{2.80}$$

$$N_{\text{outflow},V} = \int_{0^+}^{+\infty} \oiint_S \frac{2\hat{\mathbf{n}} \cdot \mathbf{S}}{\hbar\omega} \, \text{d}^2\mathbf{r} \text{d}\omega. \tag{2.81}$$

It is straightforward to show that the three above quantities represent the total number of photons that are absorbed by the medium inside volume V, the total number of photons absorbed by the free external sources inside volume V and the total number of photons that flowed outside the surface S enclosing the volume V, respectively. In a similar fashion like before, with $\hat{\mathbb{N}}_V$ we denote the same operator as in Eq. (2.67), but with the spatial integrals spanning only the volume V, which is arbitrary but shall contain all space that encompasses non-local interactions.

Finally, we would like to highlight, that, quite interestingly, time-varying media with traveling wave space-time modulation have been recently identified to possess eigenmodes that conserve the number of *pseudo-photons*, which are considered to be photons of putative negative energies for negative frequencies [186–188]. Specifically, the number of such pseudo-photons absorbed inside the medium is given by the following formula:

$$N'_{\text{medium}} = -\frac{1}{\hbar}\int_{-\infty}^{+\infty}\int_{\mathbb{R}^3} \text{Im}\left\{\mathbf{E}\cdot\mathbf{P}_{\text{e}}^{*}+\mathbf{H}\cdot\mathbf{P}_{\text{m}}^{*}\right\}\text{d}^3\mathbf{r}\text{d}\omega \tag{2.82}$$

$$= \iint_{-\infty}^{+\infty}\iint_{\mathbb{R}^3}\begin{bmatrix}\mathbf{E}(\mathbf{r},\omega)\\ \mathbf{H}(\mathbf{r},\omega)\end{bmatrix}^{\dagger}\cdot\boldsymbol{\mathcal{N}}'(\mathbf{r},\mathbf{r}',\omega,\omega')\cdot\begin{bmatrix}\mathbf{E}(\mathbf{r}',\omega')\\ \mathbf{H}(\mathbf{r}',\omega')\end{bmatrix}\text{d}^3\mathbf{r}\text{d}^3\mathbf{r}'\text{d}\omega\text{d}\omega', \tag{2.83}$$

with the 6x6 matrix $\boldsymbol{\mathcal{N}}'$ being given by

$$\boldsymbol{\mathcal{N}}' = \begin{bmatrix}\boldsymbol{\mathcal{N}}'_{\text{ee}} & \boldsymbol{\mathcal{N}}'_{\text{em}}\\ \boldsymbol{\mathcal{N}}'_{\text{me}} & \boldsymbol{\mathcal{N}}'_{\text{mm}}\end{bmatrix}, \tag{2.84}$$

with

$$\boldsymbol{\mathcal{N}}'_{\text{ee}} = \frac{\varepsilon_0}{2\text{i}\hbar}\left[\boldsymbol{\chi}_{\text{ee}}(\mathbf{r},\mathbf{r}-\mathbf{r}',\omega-\omega',\omega')-\boldsymbol{\chi}^{\dagger}_{\text{ee}}(\mathbf{r}',\mathbf{r}'-\mathbf{r},\omega'-\omega,\omega)\right], \tag{2.85}$$

$$\boldsymbol{\mathcal{N}}'_{\text{em}} = \frac{\sqrt{\varepsilon_0\mu_0}}{2\text{i}\hbar}\left[\boldsymbol{\chi}_{\text{em}}(\mathbf{r},\mathbf{r}-\mathbf{r}',\omega-\omega',\omega')-\boldsymbol{\chi}^{\dagger}_{\text{me}}(\mathbf{r}',\mathbf{r}'-\mathbf{r},\omega'-\omega,\omega)\right], \tag{2.86}$$

$$\boldsymbol{\mathcal{N}}'_{\text{me}} = \frac{\sqrt{\varepsilon_0\mu_0}}{2\text{i}\hbar}\left[\boldsymbol{\chi}_{\text{me}}(\mathbf{r},\mathbf{r}-\mathbf{r}',\omega-\omega',\omega')-\boldsymbol{\chi}^{\dagger}_{\text{em}}(\mathbf{r}',\mathbf{r}'-\mathbf{r},\omega'-\omega,\omega)\right], \tag{2.87}$$

$$\boldsymbol{\mathcal{N}}'_{\text{mm}} = \frac{\mu_0}{2\text{i}\hbar}\left[\boldsymbol{\chi}_{\text{mm}}(\mathbf{r},\mathbf{r}-\mathbf{r}',\omega-\omega',\omega')-\boldsymbol{\chi}^{\dagger}_{\text{mm}}(\mathbf{r}',\mathbf{r}'-\mathbf{r},\omega'-\omega,\omega)\right]. \tag{2.88}$$

Importantly, in view of the above it is straightforward to show that a *dispersionless* medium with the symmetry properties of Eqs. (2.74-2.76) always conserves the number of such pseudo-photons, no matter whether there is coupling between frequencies of opposite signs. Conservation of the number of true photons ($\boldsymbol{\mathcal{N}} = \mathbf{0}$) becomes equivalent to the conservation of the number of pseudo-photons ($\boldsymbol{\mathcal{N}}' = \mathbf{0}$) only when there is zero coupling between frequencies of opposite sign. In the next section, we will discuss how a class of non-stationary media can exhibit reciprocity in terms of the fluxes of the number of such pseudo-photons.

2.5 Generalized electromagnetic reciprocity in linear media

A fundamental symmetry that commonly characterizes electromagnetic systems is *reciprocity*. The etymology of the word reciprocity comes from the latin phrase *reque proque*, meaning "backward as forward". In the context of electromagnetism, reciprocity implies the following symmetry for a system: if we consider two *arbitrary* current distributions

exciting the same system, $\tilde{\mathbf{J}}_{\mathrm{A}}(\mathbf{r},t)$, $\tilde{\mathbf{J}}_{\mathrm{B}}(\mathbf{r},t)$ and generating the field distributions $\tilde{\mathbf{E}}_{\mathrm{A}}(\mathbf{r},t)$, $\tilde{\mathbf{E}}_{\mathrm{B}}(\mathbf{r},t)$ respectively, then, in a reciprocal system, there exists a moment in time τ where the hypothetical total exchange of energy between the external current $\tilde{\mathbf{J}}_{\mathrm{A}}$ and the electromagnetic field generated by $\tilde{\mathbf{J}}_{\mathrm{B}}$, reversed in time with respect to $t=\tau$, i.e., $\tilde{\mathbf{E}}_{\mathrm{B}}(\mathbf{r},2\tau-t)$, is equal to the hypothetical total exchange of energy between the external current $\tilde{\mathbf{J}}_{\mathrm{B}}$ and the electromagnetic field generated by $\tilde{\mathbf{J}}_{\mathrm{A}}$, reversed in time with respect to $t=\tau$, i.e., $\tilde{\mathbf{E}}_{\mathrm{A}}(\mathbf{r},2\tau-t)$. That hypothetical total exchange of power between a monochromatic current distribution $\tilde{\mathbf{J}}_{\mathrm{A}}(\mathbf{r},t)$ and a time reversed monochromatic field $\tilde{\mathbf{E}}_{\mathrm{B}}(\mathbf{r},2\tau-t)$ is known in the literature as the *reaction* of the field $\tilde{\mathbf{E}}_{\mathrm{B}}$ with the current source $\tilde{\mathbf{J}}_{\mathrm{A}}$ [189, 190]. In that sense, generalizing the concept of reaction to the non-monochromatic case, and referring to exchange of total energies instead of powers by introducing an extra integration over time, we can say that electromagnetic reciprocity essentially implies that the total reaction of $\tilde{\mathbf{E}}_{\mathrm{B}}$ on $\tilde{\mathbf{J}}_{\mathrm{A}}$ is equal to the total reaction of $\tilde{\mathbf{E}}_{\mathrm{A}}$ on $\tilde{\mathbf{J}}_{\mathrm{B}}$.

We have shown that the exchange of power density between an electromagnetic field and an external current source within it is given by Eq. (2.47). Using that expression we can cast the above generalized definition of Lorentz reciprocity into the following equation (see also Eq. (68) in [190]):

$$\int_{-\infty}^{+\infty}\int_{\mathbb{R}^3}\tilde{\mathbf{J}}_{\mathrm{A}}(\mathbf{r},t)\cdot\tilde{\mathbf{E}}_{\mathrm{B}}(\mathbf{r},2\tau-t)\mathrm{d}^3\mathbf{r}\mathrm{d}t=\int_{-\infty}^{+\infty}\int_{\mathbb{R}^3}\tilde{\mathbf{J}}_{\mathrm{B}}(\mathbf{r},t)\cdot\tilde{\mathbf{E}}_{\mathrm{A}}(\mathbf{r},2\tau-t)\mathrm{d}^3\mathbf{r}\mathrm{d}t, \quad (2.89)$$

or, else, in frequency domain:

$$\int_{-\infty}^{+\infty}\int_{\mathbb{R}^3}\left[\mathbf{J}_{\mathrm{A}}(\mathbf{r},\omega)\cdot\mathbf{E}_{\mathrm{B}}(\mathbf{r},\omega)-\mathbf{J}_{\mathrm{B}}(\mathbf{r},\omega)\cdot\mathbf{E}_{\mathrm{A}}(\mathbf{r},\omega)\right]e^{-2\mathrm{i}\omega\tau}\mathrm{d}^3\mathbf{r}\mathrm{d}\omega \;=\; 0. \quad (2.90)$$

When a system is reciprocal, there exists at least one moment in time τ for which two *arbitrary* source distributions with their generated fields obey the above equations of generalized Lorentz reciprocity.

Here, it is illustrative to introduce the Dyadic Green's functon (DGF) of the electromagnetic system, which constitutes the impulse response function of the linear system connecting the generated electric field with the external current sources:

$$\mathbf{E}(\mathbf{r},\omega) \;=\; \int_{-\infty}^{+\infty}\int_{\mathbb{R}^3}\overleftrightarrow{\mathbf{G}}(\mathbf{r},\mathbf{r}',\omega,\omega')\cdot\mathbf{J}(\mathbf{r}',\omega')\mathrm{d}^3\mathbf{r}'\mathrm{d}\omega'. \quad (2.91)$$

Then, we can reformulate the reciprocity condition for a system, using the last two equations, in terms of the following symmetry of its DGF:

$$\overleftrightarrow{\mathbf{G}}(\mathbf{r},\mathbf{r}',\omega,\omega') \;=\; \overleftrightarrow{\mathbf{G}}^{\mathrm{T}}(\mathbf{r}',\mathbf{r},\omega',\omega)\,e^{2\mathrm{i}(\omega-\omega')\tau}, \quad (2.92)$$

where $(^{\mathrm{T}})$ denotes a transposition of the dyadic tensor.

Note that, for a stationary system, for which there can be no coupling between the different frequencies due to the continuous translation symmetry over time, if the condition of reciprocity holds true, it holds true for arbitrary τ. Actually, the well-known definition of reciprocity for stationary systems does not involve this particular point of reflection in time τ. However, here we needed to introduce τ to generalize the definition of reciprocity

-expressed as a symmetry relation between exchanges of energy, instead of power now- for non-stationary systems. Nevertheless, our generalized definition of reciprocity reduces to the well-known definition of reciprocity for stationary systems. For example, note that Lorentz reciprocity for stationary systems is expressed by Eq. (2.90) without the integration over frequency, which is the result of it holding true for arbitrary τ [190]. Similarly, Eq. (2.92) can collapse into the well-known symmetry condition of the DGF of a reciprocal stationary system: $\overleftrightarrow{\mathbf{G}}_{\text{stationary}}(\mathbf{r},\mathbf{r}',\omega) = \overleftrightarrow{\mathbf{G}}^{\text{T}}_{\text{stationary}}(\mathbf{r}',\mathbf{r},\omega)$ [190].

Let us now consider an electromagnetic system whose non-local interactions and sources are confined inside an arbitrary space V, which is bounded by surface S (whose pointing-outwards normal unit vector we denote with $\hat{\mathbf{n}}$), and proceed to formulate the generalized Lorentz reciprocity theorem [190]. We start with the following algebraic equation that can be derived directly from Maxwell's equations in frequency domain for the A and B sets of sources distributions and fields that they generate:

$$\begin{aligned} \mathbf{J}_{\text{A}}\cdot\mathbf{E}_{\text{B}} - \mathbf{J}_{\text{B}}\cdot\mathbf{E}_{\text{A}} \quad = \\ \nabla\cdot\left[\mathbf{E}_{\text{A}}\times\mathbf{H}_{\text{B}} - \mathbf{E}_{\text{B}}\times\mathbf{H}_{\text{A}}\right] - \mathrm{i}\omega\left[\mathbf{E}_{\text{B}}\cdot\mathbf{P}_{\text{e,A}} - \mathbf{E}_{\text{A}}\cdot\mathbf{P}_{\text{e,B}} - \mathbf{H}_{\text{B}}\cdot\mathbf{P}_{\text{m,A}} + \mathbf{H}_{\text{A}}\cdot\mathbf{P}_{\text{m,B}}\right]. \end{aligned} \tag{2.93}$$

After an integration in space and frequency, application of Gauss's theorem, and use of the constitutive relations in frequency domain, the above equation readily gives the generalized Lorentz reciprocity theorem that takes the following form:

$$\begin{aligned} \int_{-\infty}^{+\infty}\int_{V}\left[\mathbf{J}_{\text{A}}(\mathbf{r},\omega)\cdot\mathbf{E}_{\text{B}}(\mathbf{r},\omega) - \mathbf{J}_{\text{B}}(\mathbf{r},\omega)\cdot\mathbf{E}_{\text{A}}(\mathbf{r},\omega)\right]e^{-2\mathrm{i}\omega\tau}\mathrm{d}^3\mathbf{r}\mathrm{d}\omega \quad = \\ \int_{-\infty}^{+\infty}\oiint_{S}\hat{\mathbf{n}}\cdot\left[\mathbf{E}_{\text{A}}(\mathbf{r},\omega)\times\mathbf{H}_{\text{B}}(\mathbf{r},\omega) - \mathbf{E}_{\text{B}}(\mathbf{r},\omega)\times\mathbf{H}_{\text{A}}(\mathbf{r},\omega)\right]e^{-2\mathrm{i}\omega\tau}\mathrm{d}^2\mathbf{r}\mathrm{d}\omega \quad + \\ \iint_{-\infty}^{+\infty}\iint_{V}\begin{bmatrix}\mathbf{E}_{\text{B}}(\mathbf{r},\omega)\\ \mathbf{H}_{\text{B}}(\mathbf{r},\omega)\end{bmatrix}^{\text{T}}\cdot\boldsymbol{\mathcal{R}}(\mathbf{r},\mathbf{r}',\omega,\omega')\cdot\begin{bmatrix}\mathbf{E}_{\text{A}}(\mathbf{r}',\omega')\\ \mathbf{H}_{\text{A}}(\mathbf{r}',\omega')\end{bmatrix}\mathrm{d}^3\mathbf{r}\mathrm{d}^3\mathbf{r}'\mathrm{d}\omega\mathrm{d}\omega' \end{aligned} \tag{2.94}$$

with the 6x6 matrix $\boldsymbol{\mathcal{R}}$ being given by

$$\boldsymbol{\mathcal{R}} \quad = \quad \begin{bmatrix}\boldsymbol{\mathcal{R}}_{\text{ee}} & \boldsymbol{\mathcal{R}}_{\text{em}}\\ \boldsymbol{\mathcal{R}}_{\text{me}} & \boldsymbol{\mathcal{R}}_{\text{mm}}\end{bmatrix}, \tag{2.95}$$

with

$$\boldsymbol{\mathcal{R}}_{\text{ee}} = \tfrac{\omega\varepsilon_0}{\mathrm{i}e^{2\mathrm{i}\omega\tau}}\left[\boldsymbol{\chi}_{\text{ee}}(\mathbf{r},\mathbf{r}-\mathbf{r}',\omega-\omega',\omega') - \tfrac{\omega'}{\omega}e^{2\mathrm{i}(\omega-\omega')\tau}\boldsymbol{\chi}^{\text{T}}_{\text{ee}}(\mathbf{r}',\mathbf{r}'-\mathbf{r},\omega'-\omega,\omega)\right], \tag{2.96}$$

$$\boldsymbol{\mathcal{R}}_{\text{em}} = \tfrac{\omega\sqrt{\varepsilon_0\mu_0}}{\mathrm{i}e^{2\mathrm{i}\omega\tau}}\left[\boldsymbol{\chi}_{\text{em}}(\mathbf{r},\mathbf{r}-\mathbf{r}',\omega-\omega',\omega') + \tfrac{\omega'}{\omega}e^{2\mathrm{i}(\omega-\omega')\tau}\boldsymbol{\chi}^{\text{T}}_{\text{me}}(\mathbf{r}',\mathbf{r}'-\mathbf{r},\omega'-\omega,\omega)\right], \tag{2.97}$$

$$\boldsymbol{\mathcal{R}}_{\text{me}} = \tfrac{\omega\sqrt{\varepsilon_0\mu_0}}{-\mathrm{i}e^{2\mathrm{i}\omega\tau}}\left[\boldsymbol{\chi}_{\text{me}}(\mathbf{r},\mathbf{r}-\mathbf{r}',\omega-\omega',\omega') + \tfrac{\omega'}{\omega}e^{2\mathrm{i}(\omega-\omega')\tau}\boldsymbol{\chi}^{\text{T}}_{\text{em}}(\mathbf{r}',\mathbf{r}'-\mathbf{r},\omega'-\omega,\omega)\right], \tag{2.98}$$

$$\boldsymbol{\mathcal{R}}_{\text{mm}} = \tfrac{\omega\mu_0}{-\mathrm{i}e^{2\mathrm{i}\omega\tau}}\left[\boldsymbol{\chi}_{\text{mm}}(\mathbf{r},\mathbf{r}-\mathbf{r}',\omega-\omega',\omega') - \tfrac{\omega'}{\omega}e^{2\mathrm{i}(\omega-\omega')\tau}\boldsymbol{\chi}^{\text{T}}_{\text{mm}}(\mathbf{r}',\mathbf{r}'-\mathbf{r},\omega'-\omega,\omega)\right]. \tag{2.99}$$

Note that we can make the surface integral in Eq. (2.94) vanish by considering that S is the surface of a sphere of radius optically much larger than the domain enclosing the system and the free current sources. There, in the far-field region, the fields should behave like outgoing spherical waves, with the electric field being perpendicular to the magnetic

field and both being tangential to the spherical surface S, which makes the surface integral vanish. Then, since in a reciprocal system the first integral term containing the current sources should vanish for arbitrary fields and sources, we get that the last integral term in Eq. (2.94) should ideally vanish as well. This only happens for $\boldsymbol{\mathcal{R}}(\mathbf{r},\mathbf{r}',\omega,\omega')=\mathbf{0}$, which implies particular symmetries for the generalized susceptibility tensor of the system. Note that for the special case of a *stationary* system the condition $\boldsymbol{\mathcal{R}}(\mathbf{r},\mathbf{r}',\omega,\omega')=\mathbf{0}$ boils down to well-known expressions for reciprocity in stationary media (see e.g. Eq. (2.3.67) in [191], Eq. (50) in [190], Eqs. (3.67,3.68) in [192]):

$$\boldsymbol{\chi}_{\mathrm{ee,stationary}}(\mathbf{r},\mathbf{r}-\mathbf{r}',\omega) = \boldsymbol{\chi}^{\mathrm{T}}_{\mathrm{ee,stationary}}(\mathbf{r}',\mathbf{r}'-\mathbf{r},\omega), \tag{2.100}$$

$$\boldsymbol{\chi}_{\mathrm{mm,stationary}}(\mathbf{r},\mathbf{r}-\mathbf{r}',\omega) = \boldsymbol{\chi}^{\mathrm{T}}_{\mathrm{mm,stationary}}(\mathbf{r}',\mathbf{r}'-\mathbf{r},\omega), \tag{2.101}$$

$$\boldsymbol{\chi}_{\mathrm{em,stationary}}(\mathbf{r},\mathbf{r}-\mathbf{r}',\omega) = -\boldsymbol{\chi}^{\mathrm{T}}_{\mathrm{me,stationary}}(\mathbf{r}',\mathbf{r}'-\mathbf{r},\omega). \tag{2.102}$$

The material parameter conditions of the latter equations have been shown to hold true by all linear, causal media characterized by microscopic reversibility in thermodynamic quasi-equilibrium [190]. Specifically, they constitute a manifestation of the Onsager-Casimir reciprocity relation for irreversible processes, known also as the "fourth law of thermodynamics" [190, 192–195]. The Onsager-Casimir reciprocity relation is based on the time reversal symmetry of the equations governing the motion of elementary particles, which is the case for microscopic Maxwell's equations governing the motion of charges. It constitutes a symmetry relation of generalized susceptibility tensors which connect "Onsager forces" (i.e., the causative agents) with "Onsager fluxes" (which are associated with such motion of elementary particles) that both exhibit either an even or odd time-reversal symmetry. In our particular case above, the "Onsager forces" and "Onsager fluxes" are the electromagnetic fields and the macroscopic polarization densities of the medium, respectively [196]. Note that the electric field and the electric polarization density, being polar vectors, exhibit an even time-reversal symmetry, whereas the magnetic field and the magnetic polarization density, being axial vectors (i.e., pseudovectors), exhibit an odd time-reversal symmetry. The Onsager-Casimir reciprocity relation supports the Lorentz reciprocity theorem for stationary systems by killing the last integral term in Eq. (2.94) from the microscopic point of view of statistical mechanics.

However, the generalization of the Lorentz reciprocity theorem to non-stationary system lacks such support from the microscopic level: unfortunately, as of now, we do not have a generalized Onsager-Casimir reciprocity relation for the susceptibility tensors of non-stationary systems from statistical mechanics. In fact, in view of Eqs. (2.96-2.99) it becomes evident that it is unrealistic for a non-stationary system to be reciprocal, i.e., to fulfill the condition of $\boldsymbol{\mathcal{R}}(\mathbf{r},\mathbf{r}',\omega,\omega')=\mathbf{0}$. Indeed, time-varying systems are known to exhibit non-reciprocity and, recently, have been strategically used to design devices that break electromagnetic reciprocity [197–199]. Non-stationary systems provide a viable alternative route to electromagnetic non-reciprocity, which has been traditionally achieved either through external magnetic field biases that break time-reversal symmetry or through nonlinear elements [190, 200].

Exactly because of the aforementioned lack of support from the microscopic level, we can attempt to quest for alternative ways to generalize the (well-established for stationary systems) symmetry of electromagnetic reciprocity to the more general case of non-stationary systems. Specifically, it is interesting to check whether the generalization of electromagnetic reciprocity can be conducted in terms of symmetries in the exchanges of number of photons between sources and time-reversed fields, instead of symmetries in the exchange of energies as we discussed above. Those two symmetries of exchanges are equivalent for stationary systems, but are *not* equivalent for non-stationary systems. Specifically, we can postulate the following alternative generalized Lorentz reciprocity

equation in frequency domain by dividing Eq. (2.90) with the energy of a single photon $\hbar|\omega|$:

$$\int_{-\infty}^{+\infty}\int_{\mathbb{R}^3}\frac{1}{\hbar|\omega|}\left[\mathbf{J}_{\mathrm{A}}(\mathbf{r},\omega)\cdot\mathbf{E}_{\mathrm{B}}(\mathbf{r},\omega)-\mathbf{J}_{\mathrm{B}}(\mathbf{r},\omega)\cdot\mathbf{E}_{\mathrm{A}}(\mathbf{r},\omega)\right]e^{-2\mathrm{i}\omega\tau}\mathrm{d}^3\mathbf{r}\mathrm{d}\omega \;=\; 0. \quad (2.103)$$

This definition of generalized Lorentz reciprocity practically states that there is a moment in time τ for which the total exchange of photons between an *arbitrary* source distribution and the time-reversed -with respect to τ- field generated by some other *arbitrary* source distribution is equal to the total exchange of photons between the second source distribution and the time-reversed -with respect to τ- field generated by the first source distribution. Similarly as before, the above equation of generalized Lorentz reciprocity implies the following symmetry condition for the DGF of the medium:

$$\overleftrightarrow{\mathbf{G}}(\mathbf{r},\mathbf{r}',\omega,\omega') \;=\; \left|\frac{\omega}{\omega'}\right|\overleftrightarrow{\mathbf{G}}^{\mathrm{T}}(\mathbf{r}',\mathbf{r},\omega',\omega)\,e^{2\mathrm{i}(\omega-\omega')\tau}. \quad (2.104)$$

Moreover, proceeding in a similar fashion like before, we can postulate the following alternative formulation of the Lorentz reciprocity theorem in terms of a balance in the number of photons instead of an energy balance as was the case for Eq. (2.94). Specifically, we have:

$$\begin{aligned}\int_{-\infty}^{+\infty}\int_{V}\frac{1}{\hbar|\omega|}\left[\mathbf{J}_{\mathrm{A}}(\mathbf{r},\omega)\cdot\mathbf{E}_{\mathrm{B}}(\mathbf{r},\omega)-\mathbf{J}_{\mathrm{B}}(\mathbf{r},\omega)\cdot\mathbf{E}_{\mathrm{A}}(\mathbf{r},\omega)\right]e^{-2\mathrm{i}\omega\tau}\mathrm{d}^3\mathbf{r}\mathrm{d}\omega \;&=\\ \int_{-\infty}^{+\infty}\oiint_{S}\frac{1}{\hbar|\omega|}\hat{\mathbf{n}}\cdot\left[\mathbf{E}_{\mathrm{A}}(\mathbf{r},\omega)\times\mathbf{H}_{\mathrm{B}}(\mathbf{r},\omega)-\mathbf{E}_{\mathrm{B}}(\mathbf{r},\omega)\times\mathbf{H}_{\mathrm{A}}(\mathbf{r},\omega)\right]e^{-2\mathrm{i}\omega\tau}\mathrm{d}^2\mathbf{r}\mathrm{d}\omega \;&+\\ \iint_{-\infty}^{+\infty}\iint_{V}\begin{bmatrix}\mathbf{E}_{\mathrm{B}}(\mathbf{r},\omega)\\ \mathbf{H}_{\mathrm{B}}(\mathbf{r},\omega)\end{bmatrix}^{\mathrm{T}}\cdot\boldsymbol{\mathcal{R}}'(\mathbf{r},\mathbf{r}',\omega,\omega')\cdot\begin{bmatrix}\mathbf{E}_{\mathrm{A}}(\mathbf{r}',\omega')\\ \mathbf{H}_{\mathrm{A}}(\mathbf{r}',\omega')\end{bmatrix}\mathrm{d}^3\mathbf{r}\mathrm{d}^3\mathbf{r}'\mathrm{d}\omega\mathrm{d}\omega' \;&\quad (2.105)\end{aligned}$$

with the 6x6 matrix $\boldsymbol{\mathcal{R}}'$ being given by

$$\boldsymbol{\mathcal{R}}' \;=\; \begin{bmatrix}\boldsymbol{\mathcal{R}}'_{\mathrm{ee}} & \boldsymbol{\mathcal{R}}'_{\mathrm{em}}\\ \boldsymbol{\mathcal{R}}'_{\mathrm{me}} & \boldsymbol{\mathcal{R}}'_{\mathrm{mm}}\end{bmatrix}, \quad (2.106)$$

with

$$\boldsymbol{\mathcal{R}}'_{\mathrm{ee}} = \tfrac{=\mathrm{i}\varepsilon_0}{\hbar e^{2\mathrm{i}\omega\tau}}\Big[\tfrac{\omega}{|\omega|}\boldsymbol{\chi}_{\mathrm{ee}}(\mathbf{r},\mathbf{r}-\mathbf{r}',\omega-\omega',\omega') - \tfrac{\omega'}{|\omega'|}e^{2\mathrm{i}(\omega-\omega')\tau}\boldsymbol{\chi}^{\mathrm{T}}_{\mathrm{ee}}(\mathbf{r}',\mathbf{r}'-\mathbf{r},\omega'-\omega,\omega)\Big], \quad (2.107)$$

$$\boldsymbol{\mathcal{R}}'_{\mathrm{em}} = \tfrac{\sqrt{\varepsilon_0\mu_0}}{\mathrm{i}\hbar e^{2\mathrm{i}\omega\tau}}\Big[\tfrac{\omega}{|\omega|}\boldsymbol{\chi}_{\mathrm{em}}(\mathbf{r},\mathbf{r}-\mathbf{r}',\omega-\omega',\omega') + \tfrac{\omega'}{|\omega'|}e^{2\mathrm{i}(\omega-\omega')\tau}\boldsymbol{\chi}^{\mathrm{T}}_{\mathrm{me}}(\mathbf{r}',\mathbf{r}'-\mathbf{r},\omega'-\omega,\omega)\Big], \quad (2.108)$$

$$\boldsymbol{\mathcal{R}}'_{\mathrm{me}} = \tfrac{\mathrm{i}\sqrt{\varepsilon_0\mu_0}}{\hbar, e^{2\mathrm{i}\omega\tau}}\Big[\tfrac{\omega}{|\omega|}\boldsymbol{\chi}_{\mathrm{me}}(\mathbf{r},\mathbf{r}-\mathbf{r}',\omega-\omega',\omega') + \tfrac{\omega'}{|\omega'|}e^{2\mathrm{i}(\omega-\omega')\tau}\boldsymbol{\chi}^{\mathrm{T}}_{\mathrm{em}}(\mathbf{r}',\mathbf{r}'-\mathbf{r},\omega'-\omega,\omega)\Big], \quad (2.109)$$

$$\boldsymbol{\mathcal{R}}'_{\mathrm{mm}} = \tfrac{\mathrm{i}\mu_0}{\hbar e^{2\mathrm{i}\omega\tau}}\Big[\tfrac{\omega}{|\omega|}\boldsymbol{\chi}_{\mathrm{mm}}(\mathbf{r},\mathbf{r}-\mathbf{r}',\omega-\omega',\omega') - \tfrac{\omega'}{|\omega'|}e^{2\mathrm{i}(\omega-\omega')\tau}\boldsymbol{\chi}^{\mathrm{T}}_{\mathrm{mm}}(\mathbf{r}',\mathbf{r}'-\mathbf{r},\omega'-\omega,\omega)\Big]. \quad (2.110)$$

Again, we can get rid of the surface integral term of Eq. (2.105) by extending the volume of integration V to infinity. Moreover, we can see that for the generalized Lorentz reciprocity in terms of number of photons to hold, we need the last volumetric integral term

in Eq. (2.105) to vanish for arbitrary source distributions inside V. This requires that $\boldsymbol{\mathcal{R}}'(\mathbf{r},\mathbf{r}',\omega,\omega')=\mathbf{0}$, which practically implies particular symmetries for the susceptibility tensor of the system. In view of Eqs. (2.107-2.110) it becomes evident that: 1) we still get the well-known symmetry conditions of the susceptibility tensors for reciprocity in stationary media, and 2) it still appears generally unrealistic for non-stationary media to exhibit reciprocity even in terms of exchanges in number of photons, instead of energy.

However, our quest for a generalization of electromagnetic reciprocity for non-stationary media does not stop here. In what follows, we will demonstrate that, interestingly enough, there exists a class of non-stationary media that exhibits reciprocity, once we generalize the latter in terms of exchanges in number of the *pseudo-photons* that we firstly discussed at the end of the previous section. We remind that those pseudo-photons differ from true photons in that they are considered to have negative energies for negative frequencies, i.e., the single pseudo-photon energy is considered to be $\hbar\omega$ instead of $\hbar|\omega|$ that is the energy of the true photon. Therefore, by assuming a quantization of energies in terms of pseudo-photons instead of true photons, we can get an alternative generalized Lorentz reciprocity equation as the following slight modification of Eq. (2.105):

$$\int_{-\infty}^{+\infty}\int_{\mathbb{R}^3}\frac{1}{\hbar\omega}\left[\mathbf{J}_{\mathrm{A}}(\mathbf{r},\omega)\cdot\mathbf{E}_{\mathrm{B}}(\mathbf{r},\omega)-\mathbf{J}_{\mathrm{B}}(\mathbf{r},\omega)\cdot\mathbf{E}_{\mathrm{A}}(\mathbf{r},\omega)\right]e^{-2\mathrm{i}\omega\tau}\mathrm{d}^3\mathbf{r}\mathrm{d}\omega \;=\; 0, \quad (2.111)$$

This definition of generalized Lorentz reciprocity practically states that there is a moment in time τ for which the total exchange of *pseudo-photons* between an *arbitrary* source distribution and the time-reversed -with respect to τ- field generated by some other *arbitrary* source distribution is equal to the total exchange of photons between the second source distribution and the time-reversed -with respect to τ- field generated by the first source distribution. Similarly as before, the above equation of generalized Lorentz reciprocity implies the following symmetry condition for the DGF of the medium:

$$\overleftrightarrow{\mathbf{G}}(\mathbf{r},\mathbf{r}',\omega,\omega') \;=\; \frac{\omega}{\omega'}\overleftrightarrow{\mathbf{G}}^{\mathrm{T}}(\mathbf{r}',\mathbf{r},\omega',\omega)\,e^{2\mathrm{i}(\omega-\omega')\tau}. \quad (2.112)$$

Moreover, proceeding in a similar fashion like before, we can postulate the following alternative formulation of the Lorentz reciprocity theorem in terms of a balance in the number of *pseudo-photons*:

$$\begin{aligned}\int_{-\infty}^{+\infty}\int_{V}\frac{1}{\hbar\omega}\left[\mathbf{J}_{\mathrm{A}}(\mathbf{r},\omega)\cdot\mathbf{E}_{\mathrm{B}}(\mathbf{r},\omega)-\mathbf{J}_{\mathrm{B}}(\mathbf{r},\omega)\cdot\mathbf{E}_{\mathrm{A}}(\mathbf{r},\omega)\right]e^{-2\mathrm{i}\omega\tau}\mathrm{d}^3\mathbf{r}\mathrm{d}\omega \;&=\\ \int_{-\infty}^{+\infty}\oiint_{S}\frac{1}{\hbar\omega}\hat{\mathbf{n}}\cdot\left[\mathbf{E}_{\mathrm{A}}(\mathbf{r},\omega)\times\mathbf{H}_{\mathrm{B}}(\mathbf{r},\omega)-\mathbf{E}_{\mathrm{B}}(\mathbf{r},\omega)\times\mathbf{H}_{\mathrm{A}}(\mathbf{r},\omega)\right]e^{-2\mathrm{i}\omega\tau}\mathrm{d}^2\mathbf{r}\mathrm{d}\omega \;&+\\ \iint_{-\infty}^{+\infty}\iint_{V}\begin{bmatrix}\mathbf{E}_{\mathrm{B}}(\mathbf{r},\omega)\\ \mathbf{H}_{\mathrm{B}}(\mathbf{r},\omega)\end{bmatrix}^{\mathrm{T}}\cdot\boldsymbol{\mathcal{R}}''(\mathbf{r},\mathbf{r}',\omega,\omega')\cdot\begin{bmatrix}\mathbf{E}_{\mathrm{A}}(\mathbf{r}',\omega')\\ \mathbf{H}_{\mathrm{A}}(\mathbf{r}',\omega')\end{bmatrix}\mathrm{d}^3\mathbf{r}\mathrm{d}^3\mathbf{r}'\mathrm{d}\omega\mathrm{d}\omega' \;&\end{aligned} \quad (2.113)$$

with the 6x6 matrix $\boldsymbol{\mathcal{R}}''$ being given by

$$\boldsymbol{\mathcal{R}}'' \;=\; \begin{bmatrix}\boldsymbol{\mathcal{R}}''_{\mathrm{ee}} & \boldsymbol{\mathcal{R}}''_{\mathrm{em}}\\ \boldsymbol{\mathcal{R}}''_{\mathrm{me}} & \boldsymbol{\mathcal{R}}''_{\mathrm{mm}}\end{bmatrix}, \quad (2.114)$$

with

$$\boldsymbol{\mathcal{R}}''_{\mathrm{ee}} = \tfrac{=\mathrm{i}\varepsilon_0}{\hbar e^{2\mathrm{i}\omega\tau}} \left[\boldsymbol{\chi}_{\mathrm{ee}}(\mathbf{r}, \mathbf{r}-\mathbf{r}', \omega-\omega', \omega') - e^{2\mathrm{i}(\omega-\omega')\tau}\boldsymbol{\chi}^{\mathrm{T}}_{\mathrm{ee}}(\mathbf{r}', \mathbf{r}'-\mathbf{r}, \omega'-\omega, \omega)\right], \quad (2.115)$$

$$\boldsymbol{\mathcal{R}}''_{\mathrm{em}} = \tfrac{\sqrt{\varepsilon_0\mu_0}}{\mathrm{i}\hbar e^{2\mathrm{i}\omega\tau}} \left[\boldsymbol{\chi}_{\mathrm{em}}(\mathbf{r}, \mathbf{r}-\mathbf{r}', \omega-\omega', \omega') + e^{2\mathrm{i}(\omega-\omega')\tau}\boldsymbol{\chi}^{\mathrm{T}}_{\mathrm{me}}(\mathbf{r}', \mathbf{r}'-\mathbf{r}, \omega'-\omega, \omega)\right], \quad (2.116)$$

$$\boldsymbol{\mathcal{R}}''_{\mathrm{me}} = \tfrac{\mathrm{i}\sqrt{\varepsilon_0\mu_0}}{\hbar, e^{2\mathrm{i}\omega\tau}} \left[\boldsymbol{\chi}_{\mathrm{me}}(\mathbf{r}, \mathbf{r}-\mathbf{r}', \omega-\omega', \omega') + e^{2\mathrm{i}(\omega-\omega')\tau}\boldsymbol{\chi}^{\mathrm{T}}_{\mathrm{em}}(\mathbf{r}', \mathbf{r}'-\mathbf{r}, \omega'-\omega, \omega)\right], \quad (2.117)$$

$$\boldsymbol{\mathcal{R}}''_{\mathrm{mm}} = \tfrac{\mathrm{i}\mu_0}{\hbar e^{2\mathrm{i}\omega\tau}} \left[\boldsymbol{\chi}_{\mathrm{mm}}(\mathbf{r}, \mathbf{r}-\mathbf{r}', \omega-\omega', \omega') - e^{2\mathrm{i}(\omega-\omega')\tau}\boldsymbol{\chi}^{\mathrm{T}}_{\mathrm{mm}}(\mathbf{r}', \mathbf{r}'-\mathbf{r}, \omega'-\omega, \omega)\right]. \quad (2.118)$$

Similarly as before, for the generalized Lorentz reciprocity in terms of number of *pseudo-photons* to hold, we need the last volumetric integral term in Eq. (2.113) to vanish for arbitrary source distributions inside V. This requires that $\boldsymbol{\mathcal{R}}''(\mathbf{r}, \mathbf{r}', \omega, \omega') = \mathbf{0}$, which practically implies particular symmetries for the susceptibility tensor of the system. First of all, let us not that, again, we still get the well-known symmetry conditions of the susceptibility tensors for reciprocity in stationary media. What is actually interesting here, though, is that we can identify a class of non-stationary media that can exhibit such reciprocity in terms of pseudo-photons. The first property of such class of media that we can identify is that they are characterized by an instantaneous response, i.e., they are *dispersionless*. In such case, in view of the inverse Fourier transform of Eqs. (2.115-2.118), the reciprocity condition $\boldsymbol{\mathcal{R}}''_{\mathrm{instant}}(\mathbf{r}, \mathbf{r}', \omega, \omega') = \mathbf{0}$ can be translated into the following three equations:

$$\tilde{\boldsymbol{\chi}}_{\mathrm{ee,instant}}(\mathbf{r}, \mathbf{r}-\mathbf{r}', t) = \tilde{\boldsymbol{\chi}}^{\mathrm{T}}_{\mathrm{ee,instant}}(\mathbf{r}', \mathbf{r}'-\mathbf{r}, 2\tau - t), \quad (2.119)$$

$$\tilde{\boldsymbol{\chi}}_{\mathrm{em,instant}}(\mathbf{r}, \mathbf{r}-\mathbf{r}', t) = -\tilde{\boldsymbol{\chi}}^{\mathrm{T}}_{\mathrm{me,instant}}(\mathbf{r}', \mathbf{r}'-\mathbf{r}, 2\tau - t), \quad (2.120)$$

$$\tilde{\boldsymbol{\chi}}_{\mathrm{mm,instant}}(\mathbf{r}, \mathbf{r}-\mathbf{r}', t) = \tilde{\boldsymbol{\chi}}^{\mathrm{T}}_{\mathrm{mm,instant}}(\mathbf{r}', \mathbf{r}'-\mathbf{r}, 2\tau - t). \quad (2.121)$$

Note the reflection in time with respect to τ in the right-hand side of the above equations.

We have just shown that such dispersionless media can be characterized by electromagnetic reciprocity in terms of number of pseudo-photons, as long as their time-varying dielectric permittivity exhibits an even time-reversal symmetry with respect to some moment in time τ (e.g. for the exemplary case of an assumed non-magnetic, isotropic and local medium). Reference [76] refers to this condition as a generalized gauge-invariant time reversal symmetry of the system. Actually, there are several references in the literature regarding this type of electromagnetic reciprocity characterizing non-stationary and dispersionless systems: see for example Eq. (117) in [190], [76, 201–203]. We would like to emphasize that, in all those works, the authors refer to reciprocity in their systems in terms of fluxes of number of true photons, but, to be precise, their considered systems actually exhibit reciprocity in terms of fluxes of number of pseudo-photons, as we discussed above. Those two are equivalent *only* if the system is operated at large enough frequencies so that there is practically no coupling between fields of positive and negative frequencies (which is the case in those works). *Only then*, the vanishing of the last integral of Eq. (2.113) directly implies the vanishing of the last integral of Eq. (2.105), which is what makes the two reciprocities in terms of fluxes of true photons and pseudo-photons equivalent. Finally, let us note that the required lack of material dispersion for such reciprocity is usually difficult to justify on physical grounds, since it requires the operation of the medium at a spectral range that is far from its material resonances. Nevertheless, this is most commonly adopted in literature as a simple model of time-varying media. Hence, such considerations of electromagnetic reciprocity do become relevant there. In a next chapter, we will derive the symmetry that reciprocity in terms of pseudo-photons implies

for an arbitrary scattering system in terms of its T-matrix representation (which we will introduce in the last section of this chapter).

2.6 Eigenmodes of the electromagnetic wave equation of local, stationary, homogeneous and isotropic media

In this section we will discuss the eigenmodes of the electromagnetic wave equation of source-free, local, stationary, homogeneous and isotropic media and then we will also present the expansions of the DGF in terms of such eigenmodes. The harmonic electromagnetic wave equation of such a medium can be directly derived from Maxwell's equations and reads as follows:

$$\left(\nabla \times \nabla \times -k^2\right) \mathbf{E} \;=\; 0, \tag{2.122}$$

where k denotes the wavenumber of the harmonic electromagnetic wave, which is related with the frequency of the wave ω and the material properties of the medium according to the dispersion relation $k^2 = \omega^2 \varepsilon \mu$ (or $k = \omega\sqrt{\varepsilon\mu}$), with ε, μ being the dielectric permittivity and the magnetic permeability of the medium respectively. By employing the vector identity $\nabla \times \nabla \times \;=\; \nabla\nabla \cdot -\nabla^2$ and taking into consideration that the electromagnetic fields in source-free space are solenoidal, we can recast the previous wave equation in the following alternative form:

$$\left(\nabla^2 + k^2\right) \mathbf{E} \;=\; 0. \tag{2.123}$$

Next, we can search for analytical solutions $\psi_k(\mathbf{r})$ to the correspondent scalar wave equation (Helmholtz equation) by making use of the method of separation of variables. Actually, it has been shown that there are eleven coordinate systems under which the Helmholtz equation in three-dimensional space is separable [204, 205]. To separate the solutions in three parts we need to introduce two separation constants. Those are essentially eigenvalues that correspond to a couple of commuting spatial symmetry operators in the enveloping algebra of the Helmholtz operator for each such coordinate system [204, 205]. Overall, together with the wavenumber k we end up with a set of three eigenvalues that characterize our eigensolutions. Here we will just focus on the three most common out of those eleven coordinate systems: the Cartesian, cylindrical, and spherical one. Once we express the Laplace operator into each of the three coordinate systems and solve the wave equation, we readily get its Cartesian, cylindrical, and spherical eigensolutions, which are the plane, cylindrical, and spherical waves, respectively.

Plane waves may exhibit a continuous translation symmetry along the x- and y-axis and because the linear momentum operators along the x- and y-axis, $(\hat{\mathbf{P}}_x, \hat{\mathbf{P}}_y)$, are the generators of such spatial translations respectively, plane waves are characterized, as a result, by the following set of their corresponding eigenvalues (k_x, k_y). On the other hand, cylindrical waves may exhibit a continuous translation symmetry along the z-axis and a continuous rotation symmetry along the z-axis, and because the linear momentum operator along the z-axis and the total angular momentum operator along the z-axis, $(\hat{\mathbf{P}}_z, \hat{\mathbf{J}}_z)$, are the generators of such spatial translations and rotations respectively, cylindrical waves are characterized, as a result, by the following set of their corresponding eigenvalues (k_z, μ_z). Finally, spherical waves have a 3D rotational symmetry and may exhibit as well a continuous rotation symmetry along the z-axis. Moreover, the total angular momentum squared

operator, $\hat{\mathbf{J}}^2$, commutes with the total angular momentum operator along any arbitrary axis -the z-axis included, $\hat{\mathbf{J}}_z$-, which is the generator of rotations with respect to such arbitrary axis. Therefore, spherical waves are characterized, as a result, by the following set of eigenvalues, (ν, μ_z), that correspond to those two spatial symmetry operators $(\hat{\mathbf{J}}^2, \hat{\mathbf{J}}_z)$ respectively. To be more precise here, the eigenvalue of the $\hat{\mathbf{J}}^2$ operator is $\nu(\nu+1)$.

Furthermore, two of the three coordinates of each coordinate system are associated with the two commuting spatial symmetry operators providing the two extra eigenvalues to the scalar eigenwaves. Specifically, in the Cartesian coordinate system the coordinates (x, y) are associated with the commuting operators $(\hat{\mathbf{P}}_x, \hat{\mathbf{P}}_y)$, whereas in the cylindrical coordinate system the coordinates (ϕ, z) are associated with the commuting operators $(\hat{\mathbf{P}}_z, \hat{\mathbf{J}}_z)$ and in the spherical coordinate system the coordinates (θ, ϕ) are associated with the commuting operators $(\hat{\mathbf{J}}^2, \hat{\mathbf{J}}_z)$. The second order differential equation with respect to the remaining third coordinate -after we apply the method of separation of variables- has two linearly independent families of solutions. It is convenient to pick a particular set of them depending on a desired asymptotic behavior at infinity, or at the origin. In what follows, we will use the index (ι) to differentiate between those two types of solutions.

We define the following kets in an abstract Dirac notation: $|k_x\, k_z\, k\rangle^{(\iota)}$, $|\mu_z\, k_z\, k\rangle^{(\iota)}$, $|\mu_z\, \nu\, k\rangle^{(\iota)}$, to refer to the eigenstates of the scalar Helmholtz equation in the Cartesian, cylindrical, and spherical basis, respectively, i.e., the scalar Cartesian, cylindrical, and spherical waves. Their spatial representation is given below:

$$|k_x\, k_y\, k\rangle^{(\iota)} \equiv \psi^{(\iota)}(\mathbf{r}; k_x, k_y, k) = e^{\mathrm{i}\left(k_x x + k_y y + \iota\sqrt{k^2 - k_\rho^2} z\right)}, \tag{2.124}$$

$$|\mu_z\, k_z\, k\rangle^{(\iota)} \equiv \psi^{(\iota)}_{\mu_z}(\mathbf{r}; k_z, k) = Z^{(\iota)}_{\mu_z}(k_\rho \rho)\, e^{i\mu_z \phi} e^{ik_z z}, \tag{2.125}$$

$$|\mu_z\, \nu\, k\rangle^{(\iota)} \equiv \psi^{(\iota)}_{\mu_z \nu}(\mathbf{r}; k) = \gamma_{\mu_z \nu}\, z^{(\iota)}_\nu(kr)\, \mathrm{P}^{\mu_z}_\nu(\cos\theta) e^{i\mu\phi}, \tag{2.126}$$

where $k^2 = k_x^2 + k_y^2 + k_z^2$ and $k_\rho = \sqrt{k_x^2 + k_y^2} = \sqrt{k^2 - k_z^2}$ and ι in the Cartesian case takes the values ± 1 to refer to plane waves that propagate/decay along $\pm\hat{\mathbf{z}}$, respectively. μ_z, the total angular momentum operator along the z-axis, takes integer values and for the spherical case its absolute value is bounded by ν, the total angular momentum or multipolar order of the spherical waves. $Z^{(\iota)}_{\mu_z}(x)$ denotes the cylindrical Bessel ($\iota = 1$) and the cylindrical Hankel functions of the first ($\iota = 3$) or second ($\iota = 4$) kind, of order μ_z, respectively. Whereas, $z^{(\iota)}_\nu(x)$ denotes the spherical Bessel ($\iota = 1$) and the cylindrical Hankel functions of the first ($\iota = 3$) or second ($\iota = 4$) kind, of order ν, respectively. Bessel functions are regular everywhere and are useful to expand standing waves. They are the arithmetic average of the Hankel functions of the first and second kinds. Whereas, Hankel functions of the first kind, diverge for small arguments but due to their asymptotic behavior at infinity (and with respect to our adopted time convention), can be used to expand outgoing/radiating waves. On the other hand, Hankel functions of the second kind due to their asymptotic behavior at infinity, can be used to expand incoming waves. $\mathrm{P}^{\mu_z}_\nu(x)$ are the associated Legendre functions of the first kind and $\gamma_{\mu_z \nu} = \sqrt{\frac{(2\nu+1)(\nu-\mu_z)!}{4\pi\nu(\nu+1)(\nu+\mu_z)!}}$ are some normalization coefficients.

According to Ref. [204], we can construct a set of solenoidal eigenmodes to the vectorial wave equation by making use of the scalar eigenmodes that we just discussed. We will call those eigenmodes as Vector Planar/Cylindrical/Spherical Harmonics (VPHs/VCHs/VSHs). First, we have the transverse electric (TE) vectorial eigenmodes -known as eigenmodes of magnetic type- that are defined as:

$$\mathbf{F}_{\mathrm{M}}(\mathbf{r}; k) = \nabla \times [\mathbf{v}\psi(\mathbf{r}; k)], \tag{2.127}$$

where $\mathbf{v}$ is some vector appropriate for each particular coordinate system and $\psi(k,\mathbf{r})$ are the scalar solutions of the Helmholtz equation in that system. TE eigenmodes are polarized perpendicularly to $\mathbf{v}$. Moreover, we also have the transverse magnetic (TM) vectorial eigenmodes -known as eigenmodes of electric type- that are defined as:

$$\mathbf{F}_{\mathrm{N}}(\mathbf{r};k) = \frac{\nabla\times}{k}\mathbf{F}_{\mathrm{M}}(\mathbf{r};k). \tag{2.128}$$

In contrast to TE eigenmodes, the vectorial field of the curl of TM eigenmodes is polarized perpendicularly to $\mathbf{v}$. We will introduce the symbol α which will be taking the values M,N to refer to TE and TM eigenmodes, respectively. Note, that there is also a third family of vectorial solutions to the Helmholtz wave equation, but it is longitudinal, i.e., they are used to expand electromagnetic fields in a space that hosts sources [204]. Note, also, that the TE and TM modes have the following symmetry:

$$\mathbf{F}_{\beta}(\mathbf{r};k) = \frac{\nabla\times}{k}\mathbf{F}_{\alpha}(\mathbf{r};k), \tag{2.129}$$

where $\beta \neq \alpha$.

We define the following kets in an abstract Dirac notation: $|\alpha\, k_x\, k_z\, k\rangle^{(\iota)}$, $|\alpha\, \mu_z\, k_z\, k\rangle^{(\iota)}$, $|\alpha\, \mu_z\, \nu\, k\rangle^{(\iota)}$, to refer to the eigenstates of the vectorial Helmholtz equation in the Cartesian, cylindrical and spherical basis, respectively.

Specifically, the spatial representation of VPHs reads as follows:

$$\begin{aligned}
|\mathrm{M}\, k_x\, k_y\, k\rangle^{(\iota)} \equiv \mathbf{F}_{\mathrm{M}}^{(\iota)}(\mathbf{r};k_x,k_y,k) &= \frac{1}{k_\rho}\nabla\times\left[\hat{\mathbf{z}}\,\psi^{(\iota)}(\mathbf{r};k_x,k_y,k)\right] \\
&= -\mathrm{i}\hat{\phi}_{\hat{\mathbf{k}}}\,\psi^{(\iota)}(\mathbf{r};k_x,k_y,k), \qquad (2.130)\\
|\mathrm{N}\, k_x\, k_y\, k\rangle^{(\iota)} \equiv \mathbf{F}_{\mathrm{N}}^{(\iota)}(\mathbf{r};k_x,k_y,k) &= \frac{\nabla\times}{k}\mathbf{F}_{\mathrm{M}}^{(\iota)}(\mathbf{r};k_x,k_y,k) \\
&= -\hat{\theta}_{\hat{\mathbf{k}}}^{(\iota)}\,\psi^{(\iota)}(\mathbf{r};k_x,k_y,k), \qquad (2.131)
\end{aligned}$$

where:

$$\hat{\phi}_{\hat{\mathbf{k}}}(k_x,k_y,k) = \frac{-k_y\hat{\mathbf{x}}+k_x\hat{\mathbf{y}}}{k_\rho}, \tag{2.132}$$

$$\hat{\theta}_{\hat{\mathbf{k}}}^{(\iota)}(k_x,k_y,k) = \iota\frac{\sqrt{k^2-k_\rho^2}}{kk_\rho}\left(k_x\hat{\mathbf{x}}+k_y\hat{\mathbf{y}}\right)-\frac{k_\rho}{k}\hat{\mathbf{z}}. \tag{2.133}$$

are the azimuthal and polar unit vectors that correspond to the unit vector parallel to the wavevector of propagation of the plane wave:

$$\begin{aligned}
\hat{\mathbf{k}} &= \left(k_x\hat{\mathbf{x}}+k_y\hat{\mathbf{y}}+k_z\hat{\mathbf{z}}\right)/k \qquad (2.134)\\
&= \hat{\mathbf{x}}\sin\theta_{\hat{\mathbf{k}}}\cos\phi_{\hat{\mathbf{k}}}+\hat{\mathbf{y}}\sin\theta_{\hat{\mathbf{k}}}\sin\phi_{\hat{\mathbf{k}}}+\hat{\mathbf{z}}\cos\theta_{\hat{\mathbf{k}}}, \qquad (2.135)
\end{aligned}$$

respectively, with the azimuthal and polar angles of propagation being given by the following formulas:

$$\phi_{\hat{\mathbf{k}}}(k_x,k_y) = \arctan(k_x,k_y) = \mathrm{i}\ln\left[(k_x+\mathrm{i}k_y)/k_\rho\right], \tag{2.136}$$

$$\theta_{\hat{\mathbf{k}}}(k_x,k_y,k,\iota) = \arccos(k_z/k) = -\mathrm{i}\ln\left[\iota\sqrt{1-(k_\rho/k)^2}+\mathrm{i}k_\rho/k\right]. \tag{2.137}$$

According to the equations above, there is a direct one-to-one connection between (k_x,k_y,k,ι) and $(\theta_{\hat{\mathbf{k}}},\phi_{\hat{\mathbf{k}}},k)$ and, therefore, sometimes from next on it will be convenient to refer to the VPHs with the kets $|\alpha\,\theta_{\hat{\mathbf{k}}}\,\phi_{\hat{\mathbf{k}}}\,k\rangle$ ($\equiv \mathbf{F}_\alpha(\mathbf{r};\theta_{\hat{\mathbf{k}}},\phi_{\hat{\mathbf{k}}},k)$). The spatial representation of VCHs reads as follows:

$$\begin{aligned}
|\mathrm{M}\,\mu_z\,k_z\,k\rangle^{(\iota)} \equiv \mathbf{F}^{(\iota)}_{\mathrm{M},\mu_z}(\mathbf{r};k_z,k) &= \frac{1}{k_\rho}\nabla\times\left[\hat{\mathbf{z}}\,\psi^{(\iota)}_{\mu_z}(\mathbf{r};k_z,k)\right] \\
&= e^{\mathrm{i}k_z z}e^{\mathrm{i}\mu_z\phi}\left[\mathrm{i}\mu_z\frac{Z^{(\iota)}_{\mu_z}(k_\rho\rho)}{k_\rho\rho}\hat{\rho}-\frac{\partial Z^{(\iota)}_{\mu_z}(k_\rho\rho)}{\partial(k_\rho\rho)}\hat{\phi}\right], \qquad (2.138)\\
|\mathrm{N}\,\mu_z\,k_z\,k\rangle^{(\iota)} \equiv \mathbf{F}^{(\iota)}_{\mathrm{N},\mu_z}(\mathbf{r};k_z,k) &= \frac{\nabla\times}{k}\mathbf{F}^{(\iota)}_{\mathrm{M},\mu_z}(\mathbf{r};k_z,k) \\
&= e^{\mathrm{i}k_z z}e^{\mathrm{i}\mu_z\phi}\times \\
&\quad\left[\mathrm{i}\frac{k_z}{k}\frac{\partial Z^{(\iota)}_{\mu_z}(k_\rho\rho)}{\partial(k_\rho\rho)}\hat{\rho}-\mu_z\frac{k_z}{k}\frac{Z^{(\iota)}_{\mu_z}(k_\rho\rho)}{k_\rho\rho}\hat{\phi}+\frac{k_\rho}{k}Z^{(\iota)}_{\mu_z}(k_\rho\rho)\,\hat{\mathbf{z}}\right]. \qquad (2.139)
\end{aligned}$$

And finally, the spatial representation of VSHs reads as follows:

$$\begin{aligned}
|\mathrm{M}\,\mu_z\,\nu\,k\rangle^{(\iota)} \equiv \mathbf{F}^{(\iota)}_{\mathrm{M},\mu_z\nu}(\mathbf{r};k) &= \nabla\times\left[\mathbf{r}\,\psi^{(\iota)}_{\mu_z\nu}(\mathbf{r};k)\right] \\
&= \mathrm{i}z^{(\iota)}_\nu(kr)\mathbf{f}_{\mathrm{M},\mu_z\nu}(\hat{\mathbf{r}}), \qquad (2.140)\\
|\mathrm{N}\,\mu_z\,\nu\,k\rangle^{(\iota)} \equiv \mathbf{F}^{(\iota)}_{\mathrm{N},\mu_z\nu}(\mathbf{r};k) &= \frac{\nabla\times}{k}\mathbf{F}^{(\iota)}_{\mathrm{M},\mu_z\nu}(\mathbf{r};k) \\
&= \nu(\nu+1)\frac{\psi^{(\iota)}_{\mu_z\nu}(\mathbf{r};k)}{kr}\hat{\mathbf{r}}+\tilde{z}^{(\iota)}_\nu(kr)\mathbf{f}_{\mathrm{N},\mu_z\nu}(\hat{\mathbf{r}}), \qquad (2.141)
\end{aligned}$$

where we have defined the following functions:

$$\mathbf{f}_{\mathrm{M},\mu_z\nu}(\hat{\mathbf{r}}) = \gamma_{\mu_z\nu}\left[\hat{\theta}\tau^{(1)}_{\mu_z\nu}(\theta)+\mathrm{i}\hat{\phi}\tau^{(2)}_{\mu_z\nu}(\theta)\right]e^{\mathrm{i}\mu_z\phi}, \tag{2.142}$$

$$\mathbf{f}_{\mathrm{N},\mu_z\nu}(\hat{\mathbf{r}}) = \gamma_{\mu_z\nu}\left[\hat{\theta}\tau^{(2)}_{\mu_z\nu}(\theta)+\mathrm{i}\hat{\phi}\tau^{(1)}_{\mu_z\nu}(\theta)\right]e^{\mathrm{i}\mu_z\phi}, \tag{2.143}$$

$$\tilde{z}^{(\iota)}_\nu(x) = \frac{1}{x}\frac{\partial}{\partial x}[x\,z^{(\iota)}_\nu(x)], \tag{2.144}$$

$$\tau^{(1)}_{\mu_z\nu}(\theta) = \mu_z\frac{\mathrm{P}^{\mu_z}_\nu(\cos\theta)}{\sin\theta}, \tag{2.145}$$

$$\tau^{(2)}_{\mu_z\nu}(\theta) = \frac{\partial\mathrm{P}^{\mu_z}_\nu(\cos\theta)}{\partial\theta}. \tag{2.146}$$

Note that the functions $\mathbf{f}_{\alpha,\mu_z\nu}(\hat{\mathbf{r}})$ are orthonormal in the following sense:

$$\int_0^{2\pi}\mathrm{d}\phi\int_0^{\pi}\sin\theta\mathrm{d}\theta\;\;\mathbf{f}_{\alpha,\mu_z\nu}(\hat{\mathbf{r}})\cdot\left[\mathbf{f}_{\alpha',\mu'_z\nu'}(\hat{\mathbf{r}})\right]^* = \delta_{\alpha\alpha'}\delta_{\mu_z\mu'_z}\delta_{\nu\nu'}. \tag{2.147}$$

Let us also define here the generalized spherical Bessel functions $z^{(\iota)}_{\alpha,\nu}(x) = \delta_{\alpha \mathrm{M}} z^{(\iota)}_{\nu}(x) + \delta_{\alpha \mathrm{N}} \tilde{z}^{(\iota)}_{\nu}(x)$, which will be useful in a next chapter. Note that, sometimes, we may refer to those TE and TM VSHs, as VSHs of well-defined parity, since they are invariant under parity transformation: $\mathbf{r} \to -\mathbf{r}$ (they may only pick a minus sign).

Next, let us introduce some analytical transformations between the VPHs, VCHs, and VSHs that will be useful in the next chapters of this thesis. Specifically, the transformation of VPHs into a series of regular ($\iota = 1$) VCHs reads as follows:

$$|\alpha\, \theta_{\hat{\mathbf{k}}}\, \phi_{\hat{\mathbf{k}}}\, k\rangle \;=\; \sum_{\mu_z} C_{\mu_z}(\phi_{\hat{\mathbf{k}}})\, |\alpha\, \mu_z\, \left[k_z = k\cos\theta_{\hat{\mathbf{k}}}\right]\, k\rangle^{(1)}\,, \tag{2.148}$$

where the transformation coefficients are given by:

$$C_{\mu_z}(\phi_{\hat{\mathbf{k}}}) \;=\; \mathrm{i}^{\mu_z} e^{-\mathrm{i}\mu_z \phi_{\hat{\mathbf{k}}}}. \tag{2.149}$$

The opposite transformation, i.e., the expansion of VCHs into an angular spectrum of VPHs, is given by the formulas below:

$$|\alpha\, \mu_z\, k_z\, k\rangle^{(1)} \;=\; \frac{1}{2\pi}\int_0^{2\pi} \mathrm{d}\phi_{\hat{\mathbf{k}}}\, C_{-\mu_z}(\phi_{\hat{\mathbf{k}}})\, |\alpha\, \left[\theta_{\hat{\mathbf{k}}} = \arccos(\mathrm{k_z/k})\right]\, \phi_{\hat{\mathbf{k}}}\, k\rangle\,, \tag{2.150}$$

$$|\alpha\, \mu_z\, k_z\, k\rangle^{(3)} \;=\; \frac{1}{\pi}\int_{C^{\phi_0}} \mathrm{d}\phi_{\hat{\mathbf{k}}}\, C_{-\mu_z}(\phi_{\hat{\mathbf{k}}})\, |\alpha\, \left[\theta_{\hat{\mathbf{k}}} = \arccos(\mathrm{k_z/k})\right]\, \phi_{\hat{\mathbf{k}}}\, k\rangle\,,$$

$$,\qquad\qquad \text{for}\quad x\cos\phi_0 + y\sin\phi_0 > 0, \tag{2.151}$$

where for the radiating ($\iota = 3$) VCHs we need to take into account also evanescent waves by integrating over a contour on the complex azimuthal-angle-of-propagation plane with $C^{\phi_0} = [\phi_0 - \pi/2 + \mathrm{i}\infty, \phi_0 - \pi/2] \cup [\phi_0 - \pi/2, \phi_0 + \pi/2] \cup [\phi_0 + \pi/2, \phi_0 + \pi/2 - \mathrm{i}\infty]$ and $\phi_0 \in [0, 2\pi]$.

Furthermore, the transformation of VPHs into a series of regular ($\iota = 1$) VSHs is given by the formula below:

$$|\alpha\, \theta_{\hat{\mathbf{k}}}\, \phi_{\hat{\mathbf{k}}}\, k\rangle \;=\; \sum_{\nu\mu_z,\alpha'} 4\pi S^{\alpha}_{\alpha',-\mu_z\nu}(\pi - \theta_{\hat{\mathbf{k}}}, \phi_{\hat{\mathbf{k}}})\, |\alpha'\, \mu_z\, \nu\, k\rangle^{(1)}\,, \tag{2.152}$$

where the transformation coefficients are given by:

$$S^{\alpha}_{\alpha',\mu_z\nu}(\theta_{\hat{\mathbf{k}}}, \phi_{\hat{\mathbf{k}}}) \;=\; \mathrm{i}^{3-\nu}\gamma_{\mu_z\nu}\, \tau^{(1+\delta_{\alpha\alpha'})}_{\mu_z\nu}\left(\theta_{\hat{\mathbf{k}}}\right) e^{i\mu_z\phi_{\hat{\mathbf{k}}}}. \tag{2.153}$$

The opposite transformation, i.e., the expansion of VSHs into an angular spectrum of VPHs, is given by the formulas below:

$$|\alpha\, \mu_z\, \nu\, k\rangle^{(1)} \;=\; \frac{1}{4\pi}\sum_{\alpha'}\int_0^{2\pi} \mathrm{d}\phi_{\hat{\mathbf{k}}}\int_0^{\pi} \sin\theta_{\hat{\mathbf{k}}}\mathrm{d}\theta_{\hat{\mathbf{k}}}\, S^{\alpha'}_{\alpha,\mu_z\nu}(\theta_{\hat{\mathbf{k}}}, \phi_{\hat{\mathbf{k}}})\, |\alpha'\, \theta_{\hat{\mathbf{k}}}\, \phi_{\hat{\mathbf{k}}}\, k\rangle\,, \tag{2.154}$$

$$|\alpha\, \mu_z\, \nu\, k\rangle^{(3)} \;=\; \frac{1}{2\pi}\sum_{\alpha'}\int_0^{2\pi} \mathrm{d}\phi_{\hat{\mathbf{k}}}\int_{C^{\pm}} \sin\theta_{\hat{\mathbf{k}}}\mathrm{d}\theta_{\hat{\mathbf{k}}}\, S^{\alpha'}_{\alpha,\mu_z\nu}(\theta_{\hat{\mathbf{k}}}, \phi_{\hat{\mathbf{k}}})\, |\alpha'\, \theta_{\hat{\mathbf{k}}}\, \phi_{\hat{\mathbf{k}}}\, k\rangle\,,$$

$$\text{for}\;\; \mathrm{z} \gtrless 0, \tag{2.155}$$

where for the radiating ($\iota = 3$) VSHs we need to take into account also evanescent waves by integrating over a contour on the complex polar-angle-of-propagation plane with $C^+ = [0, \frac{\pi}{2} - \mathrm{i}\infty]$ and $C^- = [\frac{\pi}{2} + \mathrm{i}\infty, \pi]$.

Finally, let us also expand the Dyadic Green's function of such a local, stationary, homogeneous, and isotropic medium in terms of its just discussed eigenmodes. The wave equation of the medium (with wavenumber $k(\omega)$) once we include current sources $\mathbf{J}$ reads as follows:

$$\left(\nabla \times \nabla \times -k^2\right) \mathbf{E} \quad = \quad \mathrm{i}\omega\mu\mathbf{J}, \tag{2.156}$$

and, therefore, its solution with respect to the DGF of the medium, $\overleftrightarrow{\mathbf{G}}$. is given by:

$$\mathbf{E}(\mathbf{r}, \omega) \quad = \quad \mathrm{i}\omega\mu \int_{\mathbb{R}^3} \overleftrightarrow{\mathbf{G}}(\mathbf{r}, \mathbf{r}'; k) \cdot \mathbf{J}(\mathbf{r}', \omega) \mathrm{d}^3\mathbf{r}, \tag{2.157}$$

with the DGF of the medium being the solution of the following differential equation:

$$\left(\nabla \times \nabla \times -k^2\right) \overleftrightarrow{\mathbf{G}}(\mathbf{r}, \mathbf{r}'; k) \quad = \quad \overleftrightarrow{\mathbf{I}}\, \delta(\mathbf{r} - \mathbf{r}'), \tag{2.158}$$

with $\overleftrightarrow{\mathbf{I}}$ being the unit dyad. According to [206], avoiding to refer to the singularity at $\mathbf{r} = \mathbf{r}'$, the expansion of the DGF of such a medium in terms of series of either VPHs:

$$\begin{aligned} \overleftrightarrow{\mathbf{G}}(\mathbf{r}, \mathbf{r}'; k) \quad &\equiv \quad \frac{\mathrm{i}}{8\pi^2} \sum_{\alpha} \iint_{-\infty}^{+\infty} \frac{\mathrm{d}k_x \mathrm{d}k_y}{\sqrt{k^2 - k_\rho^2}} \times \\ &\times \quad \begin{cases} \mathbf{F}_\alpha^{(-)}(\mathbf{r}; k_x, k_y, k) \otimes \mathbf{F}_\alpha^{(+)}(\mathbf{r}'; -k_x, -k_y, k), & \text{for } \; z < z', \\ \mathbf{F}_\alpha^{(+)}(\mathbf{r}; k_x, k_y, k) \otimes \mathbf{F}_\alpha^{(-)}(\mathbf{r}'; -k_x, -k_y, k), & \text{for } \; z > z', \end{cases} \end{aligned} \tag{2.159}$$

or VCHs:

$$\begin{aligned} \overleftrightarrow{\mathbf{G}}(\mathbf{r}, \mathbf{r}'; k) \quad &\equiv \quad \frac{\mathrm{i}}{8\pi} \sum_{\mu_z, \alpha} (-1)^{\mu_z} \int_{-\infty}^{+\infty} \mathrm{d}k_z \times \\ &\times \quad \begin{cases} \mathbf{F}_{\alpha,\mu_z}^{(1)}(\mathbf{r}; k_z, k) \otimes \mathbf{F}_{\alpha,-\mu_z}^{(3)}(\mathbf{r}'; = k_z, k), & \text{for } \; \rho < \rho', \\ \mathbf{F}_{\alpha,\mu_z}^{(3)}(\mathbf{r}; k_z, k) \otimes \mathbf{F}_{\alpha,-\mu_z}^{(1)}(\mathbf{r}'; -k_z, k), & \text{for } \; \rho > \rho', \end{cases} \end{aligned} \tag{2.160}$$

or VSHs:

$$\begin{aligned} \overleftrightarrow{\mathbf{G}}(\mathbf{r}, \mathbf{r}'; k) \quad &\equiv \quad \mathrm{i}k \sum_{\nu\mu_z, \alpha} (-1)^{\mu_z} \times \\ &\times \quad \begin{cases} \mathbf{F}_{\alpha,\mu_z\nu}^{(1)}(\mathbf{r}; k) \otimes \mathbf{F}_{\alpha,-\mu_z\nu}^{(3)}(\mathbf{r}'; k), & \text{for } \; r < r' \\ \mathbf{F}_{\alpha,\mu_z\nu}^{(3)}(\mathbf{r}; k) \otimes \mathbf{F}_{\alpha,-\mu_z\nu}^{(1)}(\mathbf{r}'; k), & \text{for } \; r > r' \end{cases} \end{aligned} \tag{2.161}$$

reads as above. We denote with the symbol ($\otimes$) the tensor product between the two vector fields.

2.7 Electromagnetic fields as eigenstates of the helicity operator: an appropriate framework to study electromagnetic chirality

In this section, we will introduce the Riemann-Silberstein vectors, i.e., the eigenstates of the helicity operator, which can provide an alternative representation of Maxwell's fields. We will briefly discuss why such an alternative framework for electromagnetism is convenient to study phenomena of electromagnetic chirality. Finally, we will also discuss the emergence of an alternative set of eigenmodes of the vectorial Helmholtz wave equation with well-defined helicity.

The helicity operator $\hat{\mathbf{\Lambda}}$ is defined as [207]:

$$\hat{\mathbf{\Lambda}} = \frac{\hat{\mathbf{J}}\cdot\hat{\mathbf{P}}}{|\hat{\mathbf{P}}|} = \frac{\nabla\times}{k}, \tag{2.162}$$

where $\hat{\mathbf{J}} = -\mathrm{i}\mathbf{r}\times\nabla + \hat{\mathbf{S}}$ is the total angular momentum operator vector and $\hat{\mathbf{S}}$ is the vector of spin-1 matrices. $\hat{\mathbf{P}} = -\mathrm{i}\nabla$ is the linear momentum vector operator. The latter equation above constitutes a particular representation of the helicity operator for the case of monochromatic fields that obey Eq. (2.123).

Let us now introduce the helicity basis as an alternative framework of electromagnetism. To begin with, we consider a local, stationary, and isotropic medium with no magnetoelectric coupling inside which a distribution of dipolar emitters (such us e.g. molecules) and external sources are embedded. Maxwell's equations there take the following form then:

$$\nabla\times\mathbf{E} = \mathrm{i}\omega\mu\mathbf{H} + \mathrm{i}\omega\mathbf{p}_\mathrm{m}, \tag{2.163}$$
$$\nabla\times\mathbf{H} = -\mathrm{i}\omega\varepsilon\mathbf{E} - \mathrm{i}\omega\mathbf{p}_\mathrm{e} + \mathbf{J}, \tag{2.164}$$
$$\nabla\cdot[\varepsilon\mathbf{E}+\mathbf{p}] = \rho, \tag{2.165}$$
$$\nabla\cdot[\mu\mathbf{H}+\mathbf{m}] = 0, \tag{2.166}$$

with ε, μ being the dielectric permittivity and the magnetic permeability of the medium, respectively, and $\mathbf{p}_\mathrm{e}, \mathbf{p}_\mathrm{m}$ denote the electric and magnetic dipole moments, respectively. Note that the magnetic dipole moment in the literature is commonly defined as $\mathbf{m} = \mathbf{p}_\mathrm{m}/\mu_0$, but here we use different conventions to be consistent with our initial ones. This as well implies that the polarizabilities that we will be introducing in what follows shall differ also from their conventional definitions.

By introducing the following quantities to transit to the new, helical basis:

$$\mathbf{G}_\lambda = \frac{\mathbf{E}+\lambda\mathrm{i}Z\mathbf{H}}{\sqrt{2}}, \tag{2.167}$$
$$\mathbf{p}_\lambda = \frac{(\mathbf{p}_\mathrm{e}/\varepsilon)+\lambda\mathrm{i}Z(\mathbf{p}_\mathrm{m}/\mu)}{\sqrt{2}}, \tag{2.168}$$

we can recast the above Maxwell's equations into the following alternative form:

$$\hat{\mathbf{\Lambda}}\mathbf{G}_\lambda = \lambda\mathbf{G}_\lambda + \lambda\mathbf{p}_\lambda + \lambda\frac{\mathrm{i}\mathbf{J}}{\omega\varepsilon\sqrt{2}}, \tag{2.169}$$
$$\nabla\cdot[\mathbf{G}_\lambda+\mathbf{p}_\lambda] = \frac{\rho}{\varepsilon\sqrt{2}}, \tag{2.170}$$

with $\lambda = \pm 1$ being the eigenvalues of the helicity operator $\hat{\mathbf{\Lambda}}$, with corresponding eigenstates the Riemann–Silberstein vectors $\mathbf{G}_\lambda$ [207]. $\mathbf{p}_\lambda$ denotes the helical dipole moments embedded inside the medium, $k = \omega\sqrt{\mu\varepsilon}$ is the wavenumber of the medium and $Z = \sqrt{\mu/\varepsilon}$ is its wave-impedance. Note that, once we look at the interface conditions of the electromagnetic fields between two media, we can show that there is no scattering of fields of opposite helicity from one medium to the other as long as the two media share the same wave-impedance. Importantly, note also that the eigenstates of helicity are defined with respect to the electromagnetic properties of a particular background medium characterized by ε, μ. What is an eigenstate of well-defined helicity for that medium, may be a mixture of helical eigenstates in another medium (e.g. free space) that does not have the same wave-impedance.

In view of the above definitions, we can also recast the polarizability tensor of the emitters in the helicity basis. Specifically, we have:

$$\begin{bmatrix}\mathbf{p}_\mathrm{e}\\ \mathbf{p}_\mathrm{m}\end{bmatrix} = \begin{bmatrix}\boldsymbol{\alpha}_\mathrm{ee} & \boldsymbol{\alpha}_\mathrm{em}\\ \boldsymbol{\alpha}_\mathrm{me} & \boldsymbol{\alpha}_\mathrm{mm}\end{bmatrix}\cdot\begin{bmatrix}\mathbf{E}\\ \mathbf{H}\end{bmatrix} \quad \Rightarrow \quad \begin{bmatrix}\mathbf{p}_+\\ \mathbf{p}_-\end{bmatrix} = \mathbf{A}_\mathrm{H}\cdot\begin{bmatrix}\mathbf{G}_+\\ \mathbf{G}_-\end{bmatrix}, \quad \text{with :} \tag{2.171}$$

$$\mathbf{A}_\mathrm{H} = \begin{bmatrix}\boldsymbol{\alpha}_{++} & \boldsymbol{\alpha}_{+-}\\ \boldsymbol{\alpha}_{-+} & \boldsymbol{\alpha}_{--}\end{bmatrix} = \begin{bmatrix}\frac{\boldsymbol{\alpha}_\mathrm{ee}}{2\varepsilon} + \frac{\boldsymbol{\alpha}_\mathrm{mm}}{2\mu} - \frac{\mathrm{i}(\boldsymbol{\alpha}_\mathrm{em}-\boldsymbol{\alpha}_\mathrm{me})}{2\sqrt{\mu\varepsilon}} & \frac{\boldsymbol{\alpha}_\mathrm{ee}}{2\varepsilon} - \frac{\boldsymbol{\alpha}_\mathrm{mm}}{2\mu} + \frac{\mathrm{i}(\boldsymbol{\alpha}_\mathrm{em}+\boldsymbol{\alpha}_\mathrm{me})}{2\sqrt{\mu\varepsilon}}\\ \frac{\boldsymbol{\alpha}_\mathrm{ee}}{2\varepsilon} - \frac{\boldsymbol{\alpha}_\mathrm{mm}}{2\mu} - \frac{\mathrm{i}(\boldsymbol{\alpha}_\mathrm{em}+\boldsymbol{\alpha}_\mathrm{me})}{2\sqrt{\mu\varepsilon}} & \frac{\boldsymbol{\alpha}_\mathrm{ee}}{2\varepsilon} + \frac{\boldsymbol{\alpha}_\mathrm{mm}}{2\mu} + \frac{\mathrm{i}(\boldsymbol{\alpha}_\mathrm{em}-\boldsymbol{\alpha}_\mathrm{me})}{2\sqrt{\mu\varepsilon}}\end{bmatrix}. \tag{2.172}$$

In Eq. (2.169), we can see that, for a source-free medium, the Riemann-Silberstein vectors of opposite helicity λ only couple to each other through the polarizability tensor of the dipolar emitters. Emitters that do not couple the two helical fields are called *dual* [208]. The polarizability tensor of a dual emitter has the following symmetries:

$$\boldsymbol{\alpha}_{+-} = \boldsymbol{\alpha}_{-+} = 0, \quad \text{or equivalently :} \quad \frac{\boldsymbol{\alpha}_\mathrm{ee}}{\varepsilon} = \frac{\boldsymbol{\alpha}_\mathrm{mm}}{\mu}, \quad \boldsymbol{\alpha}_\mathrm{em} = -\boldsymbol{\alpha}_\mathrm{me}. \tag{2.173}$$

Let us here relate the property of duality with electromagnetic chirality. An object is said to be *chiral* if it lacks any mirror symmetry plane. Chirality comes from the greek word "$\chi\varepsilon\iota\rho$", meaning "hand", which is our most familiar chiral object. Therefore, we frequently refer to chirality as handedness. The mirror image of a chiral object is called its *enantiomer*. Importantly, *while helicity commutes with arbitrary translations and rotations, it anticommutes with any mirror symmetry transformation with respect to an arbitrary axis*, i.e., any such arbitrary mirror transformation of electromagnetic fields of well-defined helicity flips the helicity sign and, as a result, the reflected fields never coincide with the initial ones no matter how we translate or rotate them. That is the actual geometric definition of chirality. Therefore we can say that electromagnetic fields of pure helicity are chiral. Such chiral light comes also into pairs of enantiomers which we label through the eigenvalue of helicity $\lambda = \pm 1$. Consequently, we can see that dual emitters always preserve the chirality of the fields in that regard. Finally, note that electromagnetic fields of generally mixed helicity can also be chiral, though, i.e., they can still lack the ability to be superimposed on their mirror images by translations and rotations.

Chiroptical sensing, i.e., probing the geometrical chirality of an object with electromagnetic waves, finds numerous applications from biochemistry to nanotechnology. Chiroptical sensing techniques provide means to differentiate between the two enantiomers through optical measurements, which can be of major importance in biochemistry, for example.

Roughly speaking, the final goal is to probe the target sample with light and imprint the chiral properties of the sample on the chirality of light that can be afterwards optically measured. Arguably, and as we shall see in what follows, the helicity basis provides therefore an appropriate framework of electromagnetism to analyze and design optical systems with respect to their interaction with chiral light.

Nevertheless, designing a realistic experiment and constructing a measurement that properly imprints the geometric chirality of the sample on the chirality of light is far from trivial. The optical measurement needs to detect the presence of chirality in the sample and also needs to distinguish between the two enantiomeric samples. It should also be insensitive to rotations and translations of the sample. Ideally, it should also be able to somehow quantify the degree of chirality of the sample, i.e., the degree of geometric dissimilarity between the two enantiomers. The above pose as rather strict requirements for the design of an experimental measure of the chirality of the sample. In what follows we will effectively relax the requirement for invariance of the sample under rotations and translations by introducing random disorder and we will briefly present a common example of experimental measure of the geometric chirality of a target sample probed by chiral light.

A medium that hosts a dense, large ensemble of randomly places and oriented dipolar emitters, is commonly described macroscopically considering an averaged polarization with a corresponding *isotropic* -due to the rotational averaging- susceptibility tensor:

$$\langle \begin{bmatrix} \mathbf{p}_{\mathrm{e}} \\ \mathbf{p}_{\mathrm{m}} \end{bmatrix} \rangle = \begin{bmatrix} \mathbf{P}_{\mathrm{e,av}} \\ \mathbf{P}_{\mathrm{m,av}} \end{bmatrix} = \begin{bmatrix} \varepsilon \chi_{\mathrm{ee,av}} \mathbf{I} & \sqrt{\mu\varepsilon}\chi_{\mathrm{em,av}} \mathbf{I} \\ \sqrt{\mu\varepsilon}\chi_{\mathrm{me,av}} \mathbf{I} & \mu \chi_{\mathrm{mm,av}} \mathbf{I} \end{bmatrix} \cdot \begin{bmatrix} \mathbf{E} \\ \mathbf{H} \end{bmatrix}, \tag{2.174}$$

which we can recast in the helicity basis by defining $\mathbf{P}_{\lambda,\mathrm{av}} = \left[(\mathbf{P}_{\mathrm{e,av}}/\varepsilon) + \lambda \mathrm{i} Z (\mathbf{P}_{\mathrm{m,av}}/\mu) \right] / \sqrt{2}$:

$$\begin{bmatrix} \mathbf{P}_{+,\mathrm{av}} \\ \mathbf{P}_{-,\mathrm{av}} \end{bmatrix} = \boldsymbol{\chi}_{\mathrm{H,av}} \cdot \begin{bmatrix} \mathbf{G}_{+} \\ \mathbf{G}_{-} \end{bmatrix}, \quad \text{with :} \tag{2.175}$$

$$\begin{aligned} \boldsymbol{\chi}_{\mathrm{H,av}} &= \begin{bmatrix} \chi_{++,\mathrm{av}} \mathbf{I} & \chi_{+-,\mathrm{av}} \mathbf{I} \\ \chi_{-+,\mathrm{av}} \mathbf{I} & \chi_{--,\mathrm{av}} \mathbf{I} \end{bmatrix} \\ &= \begin{bmatrix} \frac{\chi_{\mathrm{ee,av}} + \chi_{\mathrm{mm,av}} - \mathrm{i}(\chi_{\mathrm{em,av}} - \chi_{\mathrm{me,av}})}{2} \mathbf{I} & \frac{\chi_{\mathrm{ee,av}} - \chi_{\mathrm{mm,av}} + \mathrm{i}(\chi_{\mathrm{em,av}} + \chi_{\mathrm{me,av}})}{2} \mathbf{I} \\ \frac{\chi_{\mathrm{ee,av}} - \chi_{\mathrm{mm,av}} - \mathrm{i}(\chi_{\mathrm{em,av}} + \chi_{\mathrm{me,av}})}{2} \mathbf{I} & \frac{\chi_{\mathrm{ee,av}} + \chi_{\mathrm{mm,av}} + \mathrm{i}(\chi_{\mathrm{em,av}} - \chi_{\mathrm{me,av}})}{2} \mathbf{I} \end{bmatrix}, \end{aligned} \tag{2.176}$$

where, again, for the averaged induced polarization to be dual, we get the following conditions:

$$\chi_{+-,\mathrm{av}} = \chi_{-+,\mathrm{av}} = 0, \quad \text{or equivalently :} \quad \chi_{\mathrm{ee,av}} = \chi_{\mathrm{mm,av}}, \quad \chi_{\mathrm{em,av}} = -\chi_{\mathrm{me,av}}. \tag{2.177}$$

In terms of the induced averaged polarizations, a parity transformation of a large random ensemble of emitters should correspond to a large random ensemble of its enantiomers. Note that the parity transformation flips helicity. Also, note that the electric field and the electric polarization density, being polar vectors, are odd under parity symmetry and, on the other hand, the magnetic field and the magnetic polarization density, being axial vectors, i.e., pseudovectors, are even under parity symmetry. This has, as a result, the following symmetry between the helical susceptibility tensors of an averaged medium hosting some emitters and another averaged medium hosting their enantiomers (noted with prime below):

$$\boldsymbol{\chi}'_{\mathrm{H,av}} = \begin{bmatrix} \chi'_{++,\mathrm{av}} \mathbf{I} & \chi'_{+-,\mathrm{av}} \mathbf{I} \\ \chi'_{-+,\mathrm{av}} \mathbf{I} & \chi'_{--,\mathrm{av}} \mathbf{I} \end{bmatrix} = \begin{bmatrix} \chi_{--,\mathrm{av}} \mathbf{I} & \chi_{-+,\mathrm{av}} \mathbf{I} \\ \chi_{+-,\mathrm{av}} \mathbf{I} & \chi_{++,\mathrm{av}} \mathbf{I} \end{bmatrix}. \tag{2.178}$$

Note that an achiral averaged medium is characterized by the symmetry $\boldsymbol{\chi}'_{\mathrm{H,av}} = \boldsymbol{\chi}_{\mathrm{H,av}}$, since then enantiomers are identical. Such is the case when $\chi_{\mathrm{em,av}} = \chi_{\mathrm{me,av}} = 0$.

Circular dichroism, which measures the differential absorption of an optical system upon illumination with helical fields of opposite helicity, is a measure commonly used for chiroptical sensing. According to Eq. (2.53), the absorption density of the averaged chiral medium is given by:

$$\begin{aligned} A_{\mathrm{av}}(\mathbf{r},\omega) &= -\omega \mathrm{Im}\left\{\mathbf{E}\cdot\mathbf{P}^*_{\mathrm{e,av}} + \mathbf{H}\cdot\mathbf{P}^*_{\mathrm{m,av}}\right\} && (2.179)\\ &= -\omega\varepsilon \sum_{\lambda} \mathrm{Im}\left\{\mathbf{G}_{\lambda}\cdot\mathbf{P}^*_{\lambda,\mathrm{av}}\right\} && (2.180)\\ &= -\omega\varepsilon \sum_{\lambda,\lambda_0} \mathrm{Im}\left\{\chi^*_{\lambda\lambda_0,\mathrm{av}}\mathbf{G}_{\lambda}\cdot\mathbf{G}^*_{\lambda_0}\right\}. && (2.181) \end{aligned}$$

Let us now assume the following:

- The field exciting the chiral emitters is practically identical to the background field, i.e., the field that exists inside the background system without the presence of the chiral emitters. This is normally a pretty realistic assumption.
- The background system is non-absorbing and therefore does not contribute to the CD signal.

With the above assumptions, we can get the following simplified definition of circular dichroism density:

$$\begin{aligned} \mathrm{CD}(\mathbf{r},\omega) &= A^{+}_{\mathrm{av}}(\mathbf{r},\omega) - A^{-}_{\mathrm{av}}(\mathbf{r},\omega)\\ &= -\omega\varepsilon \sum_{\lambda,\lambda_0} \mathrm{Im}\left\{\chi^*_{\lambda\lambda_0,\mathrm{av}}\left[\mathbf{G}^{+}_{\lambda}\cdot\mathbf{G}^{+*}_{\lambda_0} - \mathbf{G}^{-}_{\lambda}\cdot\mathbf{G}^{-*}_{\lambda_0}\right]\right\}, && (2.182) \end{aligned}$$

where $\mathbf{G}^{\lambda'}_{\lambda}$ denotes the background fields of helicity λ under the excitation of the background system with a field of well-defined helicity λ'. Moreover, let us assume now the following:

- The chiral medium stays invariant upon an isometric transformation (which includes an arbitrary combination of translations, rotations, and reflections), so that for each point in space $\mathbf{r}$, there exists some other image point $\mathbf{r}_{\mathrm{image}}(\mathbf{r})$ for which we have $\chi_{\lambda\lambda_0,\mathrm{av}}(\mathbf{r},\omega) = \chi_{\lambda\lambda_0,\mathrm{av}}(\mathbf{r}_{\mathrm{image}}(\mathbf{r}),\omega)$.
- The background fields have the symmetry: $\mathbf{G}^{\pm}_{\lambda}(\mathbf{r},\omega) = \mathbf{R}(\mathbf{r})\cdot\mathbf{G}^{\mp}_{-\lambda}(\mathbf{r}_{\mathrm{image}}(\mathbf{r}),\omega)$, with $\mathbf{R}(\mathbf{r})$ being some *unitary* matrix (such as, e.g. a rotation matrix). Such is the case, for example, when the background system and the two illuminations of opposite helicity possess some mirror symmetry [209].

Then, under such additional assumptions and in view of Eqs. (2.178,2.182), it becomes straightforward to show that the quantity $\mathrm{CD}(\mathbf{r},\omega) + \mathrm{CD}(\mathbf{r}_{\mathrm{image}}(\mathbf{r}),\omega)$ is opposite to the same quantity corresponding to the enantiomeric averaged chiral medium. This, also, directly gives that the quantity is equal to zero for an achiral averaged medium. The total circular dichroism is measured as the spatial average of that quantity, and it becomes evident that it provides a means to differentiate between the two chiral enantiomers, which shall give a circular dichroism signal of opposite sign. Note that strong chiral fields

facilitated by a resonant optical system can enhance the magnitude of the CD signal, which is typically order of magnitudes weaker than the absorption signals themselves. Importantly, note that in Ref. [209] it is argued that the CD signal can be enhanced when the background field is of pure helicity. This is rather rarely the case, though, and actually requires that the background system is appropriately designed to be dual ($\mathbf{G}_{\lambda}^{\lambda'} \propto \delta_{\lambda,\lambda'}$) or anti-dual ($\mathbf{G}_{\lambda}^{\lambda'} \propto \delta_{\lambda,-\lambda'}$) in order to achieve such purity of helicity for the background fields [209].

In view of the above exemplary discussion, one can further appreciate the role of the helicity basis framework in facilitating the analysis of electromagnetic chirality in optical systems. Apart from the measure of the circular dichroism, which constitutes a rather common technique for chiroptical sensing, in a next chapter, we will investigate an alternative setup for chiroptical sensing, that has been recently proposed in the literature and that is based on the principle of spin-orbit coupling of emitters to waveguides [210]. Specifically, we will study the directional coupling of multipolar emitters of well-defined helicity into waveguides.

Let us now proceed further and present the eigenmode basis sets upon which we can expand fields of well-defined helicity λ in homogeneous space. Such fields obey the following source-free differential equation (see Eq. (2.169)):

$$\hat{\mathbf{\Lambda}}\mathbf{G}_{\lambda} = \lambda\mathbf{G}_{\lambda}. \tag{2.183}$$

In view of the symmetry of the TE/TM eigensolutions given by Eq. 2.129, -which we can rewrite here in Dirac notation (omitting the reference to the remaining two eigenvalues of the eigenstates) by using the helicity operator as follows: $|\beta\, k\rangle = \hat{\mathbf{\Lambda}}\,|\alpha\, k\rangle$, with $\beta \neq \alpha$- we can straightforwardly get the eigenstates of well-defined helicity λ in terms of the already defined TE/TM eigenstates. They are defined as follows:

$$|\lambda\, k\rangle = \frac{|\mathrm{M}\, k\rangle + \lambda\,|\mathrm{N}\, k\rangle}{\sqrt{2}} \tag{2.184}$$

and are solutions to Eq. (2.183), i.e., they are eigenstates of the helicity operator $\hat{\mathbf{\Lambda}}\,|\lambda\, k\rangle = \lambda\,|\lambda\, k\rangle$. Note that the helical eigenmodes essentially constitute an alternative to the TE/TM polarization basis for the fields.

We will refer to the VPHs, VCHs, and VSHs with well-defined helicity with the following kets $|\lambda\, k_x\, k_z\, k\rangle^{(\iota)}$ ($|\lambda\, \theta_{\hat{\mathbf{k}}}\, \phi_{\hat{\mathbf{k}}}\, k\rangle$), $|\lambda\, \mu_z\, k_z\, k\rangle^{(\iota)}$, $|\lambda\, \mu_z\, \nu\, k\rangle^{(\iota)}$, respectively. For example, by referring to the formulas of the previous section, the spatial representation of helical VPHs is analytically given by:

$$|\lambda\, \theta_{\hat{\mathbf{k}}}\, \phi_{\hat{\mathbf{k}}}\, k\rangle \equiv \mathbf{F}_{\lambda}(\theta_{\hat{\mathbf{k}}}, \phi_{\hat{\mathbf{k}}}, k; \mathbf{r}) = \hat{\mathbf{e}}_{\lambda}(\hat{\mathbf{k}})e^{\mathrm{i}k\hat{\mathbf{k}}(\theta_{\hat{\mathbf{k}}},\phi_{\hat{\mathbf{k}}})\cdot\mathbf{r}}, \tag{2.185}$$

with the polarization vector of the helical plane wave being given by:

$$\hat{\mathbf{e}}_{\lambda}(\hat{\mathbf{k}}) = \frac{-\lambda\hat{\theta}_{\hat{\mathbf{k}}} - \mathrm{i}\hat{\phi}_{\hat{\mathbf{k}}}}{\sqrt{2}} \tag{2.186}$$

$$= \hat{\mathbf{x}}\frac{-\lambda\cos\theta_{\hat{\mathbf{k}}}\cos\phi_{\hat{\mathbf{k}}} + \mathrm{i}\sin\phi_{\hat{\mathbf{k}}}}{\sqrt{2}} + \hat{\mathbf{y}}\frac{-\lambda\cos\theta_{\hat{\mathbf{k}}}\sin\phi_{\hat{\mathbf{k}}} - \mathrm{i}\cos\phi_{\hat{\mathbf{k}}}}{\sqrt{2}} + \hat{\mathbf{z}}\frac{\lambda\sin\theta_{\hat{\mathbf{k}}}}{\sqrt{2}}. \tag{2.187}$$

Importantly, note that helical VPHs with $\lambda = 1 (\lambda = -1)$ correspond to left(right)-handed

circularly polarized plane waves. Similarly, by referring to the formulas of the previous section, we can get analytical expressions for the spatial representation of helical VCHs and VSHs, as well. Expressions for the transformations between helical VPHs, VCHs, and VSHs can also be straightforwardly obtained, as well.

Furthermore, the Dyadic Green's Function of Eq. (2.183) obeying the differential equation:

$$\hat{\mathbf{\Lambda}}\overleftrightarrow{\mathbf{G}}_{\lambda}(\mathbf{r},\mathbf{r}';k) \;=\; \lambda\overleftrightarrow{\mathbf{G}}_{\lambda}(\mathbf{r},\mathbf{r}';k)+\overleftrightarrow{\mathbf{I}}\,\delta(\mathbf{r}-\mathbf{r}'), \tag{2.188}$$

is related with the Dyadic Green's Function of the corresponding Helmholtz equation according to the equation below (see Eq. (1.17) in page 43 of [211]):

$$\overleftrightarrow{\mathbf{G}}_{\lambda}(\mathbf{r},\mathbf{r}';k) \;=\; \left[\nabla\times\overleftrightarrow{\mathbf{I}}+\lambda k\overleftrightarrow{\mathbf{I}}\right]\overleftrightarrow{\mathbf{G}}(\mathbf{r},\mathbf{r}';k), \tag{2.189}$$

where $\overleftrightarrow{\mathbf{I}}$ denotes the unit dyad. The expansion of the helical DGF into the eigenmodes of source-free homogeneous isotropic media is also straightforwardly done by making use of the last equation and Eqs. (2.159-2.161).

Before closing this section, we would like to present a local conservation law of electromagnetic chirality that has been extensively studied in the literature lately [212, 213]. In analogy to Poynting's theorem dictating the flow of electromagnetic energy in media, the electromagnetic chirality conservation law follows directly from Maxwell's equations in frequency domain (Eqs. (2.8,2.9)) and it reads as follows (for our adopted conventions in macroscopic Maxwell's equations):

$$\nabla\cdot\mathbf{X}_{\text{flux}}(\mathbf{r},\omega)+\mathrm{X}_{\text{medium}}(\mathbf{r},\omega)+\mathrm{X}_{\text{sources}}(\mathbf{r},\omega) \;=\; 0, \tag{2.190}$$

where:

- $\mathbf{X}_{\text{flux}}$ denotes the flux of electromagnetic chirality and is in units of power flux density [Watts/m^2]. It is defined as:

$$\mathbf{X}_{\text{flux}} \;=\; \frac{c_0}{2\omega}\left(\mathbf{E}^*\times\nabla\times\mathbf{H}-\mathbf{H}^*\times\nabla\times\mathbf{E}\right), \tag{2.191}$$

$$\;=\; \frac{c_0}{2\omega\mathrm{i}Z_0}\sum_{\lambda}\lambda\,\mathbf{G}^*_{0,\lambda}\times\nabla\times\mathbf{G}_{0,\lambda}, \tag{2.192}$$

  where we have introduced the Riemann-Silberstein vectors $\mathbf{G}_{0,\lambda}=\left[\mathbf{E}+\lambda\mathrm{i}Z_0\mathbf{H}\right]/\sqrt{2}$ of well-defined helicity $\lambda=\pm1$ in free space (whose wave-impedance we denote with Z_0). Importantly, note that it is straightforward to show that the above expression on the infinite sphere in free space is real-valued and is exactly equal to the difference between the power flux density of transverse waves of positive helicity and those of negative helicity. That is to say that it is indicative of the difference of the power flux between left- and right-handed photons, with a positive chirality flux implying a relative abundance of left-handed photons of positive helicity.

- $\mathrm{X}_{\text{medium}}$ denotes the exchange of electromagnetic chirality between the electromagnetic fields and the polarized medium. It is in units of power density [Watts/m^3], and it is defined as:

$$\mathrm{X}_{\mathrm{medium}} = \frac{-\mathrm{i}c_0}{2}\left(\mathbf{P}_{\mathrm{e}}\cdot\nabla\times\mathbf{E}^{*}+\mathbf{E}^{*}\cdot\nabla\times\mathbf{P}_{\mathrm{e}}+\mathbf{P}_{\mathrm{m}}\cdot\nabla\times\mathbf{H}^{*}+\mathbf{H}^{*}\cdot\nabla\times\mathbf{P}_{\mathrm{m}}\right), \tag{2.193}$$

$$= \frac{-\mathrm{i}c_0\varepsilon_0}{2}\sum_{\lambda}\lambda\left(\mathbf{P}_{0,\lambda}\cdot\nabla\times\mathbf{G}^{*}_{0,\lambda}+\mathbf{G}^{*}_{0,\lambda}\cdot\nabla\times\mathbf{P}_{0,\lambda}\right), \tag{2.194}$$

where $\mathbf{P}_{0,\lambda}=\left[\mathbf{P}_{\mathrm{e}}/\varepsilon_0+\lambda\mathrm{i}Z_0\mathbf{P}_{\mathrm{m}}/\mu_0\right]/\sqrt{2}$ are defined as the polarization density vectors of well-defined helicity $\lambda=\pm1$ in free space (i.e., a polarization density generating fields of well-defined helicity in free space). An achiral medium should conserve the chirality of the fields and, therefore, should have zero total chirality exchange with them.

- $\mathrm{X}_{\mathrm{sources}}$ denotes the exchange of electromagnetic chirality between the electromagnetic fields and the external current sources. It is in units of power density [Watts/m^3], and it is defined as:

$$\mathrm{X}_{\mathrm{sources}} = \frac{c_0}{2\omega}\left(\mathbf{J}\cdot\nabla\times\mathbf{E}^{*}+\mathbf{E}^{*}\cdot\nabla\times\mathbf{J}\right), \tag{2.195}$$

$$= \frac{c_0}{2\sqrt{2}\omega}\sum_{\lambda}\left(\mathbf{J}\cdot\nabla\times\mathbf{G}^{*}_{0,\lambda}+\mathbf{G}^{*}_{0,\lambda}\cdot\nabla\times\mathbf{J}\right). \tag{2.196}$$

Finally, applying the divergence theorem for a volume V enclosed by a surface S, the law of conservation of electromagnetic chirality in its integral form reads as follows:

$$\oiint_{S}\hat{\mathbf{n}}\cdot\mathbf{X}_{\mathrm{flux}}(\mathbf{r},\omega)\,\mathrm{d}^2\mathbf{r} = -\int_{V}\mathrm{X}_{\mathrm{medium}}(\mathbf{r},\omega)+\mathrm{X}_{\mathrm{sources}}(\mathbf{r},\omega)\mathrm{d}^3\mathbf{r}. \tag{2.197}$$

2.8 Eigenmodes of waveguiding systems

In this section, we will briefly discuss the fundamentals of the electromagnetic analysis of waveguiding systems, which will be considered in a later chapter. We will focus on non-absorbing and non-magnetic waveguides made of isotropic dielectrics. We will consider them to be translationally invariant and aligned along the x-axis, which will be the optical axis of the waveguide.

Let us first discuss the emergence of some eigenvalues that characterize the eigenmoges of such waveguiding systems, based on spatial symmetry arguments. To begin with, the translation invariance of the waveguide with respect to the x-axis implies that the system is diagonal with respect to the linear momentum along the x-axis, k_x. Therefore, k_x constitutes the first appropriate eigenvalue for the waveguided modes.

We would like to highlight that, apart from the continuous translation symmetry, the waveguide belongs also to some point group. Each point group is characterized by a number of irreducible representations that transform in a particular way under the symmetry elements of the point group. We can use additional eigenvalues corresponding to particular symmetry elements of the group to characterize the eigenmodes of the waveguide with respect to the irreducible representation of the point group that it belongs. Let us mention some common examples of waveguides and the point groups that they belong to, as well as the eigenvalues that we can introduce to differentiate between eigenmodes of different irreducible representations.

For example, waveguides on top of substrates or waveguides with claddings such as ridge, or rib, or slot, or strip-loaded waveguides, typically belong to the $\mathbf{C_s}$ point group that has two irreducible representations that can be characterized through the eigenvalue of the mirror symmetry with respect to some axis that is perpendicular to the optical axis. Let us call this eigenvalues $\sigma_{\mathrm{v}} = \pm 1$. On the other hand, we can commonly have waveguides, such as maybe buried waveguides, that have a higher degree of symmetry, belonging to the $\mathbf{C_{2v}}$ point group that has four irreducible representations that can be characterized through the eigenvalues of two mirror symmetries with respect to two such symmetry axes that are perpendicular to each other and both, also, perpendicular to the optical axis. Let us call those eigenvalues $\sigma_{\mathrm{v}_1} = \pm 1$, $\sigma_{\mathrm{v}_2} = \pm 1$, respectively. In what follows in this section, we will use the generic index i that will be considered to span all such eigenvalues of the point group of the waveguide. In this section, we will use the generic index i to be considered to span all the possible eigenvalues of the point group of the waveguide. Therefore, in abstract Dirac notation, we can use the following kets to refer to the eigenmodes of the waveguide $|i\, k_x\, \omega\rangle$. Note, that we added as an extra eigenvalue the frequency ω, since the waveguide apart from the aforementioned spatial symmetries posseses also a continuous translation symmetry in time.

Let us now follow Ref. [214] and postulate the following Ansatz for the electric and magnetic fields of the eigenmodes of the waveguide:

$$\mathbf{E}_i(\mathbf{r}, \omega; k_x) = \mathbf{e}_i(y, z, \omega; k_x) e^{\mathrm{i}k_x x}, \tag{2.198}$$

$$\mathbf{H}_i(\mathbf{r}, \omega; k_x) = \mathbf{h}_i(y, z, \omega; k_x) e^{\mathrm{i}k_x x}, \tag{2.199}$$

Then we can apply this Ansatz to the Helmholtz wave equation of a dielectric medium that is characterized by a relative dielectric permittivity $\varepsilon_{\mathrm{r}}(y, z)$ and get as a result differential equations that the fields $\mathbf{e}_i(y, z, \omega; k_x), \mathbf{h}_i(y, z, \omega; k_x)$ should obey. For example, for the electric field we have:

$$\left[\nabla_\perp^2 + \varepsilon_{\mathrm{r}}(y, z) k_0^2 - k_x^2\right] \mathbf{e}_i(y, z, \omega; k_x) = \left[\nabla_\perp + \mathrm{i}k_x \hat{\mathbf{x}}\right] \cdot \left[\mathbf{e}_i(y, z, \omega; k_x) \cdot \nabla_\perp \left(\ln\left(\varepsilon_{\mathrm{r}}(y, z)\right)\right)\right], \tag{2.200}$$

where k_0 denotes the wavenumber of free space and the subscript "$_\perp$" refers to the plane perpendicular to the optical axis. Similarly, we can get another differential equation for the magnetic field profile of the mode (see Eq. (11.40b) in [214]).

Note that, for a non-absorbing waveguide, we can choose the eigenmodes to have purely real transverse (to the optical axis) components of the electromagnetic fields, and purely imaginary longitudinal components. Moreover, we have then the following symmetries between two counterpropagating modes $\mathbf{e}_i(y, z, \omega; -k_x) = \mathbf{e}_i^*(y, z, \omega; k_x)$ and $\mathbf{h}_i(y, z, \omega; -k_x) = -\mathbf{h}_i^*(y, z, \omega; k_x)$.

There is a discrete set of even number of bounded modes ($N_{\mathrm{m}}(\omega)$) that the waveguide supports for a given frequency ω. They come in pairs of counterpropagating modes with opposite k_x and same index i. Any electromagnetic field can be expanded on that discrete basis set of bounded modes, plus some extra term of non-bounded radiating fields. Specifically, we can write for the electric field (and similarly for the magnetic field):

$$\mathbf{E}(\mathbf{r}, \omega) = \mathbf{E}_{\mathrm{rad}}(\mathbf{r}, \omega) + \sum_{j=1}^{N_{\mathrm{m}}(\omega)} \mathcal{A}_j(\omega) \mathbf{E}_{i_j}(\mathbf{r}, \omega; k_{x,j}), \tag{2.201}$$

where $\mathcal{A}_j(\omega)$ are some complex amplitudes and we use the index j to span all the set of bounded modes at that frequency. We use the index i_j to refer to the point group eigenvalues that characterize the j-th bounded mode and the variable $k_{x,j}$ to denote the linear momentum along the x-axis of the j-th bounded mode.

Next, let us define the following inner product between two electromagnetic fields:

$$\langle \mathbf{EM}^{(1)}, \mathbf{EM}^{(2)} \rangle (x) = \iint_{S_\infty(x)} \frac{1}{2} \left[\mathbf{E}^{(1)*}(\mathbf{r}) \times \mathbf{H}^{(2)}(\mathbf{r}) + \mathbf{E}^{(2)}(\mathbf{r}) \times \mathbf{H}^{(1)*}(\mathbf{r}) \right] \cdot \hat{\mathbf{x}} \, \mathrm{d}y\mathrm{d}z, \tag{2.202}$$

where integration is being performed over an infinite plane perpendicular to the optical axis of the waveguide. In Ref. [214] it is first shown that the radiating fields are orthogonal to the bounded modes with respect to that inner product, i.e., we have that:

$$\langle \mathbf{EM}^{\mathrm{rad}}, \mathbf{EM}_j^{\mathrm{bound}} \rangle (x) = 0. \tag{2.203}$$

Moreover, it is shown that the bounded modes can be orthonormalized with respect to that inner product, i.e., we have that:

$$\langle \mathbf{EM}_j^{\mathrm{bound}}, \mathbf{EM}_{j'}^{\mathrm{bound}} \rangle (x) = \mathrm{sgn}(k_{x,j}) \delta_{jj'}. \tag{2.204}$$

Note that modes with different index j correspond to modes with different sets of (i, k_x). Importantly, note that the normalization is with respect to unit power flux of the bounded modes along $\mathrm{sgn}(k_{x,j})\hat{\boldsymbol{x}}$, with $\mathrm{sgn}(\cdot)$ denoting the sign function.

By making use of the above orthogonality properties, we can readily get the complex amplitudes of the bounded modes upon some arbitrary excitation (that results in a total field that we refer to with the ket $|\mathbf{EM}\rangle$) as follows:

$$\mathcal{A}_j(\omega) = \mathrm{sgn}(k_{x,j}) \langle \mathbf{EM}_j^{\mathrm{bound}}, \mathbf{EM} \rangle (x). \tag{2.205}$$

Finally, note that the power captured by each bounded waveguided mode is given by:

$$P_j(\omega) = |\mathcal{A}_j(\omega)|^2 . \tag{2.206}$$

2.9 Introduction to the T-matrix method for linear electromagnetic systems

In this section, we will introduce the fundamental notions behind the transition matrix (T-matrix) theoretical methods that can be employed to model linear electromagnetic systems, i.e., electromagnetic systems that are comprised by media whose polarization linearly depends on the electromagnetic fields through first order susceptibility tensors. Note that, operating an electromagnetic system in the linear regime typically implies low intensities of light, since otherwise weak nonlinear effects can become pronounced.

Let us consider the general case of a linear electromagnetic system characterized by the susceptibility tensor $\boldsymbol{\chi}(\mathbf{r}, \mathbf{r}-\mathbf{r}', \omega-\omega', \omega')$ (see Eq. (2.12)) and some appropriate boundary conditions, e.g. the Silver-Müller radiation condition at infinity. The electromagnetic fields are a solution of Maxwell's equations, which we can write in the following abstract form: $\hat{\mathbf{H}}(\boldsymbol{\chi})\psi = s$, where $\hat{\mathbf{H}}(\boldsymbol{\chi})$ is a linear operator representing Maxwell's equations in the medium, ψ represents the electromagnetic fields and s represents the external current sources. The fields can be decomposed into a sum of incident and scattered fields: $\psi = \psi_{\text{inc}} + \psi_{\text{sca}}$. The incident fields are normally a solution of Maxwell's equations in a background medium characterized by a susceptibility tensor $\boldsymbol{\chi}_{\text{b}}$ (normally that of free space, where $\boldsymbol{\chi}_{\text{b}} = \mathbf{0}$) and, therefore, are nontrivial solutions of source-free Maxwell's equations inside there: $\hat{\mathbf{H}}(\boldsymbol{\chi}_{\text{b}})\psi_{\text{inc}} = 0$. Hence, we have that the scattered fields are solutions of:

$$\hat{\mathbf{H}}(\boldsymbol{\chi})\psi_{\text{sca}} = s_{\text{sca}}. \quad \text{with}: \quad s_{\text{sca}} = s - \left[\hat{\mathbf{H}}(\boldsymbol{\chi}) - \hat{\mathbf{H}}(\boldsymbol{\chi}_{\text{b}})\right]\psi_{\text{inc}}. \tag{2.207}$$

where the second term in the right-hand side of the last equation corresponds to an equivalent polarization current distribution emanating from the presence of incident fields exciting the system apart from the sources s. By defining the Green's operator of $\hat{\mathbf{H}}(\boldsymbol{\chi})$ as its inverse $\hat{\mathbf{G}}(\boldsymbol{\chi}) = \hat{\mathbf{H}}^{-1}(\boldsymbol{\chi})$ we have that:

$$\psi_{\text{sca}} \quad = \quad \hat{\mathbf{G}}(\boldsymbol{\chi})s + \hat{\mathbf{T}}(\boldsymbol{\chi})\psi_{\text{inc}}, \tag{2.208}$$

where we have introduced the T-matrix operator whose definition reads as follows:

$$\hat{\mathbf{T}}(\boldsymbol{\chi}) \quad = \quad \hat{\mathbf{G}}(\boldsymbol{\chi})\hat{\mathbf{H}}(\boldsymbol{\chi}_{\text{b}}) - \hat{\mathbf{I}}. \tag{2.209}$$

That is to say that the T-matrix is a linear operator that relates the scattered with the incident fields in the absence of external current sources:

$$\psi_{\text{sca}} \quad = \quad \hat{\mathbf{T}}(\boldsymbol{\chi})\psi_{\text{inc}}. \tag{2.210}$$

Note that the linear operator $\hat{\mathbf{G}}(\boldsymbol{\chi})\hat{\mathbf{H}}(\boldsymbol{\chi}_{\text{b}})$ relates the total fields ψ with the incident fields ψ_{inc}: $\psi = \hat{\mathbf{G}}(\boldsymbol{\chi})\hat{\mathbf{H}}(\boldsymbol{\chi}_{\text{b}})\psi_{\text{inc}}$. Notably, in view of Eq. (2.208), we have that while the T-matrix operator gives the scattering response of the system upon some background field excitation, the Green's function of the system gives the scattering response of the system upon its excitation by external sources. Hence, in what follows in this section, we will always consider the external sources to be far away from our optical system, so that they effectively represent a background field excitation.

We would also like to remark that our definition of the T-matrix operator here differs from the definition of another T-matrix operator, $\mathbb{T}(\boldsymbol{\chi})$, that recently attracts attention in the literature [215–219]. There, $\mathbb{T}(\boldsymbol{\chi})$ relates the induced polarization currents in the system (instead of the scattered field) with the incident field. Once represented in frequency domain, the relation between the two T-matrix operators for non-magnetic systems reads as: $\hat{\mathbf{T}}(\boldsymbol{\chi}) = -\mathrm{i}\hat{\mathbf{G}}(\boldsymbol{\chi}_{\text{b}})\hat{\boldsymbol{\Omega}}\mathbb{T}(\boldsymbol{\chi})$, where $\hat{\boldsymbol{\Omega}}$ is a diagonal operator over frequency ω with entries the frequencies themselves. In what follows, we will always refer to $\hat{\mathbf{T}}(\boldsymbol{\chi})$ as the T-matrix operator of the optical system.

The linearity of the T-matrix operator implies that if the response of the system, once excited separately by two incident fields $\psi_{\text{inc}}^{(1)}, \psi_{\text{inc}}^{(2)}$, leads to the scattered fields $\psi_{\text{sca}}^{(1)}, \psi_{\text{sca}}^{(2)}$, respectively, then for $a^{(1)}, a^{(2)}$ being some arbitrary complex scalars, we have that, once the system gets excited by the superposition of the fields $a^{(1)}\psi_{\text{inc}}^{(1)} + a^{(2)}\psi_{\text{inc}}^{(2)}$, then its response shall be $a^{(1)}\psi_{\text{sca}}^{(1)} + a^{(2)}\psi_{\text{sca}}^{(2)}$.

Note that the T-matrix operator in its most general abstract form is a continuous infinite-dimensional operator relating incident fields in spatio-spectral space with scattered fields in spatio-spectral space. However, in practice we like to have finite and discrete representations of the T-matrix operator. For this, we need to quantize the representations of the incident and scattered fields. This generally requires the expansion of the incident and scattered fields into the eigenmodes corresponding to the zeros of the system operators $\hat{\mathbf{H}}(\boldsymbol{\chi}_{\text{b}}), \hat{\mathbf{H}}(\boldsymbol{\chi})$, respectively.

Regarding the incident fields, for the typical case of the background medium being free space, we have analytical basis sets of eigenmodes in terms of the VPHs/VCHs/VSHs that we discussed in a previous section. For example, a pulse of some arbitrary vector beam exciting the system can be conveniently represented on a basis of plane waves:

$$\mathbf{E}^{\text{inc}}(\mathbf{r}, t) = \sum_{\alpha} \int_{-\infty}^{+\infty} \int_{0}^{\pi} \int_{0}^{2\pi} \mathcal{A}_{\alpha}^{\text{inc}}(\theta_{\hat{\mathbf{k}}}, \phi_{\hat{\mathbf{k}}}, \omega) \mathbf{F}_{\alpha}(\theta_{\hat{\mathbf{k}}}, \phi_{\hat{\mathbf{k}}}, \omega/c_0; \mathbf{r}) e^{-\mathrm{i}\omega t} \sin\theta_{\hat{\mathbf{k}}} \mathrm{d}\phi_{\hat{\mathbf{k}}} \mathrm{d}\theta_{\hat{\mathbf{k}}} \mathrm{d}\omega, \tag{2.211}$$

where c_0 is the speed of light in free space and $\mathcal{A}_{\alpha}^{\text{inc}}(\theta_{\hat{\mathbf{k}}}, \phi_{\hat{\mathbf{k}}}, \omega)$ are some complex coefficients appropriately defined to represent the excitation. The continuous integrals in the above representation of the incident field can be properly discretized to lead to quantized representations. However, sometimes it is more convenient to use a series of spherical or cylindrical waves, instead of plane waves, to represent the incident fields. For example, the excitation of finite sized systems sometimes is conveniently represented by a series of spherical waves that can converge fast within the finite domain of the system with only a few terms, leading to a more compact representation (i.e., one with lower dimensionality) of the incident field. For the same reason, for cylindrical-like systems it could be more convenient to expand the incident field into a series of cylindrical waves with respect to the main axis of the system. Reducing the dimensionality of the representation of the fields is of course always desirable in practice.

On the other hand, regarding the quantization of the scattered fields, the situation gets more complicated. In general, the eigenmodes that correspond to the zeros of $\hat{\mathbf{H}}(\boldsymbol{\chi})$ are known in the literature as quasinormal modes (QNMs) [220]. They take their name from the fact that they constitute eigenmodes of typically non-Hermitian systems, i.e., open systems without energy conservation due to material and radiation losses. Their eigenfrequencies are, therefore, complex, and the spectral support of each QNM is mainly along a compact segment of the real frequencies axis. Note that the zeros of $\hat{\mathbf{H}}(\boldsymbol{\chi})$ correspond to the poles of the T-matrix operator $\hat{\mathbf{T}}(\boldsymbol{\chi})$ and, therefore, a pole expansion of the T-matrix operator is possible [221–224]. So, ideally, we would expand the scattered fields in terms of a finite set of the QNMs of the system. Then, once the QNMs of the system are calculated, it is straightforward to fill the entries of the T-matrix of the system by projecting the response of the system upon an excitation with a single individual element of the basis set for the incident fields, on the QNM basis (see e.g. Eq. (4) in [225]). However, the calculation of the QNMs of the system is itself, typically, not that trivial task. The QNMs and the corresponding complex eigenfrequencies of simple systems such as planar slabs, or cylindrical, or spherical scatterers, can be calculated analytically [226–229]. Some more complicated systems, such as arrays of spheres for example, could also be treated

in a semi-analytical way. However, in the general case, the calculation of QNMs is done purely numerically with, e.g., some finite element method (FEM) solver, and, therefore, can be quite computationally expensive, especially for optically large systems. There, the calculations are typically performed inside a finite domain bounded by perfectly matched layers (PMLs), which give rise to unphysical PML modes that one needs to distinguish against. The continuation of the fields of the QNMs outside the simulation domain needs to be performed semi-analytically *a posteriori*. Note, also, that the proper normalization of QNMs has also given rise to some academic disputes [230, 231]. We are not going to expand further on the aspects related with the QNMs, since this goes out of the scope of this thesis; however, arguably, QNMs could provide a means to construct the full T-matrix operator of a system.

Nevertheless, we are typically interested in only some smaller part rather than the full T-matrix operator, i.e., we may only care about the response of the system -that is to say the scattered fields- inside a subspace of the system. For example, 1) we may only care about the scattered fields in the far-field region of a scatterer -where we can treat the near-field region of the scatterer as a black box-, or 2) in a multiport system of waveguide ports connected with an optical circuit we may only care about the fields coupled to the waveguide ports -where, again, we can treat the near-field region with the optical circuit of the multiport system as a black box-. Those two are some rather common examples where we are only interested in the fields inside a subregion of the real-space representation of the scattered fields. This may facilitate the significant simplification of the T-matrix operator: it can provide us with some neat modal basis set that we can employ to reach a quantized, "reduced" representation of the original T-matrix operator. Specifically, we can use as a basis set the eigenmodes of a simpler system (let's refer to it as $\hat{\mathbf{H}}(\boldsymbol{\chi}')$) that is identical to our actual system $\hat{\mathbf{H}}(\boldsymbol{\chi})$ inside the subdomain of interest (let's call it V_s). For example, we can always use a series of radiating VSHs (i.e., the radiating solutions of free space) as a basis set to expand the scattered fields from a scatterer embedded in free space. Similarly, we can always use the eigenmodes of each individual waveguide (i.e., the eigenmodes of the infinite translationally invariant waveguide embedded in free space) as a basis set to expand the waveguided fields in the far-field region of a multiport system. It is the same principle that is being used, for example, in the Fourier Modal Method (FMM), or else Rigorous Coupled Wave Analysis (RCWA). There, we have a multilayer system, with each layer being a slice of finite thickness from a 2D photonic crystal with discrete translation symmetries laterally, and the fields inside each layer are represented by the semi-analytically retrieved eigenmodes of the infinite translationally invariant 2D photonic crystal, which are used as a basis set to expand the fields in that subregion of the system.

Arguably, such a reduction of the representation of the T-matrix operator potentially enables us to use eigenmodes of simpler systems -that can be efficiently, either (semi-) analytically or with rather low computational effort, retrieved- to represent the fields of the original complex system inside some subdomain of interest. In a next chapter, we will employ a T-matrix operator that connects the radiated fields of an emitter, expanded in a multipolar basis of well-defined helicity, with the complex amplitudes of the guided modes of an adjacent waveguide. We will calculate such a T-matrix to study the directional coupling of the multipolar emissions to the waveguide.

Moreover, other considerations can help us to reduce further the representation of the T-matrix operator. Specifically, our system may be invariant with respect to some symmetries. Such invariance under symmetry transformations can render it diagonal with respect to some properly selected eigenvalues, and we may be interested about the response of the system associated only with some range of those eigenvalues. For example, stationary systems are diagonal with respect to frequency ω and we may be interested to work only

with a reduced representation of the T-matrix operator that is associated with a particular frequency of interest. Likewise, translationally invariant systems along some axis are diagonal with respect to the linear momentum along that axis and we may be interested to study the response of the system upon some particular illumination direction, which enables us also to work with an appropriately reduced representation of the T-matrix operator by focusing on the part associated with the linear momentum component of our interest. As another example, we can mention the case of rotationally symmetric systems that are diagonal with respect to the projection of the angular momentum along their axis of symmetry. In such a case, we may be interested in probing the system with vector beams of particular orbital angular momentum propagating along the symmetry axis of the system. And then, we can also work with a reduced representation of the T-matrix operator of the system by focusing on the part associated with the angular momentum eigenvalues of our interest.

It becomes obvious that employing a set of eigenmodes with appropriately chosen eigenvalues, tailored to the symmetries of the system, becomes instrumental in attaining a reduced, quantized representation of the T-matrix operator. In a next chapter, we will develop a Floquet Mie theory to study light scattering from a non-stationary sphere whose electromagnetic properties vary periodically in time. The T-matrix operator corresponding to such a scattering system is not diagonal any more with respect to frequency, since the continuous translation symmetry of the system over time is broken and replaced by a discrete translation symmetry in time. The latter renders our scattering system a temporal photonic crystal which we can better study after we introduce a temporal Floquet frequency that diagonalizes its T-matrix operator in frequency domain.

Having discussed the above fundamental aspects pertained to the T-matrix theory, let us now move to more practical aspects associated with the T-matrix method as a tool to analyze electromagnetic scattering processes. Arguably, Mie theory has provided us with the archetype of electromagnetic scattering theory: that of light scattered by a sphere [3]. The Mie coefficients constitute the elements of the T-matrix of a spherical scatterer embedded inside an infinite medium and give the scattered field outside with respect to the incident field, with both being represented in a basis of VSHs. Waterman introduced later the notion of the T-matrix [232–234], and since then there have been significant efforts to extend its scope for more complicated scattering systems [235].

Waterman's T-matrix corresponds to a particular category of T-matrix operators: those that treat a scattering system as a black box and focus only on the scattered fields outside the scattering system that get radiated upon some excitation with an incident field. This category of T-matrices is practically quite special, as we shall see, and attracts a lot of attention. Arguably, its major strength is associated with the remarkably efficient way that it can be used to deal with multi-scattering phenomena of scatterers embedded inside a medium [236]. It is not a coincidence that in the last decades, the development of T-matrix methods has been largely driven by the scientific community that was interested in light scattering from aerosols in the atmosphere [237, 238]. Recently, there has also been interest in the method for the modeling of the optical response of disordered media [239]. In what follows, we will discuss the generalization of the methods that make use of such "black box" type of T-matrices to model the coupling of scatterers with their environment to deal with complex multi-scattering phenomena in a hierarchical way. Our final goal is to divide an extended optical system into constituent subsystems and construct a matrix representation of light interaction with the individual subsystems, and, finally, use it to connect all of them together.

Let us consider a finite linear optical system. That system we can recast into a hierarchical optical network as long as we are able to divide it into a finite number of subdomains/components, N_{c}, (and let's call the subdomains V_i, with i taking values from

1 till N_c) that are connected with each other via some closed surface interfaces that they share (which we can call Σ_j, with the index j running through all such interfaces). We require that in the vicinity of the designated ports/interfaces we have a fixed homogeneous medium, which is a significant restriction to the process of dividing the system into subdomains. As we will discuss in what follows, this requirement aims to facilitate the employment of a basis set of electromagnetic waves to expand the incident and scattered fields across the ports. Each subdomain V_i is topologically of genus g_i, depending on the number of inclusions that it has. The number of ports connected to V_i is then $N_{p,i} = g_i + 1$. We will refer to them as $\Sigma_{j(i_n)}$, with n being an index that takes values from 0 till $N_{p,i} - 1$. As a convention, we consider that the port with $n = 0$ is the one fully enclosing V_i in its interior and we call it the "parent" port. We call the rest of the ports with $0 < n \leq N_{p,i} - 1$ as the "children" ports, that are g_i in number. Note that we can construct a tree representation of such a hierarchical optical network that can assist our analysis of the system. See Fig. 2.1 for a sketch of such a process of recasting an optical system into a hierarchical optical network.

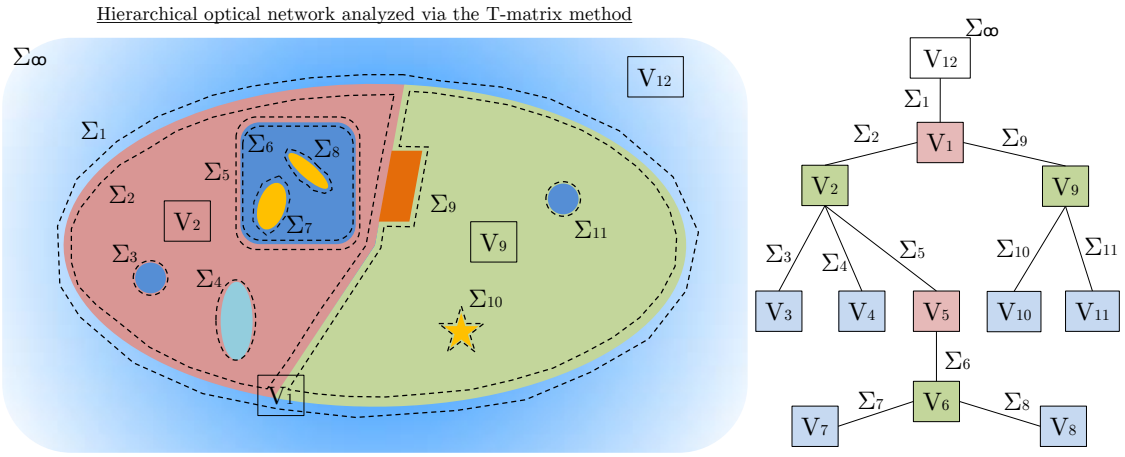

Figure 2.1: Facilitating the analysis of complex, multi-scale optical systems through a multi-scattering approach between its constituent subsystems via the T-matrix method that recasts the system into a hierarchical optical network. Each subsystem is represented by its own T-matrix, and the coupling between the subsystems can be represented by a tree diagram.

Let us now consider each subdomain V_i as an isolated, independent scattering system which can only be illuminated by some excitation emanating from the exterior of V_i and illuminating V_i through its $N_{p,i}$ ports. Note that we would also like to avoid the case of any non-local coupling between the constituent subsystems (it is still fine to have non-local interactions inside the subsystem, though, since we are generally treating it as a black box), so that the interaction between the subsystems takes place solely by means of a scattering process through the ports/interfaces. Importantly, note that for such an abstracted scattering component we consider the homogeneous material in the vicinity of each port to be extended everywhere outside of V_i, both at the infinite exterior domain and inside the inclusions that it may have. We want to construct a T-matrix representation of such an abstracted scattering component, where we consider as an input the incident fields emanating from the exterior of V_i and as an output the scattered fields outside of V_i. The ability to construct such matrix representations of the subsystems, mathematically, is related with the compactness of the operator of the subsystem [240]. Let us assume, now, a finite basis set with which the field over the port Σ_j can be expanded into a set of modes that are standing waves in the interior of Σ_j (let's refer to the corresponding

amplitudes of this expansion with the complex vectors $\psi_{\mathrm{stnd},j}$) and a set of modes that are radiating inside the exterior of Σ_j (which we represent with a complex vector $\psi_{\mathrm{rad},j}$), once we assume there an infinite homogeneous background medium assigned with the material of the port. We can introduce now the T-matrix of the considered abstracted subsystem of V_i, $\hat{\mathbf{T}}_i$, that will connect the incident through the ports fields ($\psi_{\mathrm{inc},i}$) inside V_i, with the scattered through the ports fields outside V_i ($\psi_{\mathrm{sca},i}$). We can write then the following equation in a matrix form:

$$\psi_{\mathrm{sca},i} = \hat{\mathbf{T}}_i \cdot \psi_{\mathrm{inc},i}, \quad \Rightarrow \tag{2.212}$$

$$\begin{bmatrix} \psi_{\mathrm{rad},j(i_0)} \\ \psi_{\mathrm{stnd},j(i_1)} \\ \vdots \\ \psi_{\mathrm{stnd},j(i_{g_i})} \end{bmatrix} = \begin{bmatrix} \hat{\mathbf{T}}_{i,00} & \hat{\mathbf{T}}_{i,01} & \cdots & \hat{\mathbf{T}}_{i,0g_i} \\ \hat{\mathbf{T}}_{i,10} & \hat{\mathbf{T}}_{i,11} & \cdots & \hat{\mathbf{T}}_{i,1g_i} \\ \vdots & \vdots & \ddots & \vdots \\ \hat{\mathbf{T}}_{i,g_i0} & \hat{\mathbf{T}}_{i,g_i1} & \cdots & \hat{\mathbf{T}}_{i,g_ig_i} \end{bmatrix} \cdot \begin{bmatrix} \psi_{\mathrm{stnd},j(i_0)} \\ \psi_{\mathrm{rad},j(i_1)} \\ \vdots \\ \psi_{\mathrm{rad},j(i_{g_i})} \end{bmatrix}. \tag{2.213}$$

Note that the scattered fields from the parent port are of radiating type, while those from the children ports are of standing wave type. Conversely, while the incident fields from the children ports are of radiating type, those from the parent port are of standing wave type.

We can now start from the last two "generations" of our tree representing the hierarchical optical network and recombine the children nodes with their parent into a single new "family" node, in an attempt to account for multi-scattering processes taking place among them (ingoring for now the rest of their environment as homogeneous space). Our goal is to substitute the two generations with an effective T-matrix representing the interaction of the whole "family", now, with its environment. That effective T-matrix, which we will call as $\hat{\tilde{\mathbf{T}}}_i$ (with the index i referring to the subdomain index of the parent of the family), will be of zero genus topologically, since we will have already taken into account multi-scattering interactions within the family, i.e., it will treat the family as a "black box" and will only represent its interaction with its outside environment, that of the older generations. Note that, proceeding like this, we can climb the tree upwards, generation by generation, finally getting the T-matrix that represents the extended family of all the generations, which will allow us to treat the whole optical system as a black box and represent its interaction with the background medium through its final T-matrix.

In order to calculate the effective T-matrix of the families at the bottom generations of the tree (let's call them $\hat{\tilde{\mathbf{T}}}_{\mathrm{f}}$, with the index f standing for "family") we proceed as follows. First, note that the nodes of the bottom generation of the tree are always of zero genus topologically. Let's assume the index n_{c} taking values from 1 till g_{p} (the topological genus of the parent), which denotes the number of the children of the considered family. This means that applying Eq. (2.213) for the subsystem of each child we get that:

$$\psi_{\mathrm{rad,c},n_{\mathrm{c}}} = \hat{\mathbf{T}}_{n_{\mathrm{c}}} \cdot \psi_{\mathrm{stnd,c},n_{\mathrm{c}}}, \tag{2.214}$$

while applying the same equation for the subsystem of the parent we have:

$$\begin{bmatrix} \psi_{\mathrm{rad,p}} \\ \psi_{\mathrm{stnd,c},1} \\ \vdots \\ \psi_{\mathrm{stnd,c},g_{\mathrm{p}}} \end{bmatrix} = \begin{bmatrix} \hat{\mathbf{T}}_{\mathrm{p},00} & \hat{\mathbf{T}}_{\mathrm{p},01} & \cdots & \hat{\mathbf{T}}_{\mathrm{p},0g_{\mathrm{p}}} \\ \hat{\mathbf{T}}_{\mathrm{p},10} & \hat{\mathbf{T}}_{\mathrm{p},11} & \cdots & \hat{\mathbf{T}}_{\mathrm{p},1g_{\mathrm{p}}} \\ \vdots & \vdots & \ddots & \vdots \\ \hat{\mathbf{T}}_{\mathrm{p},g_{\mathrm{p}}0} & \hat{\mathbf{T}}_{\mathrm{p},g_{\mathrm{p}}1} & \cdots & \hat{\mathbf{T}}_{\mathrm{p},g_{\mathrm{p}}g_{\mathrm{p}}} \end{bmatrix} \cdot \begin{bmatrix} \psi_{\mathrm{stnd,p}} \\ \psi_{\mathrm{rad,c},1} \\ \vdots \\ \psi_{\mathrm{rad,c},g_{\mathrm{p}}} \end{bmatrix}, \tag{2.215}$$

where we use the symbol "p" to refer to the T-matrix of the parent subdomain and,

also, to the parent port of the parent subdomain. Whereas, we use the symbol "c" to refer to the children ports of the parent subdomain. Combining the above two formulas readily gives the following relation for the effective T-matrix of the family (recombined parent+children) system:

$$\psi_{\mathrm{rad,p}} = \hat{\tilde{\mathbf{T}}}_{\mathrm{f}} \cdot \psi_{\mathrm{stnd,p}} \,, \tag{2.216}$$

with:

$$\begin{aligned} \hat{\tilde{\mathbf{T}}}_{\mathrm{f}} = \hat{\mathbf{T}}_{\mathrm{p},00} + \begin{bmatrix} \hat{\mathbf{T}}_{\mathrm{p},01} \\ \hat{\mathbf{T}}_{\mathrm{p},02} \\ \vdots \\ \hat{\mathbf{T}}_{\mathrm{p},0g_{\mathrm{p}}} \end{bmatrix}^{\mathrm{T}} \cdot \begin{bmatrix} \hat{\mathbf{T}}_1 & 0 & \cdots & 0 \\ 0 & \hat{\mathbf{T}}_2 & \cdots & 0 \\ \vdots & \vdots & \ddots & \vdots \\ 0 & 0 & \cdots & \hat{\mathbf{T}}_{g_{\mathrm{p}}} \end{bmatrix} \cdot \\ \begin{bmatrix} \hat{\mathbf{I}} - \hat{\mathbf{T}}_{\mathrm{p},11}\hat{\mathbf{T}}_1 & -\hat{\mathbf{T}}_{\mathrm{p},12}\hat{\mathbf{T}}_2 & \cdots & -\hat{\mathbf{T}}_{\mathrm{p},1g_{\mathrm{p}}}\hat{\mathbf{T}}_{g_{\mathrm{p}}} \\ -\hat{\mathbf{T}}_{\mathrm{p},21}\hat{\mathbf{T}}_1 & \hat{\mathbf{I}} - \hat{\mathbf{T}}_{\mathrm{p},22}\hat{\mathbf{T}}_2 & \cdots & -\hat{\mathbf{T}}_{\mathrm{p},2g_{\mathrm{p}}}\hat{\mathbf{T}}_{g_{\mathrm{p}}} \\ \vdots & \vdots & \ddots & \vdots \\ -\hat{\mathbf{T}}_{\mathrm{p},g_{\mathrm{p}}1}\hat{\mathbf{T}}_1 & -\hat{\mathbf{T}}_{\mathrm{p},g_{\mathrm{p}}2}\hat{\mathbf{T}}_2 & \cdots & \hat{\mathbf{I}} - \hat{\mathbf{T}}_{\mathrm{p},g_{\mathrm{p}}g_{\mathrm{p}}}\hat{\mathbf{T}}_{g_{\mathrm{p}}} \end{bmatrix}^{-1} \cdot \begin{bmatrix} \hat{\mathbf{T}}_{\mathrm{p},10} \\ \hat{\mathbf{T}}_{\mathrm{p},20} \\ \vdots \\ \hat{\mathbf{T}}_{\mathrm{p},g_{\mathrm{p}}0} \end{bmatrix}, \end{aligned} \tag{2.217}$$

where we have used the symbol "f" to denote the "family" effective T-matrix. The resulting family effective T-matrix borrows the ports of the parent to interact with the outer world and is of zero genus topologically. We can apply the above procedure multiple times and ascend the tree till the oldest generation to eventually get the final T-matrix of the whole system. This will allow us to represent its scattering response inside free space upon an arbitrary excitation.

The multi-scattering T-matrix theory that we developed with our derivation above is quite abstract and general, but it does find practical applications in some simple scattering scenarios. Let us discuss some of the practical aspects in view of Fig. 2.1. There, in the family tree of the optical system, we denote with blue color the subdomains that are not parents, i.e., they are of zero genus topologically. Out of those, the subdomains V_3 and V_{11} are simple spheres embedded in free space. Thus, their corresponding T-matrices can be computed analytically with simple Mie theory. From a computational perspective this is, of course, advantageous. However, the rest of the subdomains, $\mathrm{V}_4, \mathrm{V}_7, \mathrm{V}_8$, and V_{10}, need to have their T-matrices calculated numerically, which could be computationally expensive. Moreover, we can observe that the parent domains $\mathrm{V}_2, \mathrm{V}_6, \mathrm{V}_9$, denoted with green color in the tree, host practically homogeneous space. Therefore, their T-matrices can be calculated analytically, since their elements simply correspond to propagation of waves in homogeneous space. That is actually the major advantage of conventional T-matrix methods applied to multi-scattering processes: the propagation of waves between different sites is simply performed there analytically by making use of the translation addition theorem for VSHs, for example. In that case, such translation matrices are represented by the non-diagonal elements of the T-matrix of the parent subdomain in Eq. (2.215). Note, also, that Eq. (75) in Ref. [235] is just a particular representation of our Eqs. (2.214,2.215) above. Moreover, developed theories dealing with stratified, multilayer spherical scatterers or with spherical inclusions constitute also a particular manifestation of our equations above [241–243].

On the other hand, note that the parent domains $\mathrm{V}_1, \mathrm{V}_5$, denoted with red color in the figure, do not host a homogeneous medium, and, therefore, their T-matrix needs to be calculated numerically by assuming a homogeneous space continuation inside the domain of the children ports and outside the domain of the parent port. However, depending on the optical size of the system, this can be unnecessarily computationally expensive,

unless some proper boundary conditions are enforced over the children ports, so that large chunks of space, where simple propagation inside homogeneous media takes place, does not get included inside the simulation domain. In a scattering wave formalism, a special boundary condition enforcing the field over the children ports to be a superposition of the standing wave type of modes of the port would be rather beneficial in terms of reducing the computational costs.

Let us note that such a process of retrieving the T-matrix of a large and complex system in a hierarchical way, may be instrumental in attaining its response without requiring rather demanding computational resources. Simulating a smaller subdomain of the big system should only require a fraction of the computational resources needed to simulate the whole system fully numerically. We require, though, to simulate the response of subsystems upon multiple excitations, but this is also efficiently done, for example with the FEM method in frequency domain, or with the Boundary Element Method (BEM). Once we invert the numerical matrix of the system; then, getting the response of the system upon different excitations is simply a fast matrix-vector multiplication. Arguably, such a modular T-matrix-based analysis of complex optical systems, is, also, especially beneficial in cases that we have large systems composed by a small number of modules that are repeated in space, and whose T-matrix, therefore, only needs to be calculated once.

To sum up, we have deployed a generalized T-matrix method to analyze complex optical systems as hierarchical optical networks where multi-scattering processes take place between the nodes of the network and through the scattering ports that connect them. Note that, such a "black box" type of T-matrix operator is closely related with the scattering matrix (S-matrix, $\hat{\mathbf{S}}(\boldsymbol{\chi})$) of the system. The important difference is that, while the T-matrix relates the scattered fields with the incident fields (standing waves), the S-matrix relates outgoing waves with incoming waves over the ports of the system. The two matrices are related with the following equation: $\hat{\mathbf{S}}(\boldsymbol{\chi}) = \hat{\mathbf{I}} + 2\hat{\mathbf{T}}(\boldsymbol{\chi})$ [233]. The S-matrix methods celebrate this year an anniversary of two hundred years. Arguably, we can trace its origins back to the Fresnel equations describing reflection and transmission of light through a planar interface [244]. Specifically, Fresnel's coefficients practically constitute the elements of a reduced representation of the S-matrix operator describing the simplest electromagnetic scattering system: that of a single planar interface. In the realm of geometrical optics, the simple ray transfer matrix (ABCD matrix) of an optical element such as a lens, does also actually constitute a ray optics representation of the S-matrix operator of such an electromagnetic system [245]. The S-matrix has been extensively used to model stacked planar layers of homogeneous and bi-anisotropic media [246]. Moreover, it has been, accompanying the Fourier Modal Method (FMM) -or else Rigorous Coupled Wave Analysis (RCWA)- to include also bi-anisotropic layers in the stack with homogeneity along the stacking axis but with structural periodicity laterally [247]. Furthermore, it has been used as a module to complement FEM methods in frequency domain, where it was used as a semi-analytical module facilitating the rather efficient incorporation of a multilayer stack inside the simulation domain [248]. Importantly, the S-matrix method is widely used in photonic integrated circuits (PICs), where it facilitates the modular design of the circuit, with each element being typically connected with the rest of the system through waveguide ports. There, a basis set of incoming and outgoing waves of bounded modes is neatly defined, once we disregard any radiative coupling among the modules of the system [249, 250].

Note that, in layered systems, the coupling between the layers through the interface ports is naturally performed in terms of incoming and outgoing waves instead of incident and scattered waves, since incident waves would require the simultaneous excitation of both sides of the layer (which would correspond to an incident standing wave), but this

is not a very convenient approach. Similarly, it is only natural to perform the coupling between subdomains in a multiport system in terms of incoming and outgoing waves, instead of incident and scattered waves. Those two are some exemplary cases where the S-matrix analysis of the system is preferential. The rest of the analysis that we previously performed for the T-matrix approach remains largely the same. Here, we will only spot the key differences between the T-matrix and S-matrix analysis of complex optical systems recasted into hierarchical optical networks. As we discussed already, the most important difference is that we need to employ a different basis set to expand the fields at the vicinity of the ports, that is in terms of incoming and outgoing waves. Specifically, Eq. (2.212) would need to take the following form instead:

$$\psi_{\text{out},i} \quad = \quad \hat{\mathbf{S}}_i \cdot \psi_{\text{in},i}, \tag{2.218}$$

Note that the incoming fields through a port inside a subdomain are equal to the outgoing (from the same port) fields from a neighboring subdomain, and, also, the opposite. Let us, also, mention another practical difference between the two matrix methods. The numerical calculation with full-wave simulations of the S-matrix of a subdomain of non-zero genus topologically, requires setting up proper absorbers at the boundaries of the simulation domain. For example, one would need to place perfectly matched layers (PMLs) in curvilinear coordinates that absorb outgoing waves at the parent port, but, on the other hand, absorb *incoming* waves at the children ports.

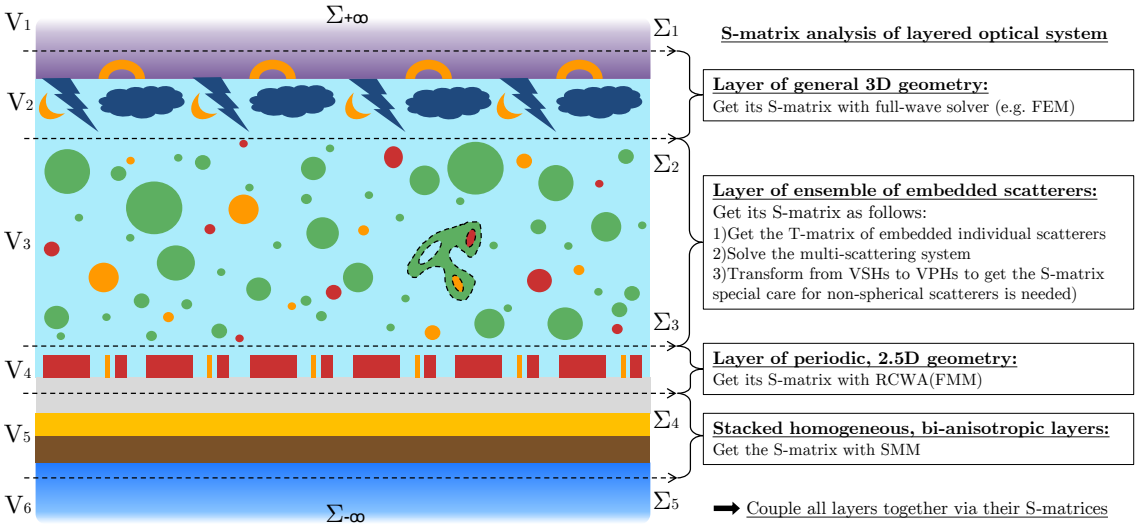

Figure 2.2: Sketch of the S-matrix analysis of a layered optical system. Each subsystem is represented by its own S-matrix, which is optimally retrieved by employing an appropriate method. The coupling between the layers is performed on a plane-wave basis whereas the coupling between the scatterers in the middle layer is typically performed on a spherical-wave basis.

In Fig. 2.2 we sketch a potential application of the S-matrix method that treats the coupling between the layers of a stratified optical system. Equation (25) of Ref. [246], which constitutes the cornerstone of such S-matrix method (SMM), can be used to stack layers whose incoming and outgoing waves are represented in the VPHs basis with the S-matrix method. Using the T-matrix method to solve for multi-scattering processes taking place among an ensemble of scatterers embedded inside an homogeneous space, we are able to retrieve the S-matrix of such a layer in the middle of the stack, which can be used

for the modeling of the coupling with the rest of the layers. Different techniques can be employed to efficiently calculate the S-matrices of the different layers.

Before closing this section, we would like to highlight that we intentionally left our theoretical analysis of the T-matrix methods rather abstract. A key ingredient for the practical implementation of those T-matrix methods is actually the adoption of particular, and not abstract, basis sets to appropriately expand the input and output fields of the matrix representations of the systems. It's only then that the matrices that we have been using for the analysis get materialized and become disposable for practical use. Apart from special cases, the preparation of appropriate basis sets to expand the electromagnetic inputs and outputs of an optical system interacting with its environment, is far from trivial. Very practical issues such as the completeness and the domain of validity of the adopted representations, or the minimization of the dimensionality of the representations for efficient numerical calculations, need to be taken into account. Note that typically, the T-matrix methods involve solving dense linear systems of equations, whereas other numerical full-wave methods (like the FEM method) are characterized by sparse matrix representations. However, what makes the T-matrix methods in many cases preferential is typically their significantly lower dimensionality of the problem.

In a next chapter, we will present a novel representation of radiating fields from scatterers of arbitrary geometry that can be used to tackle the famous problem of the Rayleigh Hypothesis, that is related with the problematic representation of the scattered fields in the near-field region of non-spherical scatterers when we use a simple series of radiating spherical waves for the representation of the output of the T-matrices.

3 — EM scattering from spherical scatterers made of time-varying materials: a T-matrix-based analysis

3.1 Introduction

In this chapter, we will discuss time-varying scattering systems under the prism of the T-matrix formalism. First of all, in the second section, we discuss electromagnetism in bulk time-varying media. We derive the generalized dispersion relation of such media, and we study the band structure of periodically modulated media leading to photonic time crystals. Finally, we construct the spatiospectral eigenmodes of such bulk media, and we study an exemplary case of employing such a modal analysis to homogenize them. Next, in the third section, we develop a Floquet-Mie theory that provides the T-matrix of time-varying spherical scatterers (also multilayered ones), and we discuss its structure based on an exemplary case. In the fourth section, we provide several numerical comparisons between results obtained with our Floquet-Mie theory and results from a full-wave, time-domain solver, showing an excellent agreement between the two. In what follows, in the fifth section, we discuss the breaking of energy conservation in time-varying scatterers, and we demonstrate that their T-matrices possess singular modes characterized by negative absorption, i.e., indicating generation of energy. We, also, present results of driving a time-varying sphere into a lasing state by parametric Mie resonances. We show that the latter additionally allow for the engineering of the radiation pattern of the amplified emissions. Finally, in the last section, we discuss generalized reciprocity in time-varying scatterers, and we derive the symmetries that it entails with respect to their T-matrices.

3.2 Electromagnetic waves inside bulk time-varying media

In this section, we will analyze the physics of electromagnetic waves inside bulk time-varying media. Specifically, we will consider the case of linear, homogeneous, isotropic, non-magnetic media, without spatial dispersion. First, we will develop an eigenmode analysis of electromagnetic waves inside such media, we will discuss then the generalized dispersion relation of such media, and, finally, we will present an exemplary case of how such a modal analysis of the media can be used to homogenize them. The numerical calculations in this section have been performed in collaboration with Dr. Grigorii Ptitcyn.

The constitutive relations of such media in frequency domain reads as follows:

$$\begin{bmatrix}\mathbf{P}_{\mathrm{e}}(\mathbf{r},\omega)\\ \mathbf{P}_{\mathrm{m}}(\mathbf{r},\omega)\end{bmatrix} = \int_{-\infty}^{+\infty} \varepsilon_0 \chi_{\mathrm{ee}}(\omega-\omega',\omega') \begin{bmatrix}\mathbf{I} & \mathbf{0}\\ \mathbf{0} & \mathbf{0}\end{bmatrix} \cdot \begin{bmatrix}\mathbf{E}(\mathbf{r},\omega')\\ \mathbf{H}(\mathbf{r},\omega')\end{bmatrix} \mathrm{d}\omega', \tag{3.1}$$

with $\chi_{\mathrm{ee}}(\omega-\omega',\omega')$ being the susceptibility that characterizes the bulk medium. Please note, the first frequency argument is the consequence of the time-variation, whereas the second frequency argument is the ordinary dispersion. It practically relates linearly the

electric polarization density $\mathbf{P}_{\mathrm{e}}(\mathbf{r},\omega)$ induced at frequency ω with a monochromatic electric field $\mathbf{E}(\mathbf{r},\omega')$ of frequency ω' that polarizes the medium (see Section 2.2).

Combining Eqs. (2.8, 2.9) with the aforementioned constitutive relations, gives us the following integro-differential equation that the electric field inside such a bulk medium obeys:

$$\nabla\times\nabla\times\mathbf{E}(\mathbf{r},\omega)=k_0^2(\omega)\left[\mathbf{E}(\mathbf{r},\omega)+\int_{-\infty}^{+\infty}\chi_{\mathrm{ee}}(\omega-\omega',\omega')\mathbf{E}(\mathbf{r},\omega')\mathrm{d}\omega'\right], \tag{3.2}$$

where $k_0(\omega)=\omega\sqrt{\mu_0\varepsilon_0}=\omega/c_0$ is the wavenumber of free space. Note that, for dispersionless media, the susceptibility $\chi_{\mathrm{ee}}(\omega-\omega',\omega')$ becomes invariant with respect to its second argument and the wave equation simplifies [251].

Next, let us calculate the eigensolutions of the above homogeneous integro-differential equation. Importantly, note that its operator is non-diagonal in terms of the frequency ω: the constitutive relations of the time-varying medium introduce coupling among the fields of different frequencies. These eigensolutions will be the fundamental solutions to the source-free Maxwell's equations of such a medium and, therefore, they are of major importance since they can be used as a basis set to expand the fields inside such a medium.

To calculate them, it is instrumental to make use of the method of separation of variables. Specifically, we seek for solutions of the electric field $\mathbf{E}(\mathbf{r},\omega)$ that have the following form:

$$\mathbf{E}(\mathbf{r},\omega) \;=\; \int\mathcal{A}(\kappa)S_\kappa(\omega)\mathbf{F}_\kappa(\mathbf{r})\mathrm{d}\kappa, \tag{3.3}$$

where $\mathcal{A}(\kappa)$ is a complex amplitude that we introduced. Importantly, note that in this Ansatz that we introduced, the dependency of the eigensolutions on the spatial and frequency arguments is separated. Specifically, we introduce the separation constant κ^2, and we obtain the following set of coupled (through the separation constant) equations for the spatial and vectorial part of the eigensolutions, $\mathbf{F}_\kappa(\mathbf{r})$, and for the spectral and scalar part of the eigensolutions, $S_\kappa(\omega)$:

$$\nabla\times\nabla\times\mathbf{F}_\kappa(\mathbf{r}) \;=\; \kappa^2\mathbf{F}_\kappa(\mathbf{r}), \tag{3.4}$$

$$k_0^2(\omega)\left[S_\kappa(\omega)+\int_{-\infty}^{+\infty}\chi_{\mathrm{ee}}(\omega-\omega',\omega')S_\kappa(\omega')\mathrm{d}\omega'\right] \;=\; \kappa^2S_\kappa(\omega). \tag{3.5}$$

Note that, both of the above equations constitute themselves eigenvalue type of equations with κ^2 being their common eigenvalue. $\mathbf{F}_\kappa(\mathbf{r})$ is the corresponding eigensolution of the differential operator of the first equation and $S_\kappa(\omega)$ is the corresponding eigensolution of the integral operator of the second equation.

We can straightforwardly recognize that the first equation for the spatial and vectorial profile of the eigensolution, $\mathbf{F}_\kappa(\mathbf{r})$, is an ordinary monochromatic electromagnetic wave equation with wavenumber κ. We have explored in detail the eigensolutions of this differential equation in section 2.6. Equation (3.4) shares the same eigensolutions with Eq. (2.122) and we refer the reader to section 2.6 for a detailed discussion of those. We remind that we have identified three types of eigensolutions for the electromagnetic wave equation: the planar waves (VPHs), the cylindrical waves (VCHs), and the spherical waves

(VSHs). For example, VPHs can be used to expand the fields inside a homogeneous half space (or planar slab), while VCHs can be used to expand the fields inside a homogeneous infinite cylinder (or cylindrical shell), and VSHs can be used to expand the fields inside a homogeneous sphere (or spherical shell). In a next section of this chapter, we will focus on the case of electromagnetic scattering by time-varying spherical scatterers, and, therefore, we will employ the VSHs as a basis set to expand the fields inside the scatterers.

From Eqs. (2.10, 3.3 and 3.5) we get that the spatial eigenfunctions $\mathbf{F}_\kappa(\mathbf{r})$ in source-free space are solenoidal for $\kappa \neq 0$, i.e., $\nabla \cdot \mathbf{F}_\kappa(\mathbf{r}) = 0$ for $\kappa \neq 0$. On the other hand, when $\kappa = 0$, it is straightforward to show from Eqs. (2.9, 3.3 and 3.4) that the magnetic field becomes irrotational, i.e., $\nabla \times \mathbf{H}(\mathbf{r}, \omega) \propto S_\kappa(\omega) \nabla \times \nabla \times \mathbf{F}_\kappa(\mathbf{r}) = 0$, for $\kappa = 0$. For vanishing wavenumbers κ, we have a non-zero induced electric charge density distribution since the divergence of $\mathbf{F}_0(\mathbf{r})$ does not have to be zero in that case. Such implications that arise for $\kappa = 0$, where the electric field ceases to be solenoidal, will be disregarded in what follows. In a next section of this chapter, this will allow us to expand the fields inside the source-free time-varying scatterer using only the solenoidal (TE and TM) spherical waves while avoiding the third multipolar family of longitudinal spherical waves [204].

Let us now discuss the second equation (Eq. (3.5)) that we got by applying the method of separation of variables to the electromagnetic wave equation. This equation is obeyed by the spectral part of the eigensolutions, $S_\kappa(\omega)$. It constitutes the generalization of the dispersion relation of homogeneous, local, and isotropic, time-varying media. This becomes obvious once we take its stationary limit, which reads as follows:

$$\left\{\kappa^2 - k_0^2(\omega)[1 + \chi_{\text{ee,stationary}}(\omega)]\right\} S_\kappa(\omega) \quad = \quad 0, \tag{3.6}$$

which implies that we have a wavenumber $\kappa(\omega) = k_0(\omega)\sqrt{1 + \chi_{\text{ee,stationary}}(\omega)}$ for each frequency ω. For non-stationary media, the situation though becomes more complicated. The important thing to notice here is that, due to the time-variance of the medium, the symmetry of invariance of the system under continuous temporal translations is broken, and, therefore, a coupling among different frequency components arises. In fact, once we assume that the integral operator on the left-hand side of Eq. (3.5) is compact, then by virtue of the spectral theorem of compact operators we can deduce that the equation has a countable number of eigensolutions -the spectral eigenfunctions $S_\kappa(\omega)$-, each with its corresponding eigenvalue κ^2, i.e., its corresponding wavenumber. That is to say that now we have waves-eigenmodes of particular spectral composition (which is implied by the eigenfunctions $S_\kappa(\omega)$) that propagate inside the time-varying medium with different wavenumbers κ (which are the corresponding eigenvalues to the eigenfunctions $S_\kappa(\omega)$). This is a major difference between eigenwaves inside stationary and time-varying media.

To solve Eq. (3.5), it is instrumental to consider a periodicity in the temporal variation of the non-stationary medium. Note that non-periodic time-varying media can be practically treated also as artificially periodic with a period that is large enough to allow for the relaxation of the system within a period. Media that periodically vary in time have been attracting recently considerable attention from the scientific community and they are known as photonic time crystals (PTCs) [252, 253]. They are characterized by a discrete translation symmetry in time: $\tilde{\chi}_{\text{ee}}(t, t-\tau) = \tilde{\chi}_{\text{ee}}(t + jT_{\text{m}}, t-\tau)$, with T_{m} being the modulation period and $j \in \mathbb{Z}$. Consequently, the Fourier transform of the electric susceptibility becomes discrete: $\chi_{\text{ee}}(\omega - \omega', \omega') = \sum_j \delta(\omega - \omega' - j\omega_{\text{m}})\chi'_{\text{ee},j}(\omega)$, with $\omega_{\text{m}} = 2\pi/T_{\text{m}}$ being the modulation frequency of the periodically time-varying medium. Hence, for such a system with discrete translational symmetry in time, it is instructive to introduce a new eigenvalue, the Floquet frequency Ω, which we can consider to take values within the frequency range $(0, \omega_{\text{m}})$. Electromagnetic fields with well-defined Floquet frequency Ω possess the following discrete translation symmetry in time:

$$\hat{\mathbf{T}}_{\mathrm{t}}(t_0)\ |\tilde{\mathbf{EM}}(\mathbf{r},t;\Omega)\rangle \equiv |\tilde{\mathbf{EM}}(\mathbf{r},t+t_0;\Omega)\rangle = e^{-\mathrm{i}\Omega t_0}\,|\tilde{\mathbf{EM}}(\mathbf{r},t;\Omega)\rangle\,, \quad \text{for} \quad t_0 = jT_{\mathrm{m}}, \quad j\in\mathbb{Z} \tag{3.7}$$

where with $\hat{\mathbf{T}}_{\mathrm{t}}(t_0)$ we denote the temporal translation operator with translation t_0, and with the abstract notation $|\tilde{\mathbf{EM}}(\mathbf{r},t;\Omega)\rangle$ we denote such a (complex-valued) electromagnetic field.

After we introduced periodicity in the time-variance of the medium, i.e., after we restricted our analysis to PTCs, Eq. (3.5) takes the following discretized form:

$$k_0^2(\Omega_j)\left[S_\kappa(\Omega_j)+\sum_{l=1}^{N_\Omega}\chi_{\mathrm{ee}}(\Omega_j-\Omega_l,\Omega_l)S_\kappa(\Omega_l)\right]=\kappa^2(\Omega)S_\kappa(\Omega_j), \tag{3.8}$$

where

$$\Omega_j=\Omega+(j+j_0-1)\,\omega_{\mathrm{m}} \tag{3.9}$$

with $j=1,2,\ldots,N_\Omega$ and j_0 being an integer that we chose appropriately for the truncated spectral window of interest. N_Ω is the total number of frequencies of the discretized and truncated spectrum. Note that, for practical purposes, we also introduced a truncation of the infinite spectrum. By letting $j_0\to-\infty$ and $N_\Omega\to+\infty$ we can lighten the spurious effects of spectral truncation. In general, N_Ω needs to be chosen large enough, and j_0 needs to be chosen such that significant numerical leakage of the spurious truncation errors inside our spectral region of interest is avoided.

We see that the Floquet frequency Ω constitutes an appropriate eigenvalue to characterize PTCs. It characterizes an infinite periodic comb of frequencies (with period ω_{m}) passing through the frequency Ω. Equation (3.9) gives the frequencies of such a spectral comb within an arbitrarily truncated spectral window. Importantly, because of the medium's periodic time modulation, only the frequencies contained in each such spectral comb are coupled to each other. There is no coupling among frequencies belonging to spectral combs of different Floquet frequencies Ω. Therefore, for each Floquet frequency Ω, Eq. (3.8), repeated for all values of the index j, forms a linear system of equations that can be written in matrix form as follows:

$$\hat{\mathbf{K}}(\Omega)\cdot\vec{S}_\kappa(\Omega) \;=\; \kappa^2(\Omega)\;\vec{S}_\kappa(\Omega), \tag{3.10}$$

where we have defined the vector:

$$\vec{S}_\kappa(\Omega) \;=\; \left[S_\kappa(\Omega_1)\;\cdots\;S_\kappa(\Omega_{N_\Omega})\right]^{\mathrm{T}}, \tag{3.11}$$

and the matrices:

$$\hat{\mathbf{K}}(\Omega) \;=\; \hat{\mathbf{k}}_0^2(\Omega)\cdot\left[\hat{\mathbf{I}}+\hat{\boldsymbol{\chi}}_{\mathrm{ee}}(\Omega)\right], \tag{3.12}$$

$$\hat{\mathbf{k}}_0(\Omega) \;=\; \mathrm{diag}\left[k_0(\Omega_1)\;\cdots\;k_0(\Omega_{N_\Omega})\right], \tag{3.13}$$

with the j-th-row-, l-th-column-element of the matrix $\hat{\boldsymbol{\chi}}_{\mathrm{ee}}(\Omega)$ being equal to $\chi_{\mathrm{ee}}(\Omega_j-\Omega_l,\Omega_l)$.

As a result, in the eigenvalue type of equation (3.10), we end up with a matrix $\hat{\mathbf{K}}(\Omega)$ of finite dimensions $N_\Omega\times N_\Omega$, whose N_Ω eigenvalues $\kappa_i^2(\Omega)$ and corresponding eigenvectors $\vec{S}_{\kappa_i}(\Omega)$ can be calculated numerically for each Floquet frequency Ω. Note that we use the

index $i = 1, \ldots, N_\Omega$ to enumerate the eigenvalues and their corresponding eigenvectors. Note, also, that in the limit of $T_\mathrm{m} \to \infty$, $j_0 \to -\infty$, $N_\Omega \to \infty$, we get the general case of non-periodically modulated time-varying media. In this case, the discrete set of eigenvalues $\kappa_i^2(\Omega)$ becomes a continuum of eigenvalues κ in the complex plane, and the corresponding eigenvectors $\vec{S}_{(\kappa_i)}(\Omega)$ become the original spectral eigenfunctions $S_\kappa(\omega)$.

As discussed before, the matrix $\hat{\boldsymbol{\chi}}_{\mathrm{ee}}(\Omega)$ is diagonal for a stationary medium, and, therefore, so is $\hat{\mathbf{K}}(\Omega)$. As a result, we get a direct relation between the eigenvalues $\kappa_i(\Omega)$ and the frequency dependent wavenumbers inside the medium, contained on the main diagonal of the matrix $\hat{\mathbf{K}}(\Omega)$ for the different frequencies of the considered truncated spectral comb. The eigenvectors $\vec{S}_{(\kappa_i)}(\Omega)$ are then monochromatic, and there is no coupling among frequencies. However, upon temporal modulation, the matrix $\hat{\mathbf{K}}(\Omega)$ is not diagonal and to each eigen-wavenumber $\kappa_i(\Omega)$ corresponds an eigenvector $\vec{S}_{\kappa_i}(\Omega)$ whose elements characterize the spectral content of the mode distributed among each of the N_Ω frequencies of the considered truncated spectral comb.

Finally, for a truncated frequency spectrum, the expansion of the fields in Eq. (3.3) inside a PTC can now take the following form within the Hilbert space $\mathscr{H}$ of finite dimensions constructed for a periodically modulated, time-varying medium:

$$\mathbf{E}(\mathbf{r},\omega) \;=\; \int_{0^+}^{\omega_\mathrm{m}^-} \sum_{i,j=1}^{N_\Omega} \mathcal{A}_i(\Omega)\delta(\omega-\Omega_j)S_{\kappa_i}(\Omega_j)\mathbf{F}_{\kappa_i}(\mathbf{r})\mathrm{d}\Omega, \tag{3.14}$$

with $\mathcal{A}_i(\Omega)$ being complex amplitudes. The above equation constitutes our general Ansatz to expand fields inside PTCs. We can rewrite it in abstract Dirac notation in the following way:

$$|\mathbf{EM}\rangle \;=\; \int_{0^+}^{\omega_\mathrm{m}^-} \sum_{i=1}^{N_\Omega} \mathcal{A}_i(\Omega)\,|\kappa_i(\Omega)\;\;\Omega\rangle\,\mathrm{d}\Omega, \qquad \text{with :} \tag{3.15}$$

$$|\kappa_i(\Omega)\;\;\Omega\rangle \;\equiv\; \sum_{j=1}^{N_\Omega} \delta(\omega-\Omega_j)S_{\kappa_i}(\Omega_j)\mathbf{F}_{\kappa_i}(\mathbf{r}). \tag{3.16}$$

In Fig. 3.1 we present an exemplary case where we study the temporal dispersion of electromagnetic waves inside bulk PTCs. To start with, we consider the simple case of a stationary dispersive medium described by a single Lorentz-type oscillator with natural resonance frequency $\omega_{0,n}$, damping coefficient $\gamma_n = \omega_{0,n}/8$ and bulk electron density $N_0 = 11\omega_{0,n}^2 m_\mathrm{e}\varepsilon_0/q_\mathrm{e}^2$ (see Eq. (2.44) and the analysis of phenomenological models of electromagnetic media included in that section). The medium's electric susceptibility $\chi_0(\omega) = \frac{q_\mathrm{e}^2 N_0}{m_\mathrm{e}\varepsilon_0}\frac{1}{\omega_{0,n}^2-\omega^2-\mathrm{i}\gamma_n\omega}$ is plotted in Figure 3.1(a).

Then, we study the effect of a time-variation in such a dispersive medium by assuming that the bulk electron density of the Lorentz oscillator varies time-harmonically according to $\tilde{N}_{\mathrm{e},n}(t) = N_0\,[1 + M\cos(\omega_\mathrm{m} t)]$, with M being a modulation amplitude. According to Eq. (2.44), the susceptibility of such a medium is given by:

$$\chi_{\mathrm{ee}}(\omega-\omega',\omega') \;=\; \frac{\chi_0(\omega)}{\sqrt{2\pi}N_0}N_{\mathrm{e},n}(\omega-\omega'), \tag{3.17}$$

with

$$N_{\mathrm{e},n}(\omega-\omega') \;=\; \sqrt{2\pi}N_0\left[\delta(\omega-\omega') + M\frac{\delta(\omega-\omega'+\omega_\mathrm{m})+\delta(\omega-\omega'-\omega_\mathrm{m})}{2}\right]. \tag{3.18}$$

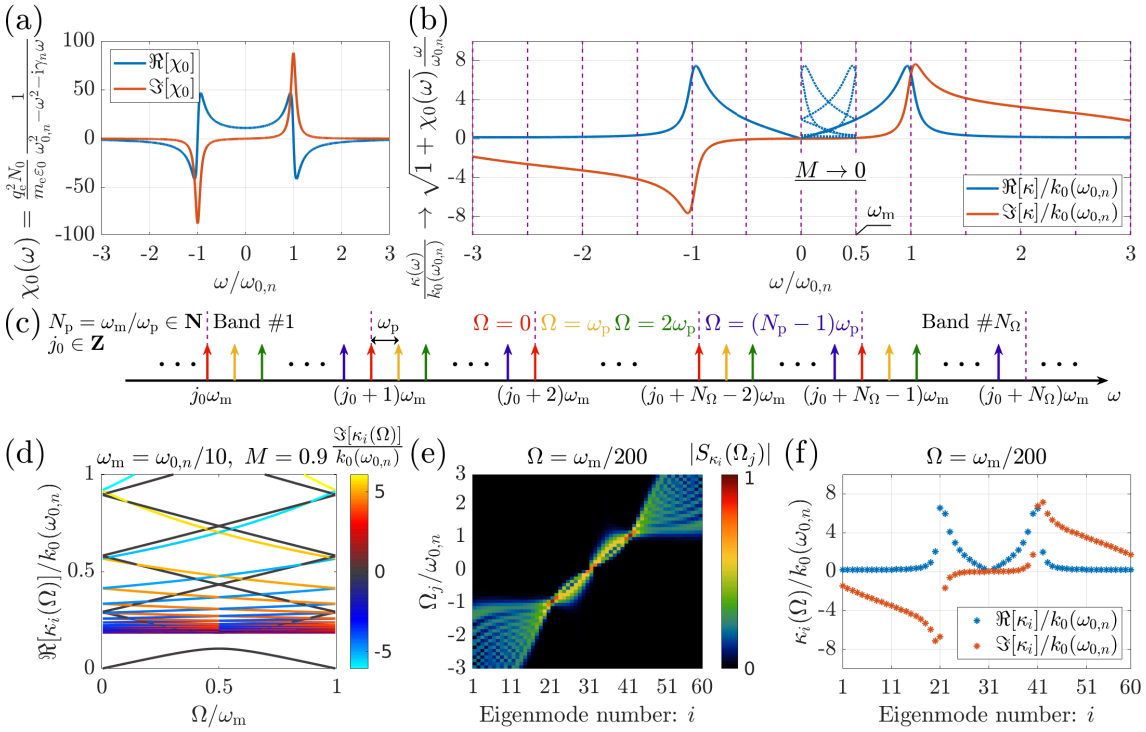

Figure 3.1: Temporal dispersion of electromagnetic waves inside bulk PTCs: (a) The electric susceptibility of an unmodulated medium with Lorentzian dispersion. (b) The folding of the band structure the weak modulation strength limit. (c) Spectral combs of the PTC characterized by a Floquet frequency Ω, among which there exists spectral coupling due to the periodic temporal modulation of the medium. (d) The band structure diagram for the case of large modulation strength, where a band gap appears. (e) Plot of the spectral content of the eigenmodes $|S_{\kappa_i}(\Omega_j)|$, highlighting the introduced spectral coupling. (f) Plot of the eigenvalues, i.e., the wavenumbers κ_i, that correspond to the eigenmodes presented in (e). Adapted with permission from Ref. [A1] © John Wiley and Sons.

First, it is instructive to study the limiting case of very small modulation strengths $M \to 0$. In analogy to periodically spatially modulated materials, this case would correspond to an empty-lattice approximation. That is to say that we still introduce the periodicity even though there is practically no modulation. In this case, the integral operator in Eq. (3.5) remains predominantly diagonal, with very small off-diagonal terms proportional to the modulation strength M (see Eq. (3.18)). This property indicates a weak spectral coupling among frequencies, which implies that the spectral eigenfunctions $S_\kappa(\omega)$ tend to delta distributions, i.e., they tend to associate a unique wavenumber κ to each frequency ω, as is the case for the usual dispersion relation of stationary media. Therefore, we get that $\kappa(\omega) \to \sqrt{[1+\chi_0(\omega)]\,\omega^2/c_0^2}$, as $M \to 0$. In Fig. 3.1(b), we demonstrate how the band structure of such a system is formed by folding the wavenumbers $\kappa(\omega)$ into the fundamental spectral band. We consider that this spectral band encompasses all the Floquet frequencies Ω from 0 to ω_m. The blue dashed lines show the band structure formed by folding the solid blue line within the fundamental spectral band for the case where $\omega_m = \omega_{0,n}/2$. The folding takes place periodically, and we denote the folding frequencies by the dashed purple lines.

Next, in Fig. 3.1(c), we illustrate the truncated discrete spectral response of a system periodically modulated at a frequency ω_m and excited by a periodic excitation. The

superperiod of the combined periodicities of the modulation and excitation is denoted with $T_\mathrm{p} = 2\pi/\omega_\mathrm{p}$, with $\omega_\mathrm{p} = \omega_\mathrm{m}/N_\mathrm{p}$, and with $N_\mathrm{p} \in \mathbb{N}$. Note that the spectrum can be separated into a set of N_p finite combs of frequencies with a periodicity of ω_m. We highlight each such comb of frequencies corresponding to a different Floquet frequency Ω with a different color. As we discussed before, inside such a PTC coupling occurs only among the frequencies of each such spectral comb. Here, a truncated spectral window of N_Ω bands is illustrated, which corresponds, also, to the number of frequencies of each such truncated spectral comb.

As a next step, we study the dispersion relation of the PTC for the case of a strong modulation $M = 0.9$. For our exemplary case, we consider a modulation frequency $\omega_\mathrm{m} = \omega_{0,n}/10$. Specifically, we solve Eq. (3.10) numerically and calculate the eigenvalues and eigenvectors that correspond to each Floquet frequency Ω, i.e., to each spectral comb. In Fig. 3.1(d), we plot the band structure of the PTC, i.e., the set of eigenvalues/wavenumbers that correspond to each Floquet frequency Ω. Note that the color of the line in this figure encodes the imaginary part of the eigenvalues/wavenumbers. Generally, positive and negative imaginary values should be expected to correspond to spectral eigenmodes with predominant spectral content over positive and negative frequencies, respectively.

In Fig. 3.1(d), we focus on the region of eigenvalues with a small real part, i.e., on the first bands of the band structure. There, we can observe that a band gap in the lower band is introduced by the strong temporal modulation of the medium [101, 254, 255]. Opening a band gap is indicative of strong first order spectral coupling between the almost symmetric positive and negative frequencies of the spectral comb. That symmetry is perfect at the center of the band structure where $\Omega = \omega_\mathrm{m}/2$ and this is where the band gap actually opens. Note that in our exemplary case, we only open the band gap between the first two bands, because our periodic modulation consists of a single harmonic modulation of frequency ω_m, introducing a first order coupling between frequencies of opposite sign that solely reside in the first two bands. Introducing higher harmonics in the periodic modulation of the medium (i.e., of frequencies $2\omega_\mathrm{m}$, $3\omega_\mathrm{m}$, etc.) would facilitate the opening of band gaps of the higher bands as well. That is because there would be direct coupling between frequencies of opposite sign residing within those bands. Finally, note that inside the momentum band gap there are typically two modes that have purely imaginary eigenfrequencies of opposite sign [255]. The amplifying mode of the two is responsible for parametric amplification effects in time-modulated media. In a next section, we will drive a time-modulated sphere into a lasing state by means of such parametric amplification effects.

In Fig. 3.1(e), we plot the eigenvectors, and in Fig. 3.1(f), we plot the corresponding eigenvalues of the subsystem with Floquet frequency $\Omega = \omega_\mathrm{m}/200$. Note that Fig. 3.1(f) is a cut of the band structure of Fig. 3.1(d) at $\Omega/\omega_\mathrm{m} = 1/200$. The eigenmodes are ordered with respect to ascending eigenmode central frequency. The latter is defined as the following sum: $\sum_j \Omega_j \left|S_{\kappa_i}(\Omega_j)\right|^2$. In view of Fig. 3.1(e), we can observe that each eigenmode has a different spectral content distributed over the frequencies of the spectral comb characterized by the particular Floquet frequency Ω. Note, also, that the spectral support of the eigenmodes becomes wider for those that mainly support high frequencies, whereas for the eigenmodes that mainly support the frequencies $\Omega_j/\omega_{0,n} \approx \pm 1$ the spectral support becomes minimally narrow, since there the resonant material losses of the Lorentz-oscillator prevent further strong spectral coupling. Moreover, note that modes 30 and 31 belong to the two lowest bands of the band structure and they are the ones that form the band gap. They have a spectral content in the lower frequencies of the spectral comb and they can exhibit first order spectral coupling between positive and negative frequencies, which, as we discussed before, is responsible for the opening of the band gap at $\Omega = \omega_\mathrm{m}/2$. On the other hand, modes 1-21 and 42-60, whose eigenvalues have a large imaginary part,

correspond to the points of the blue/red lines in Figure 3.1(d) that are almost parallel to the x-axis and interfere inside the band gap region. Furthermore, as discussed previously, the matrix with the eigenvectors plotted in Figure 3.1(e) shall approach the identity matrix in the limit of vanishing modulation $M \to 0$. Hence, the degree of non-diagonality of the matrix $\hat{\mathbf{S}}(\Omega)$ is indicative of the strength of the spectral coupling that gets introduced by the temporal modulation of the medium.

In Fig. 3.1(f), we plot the eigenvalues/wavenumbers associated with the corresponding eigenvectors of Fig. 3.1(e). They are also sorted in a similar way. Let us note the resemblance of Fig. 3.1(f) with the unmodulated case illustrated in Fig. 3.1(b). The sorted wavenumbers of the strongly-modulated case appear to be quite similar to those of the unmodulated case. However, we can still have quite significant deviations, as it is indicated by the presence of the open band gap in Figure 3.1(d). Those deviations are stronger as the Floquet frequency Ω approaches half of the modulation frequency ω_m.

Before closing this section, and to further appreciate the modal analysis of bulk PTCs that we just presented, let us also discuss a simple method to homogenize such media. Let us focus on the simple case of dispersionless PTCs with instantaneous response where the constitutive relation reads as follows:

$$\tilde{\mathbf{P}}_\mathrm{e}(t) \quad = \quad \varepsilon_0 \tilde{\chi}_\mathrm{ee,instant}(t) \tilde{\mathbf{E}}(t), \tag{3.19}$$

where the susceptibility $\tilde{\chi}_\mathrm{ee,instant}(t)$ varies periodically in time with a period of $T_\mathrm{m} = 2\pi/\omega_\mathrm{m}$.

The homogenization of the PTC consists of finding an effective stationary susceptibility to describe the evolution of the polarization of the medium accurately enough:

$$\mathbf{P}_\mathrm{e}(\omega) \quad = \quad \varepsilon_0 \chi_\mathrm{ee,eff}(\omega) \mathbf{E}(\omega). \tag{3.20}$$

Recently, the homogenization of time-varying media has been attracting lots of attention by the scientific community and, for example, in Ref. [256] it was shown that, employing the transfer matrix method to describe the evolution of waves inside such PTCs, we can get the following theoretical expression for the effective susceptibility of homogenized PTCs (note that it is dispersionless, i.e., it has no frequency dependence):

$$\chi^\mathrm{theo}_\mathrm{ee,eff}(\omega) \quad = \quad \frac{1}{\frac{1}{T_\mathrm{m}} \int_0^{T_\mathrm{m}} \frac{1}{1+\tilde{\chi}_\mathrm{ee,instant}(t)} \mathrm{d}t} - 1. \tag{3.21}$$

Let us now proceed with a numerical analysis of the generalized dispersion relation that characterizes such a PTC, with our final goal being to numerically estimate and verify the theoretical prediction of the effective susceptibility that homogenizes such a medium. For this, we first need to acquire the eigenvalues/wavenumbers $\kappa_i(\Omega)$ and the corresponding eigenvectors $\vec{S}_{\kappa_i}(\Omega)$ with the spectral content of each eigenmode of the PTC. We do this by solving Eq. (3.10). As a next step, we identify modes of the PTC with maximal spectral content ratio at some frequency ω, i.e., we find the index of the mode $i = i'(\omega)$ that maximizes the quantity $|S_{\kappa_i}(\Omega_j = \omega)|^2$, for $i = 1, 2, \ldots . N_\Omega$. The closest that quantity is to one (which is its upper limit), the closest that the i-th eigenmode of the PTC corresponds to a monochromatic mode with frequency ω. Therefore, we can call this metric ($|S_{\kappa_i}(\Omega_j = \omega)|^2$) as the degree of monochromaticity of the i-th eigenmode of

the PTC. It is desirable to maximize the degree of monochromaticity since an effective, homogenized medium possesses continuous translation symmetry in time. Therefore, it is characterized by monochromatic modes since there is no spectral coupling. Once we have identified the presence of such a mode with a close to unity spectral content ratio ($|S_{\kappa_{i'(\omega)}}(\Omega_j = \omega)|^2 \to 1$), which is an indicator for the homogenizability of the medium, we collect its corresponding eigenvalue $\kappa_{i'(\omega)}(\Omega)$, and we estimate numerically the dispersive effective susceptibility of the medium by making use of the following formula:

$$\chi^{\text{num}}_{\text{ee,eff}}(\omega) \quad = \quad \frac{\kappa^2_{i'(\omega)}(\Omega)}{k_0^2(\omega)} - 1. \tag{3.22}$$

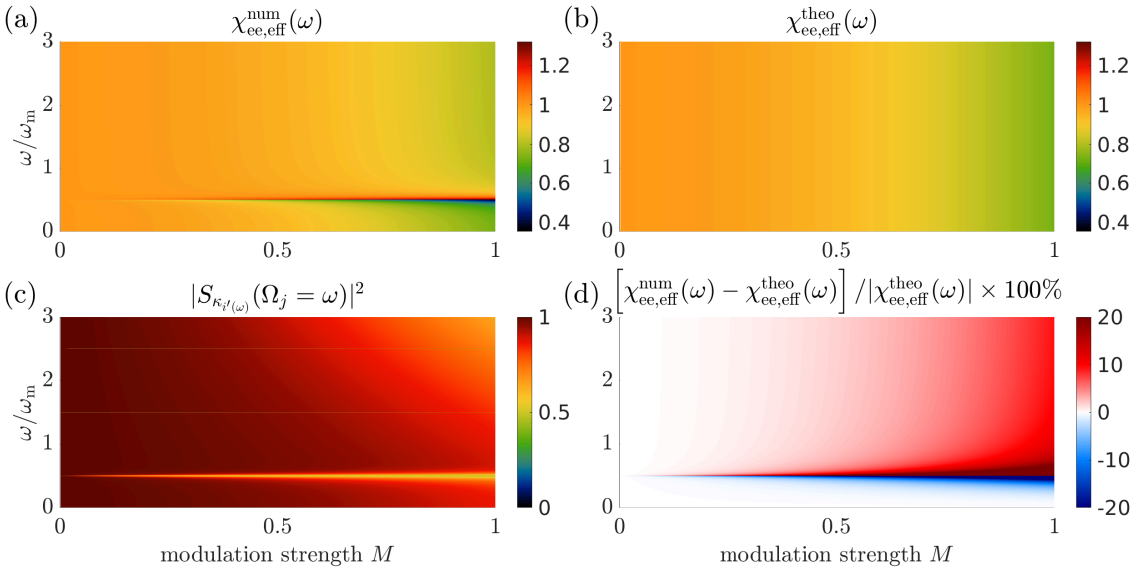

Figure 3.2: Homogenization of PTC with instantaneous response given by the susceptibility $\tilde{\chi}_{\text{ee,instant}}(t) = 1 + M\cos(\omega_{\text{m}}t)$: (a) The numerical estimation of the effective susceptibility. (b) The theoretical estimation of the effective susceptibility. (c) The spectral content ratio, i.e., the degree of monochromaticity of the eigenmode of the PTC. A value close to one corresponds to a quasi-monochromatic eigenmode, which is indicative of the homogenizability of the PTC. (d) Relative difference between the numerically obtained and the theoretical effective susceptibility of the considered PTC.

Let us now consider the exemplary case where $\tilde{\chi}_{\text{ee,instant}}(t) = 1 + M\cos(\omega_{\text{m}}t)$, with M being a modulation strength, and attempt to compare the numerical with the theoretical predictions of the effective susceptibility that homogenizes such a PTC. The susceptibility of such a medium in frequency domain is given by:

$$\chi_{\text{ee,instant}}(\omega - \omega', \omega') \quad = \quad \delta(\omega - \omega') + M\frac{\delta(\omega - \omega' + \omega_{\text{m}}) + \delta(\omega - \omega' - \omega_{\text{m}})}{2}, \tag{3.23}$$

and, as described earlier, can be used to fill elementwise the matrix $\hat{\boldsymbol{\chi}}_{\text{ee}}(\Omega)$ in order to solve Eq. (3.10).

In Fig. 3.2(a) we plot the numerically extracted (by making use of Eq. (3.22)) effective susceptibility of the considered PTC and in Fig. 3.2(b) we plot its theoretically predicted

(from Eq. (3.21)) effective susceptibility. We can generally observe a good agreement between the two. As expected, the effective susceptibility is close to one, i.e., its non-modulated value, for small modulation strengths M. Moreover, for large modulation strengths close to unity the effective susceptibility approaches the value of 0.8, i.e., smaller than its non-modulated value.

A major difference between the numerical and the theoretical effective susceptibility arises around the frequency $\omega = \omega_{\mathrm{m}}/2$. There, we have the regime of the opening of the band gap of the PTC, where there is strong coupling between positive and negative frequencies. As we can see from Fig. 3.2(c), in this regime, we have a low degree of monochromaticity for the eigenmode of the PTC, i.e., it is not a regime where the medium is homogenizable. Note that this predominantly happens only around the frequency $\omega = \omega_{\mathrm{m}}/2$, because our periodic modulation consists of only a single sinusoidal harmonic. As we discussed previously, the introduction of higher harmonics in the periodic modulation can, in a similar way, open the band gap at higher frequencies as well.

Figure 3.2(d) plots the relative difference between the numerical and theoretical predictions. We can see that there is nearly perfect agreement between the two in the large modulation frequency limit of $\omega/\omega_{\mathrm{m}} \to 0$. Moreover, as was to be expected, the homogenizability of the medium depends significantly on the modulation strength, which is responsible for the strength of the spectral couplings that get introduced through the temporal modulation of the medium. For small modulation strengths we generally have quasi-monochromatic modes of high degree of monochromaticity, whereas, as the modulation strength approaches unity, we see that the degree of monochromaticity of the modes deteriorates, which is an indication that the medium cannot be accurately homogenized in that regime.

Note, also, that for $\omega > \omega_{\mathrm{m}}/2$ we generally have a numerical overestimation of the effective permittivity of the medium, whereas for $\omega < \omega_{\mathrm{m}}/2$ we generally have a numerical underestimation of the effective permittivity of the medium. Arguably, attempts to homogenize the medium for $\omega > \omega_{\mathrm{m}}/2$ and large modulation strengths should be treated with extra care. We would like to emphasize that, while in our numerical analysis we focus our attention on specific modes of the PTC that exhibit maximal degree of monochromaticity at the frequency of interest, simultaneously there generally exists a plethora of other modes that the medium supports and can couple with, which can hinder significantly in practice attempts to homogenize the medium.

Finally, let us note that we used a large number of frequencies in the truncated spectral combs ($N_\Omega = 150$) to conduct the modal analysis of the medium and get the numerically predicted values of the effective susceptibilities with high accuracy.

3.3 Floquet-Mie theory: a T-matrix approach to study light scattering by a periodically time-varying spherical scatterer

In this section, we will develop a T-matrix-based Floquet-Mie theory that treats semi-analytically the problem of light scattering from a sphere made of a medium whose electromagnetic properties vary periodically in time. We will also treat the more general problem of a multilayer spherical scatterer consisting of a core and multiple shells, and we will provide numerical results discussing the structure of an exemplary case of such a T-matrix. The numerical simulations in this section have been performed in collaboration with Dr. Grigorii Ptitcyn.

In Fig. 3.3 we plot an illustration of the considered scattering system that we will analyze via the T-matrix method in this section. We consider that the electric susceptibility

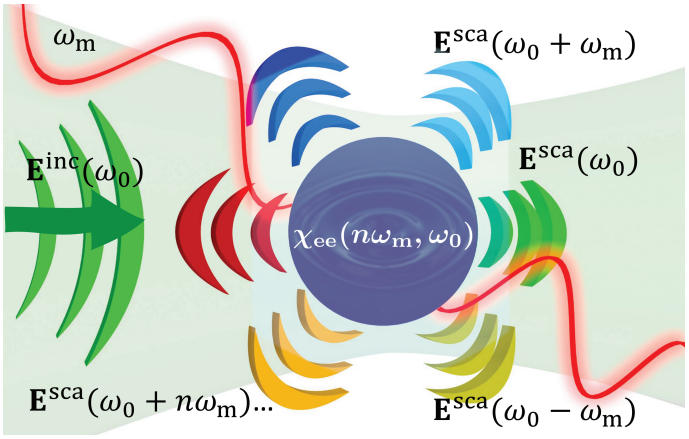

Figure 3.3: Illustration of light scattering by a sphere whose material properties are externally modulated with a frequency of ω_m. In an inelastic scattering process, a monochromatic excitation of such a scatterer at frequency ω_0, gives a polychromatic scattering response at the spectral diffraction orders. The illustration was drawn by Dr. Grigorii Ptitcyn and adapted by Maria Labrianidou. Adapted with permission from Ref. [A1] © John Wiley and Sons.

of the spherical scatterer of radius R is externally modulated with some frequency ω_m, and we proceed with the analysis of how light interacts with such a scattering system. The electromagnetic properties of the bulk medium that comprises the considered spherical scatterer have been studied in depth in the previous section. For simplicity, we will consider that the spherical scatterer is embedded inside free space, but an extension of our upcoming analysis to the general case of an isotropic and homogeneous embedding medium is rather straightforward.

Our Floquet-Mie theory mainly stands on top of two pillars. The first pillar is the analytical representation of the incident ($\mathbf{E}^{inc}$), scattered ($\mathbf{E}^{sca}$) fields outside the scatterer, and of the induced field inside the scatterer ($\mathbf{E}^{ind}$) by employing an appropriate basis set of spherical waves. The second pillar is the enforcement of the interface conditions for the continuity of the tangential components of the fields across the surface of the scatterer.

We begin by expanding the incident field in the following series of regular VSHs [257]:

$$\mathbf{E}^{inc}(\mathbf{r},\omega) = \sum_{\nu\mu_z,\alpha} \mathcal{A}^{inc}_{\alpha,\mu_z\nu}(\omega)\mathbf{F}^{(1)}_{\alpha,\mu_z\nu}(\mathbf{r};k_0(\omega)), \tag{3.24}$$

where $k_0(\omega) = \omega/c_0$ is the free-space wavenumber and $\mathcal{A}^{inc}_{\alpha,\mu_z\nu}(\omega)$ are some complex coefficients that are considered to be known. Note that, while the above expansion of the incident field is defined all over space, we will make use of it only at $r > R$.

Accordingly, the scattered field can be expanded in the following series of radiating VSHs [257]:

$$\mathbf{E}^{sca}(\mathbf{r},\omega) = \sum_{\nu\mu_z,\alpha} \mathcal{A}^{sca}_{\alpha,\mu_z\nu}(\omega)\mathbf{F}^{(3)}_{\alpha,\mu_z\nu}(\mathbf{r};k_0(\omega)), \quad \text{for } r > R, \tag{3.25}$$

where $\mathcal{A}^{sca}_{\alpha,\mu_z\nu}(\omega)$ are some unknown complex coefficients to be determined. It is important to note that by defining the wavenumber of free space as $k_0(\omega) = \omega/c_0$, instead of $k_0(\omega) = |\omega|/c_0$, we ensure that we can use the VSHs that involve the spherical Hankel functions of

the 1st kind to refer to outgoing spherical waves also at negative frequencies. Otherwise, for the convention $k_0(\omega) = |\omega|/c_0$, we would need to switch to VSHs that involve the spherical Hankel functions of the 2nd kind in order to have outgoing spherical waves for negative frequencies. Note that the two alternative conventions are equivalent, since the spherical Hankel functions of the 1st and 2nd kind have the symmetry $\mathrm{h}_\nu^{(1)}(-x) = (-1)^\nu \mathrm{h}_\nu^{(2)}(x)$.

Finally, we can use the Ansatz of (3.14) introduced in the previous section to expand fields inside PTCs, and write the following expansion of the field induced inside the sphere in terms of a finite series of regular VSHs:

$$\mathbf{E}^{\mathrm{ind}}(\mathbf{r},\omega) \;=\; \int_{0^+}^{\omega_{\mathrm{m}}^-} \sum_{i,j=1}^{N_\Omega} \sum_{\nu\mu_z,\alpha} \mathcal{A}^{\mathrm{ind}}_{\alpha,\mu_z\nu i}(\Omega)\delta(\omega-\Omega_j) S_{\kappa_i}(\Omega_j) \mathbf{F}^{(1)}_{\alpha,\mu_z\nu}(\mathbf{r};\kappa_i(\Omega))\mathrm{d}\Omega, \qquad \text{for } r<R. \tag{3.26}$$

$\mathcal{A}^{\mathrm{ind}}_{\alpha,\mu_z\nu i}(\Omega)$ are some unknown complex coefficients to be determined. Note that they are not a function of the frequency ω, but rather a function of the Floquet frequency Ω. They, also, depend on the index i that spans all the spectral eigenmodes that belong to Ω. Note, also, that the frequencies Ω_j are functions of the Floquet frequency Ω (see Eq. (3.9)). Moreover, we would like to highlight that the eigenvalues that we calculate numerically by solving Eq. (3.10) are the wavenumbers squared $\kappa_i^2(\Omega)$. However, for the expansion of the fields, we select the principle branch of the square root to get the wavenumbers $\kappa_i(\Omega) = +\sqrt{\kappa_i^2(\Omega)}$. Note that the choice of the branch of the square root here does not really play a role, since for regular VSHs we have the symmetry $\mathbf{F}^{(1)}_{\alpha,\mu_z\nu}(\mathbf{r};-\kappa_i) = (-1)^\nu \mathbf{F}^{(1)}_{\alpha,\mu_z\nu}(\mathbf{r};\kappa_i)$. This relation follows from the respective symmetry of spherical Bessel functions. Therefore, picking the other branch of the square root would simply lead to an equivalent representation.

We would like to emphasize that the dispersion relation of the electromagnetic fields in free space is different than that inside the medium of the sphere, which is a PTC. Therefore, while for the incident and scattered fields we employed an expansion of the fields into a series of spherical waves that respects the dispersion relation of free space, for the induced field inside the spherical scatterer we employed an expansion into a series of spherical waves that respects the dispersion relation of the bulk PTC that the sphere is made of. As we discussed previously, due to the periodic time variance of the medium, it is instructive to introduce as an eigenvalue the Floquet frequency Ω that characterizes spectral combs among which there is spectral coupling. Inside the scatterer, there is no unique wavenumber corresponding to each frequency anymore, and instead, we have a bunch of wavenumbers corresponding to modes of different spectral composition with respect to the frequencies of the spectral combs.

To conclude with the first pillar of our Floquet-Mie theory, note that the respective series expansions of the incident, scattered, and induced magnetic fields can be taken by making use of the Maxwell-Faraday equation (2.9), together with the property of Eq. (2.129).

As a next step, after we introduced finite-dimensional representations of the fields, to solve our electromagnetic scattering problem we need to specify the unknown complex amplitudes $\mathcal{A}^{\mathrm{sca}}_{\alpha,\mu_z\nu}(\omega)$, $\mathcal{A}^{\mathrm{ind}}_{\alpha,\mu_z\nu i}(\Omega)$ given the amplitudes $\mathcal{A}^{\mathrm{inc}}_{\alpha,\mu_z\nu}(\omega)$. This can do this by imposing the following interface conditions on the surface of the sphere:

$$\hat{\mathbf{r}}\times\Big[\mathbf{E}^{\mathrm{ind}}(\mathbf{r},\omega)-\mathbf{E}^{\mathrm{sca}}(\mathbf{r},\omega)-\mathbf{E}^{\mathrm{inc}}(\mathbf{r},\omega)\Big]\Big|_{r=R} \;=\; 0, \tag{3.27}$$

$$\hat{\mathbf{r}}\times\Big[\mathbf{H}^{\mathrm{ind}}(\mathbf{r},\omega)-\mathbf{H}^{\mathrm{sca}}(\mathbf{r},\omega)-\mathbf{H}^{\mathrm{inc}}(\mathbf{r},\omega)\Big]\Big|_{r=R} \;=\; 0. \tag{3.28}$$

Those interface conditions enforce the continuity of the tangential components of the fields across the spherical surface of the scatterer, according to Maxwell's equations. To proceed further, we need to make use of the following orthogonality property of the VSHs: [258]

$$\frac{\oint_{S_R}\left[\hat{\mathbf{r}}\times\mathbf{F}^{(\iota)}_{\alpha,\mu_z\nu}(\mathbf{r};\kappa)\right]\cdot\mathbf{F}^{(\iota')}_{\alpha',-\mu'_z\nu'}(\mathbf{r};\kappa')\,\mathrm{d}s}{(-1)^{\mu_z+\delta_{\alpha\mathrm{N}}}R^2\,z^{(\iota')}_{\alpha',\nu}(\kappa' R)} = \delta_{\alpha'\beta}\delta_{\mu'_z\mu_z}\delta_{\nu'\nu}\;z^{(\iota)}_{\alpha,\nu}(\kappa R), \tag{3.29}$$

where integration is done over the spherical surface S_R of radius R, upon which we need to enforce the above interface conditions. With $z^{(\iota)}_{\alpha,\nu}(x)$ we denote the generalized spherical Bessel functions which we have defined in the sixth section of the previous chapter.

Finally, by substituting Eqs. (3.24-3.26) into Eqs. (3.27, 3.28), and by making use of Eq. (3.29), we readily get the following inhomogeneous system of equations that needs to be solved to calculate the unknown amplitudes:

$$\sum_i \mathcal{A}^{\mathrm{ind}}_{\alpha,\mu_z\nu i}(\Omega)S_{\kappa_i}(\Omega_j)z^{(1)}_{\alpha,\nu}(x_i) = \mathcal{A}^{\mathrm{sca}}_{\alpha,\mu_z\nu}(\Omega_j)z^{(3)}_{\alpha,\nu}(x_j)+\mathcal{A}^{\mathrm{inc}}_{\alpha,\mu_z\nu}(\Omega_j)z^{(1)}_{\alpha,\nu}(x_j), \tag{3.30}$$

$$\sum_i \kappa_i(\Omega)\mathcal{A}^{\mathrm{ind}}_{\alpha,\mu_z\nu i}(\Omega)S_{\kappa_i}(\Omega_j)z^{(1)}_{\beta,\nu}(x_i) = k_0(\Omega_j)\left[\mathcal{A}^{\mathrm{sca}}_{\alpha,\mu_z\nu}(\Omega_j)z^{(3)}_{\beta,\nu}(x_j)+\mathcal{A}^{\mathrm{inc}}_{\alpha,\mu_z\nu}(\Omega_j)z^{(1)}_{\beta,\nu}(x_j)\right], \tag{3.31}$$

where we have defined $x_i=\kappa_i(\Omega)R$ and $x_j=k_0(\Omega_j)R$. Let us note that the last two equations are equivalent to Eqs. (22, 23) of Ref. [114]. Notice that those equations couple the incident and scattered complex amplitudes among the frequencies of each spectral comb characterized by a Floquet frequency Ω.

Next, by introducing the following definitions of column vectors

$$\vec{\mathcal{A}}^{\mathrm{inc}}_{\alpha,\mu_z\nu}(\Omega) = \left[\mathcal{A}^{\mathrm{inc}}_{\alpha,\mu_z\nu}(\Omega_1)\cdots\mathcal{A}^{\mathrm{inc}}_{\alpha,\mu_z\nu}(\Omega_{N_\Omega})\right]^{\mathrm{T}}, \tag{3.32}$$

$$\vec{\mathcal{A}}^{\mathrm{sca}}_{\alpha,\mu_z\nu}(\Omega) = \left[\mathcal{A}^{\mathrm{sca}}_{\alpha,\mu_z\nu}(\Omega_1)\cdots\mathcal{A}^{\mathrm{sca}}_{\alpha,\mu_z\nu}(\Omega_{N_\Omega})\right]^{\mathrm{T}}, \tag{3.33}$$

$$\vec{\mathcal{A}}^{\mathrm{ind}}_{\alpha,\mu_z\nu}(\Omega) = \left[\mathcal{A}^{\mathrm{ind}}_{\alpha,\mu_z\nu 1}(\Omega)\cdots\mathcal{A}^{\mathrm{ind}}_{\alpha,\mu_z\nu N_\Omega}(\Omega)\right]^{\mathrm{T}}, \tag{3.34}$$

and the following $N_\Omega\times N_\Omega$ matrices:

$$\hat{\mathbf{S}}(\Omega) = \left[\vec{S}_{\kappa_1}(\Omega)\cdots\vec{S}_{\kappa_{N_\Omega}}(\Omega)\right], \tag{3.35}$$

$$\hat{\boldsymbol{\kappa}}(\Omega) = \mathrm{diag}[\kappa_1(\Omega)\cdots\kappa_{N_\Omega}(\Omega)], \tag{3.36}$$

$$\hat{\mathbf{Z}}^{(\iota)}_{\alpha,\nu}(\Omega) = \mathrm{diag}\left[z^{(\iota)}_{\alpha,\nu}(\kappa_1(\Omega)R)\cdots z^{(\iota)}_{\alpha,\nu}(\kappa_{N_\Omega}(\Omega)R)\right], \tag{3.37}$$

$$\hat{\tilde{\mathbf{Z}}}^{(\iota)}_{\alpha,\nu}(\Omega) = \mathrm{diag}\left[z^{(\iota)}_{\alpha,\nu}(k_0(\Omega_1)R)\cdots z^{(\iota)}_{\alpha,\nu}(k_0(\Omega_{N_\Omega})R)\right], \tag{3.38}$$

together with the definitions in Eqs. (3.11, 3.13), we can recast the above set of equations in the following matrix form:

$$\begin{bmatrix}\hat{\mathbf{S}}\cdot\hat{\mathbf{Z}}^{(1)}_{\alpha,\nu} & -\hat{\tilde{\mathbf{Z}}}^{(3)}_{\alpha,\nu}\\ \hat{\mathbf{S}}\cdot\hat{\boldsymbol{\kappa}}\cdot\hat{\mathbf{Z}}^{(1)}_{\beta,\nu} & -\hat{\mathbf{k}}_0\cdot\hat{\tilde{\mathbf{Z}}}^{(3)}_{\beta,\nu}\end{bmatrix}\cdot\begin{bmatrix}\vec{\mathcal{A}}^{\mathrm{ind}}_{\alpha,\mu_z\nu}\\ \vec{\mathcal{A}}^{\mathrm{sca}}_{\alpha,\mu_z\nu}\end{bmatrix} = \begin{bmatrix}\hat{\tilde{\mathbf{Z}}}^{(1)}_{\alpha,\nu} & \hat{\mathbf{0}}\\ \hat{\mathbf{0}} & \hat{\mathbf{k}}_0\cdot\hat{\tilde{\mathbf{Z}}}^{(1)}_{\beta,\nu}\end{bmatrix}\cdot\begin{bmatrix}\vec{\mathcal{A}}^{\mathrm{inc}}_{\alpha,\mu_z\nu}\\ \vec{\mathcal{A}}^{\mathrm{inc}}_{\alpha,\mu_z\nu}\end{bmatrix}, \tag{3.39}$$

where $\beta \neq \alpha$, $\hat{\mathbf{0}}$ is a matrix with dimensions $N_\Omega \times N_\Omega$ filled with zeros and the matrix $\hat{\mathbf{k}}_0$ has been introduced in the previous section. Note that, in the above equation, we dropped for simplicity the dependencies on the Floquet frequency Ω.

Let us introduce now the following T-matrix:

$$\hat{\mathbf{T}}_{\alpha,\nu}(\Omega) = \begin{bmatrix} \hat{\mathbf{T}}^{11}_{\alpha,\nu} & \hat{\mathbf{T}}^{12}_{\alpha,\nu} \\ \hat{\mathbf{T}}^{21}_{\alpha,\nu} & \hat{\mathbf{T}}^{22}_{\alpha,\nu} \end{bmatrix} = \begin{bmatrix} \hat{\mathbf{S}} \cdot \hat{\mathbf{Z}}^{(1)}_{\alpha,\nu} & -\hat{\hat{\mathbf{Z}}}^{(3)}_{\alpha,\nu} \\ \hat{\mathbf{k}}_0^{-1} \cdot \hat{\mathbf{S}} \cdot \hat{\boldsymbol{\kappa}} \cdot \hat{\mathbf{Z}}^{(1)}_{\beta,\nu} & -\hat{\hat{\mathbf{Z}}}^{(3)}_{\beta,\nu} \end{bmatrix}^{-1} \cdot \begin{bmatrix} \hat{\hat{\mathbf{Z}}}^{(1)}_{\alpha,\nu} & \hat{\mathbf{0}} \\ \hat{\mathbf{0}} & \hat{\hat{\mathbf{Z}}}^{(1)}_{\beta,\nu} \end{bmatrix}. \quad (3.40)$$

By introducing, also, the following two T-matrices with dimensions $N_\Omega \times N_\Omega$:

$$\hat{\mathbf{T}}^{\mathrm{ind}}_{\alpha,\nu}(\Omega) = \hat{\mathbf{T}}^{11}_{\alpha,\nu} + \hat{\mathbf{T}}^{12}_{\alpha,\nu}, \quad (3.41)$$

$$\hat{\mathbf{T}}^{\mathrm{sca}}_{\alpha,\nu}(\Omega) = \hat{\mathbf{T}}^{21}_{\alpha,\nu} + \hat{\mathbf{T}}^{22}_{\alpha,\nu}, \quad (3.42)$$

we finally end up with the following expressions for the complex amplitudes of the induced and scattered fields that are connected with the incident amplitudes via the introduced T-matrices:

$$\vec{\mathcal{A}}^{\mathrm{ind}}_{\alpha,\mu_z\nu}(\Omega) = \hat{\mathbf{T}}^{\mathrm{ind}}_{\alpha,\nu}(\Omega) \cdot \vec{\mathcal{A}}^{\mathrm{inc}}_{\alpha,\mu_z\nu}(\Omega), \quad (3.43)$$

$$\vec{\mathcal{A}}^{\mathrm{sca}}_{\alpha,\mu_z\nu}(\Omega) = \hat{\mathbf{T}}^{\mathrm{sca}}_{\alpha,\nu}(\Omega) \cdot \vec{\mathcal{A}}^{\mathrm{inc}}_{\alpha,\mu_z\nu}(\Omega). \quad (3.44)$$

The last two equations solve the scattering problem that we studied. The T-matrix $\hat{\mathbf{T}}^{\mathrm{ind}}_{\alpha,\nu}(\Omega)$ can be used to calculate the field induced inside the scatterer, whereas the T-matrix $\hat{\mathbf{T}}^{\mathrm{sca}}_{\alpha,\nu}(\Omega)$ can be used to calculate the scattered field outside the scatterer.

Let us now briefly discuss the generalization of the T-matrix method that we just presented for the case of a multilayer spherical scatterer with N_l coating layers. Each layer, together with the core of the scatterer, is considered to have different material properties, but the whole system overall shall possess a discrete translation symmetry in time with a period of $T_\mathrm{m} = 2\pi/\omega_\mathrm{m}$. Moreover, we employ again the Floquet frequency Ω spanning the range between zero and ω_m to construct spectral combs among which there will be spectral couplings. We consider again the spherical scatterer to be embedded in free space. Note, that each individual layer of the scatterer and its core shall have a different modulation frequency or may even be stationary. The important thing is that, overall, the whole system shall be characterized with a super-periodicity specified by T_m, i.e., the different modulation frequencies must be commensurable. We consider that the material properties of the core of the scatterer is characterized by a set of wavenumbers $\kappa^{(\mathrm{c})}_i(\Omega)$ and corresponding spectral eigenvectors $\vec{S}^{(\mathrm{c})}_{\kappa_1}(\Omega)$ with elements $S^{(\mathrm{c})}_{\kappa_i}(\Omega_j)$, whereas the l-th layer (with $l = 1, 2, \ldots, N_\mathrm{l}$) is characterized by a set of $\kappa^{(l)}_i(\Omega)$ and corresponding spectral eigenvectors $\vec{S}^{(l)}_{\kappa_1}(\Omega)$ with elements $S^{(l)}_{\kappa_i}(\Omega_j)$. Similarly as in Eqs. (3.35, 3.35), we also define the square matrices $\hat{\mathbf{S}}^{(\mathrm{c})}$, $\hat{\mathbf{S}}^{(l)}$, $\hat{\boldsymbol{\kappa}}^{(\mathrm{c})}$, $\hat{\boldsymbol{\kappa}}^{(l)}$ that characterize the material properties of the core and each layer of the scatterer. The outer radius of the l-th layer is denoted with $R^{(l)}$ and the radius of the core is denoted with $R^{(\mathrm{c})} \equiv R^{(l=N_\mathrm{l}+1)}$. $l = 1$ corresponds to the outermost layer.

The representations of the incident and scattered field outside the scatterer remain identical to those of Eqs. (3.24, 3.25). The representation of the field inside the core of

the spherical scatterer is the same as that of Eq. (3.26) involving only standing wave type of VSHs:

$$\mathbf{E}^{\text{core}}(\mathbf{r},\omega) \;=\; \int_{0^+}^{\omega_{\text{m}}^-} \sum_{i,j=1}^{N_\Omega} \sum_{\nu\mu_z,\alpha} \mathcal{A}^{\text{core}}_{\alpha,\mu_z\nu i}(\Omega)\delta(\omega-\Omega_j) S^{(\text{c})}_{\kappa_i}(\Omega_j)\mathbf{F}^{(1)}_{\alpha,\mu_z\nu}(\mathbf{r};\kappa_i^{(\text{c})}(\Omega))\text{d}\Omega, \quad \text{for } r < R^{(\text{c})}. \tag{3.45}$$

However, the representation of the field inside the l-th layer shall involve both incoming and outgoing spherical waves (which correspond to the spherical Hankel functions of the first and second kind respectively) and reads as follows:

$$\begin{aligned}\mathbf{E}^{(l)}(\mathbf{r},\omega) \;=\; & \int_{0^+}^{\omega_{\text{m}}^-} \sum_{i,j=1}^{N_\Omega} \sum_{\nu\mu_z,\alpha} \delta(\omega-\Omega_j) S^{(l)}_{\kappa_i}(\Omega_j) \\ & \left[\mathcal{A}^{(l),\text{out}}_{\alpha,\mu_z\nu i}(\Omega)\mathbf{F}^{(3)}_{\alpha,\mu_z\nu}(\mathbf{r};\kappa_i^{(l)}(\Omega)) + \mathcal{A}^{(l),\text{in}}_{\alpha,\mu_z\nu i}(\Omega)\mathbf{F}^{(4)}_{\alpha,\mu_z\nu}(\mathbf{r};\kappa_i^{(l)}(\Omega))\right]\text{d}\Omega, \\ & \text{for } R^{(l+1)} < r < R^{(l)}. \end{aligned} \tag{3.46}$$

Defining the following square, diagonal matrices with the generalized spherical Bessel functions:

$$\hat{\mathbf{Z}}^{(\iota,l,l')}_{\alpha,\nu}(\Omega) \;=\; \text{diag}\Big[z^{(\iota)}_{\alpha,\nu}(\kappa_1^{(l)}(\Omega)R^{(l')}) \cdots z^{(\iota)}_{\alpha,\nu}(\kappa^{(l)}_{N_\Omega}(\Omega)R^{(l')})\Big], \tag{3.47}$$

we can proceed in the same way as previously and enforce the interface conditions for the continuity of the tangential fields across all spherical interfaces of the multilayer scatterer, and, finally, get a set of linear equations that connect the unknown complex coefficients with the known incident complex coefficients. Specifically, by enforcing the interface conditions on the outer layer interface, the l-th in-between layer interface and the core layer interface, gives the following system of equations, respectively:

$$\begin{aligned} &\begin{bmatrix}\hat{\mathbf{S}}^{(1)} & \hat{\mathbf{0}} \\ \hat{\mathbf{0}} & \hat{\mathbf{k}}_0^{-1}\cdot\hat{\mathbf{S}}^{(1)}\cdot\hat{\boldsymbol{\kappa}}^{(1)}\end{bmatrix}\cdot\begin{bmatrix}\hat{\mathbf{Z}}^{(3,1,1)}_{\alpha,\nu} & \hat{\mathbf{Z}}^{(4,1,1)}_{\alpha,\nu} \\ \hat{\mathbf{Z}}^{(3,1,1)}_{\beta,\nu} & \hat{\mathbf{Z}}^{(4,1,1)}_{\beta,\nu}\end{bmatrix}\cdot\begin{bmatrix}\vec{\mathcal{A}}^{(1),\text{out}}_{\alpha,\mu_z\nu} \\ \vec{\mathcal{A}}^{(1),\text{in}}_{\alpha,\mu_z\nu}\end{bmatrix} = \\ &\qquad\qquad\begin{bmatrix}\hat{\mathring{\mathbf{Z}}}^{(1)}_{\alpha,\nu} & \hat{\mathring{\mathbf{Z}}}^{(3)}_{\alpha,\nu} \\ \hat{\mathring{\mathbf{Z}}}^{(1)}_{\beta,\nu} & \hat{\mathring{\mathbf{Z}}}^{(3)}_{\beta,\nu}\end{bmatrix}\cdot\begin{bmatrix}\vec{\mathcal{A}}^{\text{inc}}_{\alpha,\mu_z\nu} \\ \vec{\mathcal{A}}^{\text{sca}}_{\alpha,\mu_z\nu}\end{bmatrix}, \end{aligned} \tag{3.48}$$

$$\begin{aligned} &\begin{bmatrix}\hat{\mathbf{S}}^{(l)} & \hat{\mathbf{0}} \\ \hat{\mathbf{0}} & \hat{\mathbf{S}}^{(l)}\cdot\hat{\boldsymbol{\kappa}}^{(l)}\end{bmatrix}\cdot\begin{bmatrix}\hat{\mathbf{Z}}^{(3,l,l)}_{\alpha,\nu} & \hat{\mathbf{Z}}^{(4,l,l)}_{\alpha,\nu} \\ \hat{\mathbf{Z}}^{(3,l,l)}_{\beta,\nu} & \hat{\mathbf{Z}}^{(4,l,l)}_{\beta,\nu}\end{bmatrix}\cdot\begin{bmatrix}\vec{\mathcal{A}}^{(l),\text{out}}_{\alpha,\mu_z\nu} \\ \vec{\mathcal{A}}^{(l),\text{in}}_{\alpha,\mu_z\nu}\end{bmatrix} = \\ &\begin{bmatrix}\hat{\mathbf{S}}^{(l-1)} & \hat{\mathbf{0}} \\ \hat{\mathbf{0}} & \hat{\mathbf{S}}^{(l-1)}\cdot\hat{\boldsymbol{\kappa}}^{(l-1)}\end{bmatrix}\cdot\begin{bmatrix}\hat{\mathbf{Z}}^{(3,l-1,l)}_{\alpha,\nu} & \hat{\mathbf{Z}}^{(4,l-1,l)}_{\alpha,\nu} \\ \hat{\mathbf{Z}}^{(3,l-1,l)}_{\beta,\nu} & \hat{\mathbf{Z}}^{(4,l-1,l)}_{\beta,\nu}\end{bmatrix}\cdot\begin{bmatrix}\vec{\mathcal{A}}^{(l-1),\text{out}}_{\alpha,\mu_z\nu} \\ \vec{\mathcal{A}}^{(l-1),\text{in}}_{\alpha,\mu_z\nu}\end{bmatrix}, \end{aligned} \tag{3.49}$$

$$\begin{aligned} &\begin{bmatrix}\hat{\mathbf{S}}^{(N_\text{l})} & \hat{\mathbf{0}} \\ \hat{\mathbf{0}} & \hat{\mathbf{S}}^{(N_\text{l})}\cdot\hat{\boldsymbol{\kappa}}^{(N_\text{l})}\end{bmatrix}\cdot\begin{bmatrix}\hat{\mathbf{Z}}^{(3,N_\text{l},\text{c})}_{\alpha,\nu} & \hat{\mathbf{Z}}^{(4,N_\text{l},\text{c})}_{\alpha,\nu} \\ \hat{\mathbf{Z}}^{(3,N_\text{l},\text{c})}_{\beta,\nu} & \hat{\mathbf{Z}}^{(4,N_\text{l},\text{c})}_{\beta,\nu}\end{bmatrix}\cdot\begin{bmatrix}\vec{\mathcal{A}}^{(N_\text{l}),\text{out}}_{\alpha,\mu_z\nu} \\ \vec{\mathcal{A}}^{(N_\text{l}),\text{in}}_{\alpha,\mu_z\nu}\end{bmatrix} = \\ &\qquad\qquad\begin{bmatrix}\hat{\mathbf{S}}^{(\text{c})} & \hat{\mathbf{0}} \\ \hat{\mathbf{0}} & \hat{\mathbf{S}}^{(\text{c})}\cdot\hat{\boldsymbol{\kappa}}^{(\text{c})}\end{bmatrix}\cdot\begin{bmatrix}\hat{\mathbf{Z}}^{(1,\text{c},\text{c})}_{\alpha,\nu} & \hat{\mathbf{0}} \\ \hat{\mathbf{0}} & \hat{\mathbf{Z}}^{(1,\text{c},\text{c})}_{\beta,\nu}\end{bmatrix}\cdot\begin{bmatrix}\vec{\mathcal{A}}^{\text{core}}_{\alpha,\mu\nu} \\ \vec{\mathcal{A}}^{\text{core}}_{\alpha,\mu\nu}\end{bmatrix}. \end{aligned} \tag{3.50}$$

This system of equations can be solved with the transfer matrix method. There, the

coefficients of the fields inside one layer are related with the coefficients of the fields inside a previous layer via a transfer matrix that is straightforwardly given by the equations above. Cascading those transfer matrices by proceeding serially, layer by layer, provides a global transfer matrix that connects the coefficients of the fields in free space with the coefficients of the fields at the core of the multilayer spherical scatterer. Such approach, enables us to solve the problem and calculate the T-matrix of the scatterer connecting the incident with the scattered field coefficients. However, this method was proven to be numerically unstable since the condition number of the linear set of equations can be in practice rather large. This holds especially for large multipolar orders. In such case, special care needs to be taken, and, potentially, a proper preconditioning of the system of equations is required for its numerically stable solution. In practice, calculating the elements of the desired T-matrix column-wise by exciting separately with each incident monochromatic multipole of unitary complex amplitude and solving the above system of equations, has proven to give significantly more numerically stable results.

Finally, let us discuss some important symmetry properties of the above T-matrices, which arise from the spatio-temporal symmetries of the corresponding scattering system that they represent. Note that the symmetries of the T-matrix of a multilayer sphere is identical to that of a homogeneous sphere since the two possess the same symmetries. First of all, because the considered scatterer is non-stationary, we end up having a T-matrix that is non-diagonal with respect to the frequency ω. As we discussed, this property implies an inelastic scattering process. In the particular case of a time-modulated scatterer with discrete translational symmetry over time, i.e., for the case of periodic modulation, the Floquet theorem applies and we get a T-matrix that is block diagonal over frequency ω, with each block involving a comb of frequencies characterized by the Floquet frequency Ω and a period of $\omega_\mathrm{m} = 2\pi/T_\mathrm{m}$. This is the sole change that the structure of the T-matrix undergoes due to the introduced periodic time-variance of the scattering system: the symmetry of the invariance of frequency during the scattering process is broken. Nevertheless, the spatial symmetries of the system of the spherical scatterer continue to be the same as in the stationary case. That is to say, that a rotationally invariant scatterer with respect to the z-axis, gives a T-matrix that is diagonal with respect to the eigenvalue μ_z, the angular momentum along the z-axis, the rotational invariance of the scatterer along an arbitrary axis, due to its spherical symmetry, implies a T-matrix that is also diagonal with respect to the multipolar order ν. Furthermore, due to the parity symmetry of the scatterer, i.e., due to its invariance with respect to a point inversion, we also get a T-matrix that is diagonal with respect to the eigenvalue α, since the TE and TM VSHs of fixed multipolar order $\nu \pmod 2$ have an opposite parity symmetry.

Scatterers of different, non-spherical geometry, shall generally break those spatial symmmetry properties of their T-matrices, allowing for non-zero T-matrix transitions between the different components of the basis sets that represent the input and output fields. Symmetry protected zeros of the T-matrix elements, i.e., of the scattering channels, shall loose their protection by symmetry in such a case. Note, though, that while the T-matrices of non-stationary spherical scatterers are rather efficiently computed semi-analytically with the methods that we just presented in this section, the numerical calculation of the T-matrices of non-stationary scatterers of arbitrary geometry is rather computationally heavy. It would generally require the operation of multiple frequency domain full-wave solvers in parallel, one for each frequency of a considered spectral comb, that are coupled through each other with the spectrally non-diagonal susceptibility tensors of the periodically time-varying media that comprise the scatterers. However, we can still make use of the T-matrices of individual spherical scatterers to efficiently study more complicated multi-scattering systems. Conventional, T-matrix-based multiscattering methods can be generalized to study such systems. Specifically, in Ref. [A2], we study the optical re-

sponse of lattices of periodically arranged time-varying spherical scatterers. The band structure of exotic, four dimensional photonic crystals, with the fourth-dimension being a synthetic one, that of the temporal frequency, can, therefore, be also studied in this way. Spatiotemporal photonic crystals are recently attracting significant attention, since they generally offer hybrid energy-momentum band gaps, inside which light can propagate in extraordinary new ways [109].

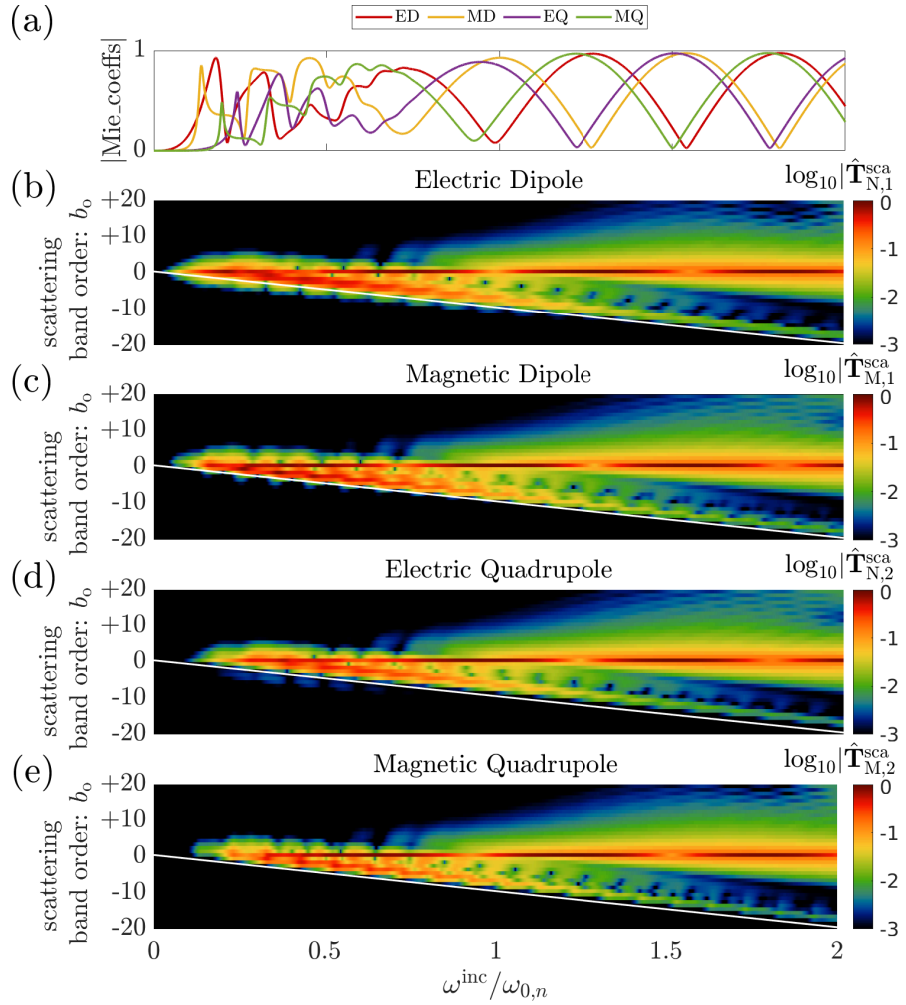

Figure 3.4: The T-matrix elements of a time-varying and dispersive sphere: (a) Plot of the absolute value of the Mie coefficients that correspond to the non-modulated sphere. (b-e) Plots of the T-matrix elements of the sphere with introduced strong, periodic time modulation, for different multipolar orders. The periodic time modulation of the scatterer leads to an inelastic scattering process with spectral coupling taking place among the different input and output spectral diffraction orders $\omega^{\mathrm{sca}} = \omega^{\mathrm{inc}} + b_{\mathrm{o}}\omega_{\mathrm{m}}$. Adapted with permission from Ref. [A1] © John Wiley and Sons.

In order to facilitate the discussion of the structure of the T-matrices that we have been calculating, let us now demonstrate some numerical results from an exemplary case of a T-matrix of a homogeneous and dispersive spherical scatterer whose material properties are periodically modulated in time.

Figure 3.4(a) plots the Mie coefficients (up to the quadrupolar order), i.e., the elements of the T-matrix, of the exemplary scatterer in the unmodulated case [257]. We consider the same material dispersion as the one used in Fig. 3.1(a), and we consider the radius of the sphere R to be equal to the free-space wavelength that corresponds to the

resonance frequency of the Lorentz oscillator that characterizes the material dispersion of the sphere, i.e., $R = 2\pi c_0/\omega_{0,n}$. In Fig. 3.4(a), at very low frequencies, we observe the Rayleigh scattering region where the Mie coefficients diminish rapidly in amplitude. At low frequencies, away from the resonance frequency of the Lorentz oscillator where the material losses are minimized, we note the appearance of sharp and densely packed multipolar resonances. On the other hand, at frequencies larger than the resonance frequency of the Lorentz oscillator, we have a material with negative dielectric permittivity (see Fig. 3.1(a)). This indicates the presence of multipolar modes of much lower quality factors that are spectrally well-separated.

Next, we introduce time modulation to the material from which the sphere is made. Specifically, we consider that the bulk electron density of the material is again modulated harmonically with a modulation frequency of $\omega_{\mathrm{m}} = \omega_{0,n}/10$ and a modulation strength of $M = 0.9$. This was also the exemplary case that we studied in Figs. 3.1(d-f). In Figs. 3.4(b-e), we plot the absolute values of the elements of T-matrices of such a time-modulated sphere, which are given by Eq. (3.42). We plot our results in a logarithmic scale and we consider multipoles up to the quadrupolar order. Note that we combine the calculated results for the T-matrices of all the Floquet frequencies in a single plot. While the x-axis corresponds to the frequency ω^{inc} of the incident multipolar excitation, the y-axis corresponds to the scattered band order of the radiating multipoles. The output frequency ω^{sca} of the radiated multipole at a scattering band order b_{o} is given by the following formula: $\omega^{\mathrm{sca}} = \omega^{\mathrm{inc}} + b_{\mathrm{o}}\omega_{\mathrm{m}}$. A zero scattering band order ($b_{\mathrm{o}} = 0$) corresponds to the case where the frequencies of the incident and scattered multipoles coincide. Therefore, in the limit of low modulation strengths $M \to 0$, we shall have a predominant response solely at the zero scattering band order, $b_{\mathrm{o}} = 0$. The color of the plots encodes the amplitude of a radiated multipole at frequency ω^{sca} once the sphere is excited by a single multipole of unit amplitude at frequency ω^{inc}. Note, also, that the white diagonal lines in Figs. 3.4(b-e) denote an output frequency being zero, i.e., $\omega^{\mathrm{sca}} = 0$.

Let us now discuss some interesting features that we observe in Figs. 3.4(b-e). First of all, we see that, due to the temporal modulation of the material properties of the sphere, the scatterer scatters light with an inelastic scattering process: a monochromatic excitation gives rise to a polychromatic response. We generally get a resonant scattering transition for the doubly resonant case where the sphere is at resonance simultaneously at the input and output frequencies ω^{inc} and ω^{sca}. This, of course, happens predominantly when the input and output frequencies coincide. However, there are also some other cases where such a resonant inelastic scattering process takes place. For example, we can see that there are strong transitions along diagonal lines parallel to the white ones, where we have a constant output frequency ω^{sca} that shall be associated with a sharp multipolar resonance supported by the sphere there. We can observe that such sharp resonances have a significant spectral echo predominantly in negative scattering band orders. The strength of those transitions, though, weakens as the spectral distance between the input and output frequencies increases. Additionally, we observe the emergence of sharper features with even stronger transitions that appear as a beating pattern along those diagonal spectral lines. We can associate these features with the simultaneous presence of sharp multipolar resonances at the respective input frequencies, leading to enhanced double-resonant effects. The periodicity of the beating pattern along those diagonal spectral lines is related to the modulation frequency ω_{m} and it indicates a spectral echo of a multipolar resonance at the input frequency. Another rather interesting feature that we can observe, is that there even emerges some coupling between input and output frequencies of opposite sign. This can lead to interesting phenomena such as parametric amplification [259, 260] and non-reciprocity [96]. Finally, let us note that, as expected, for low input frequencies, the response of the sphere is weak, especially for larger multipolar orders, since in this case

the optical size of the sphere is small.

3.4 Numerical comparison of the semi-analytical Floquet-Mie theory against a full-wave solver

In this section, we will compare results obtained from the semi-analytical Floquet-Mie theory that we developed in the previous section, against results from a full-wave solver, specifically from a time-domain finite element solver [261]. The numerical simulations in this section have been performed in collaboration with Dr. Grigorii Ptitcyn and Dr. Theodosis Karamanos.

Before proceeding, let us define a couple of observable scattering quantities, specifically the total scattered and absorbed power by an arbitrary scatterer. Following Eq. (5.18) of Ref. [257], as well as our conventions for the Fourier transforms of the fields (Eq. (2.7)) and the expressions of Eqs. (3.24, 3.25) for the expansion of incident and scattered fields into a series of VSHs, we readily get the following expressions for the total scattered energy W^{sca}:

$$\begin{aligned} W^{\mathrm{sca}} &= \int_{0^+}^{\omega_{\mathrm{m}}^-} \sum_{j=1}^{N_\Omega} P^{\mathrm{sca}}(\Omega_j)\,\mathrm{d}\Omega \\ &= \int_{0^+}^{\omega_{\mathrm{m}}^-} \sum_{j=1}^{N_\Omega} \sum_{\nu\mu_z,\alpha} \frac{\left|\mathcal{A}^{\mathrm{sca}}_{\alpha,\mu_z\nu}(\Omega_j)\right|^2}{Z_0 k_0^2(\Omega_j)}\,\mathrm{d}\Omega, \end{aligned} \tag{3.51}$$

and for the total extinction energy W^{ext}:

$$\begin{aligned} W^{\mathrm{ext}} &= \int_{0^+}^{\omega_{\mathrm{m}}^-} \sum_{j=1}^{N_\Omega} P^{\mathrm{ext}}(\Omega_j)\,\mathrm{d}\Omega \\ &= -\int_{0^+}^{\omega_{\mathrm{m}}^-} \sum_{j=1}^{N_\Omega} \sum_{\nu\mu_z,\alpha} \frac{\Re\left\{\left[\mathcal{A}^{\mathrm{inc}}_{\alpha,\mu_z\nu}(\Omega_j)\right]^* \mathcal{A}^{\mathrm{sca}}_{\alpha,\mu_z\nu}(\Omega_j)\right\}}{Z_0 k_0^2(\Omega_j)}\,\mathrm{d}\Omega, \end{aligned} \tag{3.52}$$

where $P^{\mathrm{sca}}(\omega)$, $P^{\mathrm{ext}}(\omega)$ are the total scattered and extinction powers, respectively, and Z_0 is the wave-impedance of free space. Note that the total absorbed energy is given by:

$$W^{\mathrm{abs}} = W^{\mathrm{ext}} - W^{\mathrm{sca}}. \tag{3.53}$$

In our comparisons in this section, we will focus on comparing the scattered near-fields both in time and frequency domain, as well as the far-field scattered power spectra. Locating the spherical scatterers at the origin of the coordinate system, we will be exciting them with an x-polarized plane wave propagating along the z-axis and having a Gaussian pulse envelope with width T_0 and carrier frequency ω_0. In time domain is given by:

$$\tilde{\mathbf{E}}^{\mathrm{inc}}(\mathbf{r},t) = E_0\,\hat{\mathbf{x}}\, e^{-\frac{(t-t_0-z/c_0)^2}{2T_0^2}} \cos[\omega_0(t-t_0-z/c_0)], \tag{3.54}$$

whereas its representation in the frequency domain is given by

$$\mathbf{E}^{\mathrm{inc}}(\mathbf{r},\omega) \;=\; \hat{\mathbf{x}}\, e^{\mathrm{i}\omega z/c_0}\frac{E_0 T_0}{2}\left[e^{-\frac{T_0^2(\omega_0-\omega)^2}{2}}+e^{-\frac{T_0^2(\omega_0+\omega)^2}{2}}\right]e^{\mathrm{i}\omega t_0}, \tag{3.55}$$

with t_0 being a time delay that we introduce for the proper injection of the incident pulse inside the simulation domain of the time-domain full-wave solver. Specifically, in our simulations we choose to temporally center our excitation pulse at $t_0 = 8T_0$, and we also set $E_0 = 1\mathrm{V/m}$.

Expanding the plane wave $\hat{\mathbf{x}}e^{\mathrm{i}\omega z/c_0}$ in a series of VSHs around the origin of the coordinate system (see Eq. (2.152)), we get the following expression for the incident spherical amplitudes in the representation of Eq. (3.24):

$$\mathcal{A}^{\mathrm{inc}}_{\alpha,\mu_z\nu}(\omega) \;=\; E_0 T_0 \pi\, \mathrm{i}^{\nu+1}\gamma_{-1\nu}\left[\delta_{\mu_z,1}+(-1)^{\delta_{\alpha\mathrm{N}}}\delta_{\mu_z,-1}\right]\left[e^{-\frac{T_0^2(\omega_0-\omega)^2}{2}}+e^{-\frac{T_0^2(\omega_0+\omega)^2}{2}}\right]e^{\mathrm{i}\omega t_0}. \tag{3.56}$$

Note that the above equation holds true only for positive frequencies ω. For the negative frequencies we can make use of the following symmetry property that satisfies the condition for real fields in time domain: $\mathcal{A}^{\mathrm{inc}}_{\alpha,\mu\nu}(-\omega) = (-1)^{\nu+\mu+\delta_{\alpha N}}\left[\mathcal{A}^{\mathrm{inc}}_{\alpha,-\mu\nu}(\omega)\right]^*$. Let us also note that, while for our semi-analytical calculations we use an infinitely extended plane wave, for the full-wave simulations we make use of a paraxial Gaussian beam with an optically large waist to approximate the plane-wave excitation in our numerical setup. This discrepancy may lead to only minor differences in our comparisons.

We will begin the numerical comparisons with two cases of light scattering by a homogeneous sphere made of a periodically time-varying medium, where again we adopt the same Lorentz oscillator model with sinusoidally modulated bulk electron density to account for material dispersion and temporal modulation (see Eqs. (3.17, 3.18)). Importantly, note that the electromagnetic properties of the time-varying media in the full-wave solver are imposed by embedding the partial differential equation that the electric polarization density of the considered media obey (Eq. (2.43)), in accordance with the susceptibility tensor of Eq. (3.17). In parallel with Maxwell's equations, the time-domain full-wave solver discretizes, also, in time and solves the Lorentzian differential equation for the polarization of the medium.

We name the first case as "slow modulation, weak dispersion" since we consider a relatively slow but still strong modulation of the medium of the scatterer and an excitation in a spectral window characterized by weak material dispersion, i.e., far away from the resonance of the Lorentz oscillator. On the other hand, our second case also considers a strong modulation amplitude, but now with a fast modulation frequency and, moreover, we consider an excitation in a spectral window centered around the resonance frequency of the Lorentz oscillator, where we encounter maximal dispersion. Hence, we name this second case as "fast modulation, strong dispersion". The parameters of the simulations for the two considered cases are listed in Table (3.1).

Figure 3.5 includes our results for the first case of "slow modulation, weak dispersion" that we study. First, we compare the fields at two arbitrarily chosen spatial points in the near-field region of the scatterer, with the one being behind (point A) and the other above (point B) the scatterer. Specifically, in Fig. 3.5(a) we compare the time domain signals of the x-component of the scattered electric field at point A and the y-component of the scattered magnetic field at point B. We use the label "Analytical" to refer to our results from the Floquet-Mie theory, and we use the label "Numerical" to refer to our results from the full-wave solver. The transient signals enable us to observe echoes of the incident pulse after the impact, where we can see an excelent agreement between the two methods.

quantities given with respect to the Lorentz oscillator resonant frequency $\omega_{0,n}$	slow modulation, weak dispersion	fast modulation, strong dispersion
damping coefficient: γ_n	$\omega_{0,n}/8$	$\omega_{0,n}/120$
bulk electron density: N_0	$11\omega_{0,n}^2 m_e \varepsilon_0 / q_e^2$	$1.12\omega_{0,n}^2 m_e \varepsilon_0 / q_e^2$
modulation strength: M	0.9	0.9
modulation frequency: ω_m	$\omega_{0,n}/15$	$\omega_{0,n}/2$
pulse central frequency: ω_0	$0.3\omega_{0,n}$	$\omega_{0,n}$
pulse temporal width: T_0	$2.9 \times 2\pi/\omega_{0,n}$	$1.934 \times 2\pi/\omega_{0,n}$
sphere radius: R	$7.095\, c_0/\omega_{0,n}$	$1.824\, c_0/\omega_{0,n}$
position of observation point A: $\mathbf{r}_A$	$(0,0,1.43R)$	$(0,0,2.432R)$
position of observation point B: $\mathbf{r}_B$	$(1.43R,0,0)$	$(2.432R,0,0)$
radius of spherical surface of observation	$1.43R$	$2.432R$
spectral window of observation (statistics)	$[0.1\omega_{0,n}, 0.93\omega_{0,n}]$	$[0.827\omega_{0,n}, 1.172\omega_{0,n}]$

Table 3.1: The parameters of the two simulated cases for the numerical comparison.

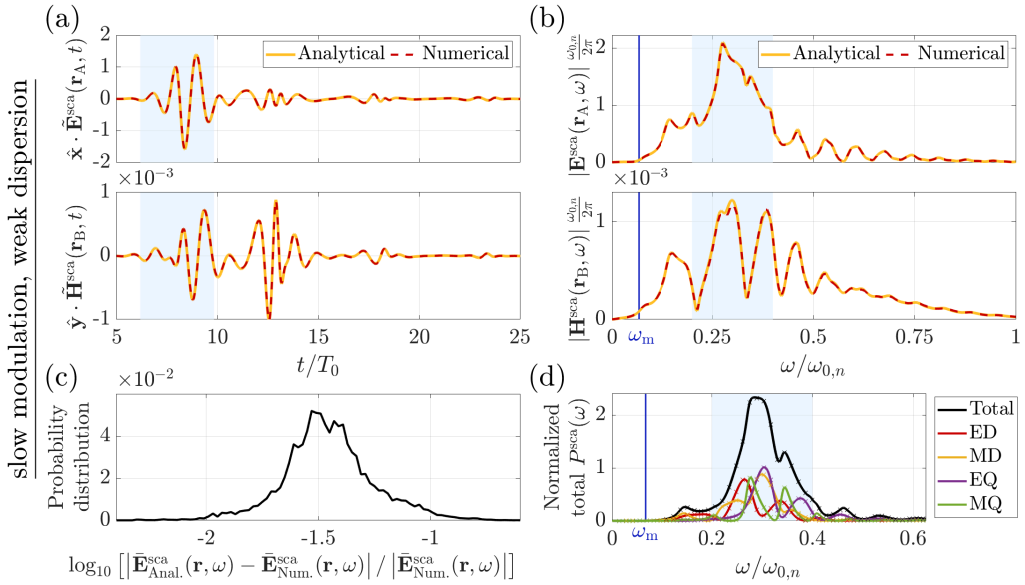

Figure 3.5: Comparisons between analytical and numerical results for the "slow modulation, weak dispersion" case: (a) Comparison of time domain near-field signals at points A,B. (B) Comparison of the frequency domain near-field spectra at points A,B. (c) Log. relative difference statistics between the analytical and numerical results, for the scattered fields over a spherical surface of observation in the near-field region of the scatterer and over a spectral window of observation. (d) Comparison of the far-field scattered power spectra. Adapted with permission from Ref. [A1] © John Wiley and Sons.

Moreover, in Fig. 3.5(b), we also compare the spectra of the scattered electric (mangetic) field at point A (B) in frequency domain. There, we observe again an excelent agreement between the two methods and we can also see the inelastic scattering process taking place with significant spectral leakage outside of the spectral window of our excitation. Note that the light-blue shaded regions in the figure highlight the temporal/spectral window

where 99% of the energy of the incident Gaussian pulse resides.

Next, in Fig. 3.5(c) we plot the probability distribution of the logarithmic relative difference between the fields calculated analytically and numerically. These plots involve the error statistics among a considered large distribution of points over a spherical surface surrounding the scatterer (in its near field region), and, also, over a broadband spectral window. See Table (3.1) for the radius of the spherical surface and the location of the spectral window. We can observe that the recorded relative errors are mainly distributed within the range of $[1\%, 10\%]$.

Finally, in Fig. 3.5(d) we plot the normalized far-field scattered power spectra together with their multipolar decomposition. Solid lines denote the analytical results, whereas cross markers denote the numerical results. The values of the total scattered power are plotted with a black solid line. The individual multipolar contributions (up to the quadrupolar order) are plotted with colored solid lines. The scattered power spectra are normalized to the spectral peak of the total power flux of the incident field passing through the geometrical cross-section of the scatterer. Equation (3.51) is used to evaluate the scattered power with respect to the scattered multipolar amplitudes $\mathcal{A}^{\text{sca}}_{\alpha,\mu_z\nu}(\omega)$. While those are readily available within the Floquet-Mie theory, we use a surface integral (see, e.g., also Eq. (5.175) from Ref. [257]) to extract them from the full-wave simulations by evaluating projections of the scattered fields, located over the spherical surface of observation in the near-field region of the scatterer, on the multipolar basis of VSHs. Specifically, by making use of the orthogonality property of Eq. (2.147), we evaluate the following integrals over a closed spherical surface $S_{R'}$ surrounding the scatterer to get the scattered spherical amplitudes:

$$\mathcal{A}^{\text{sca}}_{\alpha,\mu_z\nu}(\omega) \quad = \quad \frac{(-\mathrm{i})^{\delta_{\alpha\mathrm{M}}}}{R'^2 z^{(3)}_{\alpha,\nu}(k_0(\omega)R')} \oiint_{S_{R'}} \mathbf{E}^{\text{sca}}(\mathbf{r},\omega)\cdot[\mathbf{f}_{\alpha,\mu_z\nu}(\hat{\mathbf{r}})]^* \,\mathrm{d}^2\mathbf{r}. \tag{3.57}$$

We observe again a an excellent agreement between the two methods all over across the rich multipolar spectrum.

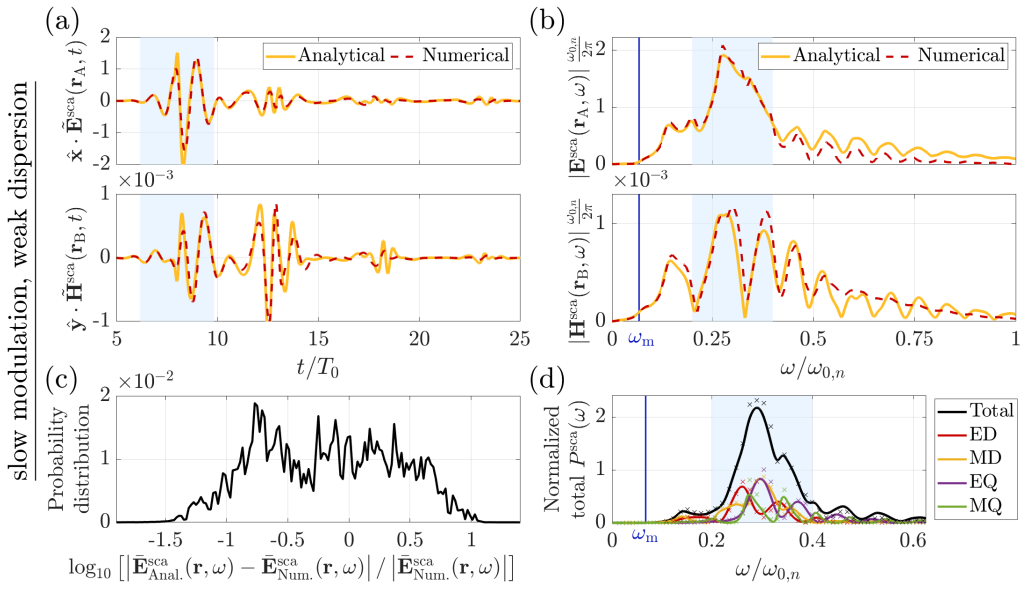

Figure 3.6: The effect of ignoring dispersion in the "slow modulation, weak dispersion" case: (a-d) Similarly as Fig. 3.5(a-d). Adapted with permission from Ref. [A1] © John Wiley and Sons.

Next, before moving to our second case study, let us discuss the effect of ingoring

dispersion in our model. It is common in the literature of electromagnetism in time-varying media to ignore dispersion, and we would like to highlight in what way this can compromise our models and results. In Fig. 3.6, we study the same case as in Fig. 3.5, but now the "Analytical" part of our results that get compared refers to results obtained from the Floquet-Mie theory but with the dispersion effects "turned off". Specifically, instead of using Eq. (3.17) to model the time varying medium, we neglect dispersion and adopt the following susceptibility tensor (note the slight difference between the previous and the new formula):

$$\chi_{\mathrm{ee}}(\omega-\omega',\omega') \quad = \quad \frac{\chi_0(\omega_0)}{\sqrt{2\pi}N_0}N_{\mathrm{e},n}(\omega-\omega'). \tag{3.58}$$

Note, also, that we leave dispersion intact for our full-wave simulations. What we observe is the emergence of relatively small differences in the measurements. That is mainly because we excite the sphere in a spectral region of small frequencies where dispersion is weak. However, the inelastic scattering response at larger frequencies (where dispersion becomes prominent) is characterized by significantly larger discrepancies. As indicated in Fig. 3.6(c) the relative differences in the near fields often exceed 100%.

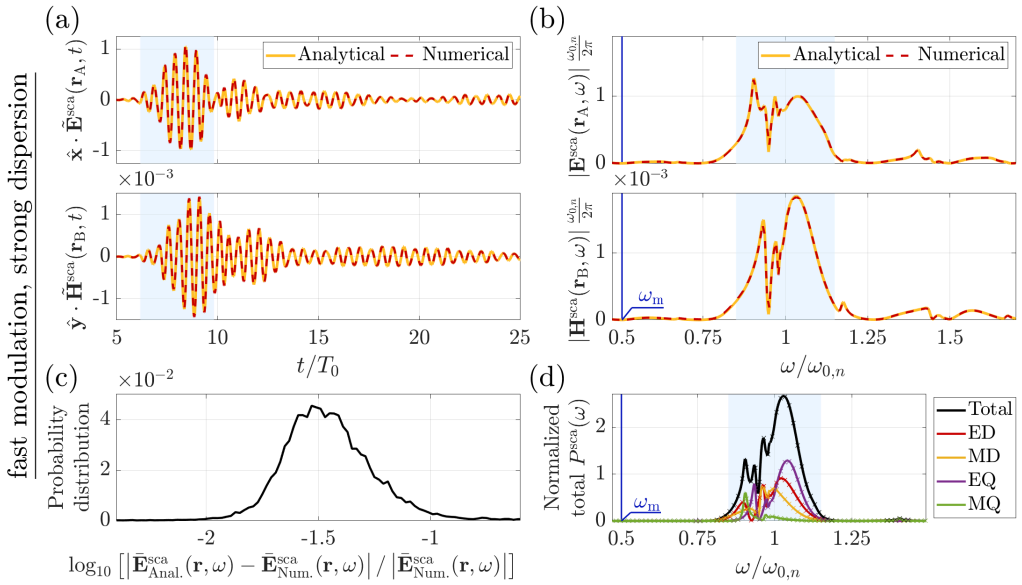

Figure 3.7: Comparisons between analytical and numerical results for the "fast modulation, strong dispersion" case: (a-d) Similarly as Fig. 3.5(a-d). Adapted with permission from Ref. [A1] © John Wiley and Sons.

Next, we move to our second case study of "fast modulation, strong dispersion". Our results for this case are plotted in Fig. 3.7. Similarly as in Fig. 3.5, we generally see an excellent agreement between the analytical and the numerical results, even though now we operate our scattering system in a more challenging regime where the modulations are fast and the material dispersion is strong. Note that the inelastic scattering process is weaker in comparison to our previous study case. This is because we excite the scatterer in a spectral region around the Lorentz oscillator where the material losses get maximal, hindering the efficient spectral leakage to neighboring frequencies through inelastic scattering processes. Note the weak echo of the multipolar resonances that get directly excited by the illuminating Gaussian pulse inside the light-blue-shaded region at frequencies larger than $1.25\omega_{0,n}$. In contrast to our previous case study, here the modulation frequency

is (marginally) larger than the spectral width of the illuminating pulse, allowing for a practically clean spectral separation of the elastic and inelastic scattering processes.

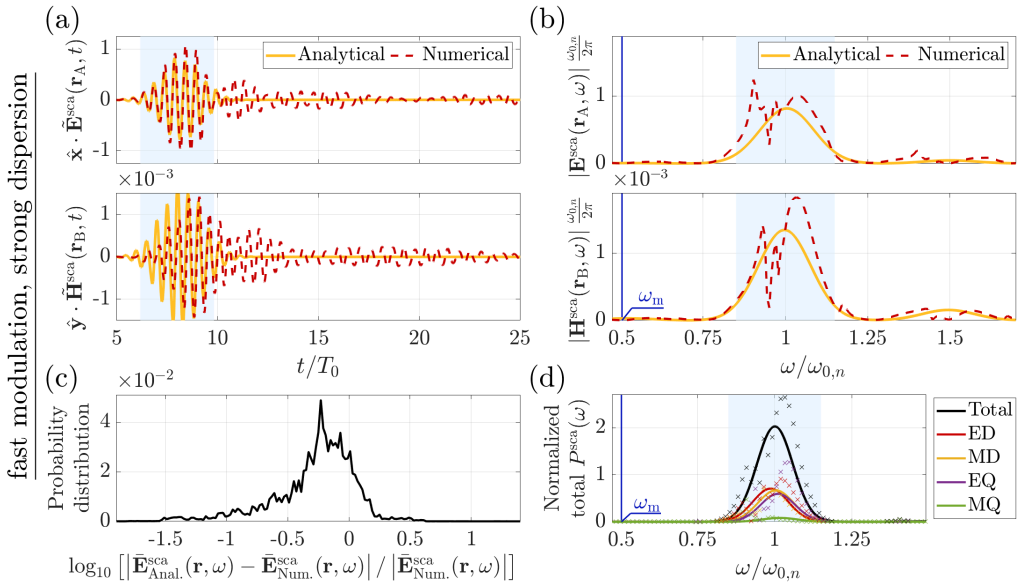

Figure 3.8: The effect of ignoring dispersion in the "fast modulation, strong dispersion" case: (a-d) Similarly as Fig. 3.5(a-d). Adapted with permission from Ref. [A1] © John Wiley and Sons.

Finally, in Fig. 3.8 (similarly as with Fig. 3.6) we illustrate again the effect of ignoring material dispersion for the "fast modulation, strong dispersion" case study. As it was to be expected, in this case the effects of ignoring material dispersion lead to much more prominent discrepancies compared to the previous case study. Now, there are striking differences between the compared spectra and transient signals. Transparent conducting oxides (TCOs), such us aluminium-doped zinc oxides (AZOs) and tin-doped indium oxides (ITOs), operated in their epsilon-near-zero (ENZ) regime have been recently studied and proposed as material platforms that can exhibit relatively pronounced time-varying properties. Yet their time-varying material properties have been commonly modeled with dispersionless models, even though dispersion in the ENZ regime is typically rather strong [79, 262, 263]. Accounting for dispersion in such cases should be instrumental to achieve an accurate modeling of the optical response of such time-varying systems.

Importantly, let us highlight that the full-wave simulations are considerably more demanding in terms of required computational resources in comparison to calculation of the Floquet-Mie theory. For example, while the full-wave simulation for the first case study lasted for 12 days requiring 110 gigabytes of RAM, and for the second case study it lasted for 5 days requiring 43 gigabytes of RAM, the semi-analytical algorithm implementing the Floquet-Mie theory uses less than 2 gigabytes of RAM to calculate T-matrices and only needs approximately 15 seconds for both case studies. The differences in computational efficiency are striking.

We will close this section with a last set of simulations where we compare analytical and numerical results for the case of a multilayer spherical scatterer. Specifically, we will be considering a spherical scatterer comprised of a core and two coating layers, with each of those three concentric subdomains being characterized by different generalized dispersion relation. We borrow all the simulation parameters from the "slow modulation, weak dispersion" case and we introduce modifications relative to them according to Table 3.2.

In Fig. 3.9, we plot a comparison of the scattered fields at points A and B of the previous study case ("slow modulation, weak dispersion") both in time and frequency domain. We

	first layer	second layer	core
Lorentz oscillator frequency: $\omega_{0,n}$	1×	1.1×	0.85×
damping coefficient: γ_n	1×	0.7×	1.5×
bulk electron density: N_0	1×	1.5×	1×
modulation strength: M	1×	0×	2/3×
sphere radius: R	1×	22/35×	12/35×

Table 3.2: The parameters for the simulation of the considered multilayer sphere. The ones that are not mentioned in this table are identical to those from the "slow modulation, weak dispersion" case in Table 3.1, whereas the ones that are mentioned are expressed relative to the correspondent quantities there.

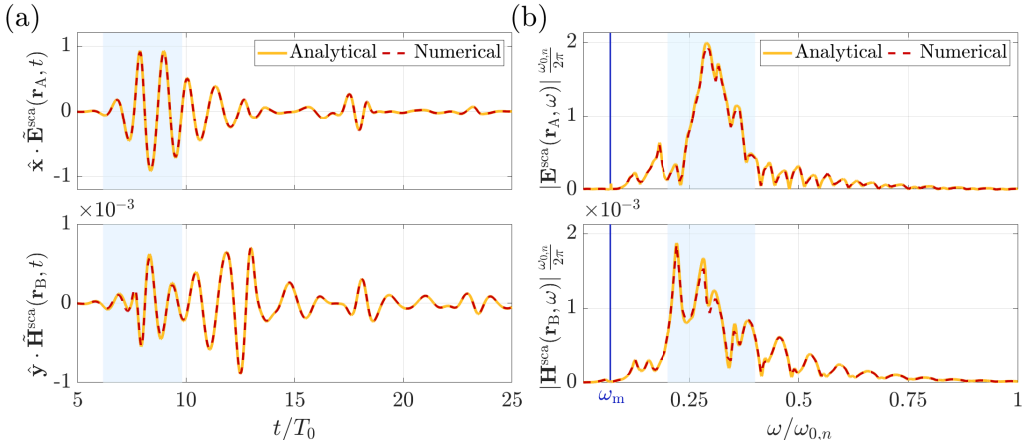

Figure 3.9: Comparisons between analytical and numerical results for the case of a multilayer spherical scatterer: (a) Comparison of time domain near-field signals at points A,B. (B) Comparison of the frequency domain near-field spectra at points A,B.

can observe again a good agreement between the fields calculated with the full-wave solver and the Floquet-Mie theory algorithm. Note, though, that the system of equations in the multilayer case becomes numerically ill-conditioned more easily than before and special attention is required especially in cases where the T-matrix encompasses large spectral ranges or involves radiuses that differ a lot in length. The described situation deteriorates for large multipolar orders.

3.5 Time-varying scatterers as active optical components: driving a time-modulated sphere into a lasing state

In this section, we will discuss the breaking of energy conservation in time-varying scatterers through a T-matrix-assisted analysis. Specifically, we will perform a singular value decomposition of the T-matrix of a time-varying spherical scatterer and demonstrate how it is characterized by a set of active singular modes that are able to generate electromagnetic energy, i.e., transform energy obtained from the external temporal modulation of the media into radiating photons. Moreover, as an exemplary case we will present results of driving a time-varying spherical scatterer into a lasing state and we will discuss the differences against lasing states obtained from active but stationary media. The numerical

simulations in this section have been performed in collaboration with Dr. Grigorii Ptitcyn and Dr. Viktar Asadchy.

To begin with, we want to refer the reader to Section 2.4 where we have been discussing fundamental aspects of energy conservation in time-varying media. There, we have shown that a fundamental property of such media is their ability to break electromagnetic energy conservation. In fact, as we shall see in this section with specific examples, the external modulation of the medium is able to provide energy to the electromagnetic fields. That is to say that time-varying optical nanostructures/components can act as active elements inside optical systems. The photons generally interact with the matter and exchange energy, and, in the case of active behavior, energy is extracted from the externally temporally modulated matter and is provided to the photons.

Let us employ the T-matrix method to study under its prism such phenomena of breaking of energy conservation in time-varying scatterers. First, it is instructive to perform a singular value decomposition of the T-matrix of the scatterer, which is a technique that allows us to decompose the scattering system with respect to the orthonormal set of singular modes that characterize it [264, 265]. We will focus on spherical scatterers that we studied previously, but our results can be straightforwardly generalized to arbitrary non-spherical scatterers.

Specifically, we apply the singular value decomposition of the following T-matrix weighted by the free space wavenumbers:

$$\hat{\mathbf{k}}_0^{-1}(\Omega)\cdot\hat{\mathbf{T}}^{\mathrm{sca}}_{\alpha,\nu}(\Omega)\cdot\hat{\mathbf{k}}_0(\Omega) \;=\; \hat{\mathbf{U}}_{\alpha,\nu}(\Omega)\cdot\hat{\mathbf{\Sigma}}_{\alpha,\nu}(\Omega)\cdot\hat{\mathbf{V}}^{\dagger}_{\alpha,\nu}(\Omega), \tag{3.59}$$

where $\mathbf{\Sigma}_{\alpha,\nu}(\Omega)$ are diagonal matrices that contain the singular values $\sigma_{\alpha,\nu s}(\Omega)$ of the decomposition, and $\hat{\mathbf{U}}_{\alpha,\nu}(\Omega)$, $\hat{\mathbf{V}}_{\alpha,\nu}(\Omega)$ are matrices whose columns contain the corresponding left- and right-singular vectors, $\vec{u}_{\alpha,\nu s}(\Omega)$, $\vec{v}_{\alpha,\nu s}(\Omega)$, respectively. Note that the right- and left-singular vectors contain the incident and scattered multipolar spectra of the singular modes of the time-varying scattering system. And they can be used as a complete orthonormal basis upon which we can expand the similarly weighted multipolar amplitudes of the incident and scattered fields. Specifically, by expanding the following vectors on the full basis of the right-singular vectors:

$$\hat{\mathbf{k}}_0^{-1}(\Omega)\cdot\vec{\mathcal{A}}^{\mathrm{inc}}_{\alpha,\mu_z\nu}(\Omega) \;=\; \sum_{s=1}^{N_\Omega}\mathcal{S}^{\mathrm{inc}}_{\alpha,\mu_z\nu s}(\Omega)\vec{v}_{\alpha,\nu s}(\Omega), \tag{3.60}$$

where $\mathcal{S}^{\mathrm{inc}}_{\alpha,\mu_z\nu s}(\Omega) = \vec{v}^{\dagger}_{\alpha,\nu s}(\Omega)\cdot\vec{\mathcal{A}}^{\mathrm{inc}}_{\alpha,\mu_z\nu}(\Omega)$ are complex coefficients, we can depart from Eqs. (3.51-3.53) and arrive to the following alternative expressions for the total scattered, extinction and absorbed energies:

$$W^{\mathrm{sca}} \;=\; \frac{1}{Z_0}\int_0^{\omega_{\mathrm{m}}}\sum_{\nu\mu_z,\alpha}\sum_{s=1}^{N_\Omega}\sigma^2_{\alpha,\nu s}\left|\mathcal{S}^{\mathrm{inc}}_{\alpha,\mu_z\nu s}\right|^2\mathrm{d}\Omega, \tag{3.61}$$

$$W^{\mathrm{ext}} \;=\; -\frac{1}{Z_0}\int_0^{\omega_{\mathrm{m}}}\mathrm{d}\Omega\sum_{\nu\mu_z,\alpha}\sum_{s,s'=1}^{N_\Omega}\sigma_{\alpha,\nu s'}\Re\left\{\left[\mathcal{S}^{\mathrm{inc}}_{\alpha,\mu_z\nu s}\right]^*\mathcal{S}^{\mathrm{inc}}_{\alpha,\mu_z\nu s'}\vec{v}^{\dagger}_{\alpha,\nu s}\cdot\vec{u}_{\alpha,\nu s'}\right\}, \tag{3.62}$$

$$
\begin{aligned}
W^{\mathrm{abs}} &= -\frac{1}{Z_0}\int_0^{\omega_{\mathrm{m}}} \mathrm{d}\Omega \sum_{\nu\mu_z,\alpha} \\
&\sum_{s=1}^{N_\Omega} \sigma_{\alpha,\nu s} \left|\mathcal{S}^{\mathrm{inc}}_{\alpha,\mu_z\nu s}\right|^2 \left[\sigma_{\alpha,\nu s} + \Re\left\{\vec{v}^{\dagger}_{\alpha,\nu s}\cdot\vec{u}_{\alpha,\nu s}\right\}\right] + \\
&\sum_{\substack{s,s'=1\\ s'\neq s}}^{N_\Omega} \sigma_{\alpha,\nu s'} \Re\left\{\left[\mathcal{S}^{\mathrm{inc}}_{\alpha,\mu_z\nu s}\right]^* \mathcal{S}^{\mathrm{inc}}_{\alpha,\mu_z\nu s'} \vec{v}^{\dagger}_{\alpha,\nu s}\cdot\vec{u}_{\alpha,\nu s'}\right\},
\end{aligned}
\tag{3.63}
$$

where we dropped the dependence of the quantities on the Floquet frequency Ω for simplicity. Note that the sum in the last row of the last equation for the absorbed energy corresponds to couplings among the different singular modes.

Since the singular modes are orthogonal to each other (specifically we have: $\vec{u}^{\dagger}_{\alpha,\nu s}\cdot\vec{u}_{\alpha,\nu s'} = \vec{v}^{\dagger}_{\alpha,\nu s}\cdot\vec{v}_{\alpha,\nu s'} = \delta_{ss'}$), we can assume an excitation by a single right singular mode $\vec{v}_{\alpha,\nu s}$ and ignore the sum in the last row of the last equation. In view of Eqs. (3.61 and 3.63), let us define then the following ratio:

$$
\frac{P^{\mathrm{abs}}_{\alpha,\nu s}(\Omega)}{P^{\mathrm{sca}}_{\alpha,\nu s}(\Omega)} = -1 - \frac{\Re\left\{\vec{v}^{\dagger}_{\alpha,\nu s}\cdot\vec{u}_{\alpha,\nu s}\right\}}{\sigma_{\alpha,\nu s}}. \tag{3.64}
$$

The sign of this ratio specifies whether the spherical scatterer behaves like an active (negative sign) or passive (positive sign) optical element once excited by the particular singular mode. Specifically, we get that there is generation of energy when $\Re\left\{\vec{v}^{\dagger}_{\alpha,\nu s}\cdot\vec{u}_{\alpha,\nu s}\right\} > -\sigma_{\alpha,\nu s}$ (note that the singular values $\sigma_{\alpha,\nu s}$ are always positive). In the particular case where the weighted T-matrix becomes singular, we get a singular value $\sigma_{\alpha,\nu s}$ that goes to infinity. Then, that ratio approaches the limit value of -1 and all the energy that gets generated by the time-varying spherical scatterer gets radiated at infinity. This happens in the absence of any incident field, i.e., such a case corresponds to a lasing eigenstate of the time-varying spherical scatterer. It is a self-standing solution of electromagnetic waves that the system can host in the absence of any external excitation. In view of Eq. (3.40) -for a homogeneous spherical scatterer and similarly also for a multilayer spherical scatterer-, this happens when the determinant of the following matrix becomes zero:

$$
d_{\alpha,\nu}(\Omega) = \mathrm{Det}\left(\begin{bmatrix} \hat{\mathbf{S}}\cdot\hat{\mathbf{Z}}^{(1)}_{\alpha,\nu} & -\hat{\hat{\mathbf{Z}}}^{(3)}_{\alpha,\nu} \\ \hat{\mathbf{k}}_0^{-1}\cdot\hat{\mathbf{S}}\cdot\hat{\boldsymbol{\kappa}}\cdot\hat{\mathbf{Z}}^{(1)}_{\beta,\nu} & -\hat{\hat{\mathbf{Z}}}^{(3)}_{\beta,\nu} \end{bmatrix}\right) = 0. \tag{3.65}
$$

Then the scattering system of equations possesses non-trivial solutions. The spectral composition of the multipolar lasing states is given (in terms of the multipolar amplitudes of the induced and scattered fields) by the eigenvectors that correspond to the vanishing eigenvalues of the above matrices. We will demonstrate later how we can reach such lasing states by operating the scattering system in the regime of parametric oscillations.

Let us now make use of the time-varying spherical scatterer studied in Fig. 3.4 as an exemplary case and search for the possibility of realizing negative total absorption, even though the dispersive model of the Lorentz oscillator that is employed there is rather lossy around the resonant frequency of the oscillator. Note that such an observation has already been reported in Ref. [114], but for a lossless system without material dispersion.

To this end, we perform a singular value decomposition of the weighted T-matrices that correspond to each spectral comb with a specific Floquet frequency (Eq. (3.59)). Then, we consider an excitation of our scattering system with each right-singular vector of the decomposed matrices, i.e., we consider excitations with $\mathcal{S}^{\text{inc}}_{\alpha,\mu\nu s}(\Omega) = \delta_{\alpha\alpha'}\delta_{\mu\mu'}\delta_{\nu\nu'}\delta_{ss'}\delta(\Omega - \Omega')$ sweeping the values of α', s', Ω', with μ' being arbitrary and ν' fixed to 1 as we focus on the dipolar response of the system. For all such excitations of our system, we observe the ratio of absorbed and scattered powers (see Eq. (3.64)). Note that exciting the system with a single right-singular vector means that we excite only a single spectral comb of some Floquet frequency, with a particular spectral distribution of the power over the frequencies of the comb. Simultaneously, our excitation consists of a single incoming multipole (dipole). Therefore, it is a quite special excitation, not only spectrally but also spatially. However, an arbitrary excitation of the system can be decomposed into this basis of right-singular vectors. Exciting our system, though, with a single singular mode enables us to ignore the inter-modal couplings due to the terms in the last row of Eq. (3.63) and, therefore, facilitates and simplifies our analysis.

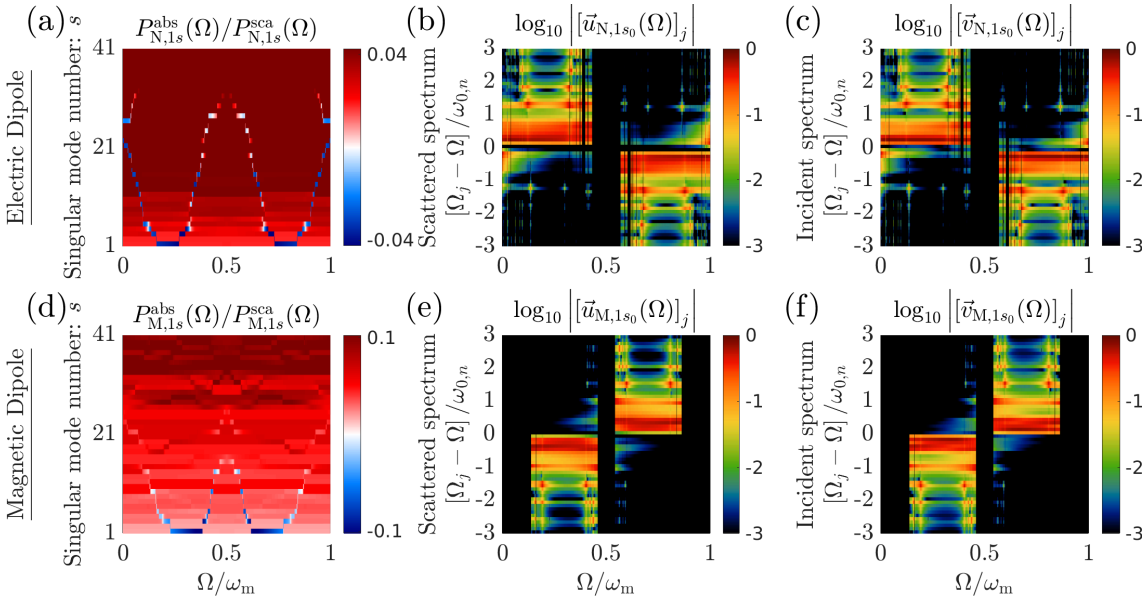

Figure 3.10: Singular value decomposition of the weighted T-matrix of the time-varying sphere studied in Fig. 3.4 revealing the presence of singular dipolar modes characterized by negative absorption, i.e., a transfer of energy from the time-varying matter to the photons in an inelastic scattering process: (a,d) Plots of the ratio of the absorbed and scattered powers under the system's excitation with its singular modes. Plots of the output (b,e) and input (c,f) discrete spectra of the left- and right-singular vectors of the singular modes that demonstrate maximally negative absorption for each Floquet frequency Ω. Adapted with permission from Ref. [A1] © John Wiley and Sons.

We plot our results in Fig. 3.10. Note that the singular modes are ordered in a descending order of their respective singular values, i.e., in a descending order of total scattered power, as it is implied by Eq. (3.61). In Fig. 3.10(a,d), we observe that for many of the spectral combs with varying Floquet frequency Ω, there exist singular modes that demonstrate significantly negative values of absorbed power. That is to say that those are modes where significant transfer of energy from the time-varying matter to the photons of the electromagnetic field takes place during the inelastic scattering process. Note that, as we discussed before, in the regime of parametric oscillations, under careful tuning of the

parameters of our system, we can reach ratios of $P^{\text{abs}}/P^{\text{sca}}$ that approach the value of -1.

The spectral content of the right-singular vectors, $\vec{v}_{\alpha,1s_0}(\Omega)$, which correspond to singular modes that demonstrate a maximally negative absorption (indicated with the index s_0), is plotted in logarithmic scale and for each Floquet frequency in Fig. 3.10(c,f). Note that these singular modes can be excited only with this particular illumination of the corresponding right-singular vectors. The black-colored columns of the figure indicate an absence of a singular mode with negative absorption for that particular Floquet frequency. In Figs. 3.10(b,e), we plot the norm of the elements of the corresponding left-singular vectors $\vec{u}_{\alpha,1s_0}(\Omega)$. Those vectors contain information about the spectral content of the scattered fields once the system gets excited by the corresponding right-singular vectors. Importantly, we observe that the input and output spectra of the singular modes that demonstrate negative absorption are characterized by a spectral distribution of power predominantly over the low frequencies where the material losses due to dispersion are low.

Note that, due to the presence of a lossy spectral region and the size of the considered sphere, we do not find any singular mode with negative absorption for the quadrupolar modes. It only becomes possible for spheres of larger size where modes of higher quality factor and multipolar order are supported. It is rather remarkable, though, that negative absorption can be achieved even in the presence of strong material losses once we optimize the system's excitation. Finally, let us note that the presence of the third row of Eq. (3.63), corresponding to inter-modal couplings, allows for the possibility of attaining negative absorption under other, more complicated, excitation schemes, that generally involve a superposition of such singular modes.

Let us now explore the regime of parametric oscillations in time-varying scatterers. A parametric oscillator is a harmonic oscillator whose physical properties/parameters vary in time. A typical mechanical example is that of a pendulum whose length is modulated in time, with a historic example being the "Botafumeiro": an 80 kg incensory at the Cathedral of Santiago de Compostela, whose chain is periodically pulled up and down via a pulley by monks, reaching speeds of 68km/h over arc lengths of 65m within 17 modulation cycles [82]. Already by 1831 and 1887, respectively, Michael Faraday and Lord Rayleigh have noticed the special case of oscillations being exciting by forces of double the frequency of the oscillation [266, 267]. Those are known as parametric resonances and are known to lead to an exponential growth of the oscillations rather than the linear growth that characterized the typical case of a driven harmonic oscillator at its resonance frequency. For an intuitive understanding of the difference between the two type of oscillations it is instructive to look at the familiar mechanical example of pumping a playground swing. There, two methods of energy insertion have been identified and they correspond to the parametric and to the driven oscillations. While a parametric oscillation involves the systematic raising and lowering of the swinger's center of mass along the swing's radial axis by standing and squatting at key points in the swing arc, with double the frequency of the oscillation, a driven oscillation may be conceived as rocking back and forth at the oscillation frequency [268].

In analogy to the mechanical parametric oscillators, (degenerate) optical parametric oscillators are used to convert input pumping light waves from a laser into output light waves of half the frequency of the input pump. It consists of an optical resonator of high quality factor, that efficiently traps light of the output frequency, and of a nonlinear crystal that acts as a gainy medium by converting the input pump light to the output light of half the frequency, via a half-frequency-generation process, that is able to compensate the losses that occur within a cycle of oscillation and, finally, drive the parametric oscillations [269, 270].

Here, similarly, we will drive a spherical scatterer into the regime of parametric os-

cillations. The spherical scatterer can trap light and act as a resonator. However, the quality factor of its resonances is typically low, although it can become significantly larger for large optical sizes of the scatterer. A quasinormal mode analysis can reveal the resonances of a stationary scatterer [228]. In our case, there is no nonlinear gainy medium that downconverts the pump light waves into the light waves of lower frequency through a half-frequency generation process like it is the case with the typical optical parametric oscillators. Instead, this optical gain is provided now by the external temporal modulation of the medium with a frequency that is double the oscillator frequency. Therefore, we will look for parametric resonances as eigenmodes of our system for the Floquet frequency $\Omega = \omega_\mathrm{m}/2$.

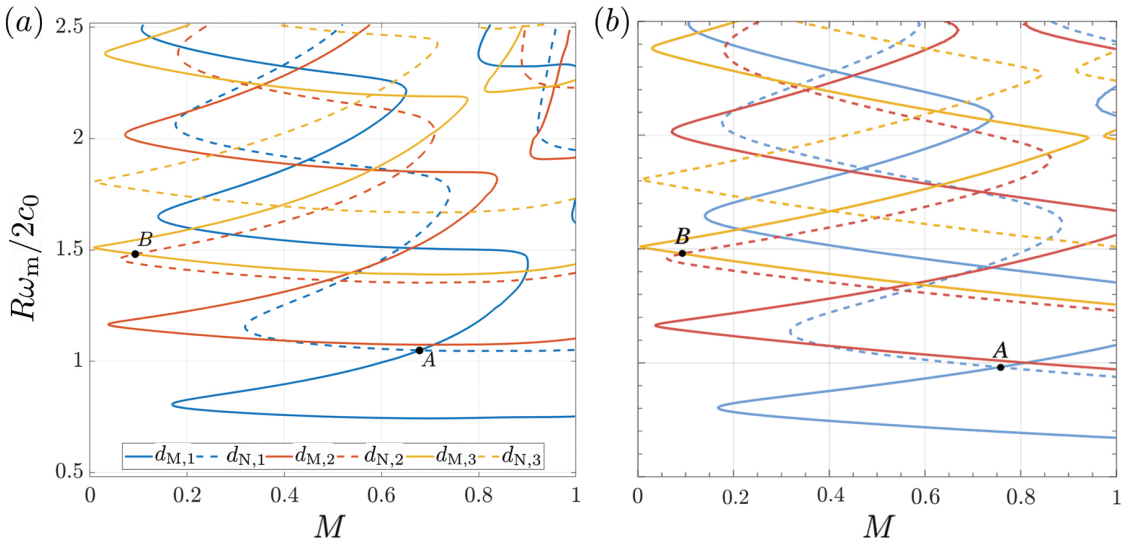

Figure 3.11: Plot of the conditions for parametric oscillations in a time-modulated spherical scatterer exhibiting parametric Mie resonances. Calculated for (a) $N_\Omega = 24$ and (b) $N_\Omega = 2$ number of frequencies. Adapted with permission from Ref. [A3] © American Physical Society.

For our exemplary study, we will consider a homogeneous sphere made of a medium whose susceptibility is described again by the same model of a single Lorentzian harmonic oscillator whose bulk electron density gets modulated harmonically in time. The bulk electron density of the unmodulated medium we select to be $N_0 = 12.25\omega_{0,n}^2 m_\mathrm{e}\varepsilon_0/q_\mathrm{e}^2$ and the modulation frequency is fixed to $\omega_\mathrm{m} = \omega_{0,n}/2$. We also consider a vanishing damping coefficient γ_n. The real part of the permittivity of the considered unmodulated, time-invariant medium at the lasing frequency $\omega_\mathrm{las} = \omega_\mathrm{m}/2$ of the parametric oscillations is $\Re\{\varepsilon_\mathrm{inv}(\omega_\mathrm{las}) = 14.07\}$. Next, we vary the radius of the sphere and the modulation strength and search numerically for solutions of Eq. (3.65) which allows us to identify cases of parametric Mie resonances. We do this for both electric and magnetic type of multipoles of up to the third multipolar order. We plot the results in Fig. 3.11. We observe that the parametric Mie resonances appear as contours in our 2D design space. In Fig. 3.11(a) the results are plotted for $N_\Omega = 24$ frequencies considered inside the spectral comb of $\Omega = \omega_\mathrm{m}/2$, while in Fig. 3.11(b) they are plotted for $N_\Omega = 2$ only, i.e., for $\omega = \pm\omega_\mathrm{m}/2$. Importantly, note that the two figures have very good agreement for small modulation strength $M < 0.3$. This indicates that parametric Mie resonances are mainly an effect of direct first-order coupling between the two frequencies $\omega = \pm\omega_\mathrm{m}/2$ via the external temporal modulation. However, for larger modulation strengths there appears to be efficient secondary spectral coupling to higher frequencies as well, and the multipolar parametric resonances become polychromatic. As a result, we get more

pronounced deviations between Fig. 3.11(a) and Fig. 3.11(b) in this regime.

Having identified the regimes where we can drive the scatterer to a lasing state by means of parametric oscillations, we will now attempt to additionally engineer the radiation pattern of the lasing state. We are able to do this since the multipolar contours with the conditions of the parametric Mie resonances intersect each other, and, therefore, we have cases of particular modulation strengths and sphere radiuses that simultaneously correspond to parametric oscillations of two different types of multipoles. Increasing the dimensionality of design space, e.g., by considering a multilayer spherical scatterer, potentially would enable us to design special cases where more than two parametric Mie resonances of different type overlap. Different multipoles have different radiation patterns, and, therefore, their superposition with appropriately selected amplitudes and phases can lead to the engineering of the emitted radiation pattern. We can get the far-field radiation pattern of the scatterer upon some excitation simply by taking the far-field approximation of the radiating VSHs. For this we make use of the following large argument approximation of the generalized Hankel functions of the first kind: $z^{(3)}_{\alpha,\nu}(x) \xrightarrow{x>>1} \frac{e^{\mathrm{i}x}}{x}(-\mathrm{i})^{\nu+\delta_{\alpha\mathrm{M}}}$. This property, together with Eqs. (3.25,2.140,2.141), readily gives:

$$\left[\mathbf{E}^{\mathrm{sca}}(\mathbf{r},\omega)\right]_{\mathrm{r}\to\infty} = \frac{e^{\mathrm{i}k_0\mathrm{r}}}{k_0\mathrm{r}}\sum_{\nu\mu_z,\alpha}\mathcal{A}^{\mathrm{sca}}_{\alpha,\mu_z\nu}(\omega)(-\mathrm{i})^{\nu}\mathbf{f}_{\alpha,\mu_z\nu}(\hat{\mathbf{r}}). \tag{3.66}$$

Let us now focus on engineering two particular extraordinary cases of radiation patterns: the well-known cases of the first and second Kerker conditions [271]. The first Kerker condition implies a vanishing back-scattering, whereas the second Kerker condition implies a vanishing forward-scattering in the radiation pattern. While commonly framed for dipolar emitters, we can generalize the Kerker conditions for arbitrary multipolar order [272]. For this, we need to apply the following two properties:

$$\gamma_{\mu_z\nu}\tau^{(\iota)}_{\mu_z\nu}(0) = \frac{\gamma_{-1\nu}}{2}\left[(-1)^{\iota}\delta_{\mu_z,-1}-\delta_{\mu_z,1}\right], \tag{3.67}$$

$$\gamma_{\mu_z\nu}\tau^{(\iota)}_{\mu\nu}(\pi) = (-1)^{\nu+\iota}\frac{\gamma_{-1\nu}}{2}\left[(-1)^{\iota}\delta_{\mu_z,-1}-\delta_{\mu_z,1}\right], \tag{3.68}$$

on Eq. (3.66) to get:

$$\begin{aligned}\left[\mathbf{E}^{\mathrm{sca}}(\mathbf{r},\omega)\right]_{\mathrm{r}\to\infty,\theta=0,\phi=0} &= \hat{\theta}\frac{e^{\mathrm{i}k_0\mathrm{r}}}{k_0\mathrm{r}}\sum_{\nu,\alpha}(-\mathrm{i})^{\nu}\frac{\gamma_{-1\nu}}{2}\left[(-1)^{\delta_{\alpha\mathrm{M}}}\mathcal{A}^{\mathrm{sca}}_{\alpha,-1\nu}(\omega)-\mathcal{A}^{\mathrm{sca}}_{\alpha,1\nu}(\omega)\right]\\ &+ \mathrm{i}\hat{\phi}\frac{e^{\mathrm{i}k_0\mathrm{r}}}{k_0\mathrm{r}}\sum_{\nu,\alpha}(-\mathrm{i})^{\nu}\frac{\gamma_{-1\nu}}{2}\left[(-1)^{\delta_{\alpha\mathrm{N}}}\mathcal{A}^{\mathrm{sca}}_{\alpha,-1\nu}(\omega)-\mathcal{A}^{\mathrm{sca}}_{\alpha,1\nu}(\omega)\right], \end{aligned}\tag{3.69}$$

$$\begin{aligned}\left[\mathbf{E}^{\mathrm{sca}}(\mathbf{r},\omega)\right]_{\mathrm{r}\to\infty,\theta=\pi,\phi=0} &= \hat{\theta}\frac{e^{\mathrm{i}k_0\mathrm{r}}}{k_0\mathrm{r}}\sum_{\nu,\alpha}\mathrm{i}^{\nu}\frac{\gamma_{-1\nu}}{2}\left[\mathcal{A}^{\mathrm{sca}}_{\alpha,-1\nu}(\omega)-(-1)^{\delta_{\alpha\mathrm{M}}}\mathcal{A}^{\mathrm{sca}}_{\alpha,1\nu}(\omega)\right]\\ &+ \mathrm{i}\hat{\phi}\frac{e^{\mathrm{i}k_0\mathrm{r}}}{k_0\mathrm{r}}\sum_{\nu,\alpha}\mathrm{i}^{\nu}\frac{\gamma_{-1\nu}}{2}\left[\mathcal{A}^{\mathrm{sca}}_{\alpha,-1\nu}(\omega)-(-1)^{\delta_{\alpha\mathrm{N}}}\mathcal{A}^{\mathrm{sca}}_{\alpha,1\nu}(\omega)\right]. \end{aligned}\tag{3.70}$$

The first generalized Kerker conditions for zero back-scattering read as follows:

$$\sum_{\nu,\alpha}\mathrm{i}^{\nu}\sqrt{2\nu+1}(-1)^{\delta_{\alpha\mathrm{M}}}\mathcal{A}^{\mathrm{sca}}_{\alpha,1\nu}(\omega) = \sum_{\nu,\alpha}\mathrm{i}^{\nu}\sqrt{2\nu+1}\mathcal{A}^{\mathrm{sca}}_{\alpha,-1\nu}(\omega) = 0, \tag{3.71}$$

whereas the second generalized Kerker conditions for zero forward-scattering are given by the following formula:

$$\sum_{\nu,\alpha}(-\mathrm{i})^{\nu}\sqrt{2\nu+1}(-1)^{\delta_{\alpha\mathrm{M}}}\mathcal{A}^{\mathrm{sca}}_{\alpha,-1\nu}(\omega) \;=\; \sum_{\nu,\alpha}(-\mathrm{i})^{\nu}\sqrt{2\nu+1}\mathcal{A}^{\mathrm{sca}}_{\alpha,1\nu}(\omega) \;=\; 0, \quad (3.72)$$

Next, we identify two cases: case A and case B (see Fig. 3.11). While in case A we have overlapping parametric Mie resonances of electric dipole and magnetic dipole type, in case B we have overlapping parametric Mie resonances of electric quadrupole and magnetic octupole type. As we mentioned in Section 2.6, VSHs of well-defined parity are eigenstates of the parity operator. Specifically, we have $\hat{\Pi}\,|\alpha\,\mu_z\,\nu\,k\rangle^{(\iota)} = (-1)^{\nu+\delta_{\alpha\mathrm{M}}}\,|\alpha\,\mu_z\,\nu\,k\rangle^{(\iota)}$, with $\hat{\Pi}$ being the parity transformation operator [A4]. This implies that at the vicinity of case A we are able to search for a first Kerker condition of zero back-scattering, while at the vicinity of case B we are able to search simultaneously for both first and second Kerker conditions. Since the two parametric Mie resonances of case B are of the same parity, by proper engineering of the relevant multipolar amplitudes and phases so that we satisfy the generalized Kerker conditions of Eqs. (3.71,3.72), we can make both forward- and back-scattering vanish. Note that a zero forward-scattering, i.e., the second Kerker condition, contradicts the optical theorem for passive scatterers, but such a contradiction does not exist for non-stationary scatterers.

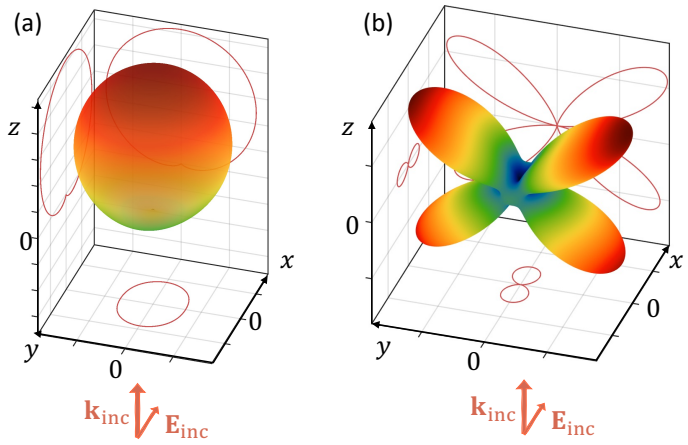

Figure 3.12: Engineering the radiation pattern of parametrically amplified emissions from time-modulated spherical scatterers exhibiting parametric Mie resonances: (a) Case A: emission with generalized first Kerker conditions satisfied. (b) Case B: emission with generalized both first and second Kerker conditions satisfied. The figure was plotted by Dr. Viktar Asadchy. Adapted with permission from Ref. [A3] © American Physical Society.

In fact, we assume an excitation of an x-polarized plane wave propagating along +z, and we search at the vicinity of points A and B, where the parametric amplification shall still be large, but finite, once we move away from the contours hosting the parametric Mie resonances, where the T-matrices of the scatterers become singular. By fine adjustments to the parameters of the model, we are able to locate an approximate first Kerker condition satisfying approximately Eq. (3.71) at the vicinity of point A around $M = 0.68$, $R\omega_{\mathrm{m}}/2c_0 = 1.048$ and exciting at a frequency of $\omega_{\mathrm{inc}} = 0.498\omega_{\mathrm{m}}$. The radiation pattern of this case is illustrated in Fig. 3.12(a) and, indeed, exhibits nearly zero back-scattering. Moreover, similarly, by fine tuning of the parameters of the model, we are able to locate a case at the vicinity of point B where we have simultaneously the approximate satisfaction of both first and second Kerker conditions of Eqs. (3.71,3.72). This happens around

$M = 0.093$, $R\omega_m/2c_0 = 1.481$ and exciting at a frequency of $\omega_{inc} = 0.4995\omega_m$. The radiation pattern of this case is illustrated in Fig. 3.12(b) and, indeed, exhibits nearly zero back- and forward scattering.

Note that in both cases A and B we are rather close to the conditions of parametric Mie resonances where absorbed power approaches the limit of minus infinity. Yet, both cases A and B exhibit rather high negative absorption because of strong parametric amplification. Specifically, for case A we have a ratio of absorption to geometric cross section around -2627.5 and a ratio of scattering to geometric cross section around 2629.2 (note that their ratio approaches the value of minus one, as we discussed previously). This is a rather strongly amplified emission if one takes into consideration that the ratio of scattering to geometric cross section for the same unmodulated sphere is just 5.5. Similarly, for case B we have a ratio of absorption to geometric cross section of -857.5 and a ratio of scattering to geometric cross section of 858.3, with its equivalent for the unmodulated case being just 2.53.

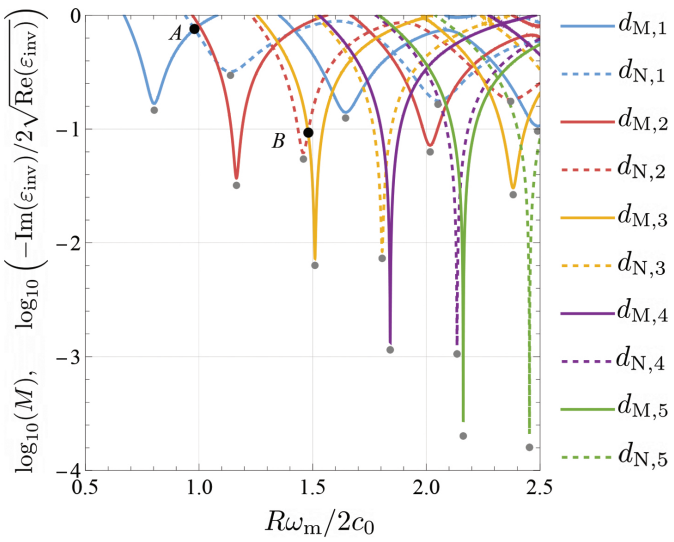

Figure 3.13: Parametric Mie resonances in time-modulated spherical scatterers VS Mie resonances in time-invariant spherical scatterers made of a gainy medium (grey dots). Adapted with permission from Ref. [A3] © American Physical Society.

Finally, let us compare the case of parametric Mie resonances with the case of Mie resonances that occur in time-invariant spherical scatterers made of a gainy medium that is modelled with a complex dielectric permittivity ε_{inv} with $\Im\{\varepsilon_{inv}\} < 0$. In Fig. 3.13 we do this comparison for the same system that we have been studying the parametric Mie resonances before. The plot in Fig. 3.13 considers also $N_\Omega = 2$ number of frequencies for the calculations and is identical to that of Fig. 3.11(b) but it is plotted in logarithmic scale or modulation strengths and for multipoles up to the fifth order. With gray dots we plot the conditions for Mie resonances in time-invariant spherical scatterers with gain. For a fair comparison we choose $\Re\{\varepsilon_{inv}\} = 14.07$ to be equal to the real part of the permittivity of the unmodulated scatterer at $\omega = \omega_m/2$.

Interestingly, we observe that the gray dots appear near the local minima of the curves of the respective curves of parametric Mie resonances. However, note that, while the x-position of the grey dots is indeed related with those corresponding minima of the curves, since it has to do with the real part of the eigenfrequencies of the quasinormal modes of the unperturbed sphere, the y-positions of the grey dots and the minima of the curves does not necessarily coincide. We were able to get varying relative positions in the y-

direction for different values of $\Re\{\varepsilon_{\text{inv}}\}$ (see the supplementary material of Ref. [A3]). However, there shall be an indirect connection between the two, since either an increase of the imaginary part of the permittivity of the sphere, or an increase of the strength of the modulation of the sphere, both constitute different means of providing gain to the system that compensates for the radiative losses of the unperturbed sphere. As a result, the complex eigenfrequencies of the quasinormal modes of the spherical scatterers move in the complex frequency plane and eventually cross the real frequency axis, if enough gain is provided. While monitoring the motion of the eigenfrequencies of the stationary scattering system for an increasing imaginary part of the permittivity is trivial (see Eqs. (30, 31) in Ref. [228]), that is not the case for the time-modulated sphere, where an eigenmode analysis is required to monitor the motion of the poles of the scattering system in the complex frequency plane as we increase the modulation strength. The curves that we plot in Fig. 3.13 essentially give the parameters for which the complex eigenfrequencies of the modulated spherical scatterers cross the real frequency axis. Note that, after this point, increasing further the level of gain in the system shall push the eigenfrequencies in the upper half of the complex frequency plane. Importantly, this renders the scattering system unstable. Note that, even though we require stability for the response of the bulk time-modulated medium, the spherical scattering system can still become unstable [273]. Special care needs to be taken then, since the Fourier transform that we employ in the first place for our analysis is not defined in the unstable regime.

Finally, note that the striking difference to be observed, though, is that the parametric Mie resonances of the time-modulated scatterers appear in curves in the design space, whereas the ordinary lasing Mie resonances for stationary, gainy spheres appear in isolated points in the design space. This makes it way more difficult in practice to engineer the radiation pattern of the lasing emissions in the second case: engineering the overlap of points is indeed more challenging than engineering the crossing of contours.

Before closing this section, we would like to highlight one last point: Notice how in Fig. 3.13 it appears possible to get parametric Mie resonances with fairly low modulation strengths even for spheres as small as the one that we studied. For example, note that we get a parametric Mie resonance of magnetic type and multipolar order $\nu = 5$ for modulation strengths as low as $M = 2.27\times10^{-4}$ and for $R\omega_{\text{m}}/2c_0$ just below 2.5. This is a rather significant finding, since one would expect that such optically small spheres would only exhibit resonances of a low quality factor and would therefore require rather large modulation strengths to compensate for their large radiation losses and drive the scatterer into a regime of parametric oscillations. Large modulation strengths are hard to achieve, since they typically require high intensities of the pump that modulates the medium, which can actually cause damage and "burn" the scatterer. We would like to note that in our study here we considered the simplified case of vanishing material losses. We expect that a further increase of the modulation strength shall be generally required to compensate for the additional material losses and drive a lossy spherical scatterer into a regime of parametric oscillations.

3.6 Reciprocity breaking in time-varying scatterers: a T-matrix analysis

In this section, we will discuss how the symmetries of reciprocity reflect upon the T-matrix of periodically modulated scatterers. We will do this for all three cases of generalized reciprocity described in Section 2.5: reciprocity in terms of exchanges of energy, reciprocity in terms of exchanges in number of true photons, and reciprocity in terms of exchanges in number of pseudo-photons.

In the context of the T-matrices of the scatterers, there are no external sources assumed

to be present. Instead, in our physical picture, we have an incident and scattered field in the homogeneous, isotropic space surrounding the scatterer, and we need to find relations between those fields belonging to two different scattering processes A, B when the scatterer is reciprocal. Since we assume that the scatterer is a PTC with discrete translation symmetry in time, we introduce the Floquet frequency Ω, and we break the full spectrum into spectral combs, each characterized by a specific Ω. Since there is no spectral coupling among the different spectral combs, we can work with each one individually. The total field outside the scatterer is the superposition of the incident and scattered fields, which we decompose into a series of VSHs:

$$\begin{aligned}\mathbf{E}(\mathbf{r},\omega) &= \int_{0^+}^{\omega_{\mathrm{m}}^-}\sum_{j=1}^{N_\Omega}\mathbf{E}_j(\mathbf{r},\Omega)\mathrm{d}\Omega, \qquad \text{with :}\\ \mathbf{E}_j(\mathbf{r},\Omega) &= \sum_{\nu\mu_z,\alpha}\mathcal{A}^{\mathrm{inc}}_{\alpha,\mu_z\nu}(\Omega_j)\mathbf{F}^{(1)}_{\alpha,\mu_z\nu}(\mathbf{r};k_j)+\mathcal{A}^{\mathrm{sca}}_{\alpha,\mu_z\nu}\mathbf{F}^{(3)}_{\alpha,\mu_z\nu}(\mathbf{r};k_j),\end{aligned} \tag{3.73}$$

where $k_j = n_j\Omega_j/c_0$ is the wavenumber of the outer space surrounding the scatterer at frequency $\omega = \Omega_j$ and with refractive index n_j. The corresponding magnetic field is given by:

$$\mathbf{H}_j(\mathbf{r},\Omega) = \frac{1}{\mathrm{i}Z_j}\sum_{\nu\mu_z,\alpha}\mathcal{A}^{\mathrm{inc}}_{\beta,\mu_z\nu}(\Omega_j)\mathbf{F}^{(1)}_{\alpha,\mu_z\nu}(k_j;\mathbf{r})+\mathcal{A}^{\mathrm{sca}}_{\beta,\mu_z\nu}\mathbf{F}^{(3)}_{\alpha,\mu_z\nu}(k_j;\mathbf{r}), \tag{3.74}$$

with $\beta \neq \alpha$ and Z_j being the wave-impedance of the surrounding medium at $\omega = \Omega_j$.

For a reciprocal scatterer in terms of exchanges of energies, we have that $\boldsymbol{\mathcal{R}}(\mathbf{r},\mathbf{r}',\omega,\omega') = \mathbf{0}$. The reciprocity theorem of Eq. (2.94) applied for a spherical surface S_R of radius R enclosing the scatterer and for an absence of external sources, then reads as:

$$\sum_j \oiint_{S_R}\hat{\mathbf{n}}\cdot\left[\mathbf{E}^{\mathrm{A}}_j(\mathbf{r},\Omega)\times\mathbf{H}^{\mathrm{B}}_j(\mathbf{r},\Omega)-\mathbf{E}^{\mathrm{B}}_j(\mathbf{r},\Omega)\times\mathbf{H}^{\mathrm{A}}_j(\mathbf{r},\Omega)\right]e^{-2\mathrm{i}\Omega_j\tau}\mathrm{d}^2\mathbf{r} = 0. \tag{3.75}$$

Substituting Eqs. (3.73 and 3.74) in the above equation, and applying the orthogonality property of Eq. (3.29), as well as the following property of the generalized spherical Bessel functions:

$$z^{(1)}_{\alpha,\nu}(x)z^{(3)}_{\beta,\nu}(x)-z^{(1)}_{\beta,\nu}(x)z^{(3)}_{\alpha,\nu}(x) = \frac{\mathrm{i}(-1)^{\delta_{\alpha\mathrm{N}}}}{x^2}, \tag{3.76}$$

we readilly get the following equation of reciprocity in terms of relations of the complex spherical amplitudes of the fields:

$$c_0^2\sum_{\nu\mu_z,\alpha}(-1)^{\mu_z}\sum_j\frac{e^{-2\mathrm{i}\Omega_j\tau}}{\Omega_j^2n_j^2Z_j}\left[\mathcal{A}^{\mathrm{inc},B}_{\alpha,\mu_z\nu}(\Omega_j)\mathcal{A}^{\mathrm{sca},A}_{\alpha,-\mu_z\nu}(\Omega_j)-\mathcal{A}^{\mathrm{inc},A}_{\alpha,\mu_z\nu}(\Omega_j)\mathcal{A}^{\mathrm{sca},B}_{\alpha,-\mu_z\nu}(\Omega_j)\right] = 0. \tag{3.77}$$

Finally, assuming monochromatic single multipole excitations in the above equation, we can retrieve the following symmetry for the T-matrix of a periodically modulated scatterer that is reciprocal in terms of exchanges of energies (expressed in Dirac notation):

$$\langle \alpha' \, \mu_z' \, \nu' \, \Omega_{j'} | \, \hat{\mathbf{T}}_{\boldsymbol{\mathcal{R}}=\mathbf{0}}(\Omega) \, | \alpha \, \mu_z \, \nu \, \Omega_j \rangle = (-1)^{\mu_z+\mu_z'} e^{2\mathrm{i}(\Omega_{j'}-\Omega_j)\tau} \frac{\Omega_{j'}^2 n_{j'}^2 Z_{j'}}{\Omega_j^2 n_j^2 Z_j} \times \langle \alpha \; -\mu_z \, \nu \, \Omega_j | \, \hat{\mathbf{T}}_{\boldsymbol{\mathcal{R}}=\mathbf{0}}(\Omega) \, | \alpha' \; -\mu_z' \, \nu' \, \Omega_{j'} \rangle \, . \quad (3.78)$$

Similarly, we can get the following symmetry for the T-matrix of a periodically modulated scatterer that is reciprocal in terms of exchanges of number of true photons ($\boldsymbol{\mathcal{R}}'(\mathbf{r}, \mathbf{r}', \omega, \omega') = \mathbf{0}$). By applying all the above on Eq. (2.105) instead of Eq. (2.94):

$$\langle \alpha' \, \mu_z' \, \nu' \, \Omega_{j'} | \, \hat{\mathbf{T}}_{\boldsymbol{\mathcal{R}}'=\mathbf{0}}(\Omega) \, | \alpha \, \mu_z \, \nu \, \Omega_j \rangle = (-1)^{\mu_z+\mu_z'} e^{2\mathrm{i}(\Omega_{j'}-\Omega_j)\tau} \frac{|\Omega_{j'}|^3 n_{j'}^2 Z_{j'}}{|\Omega_j|^3 n_j^2 Z_j} \times \langle \alpha \; -\mu_z \, \nu \, \Omega_j | \, \hat{\mathbf{T}}_{\boldsymbol{\mathcal{R}}'=\mathbf{0}}(\Omega) \, | \alpha' \; -\mu_z' \, \nu' \, \Omega_{j'} \rangle \, . \quad (3.79)$$

Furthermore, we can similarly get the following symmetry for the T-matrix of a periodically modulated scatterer that is reciprocal in terms of exchanges of number of pseudo-photons ($\boldsymbol{\mathcal{R}}''(\mathbf{r}, \mathbf{r}', \omega, \omega') = \mathbf{0}$), by applying all the above on Eq. (2.113) instead of Eq. (2.94):

$$\langle \alpha' \, \mu_z' \, \nu' \, \Omega_{j'} | \, \hat{\mathbf{T}}_{\boldsymbol{\mathcal{R}}''=\mathbf{0}}(\Omega) \, | \alpha \, \mu_z \, \nu \, \Omega_j \rangle = (-1)^{\mu_z+\mu_z'} e^{2\mathrm{i}(\Omega_{j'}-\Omega_j)\tau} \frac{\Omega_{j'}^3 n_{j'}^2 Z_{j'}}{\Omega_j^3 n_j^2 Z_j} \times \langle \alpha \; -\mu_z \, \nu \, \Omega_j | \, \hat{\mathbf{T}}_{\boldsymbol{\mathcal{R}}''=\mathbf{0}}(\Omega) \, | \alpha' \; -\mu_z' \, \nu' \, \Omega_{j'} \rangle \, . \quad (3.80)$$

Note that all those generalized reciprocity symmetries of the T-matrices of arbitrary scatterers modulated periodically in time, collapse to the well-known reciprocity condition for stationary scatterers (see Eq. (5.34) in Ref. [257]).

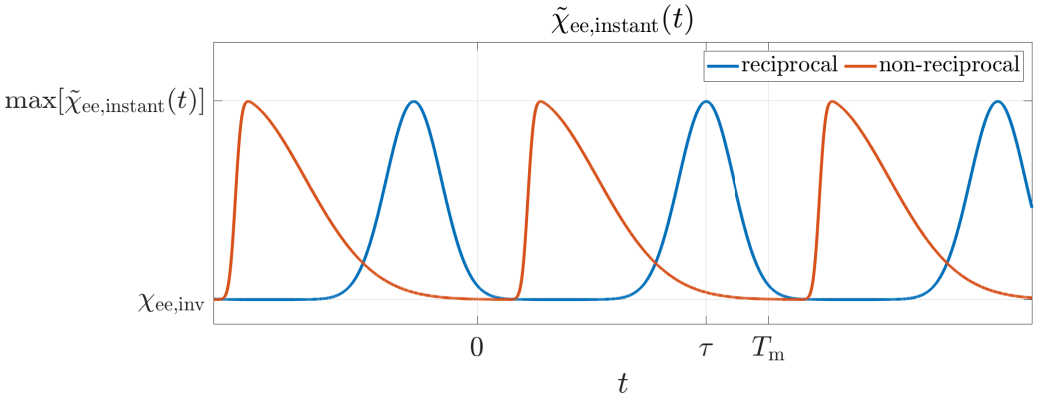

Figure 3.14: The susceptibilities of two periodically modulated, non-dispersive media with instantaneous response. The one, possessing a time reversal symmetry with respect to $t = \tau$ is reciprocal with respect to exchanges of pseudo-photons, whereas the other is non-reciprocal.

Remember, as we discussed in Section 2.5, that we were not able to identify realistic non-stationary material parameters that can satisfy the two first reciprocity conditions. However, we were able to identify a class of non-stationary material parameters that can satisfy reciprocity in terms of exchanges of pseudo-photons. The susceptibility tensors of

such reciprocal, non-stationary media shall have the symmetry properties of Eqs. (2.119-2.121). Those reciprocal time-varying media should be non-dispersive, i.e., characterized by a instantaneous response, and should also possess a time-reversal symmetry of their susceptibility with respect to a moment in time $t = \tau$. In Fig. 3.14, we illustrate an example of such reciprocal medium and a counterexample of a non-reciprocal medium that lacks such time-reversal symmetry. Let us note once again that reciprocity in terms of exchanges in number of pseudo-photons is equivalent to the reciprocity in terms of exchanges in number of true photons, only when there is no spectral coupling between frequencies of opposite sign. The parametric oscillations in time-modulated scatterers studied in the previous section is a typical example of such spectral coupling between frequencies of opposite sign.

Furthermore, note that due to the ratios of frequencies that appear in the relations above (Eqs. (3.78-3.80)), it is predicted that the spectral transitions from a lower to a larger frequency in a reciprocal time-varying scatterer shall generally be stronger than the spectral transition from a large to a smaller frequency. This is certainly not the case for the T-matrix illustrated in Fig. 3.4, since the considered scatterer there breaks reciprocity. Note that those ratios of frequencies in our relations essentially arise from the fact that our input and output states of the constructed T-matrix are not normalized in terms of energy, or number of true photons or number of pseudo-photons.

Time-varying scatterers that break such generalized reciprocity conditions can be used as optical components that, e.g., implement in the spectral dimension the functions of isolators and circulators, which are characterized by T-matrices -reduced in the spectral dimension and normalized either with respect to energy or number of true- or pseudo-photons- like the ones below [201]:

$$\hat{\mathbf{T}}_{\text{isolator}} = \begin{bmatrix} 0 & 0 \\ 1 & 0 \end{bmatrix}, \qquad \hat{\mathbf{T}}_{\text{circulator}} = \begin{bmatrix} 0 & 0 & 1 \\ 1 & 0 & 0 \\ 0 & 1 & 0 \end{bmatrix}. \tag{3.81}$$

4 — Transcending the problem of the Rayleigh Hypothesis: from the Topological Skeleton method towards the distributed T-matrix

4.1 Introduction

In this chapter, we will study some aspects concerning the region of validity of the representations of the fields employed to construct the T-matrices of scatterers. Conventional representations based on localized multipolar series are known to suffer by the problem of the Rayleigh Hypothesis. Roughly speaking, these representations are unable to represent accurately the near-fields of a non-spherical scatterer. In the second section of this chapter, we elaborate on the theoretical foundations of the problem of the Rayleigh Hypothesis and briefly describe the state-of-the-art in understanding and treating the problem. Next, in the third section of this chapter, we propose a solution to the problem of the Rayleigh Hypothesis, by introducing a novel representation scheme of the fields based on a distribution of multipolar sources across the topological skeleton of the scatterer. We discuss the theoretical and practical aspects of the topological skeleton method, and, furthermore, we present several examples and assess the performance of the method by comparing the near-fields reconstructed semi-analytically with the topological skeleton method against full-wave simulations. We demonstrate how the method is suitable to overcome the problem of the Rayleigh Hypothesis. Next, in the fourth section of this chapter, we construct a distributed T-matrix to represent scatterers of arbitrary geometry, employing the topological-skeleton-based representations of the fields that we developed. We present a four-step method to calculate such a distributed T-matrix by making use of a full-wave solver. Specifically, a prolate spheroid is considered as an example of our introduced technique in this section. Finally, in the last section of this chapter, we develop a generalization of the well-established multiple light scattering theoretical framework to account for the distributed T-matrices and we also provide an illustrative numerical example.

4.2 The problem of the Rayleigh Hypothesis in scattering of electromagnetic waves

In this section, we will introduce the problem of the Rayleigh Hypothesis. It is a fundamental problem pertinent to the scattering of electromagnetic (and not only) waves. We will briefly review the state-of-the-art treatment of the problem, and we will specifically discuss the central role of the analytic properties of the fields.

Let us begin by considering a surface S that encloses a localized *stationary* scatterer. The scatterer is embedded inside an infinite linear, isotropic, stationary and homogeneous medium. Since we restrict ourselves to the stationary case, the scattering problem can be solved for each frequency individually. We denote in the following with $k(\omega)$ and $Z(\omega)$ the

(generally frequency-dependent) wavenumber and wave-impedance that characterize the embedding medium, respectively. The treatment of a generic scattering problem requires the representation of the incident fields everywhere inside S and the representation of the scattered fields everywhere outside S. Such representations allow to construct the T-matrix of the scatterer. The T-matrix treats the scatterer as a "black box" that responds to an external excitation, and the T-matrix can be considered in the multi-scattering formalism discussed in Section 2.9. As discussed in the following, the problem of the Rayleigh Hypothesis is related with the region of validity of analytic representations of those fields: the problem arises when that region of validity does not fully coincide with the "physical domain" of the fields, i.e., either everywhere inside (for the incident field) or everywhere outside (for the scattered field) of S.

We can start the technical discussion by employing a Stratton-Chu-type integral representation of the incident and scattered fields that is valid everywhere inside their respective physical domains [206, 257, 274]. To derive them, we use at first the following property of vector fields, known as the Green's vector identity:

$$\mathbf{P}\cdot(\nabla\times\nabla\times\mathbf{Q})-\mathbf{Q}\cdot(\nabla\times\nabla\times\mathbf{P}) \;=\; \nabla\cdot\left[\mathbf{Q}\times(\nabla\times\mathbf{P})-\mathbf{P}\times(\nabla\times\mathbf{Q})\right], \quad (4.1)$$

where $\mathbf{P}$ and $\mathbf{Q}$ are some vector fields. Applying that identity to some electric field $\mathbf{E}(\mathbf{r}_0,\omega)$ and the Dyadic Green's function $\overleftrightarrow{\mathbf{G}}(\mathbf{r},\mathbf{r}_0;k)$ of the infinite background medium, which obey the wave equations of Eqs. (2.156, 2.158), respectively, and integrating over some arbitrary volume V_0 bounded by some surface S_0, and, finally, applying the divergence theorem, gives us the following formula:

$$\begin{aligned}\mathbf{E}(\mathbf{r},\omega)\delta(\mathbf{r}\in V_0) \;=\;& \mathrm{i}\omega\mu\int_{V_0}\overleftrightarrow{\mathbf{G}}(\mathbf{r},\mathbf{r}_0;k)\cdot\mathbf{J}(\mathbf{r}_0,\omega)\mathrm{d}^3\mathbf{r}_0\\ &+\int_{S_0}\overleftrightarrow{\mathbf{G}}(\mathbf{r},\mathbf{r}_0;k)\cdot\left[\hat{\mathbf{n}}'(\mathbf{r}_0)\times\nabla\times\mathbf{E}(\mathbf{r}_0,\omega)\right]\\ &+\nabla\times\overleftrightarrow{\mathbf{G}}(\mathbf{r},\mathbf{r}_0;k)\cdot\left[\hat{\mathbf{n}}'(\mathbf{r}_0)\times\mathbf{E}(\mathbf{r}_0,\omega)\right]\mathrm{d}^2\mathbf{r}_0, \end{aligned} \quad (4.2)$$

where $\delta(\mathbf{r}\in V_0)$ takes the value 1 for $\mathbf{r}\in V_0$ and the value 0 otherwise. $\hat{\mathbf{n}}'(\mathbf{r}_0)$ is the unit vector normal to the surface S_0 that points towards the interior of V_0. Let us now use the above formula to derive expressions for the incident and the scattered fields. Applying it for the space occupied by the scatterer $V_{S^{\mathrm{in}}}$ enclosed by the surface S, and considering that $\mathbf{J}(\mathbf{r}_0,\omega)=0$ inside S, gives us the following expression for the incident field that is valid everywhere inside its physical domain:

$$\begin{aligned}\mathbf{E}^{\mathrm{inc}}(\mathbf{r},\omega)\delta(\mathbf{r}\in V_{S^{\mathrm{in}}}) \;=\;& -\int_{S}\overleftrightarrow{\mathbf{G}}(\mathbf{r},\mathbf{r}_0;k)\cdot\left[\hat{\mathbf{n}}(\mathbf{r}_0)\times\nabla\times\mathbf{E}^{\mathrm{inc}}(\mathbf{r}_0,\omega)\right]\\ &+\nabla\times\overleftrightarrow{\mathbf{G}}(\mathbf{r},\mathbf{r}_0;k)\cdot\left[\hat{\mathbf{n}}(\mathbf{r}_0)\times\mathbf{E}^{\mathrm{inc}}(\mathbf{r}_0,\omega)\right]\mathrm{d}^2\mathbf{r}_0, \end{aligned} \quad (4.3)$$

where here we choose $\hat{\mathbf{n}}(\mathbf{r}_0)$ to point outwards of S. Next, we apply Eq. (4.2) to the total field in the presence of the scatterer in the infinite space surrounding the scatterer, $V_{S^{\mathrm{out}}}$. That domain is bounded by the surface S and the surface bounding a sphere of infinite radius S_∞. Decomposing the total field into the incident and the scattered field, and noting that: 1) the surface integral of the incident field over S for $\mathbf{r}\in V_{S^{\mathrm{out}}}$ vanishes according to

Eq. (4.3), 2) the surface integral of the incident field over S_∞, together with the volumetric integral involving the external current sources inside $V_{S^{\text{out}}}$, gives the incident field there, 3) the surface integral of the scattered field over S_∞ for $\mathbf{r} \in V_{S^{\text{out}}}$ vanishes. It vanished because it holds that:

$$\begin{aligned} \overleftrightarrow{\mathbf{G}}(\mathbf{r},\mathbf{r}_0;k)\cdot[\hat{\mathbf{n}}(\mathbf{r}_0)\times\nabla\times\mathbf{E}^{\text{sca}}(\mathbf{r}_0,\omega)]+\nabla\times\overleftrightarrow{\mathbf{G}}(\mathbf{r},\mathbf{r}_0;k)\cdot[\hat{\mathbf{n}}(\mathbf{r}_0)\times\mathbf{E}^{\text{sca}}(\mathbf{r}_0,\omega)] &= 0. \\ \text{for } r\ll r_0,\ \ \mathbf{r}_0\in S_\infty, & \end{aligned} \tag{4.4}$$

That statement we get from the far-field expressions of the scattered fields (see Eqs.(2.94, 2.95) in [257]), together with the far-field expression of the DGF and its curl (see Eqs. (8.55, 8.57) in [275]). Combining all these aspects, we can express the scattered field as:

$$\begin{aligned} \mathbf{E}^{\text{sca}}(\mathbf{r},\omega)\delta(\mathbf{r}\in V_{S^{\text{out}}}) &= \int_S \overleftrightarrow{\mathbf{G}}(\mathbf{r},\mathbf{r}_0;k)\cdot[\hat{\mathbf{n}}(\mathbf{r}_0)\times\nabla\times\mathbf{E}^{\text{sca}}(\mathbf{r}_0,\omega)] \\ &\quad +\nabla\times\overleftrightarrow{\mathbf{G}}(\mathbf{r},\mathbf{r}_0;k)\cdot[\hat{\mathbf{n}}(\mathbf{r}_0)\times\mathbf{E}^{\text{sca}}(\mathbf{r}_0,\omega)]\,\mathrm{d}^2\mathbf{r}_0. \end{aligned} \tag{4.5}$$

The expression is valid everywhere inside its physical domain. Note that we derive the latter equation by considering the case of a finite three-dimensional scatterer enclosed by S. However, it can be similarly derived for cylindrical-like and planar-like scatterers.

The problem of the Rayleigh Hypothesis arises once we attempt to expand the DGF in the above expression into an analytical series of eigenwaves, either a series of VPHs, or VCHs, or VSHs. In view of Eqs. (2.159-2.161), let us remind that, due to the point singularity at $\mathbf{r}=\mathbf{r}_0$, the expansion of the DGF in terms of such eigenwaves becomes discontinuous across the surface defined by fixing the coordinate that is not associated with the two commuting symmetry operators employed for the expansion of the DGF into a series of eigenwaves to that of the respective coordinate of the position of the point source. See, e.g., Eq. 7.2.63 in Ref. [204], and, also, our discussion in Section 2.6 regarding the relation between the coordinates, the commuting symmetry operator and their eigenvalues. Specifically, the expansions take the following branch forms:

$$\overleftrightarrow{\mathbf{G}}(\mathbf{r},\mathbf{r}_0;k) \equiv \sum_\alpha \iint_{-\infty}^{+\infty} \mathrm{d}k_x\mathrm{d}k_y \begin{cases} \overleftrightarrow{\mathbf{G}}^{-}_\alpha(\mathbf{r},\mathbf{r}_0;k_x,k_y,k), & \text{for } z<z_0, \\ \overleftrightarrow{\mathbf{G}}^{+}_\alpha(\mathbf{r},\mathbf{r}_0;k_x,k_y,k), & \text{for } z>z_0, \end{cases} \tag{4.6}$$

$$\overleftrightarrow{\mathbf{G}}(\mathbf{r},\mathbf{r}_0;k) \equiv \sum_{\mu_z,\alpha} \int_{-\infty}^{+\infty} \mathrm{d}k_z \begin{cases} \overleftrightarrow{\mathbf{G}}^{-}_{\alpha,\mu_z}(\mathbf{r},\mathbf{r}_0;k_z,k), & \text{for } \rho<\rho_0, \\ \overleftrightarrow{\mathbf{G}}^{+}_{\alpha,\mu_z}(\mathbf{r},\mathbf{r}_0;k_z,k), & \text{for } \rho>\rho_0, \end{cases} \tag{4.7}$$

$$\overleftrightarrow{\mathbf{G}}(\mathbf{r},\mathbf{r}_0;k) \equiv \sum_{\nu\mu_z,\alpha} \begin{cases} \overleftrightarrow{\mathbf{G}}^{-}_{\alpha,\mu_z\nu}(\mathbf{r},\mathbf{r}_0;k), & \text{for } r<r_0, \\ \overleftrightarrow{\mathbf{G}}^{+}_{\alpha,\mu_z\nu}(\mathbf{r},\mathbf{r}_0;k), & \text{for } r>r_0, \end{cases} \tag{4.8}$$

for the case of an expansion into a series of VPHs, VCHs, and VSHs, respectively. The full expressions are given in Eqs. (2.159-2.161). We can observe the planar, cylindrical and spherical surfaces of discontinuity of the DGF that pass through the point of singularity in the three cases above. As a result of the above, it becomes obvious that, selecting a particular branch of the above expansions of the DGF into the eigenwaves of the homogeneous background medium, shall generally compromise the region of validity of the resulting representations of the scattered field, generally restricting access to a part of its physical domain.

Specifically, let us assume that the surface S of our scatterer is bounded by the two planes $z = \min\{z_0\}$, $z = \max\{z_0\}$, or by the cylindrical surface $\rho = \max\{\rho_0\}$, or by the spherical surface $r = \max\{r_0\}$. Then, in view of Eqs. (4.5-4.8), and as long as we pick a single branch of the above expansions of the DGF, we can observe that: 1) a representation of the scattered field in plane waves guarantees access to the fields in the regions $z > \max\{z_0\}$ (or $z < \min\{z_0\}$), 2) a representation of the scattered field in cylindrical waves guarantees access to the fields in the region $\rho > \max\{\rho_0\}$ (i.e., outside the infinite cylinder that circumscribes the scatterer), 3) a representation of the scattered field in spherical waves guarantees access to the fields in the region r $> \max\{r_0\}$ (i.e., outside the sphere that circumscribes the scatterer). Therefore, these representations are only valid inside a part $\tilde{V}_{S^{\text{out}}}$ of the physical domain $V_{S^{\text{out}}}$. The remaining part of the physical domain, $V_{S^{\text{out}}} \backslash \tilde{V}_{S^{\text{out}}}$, corresponds to a "restricted space". In that space, the validity of our representation of the scattered field is not guaranteed. Consequently, note that a representation of the scattered field in plane/cylindrical/spherical waves constitutes a natural choice for planar/cylindrical/spherical-like scatterers, respectively, in the sense that it allows for a valid representation of the scattered fields in the largest part of their physical domain.

Importantly, let us now highlight that the analytic properties of the scattered fields have been at the core of the discussion around the problem of the Rayleigh Hypothesis. First of all, we should note that, actually, a series representation of the scattered field in the eigenwaves that we just described, generally, provides access to some small part of that "restricted volume" $V_{S^{\text{out}}} \backslash \tilde{V}_{S^{\text{out}}}$. That is to say that the above-mentioned boundaries of the regions of validity of the discussed representations are generally not the "hard boundaries". In fact, it has been mathematically shown that the position of the "hard boundaries" is related to the analytic properties of the scattered field [138].

First of all, Kyurkchan *et al.* note in [137, 138] the following:

- The scattered field, being a solution to the Helmholtz equation, hence a ramifying analytic function, has a unique analytic continuation inside the non-physical domain up to a convex envelope inside S containing the singularities of the analytic continuation.
- Singularities of the analytic continuation of the scattered field inside S always exist since the scattered field is an analytic function that vanishes at infinity according to the radiation condition.
- The positions of the singularities inside S depends on the geometry of the surface S and on the position of potential singularities of the excitation source, which appear as image-singularities of the analytic continuation of the scattered field inside the scatterer. Note that such image-singularities may appear from the presence of singularities inside neighboring scatterers as well. This can render the task of locating the presence of singularities rather cumbersome and, most importantly, dependent on the actual scattering scenario in which the individual scatterer gets involved.

Furthermore, Kyurkchan *et al.* highlight the following two points regarding the Rayleigh Hypothesis under the prism of the analytic continuation properties of the scattered fields [137, 138].

The first point is that a series representation of the scattered field in plane waves converges only in the region $z > \max\{z_{\text{s}}\}$ (or $z < \min\{z_{\text{s}}\}$), where z_{s} refers to the z-coordinate of the singularities of the analytic continuation of the scattered fields inside S. Similarly, a series representation of the scattered field in terms of cylindrical waves converges only in the region $\rho > \max\{\rho_{\text{s}}\}$, where ρ_{s} refers to the ρ-coordinate of the singularities of the analytic continuation of the scattered fields inside S. Moreover, a

series representation of the scattered field in terms of spherical waves converges only in the region $r > \max\{r_s\}$, where r_s refers to the r-coordinate of the singularities of the analytic continuation of the scattered fields inside S. The above generally constitute less severe restrictions concerning the regions of validity of the fields compared to the ones that we had initially, since, for a smooth surface S, we have that $\max\{z_s\} < \max\{z_0\}$ (and $\min\{z_s\} > \min\{z_0\}$), $\max\{\rho_s\} < \max\{\rho_0\}$, and $\max\{r_s\} < \max\{r_0\}$.

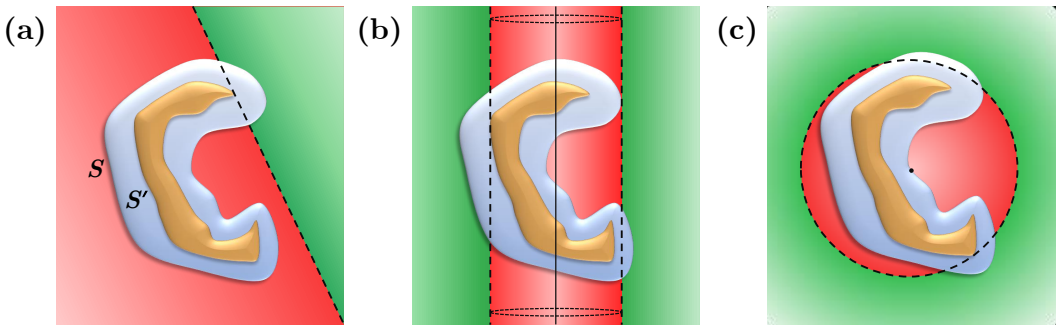

Figure 4.1: The regions of validity of analytical representations of the scattered fields of a scatterer bounded by surface S (denoted with gray color) in terms of series of a) plane waves, b) cylindrical waves, and c) spherical waves. With green color, we denote the part of the physical domain where the representation is valid, whereas with red color we denote the part of it where it is not. Surface S' encloses all the singularities of the analytical continuation of the scattered fields that are located inside the scatterer (denoted with brown color). Adapted from Ref. [A5].

This first highlighted point sheds light on the case of the Rayleigh Hypothesis that plagues representations of the scattered field based on a series of plane waves or a series of localized cylindrical/spherical waves (with fixed origin). One of the first treatments of the original Rayleigh Hypothesis issue actually showed -by making use of conformal transformations to study the analytic continuation properties of the fields- that the diffracted field by a sinusoidal grating with profile $y = b\cos(kx)$, can be represented everywhere in the physical domain -even inside the area of the corrugations- as a series of plane waves, only under the condition of $kb < 0.448$. This condition assures that all the singularities of the analytic continuation of the fields are located below the plane $y = -b$ [116, 133, 138].

Moreover, it has been recently numerically demonstrated that, for spheroids, an expansion of the scattered field in terms of a series of spherical waves emanating from the origin of the scatterer is valid only outside the sphere circumscribing the two foci of the spheroid, instead of the whole spheroid [130, 131]. This can be theoretically explained from the fact that the foci of the ellipse coincide with the singularities of the analytic continuation of the fields inside such a scatterer [137, 138]. The latter numerical simulations revealed another significant aspect of the presence of singularities: in the region where such series representations of the scattered fields fail to represent the fields with validity, they usually fail blatantly. The errors inside this "restricted volume" typically become orders of magnitude larger than the actual fields because, there, the series of the representation diverges due to the presence of the singularities [130, 131].

In Fig. 4.1, we illustrate the regions of validity of such series representations of the scattered field for the three cases of VPHs, VCHs and VSHs. It is important to note that the regions of validity of such representations of the fields are directly related with the coordinate systems with respect to which we expand the DGF into eigenwaves. Expansions into eigenwaves with respect to rotated/translated coordinate systems generally modify the region of validity of the representations. Along this line, there have been sev-

eral recent attempts to circumvent the problem of the Rayleigh Hypothesis by alternative roundabout ways that involve an interplay of different representations of the scattered fields, i.e., employing expansions into eigenwaves with respect to appropriately translated/rotated coordinate systems. In [276–278], an interplay between representations in terms of spherical and plane waves has been employed to grant access to the fields inside the circumscribing sphere of the scatterers. In that case, modeling their coupling to planar interfaces or neighboring scatterers in close proximity became feasible. That work demonstrated that a plane wave representation of the scattered fields could unlock access to an arbitrarily oriented half-space tangential to the scatterer. Furthermore, an interplay between representations of the scattered field in spherical waves with displaced origins was employed in Ref. [279]. That was done to move the spherical boundaries of the regions of validity of the representations arbitrarily. That technique facilitated the solution of the scattering problem of a dimer of disks with high aspect ratios placed at closed proximity.

Note that such approaches involve analytical transformations among the different representations employed to solve the scattering problem, and this, although analytically relatively straightforward, numerically it might be challenging [278]. However, in any case, such approaches to the problem of the Rayleigh Hypothesis avoid dealing with the core of the problem since they maintain problematic representations of the scattered fields that are not valid everywhere needed in the physical domain. Arguably, such an interplay between different field representations to access the fields into different sub-regions of the physical domain $V_{S^{\text{out}}}$, although on the one hand allows for the proper treatment of different parts of the scattering problem, on the other hand increases the complexity of the problem and may lead to unnecessary computational overhead also.

The second highlighted point is that an alternative integral representation of the scattered field in terms of radiation emanating from distributed current sources across a surface S' exists. Such representation provides full access to the fields in the entire physical domain $V_{S^{\text{out}}}$, as long as the support of the currents, i.e., surface S', circumscribes all the singularities of the analytic continuation of the scattered field, and gets circumscribed by the surface of the scatterer, S, too (see Fig. 4.1). Assuming that we know *a priori* that S' circumscribes all those singularities, we can proceed in the same way as we derived Eq. (4.5), but now integrating over the space $V_{S'^{\text{out}}}$ bounded by S' (instead of S) and S_∞. Due to the analytic continuation of $\mathbf{E}^{\text{sca}}$ inside the volume bounded by S and S' (which practically means the analytic continuation of the solution of the Helmholtz equation of the scattered field inside that "unphysical" domain), we can get the following alternative formula:

$$\begin{aligned}\mathbf{E}^{\text{sca}}(\mathbf{r},\omega)\delta(\mathbf{r}\in V_{S'^{\text{out}}}) \;=\; & \int_{S'} \overleftrightarrow{\mathbf{G}}(\mathbf{r},\mathbf{r}_0;k)\cdot[\hat{\mathbf{n}}(\mathbf{r}_0)\times\nabla\times\mathbf{E}^{\text{sca}}(\mathbf{r}_0,\omega)] \\ & +\nabla\times\overleftrightarrow{\mathbf{G}}(\mathbf{r},\mathbf{r}_0;k)\cdot[\hat{\mathbf{n}}(\mathbf{r}_0)\times\mathbf{E}^{\text{sca}}(\mathbf{r}_0,\omega)]\,\mathrm{d}^2\mathbf{r}_0. \qquad (4.9)\end{aligned}$$

Hence, with the latter equation, we end up with a representation of the scattered field based on a current distribution over a more compact (with which, in this work, we mean more compressed/economical) support of currents, S', than the surface S, where the current sources are distributed in the representation of Eq. 4.5. Note that there are several semi-analytical methods to solve scattering problems, such as the Method of Auxiliary Sources or the Multiple Multipoles Method, which adopt such an integral representation of the scattered field based on a distribution of radiating auxiliary current sources inside the scatterer [144, 280, 281]. There, it has been numerically demonstrated in several cases that such methods have a stable performance only when the auxiliary radiating current sources are distributed over a closed contour that circumscribes all the singularities of

the analytic continuation of the fields inside the non-physical domain [138, 282]. Initially, a substantial problem with these methods was the optimal placement of these auxiliary sources inside the scatterer, and, arguably, the analytic properties of the continuation of the fields inside the scatterer provided significant guidance in that regard. An algebraic theoretical framework that locates *a priori* the position of the shape-related singularities inside a scatterer of arbitrary geometry has been developed [137, 138]. However, one could claim that, in practice, the scientific community has barely capitalized on this analysis so far. This is probably related to the mathematical complexity of the task of locating the singularities of the analytic continuation of the fields in the case of an arbitrary scattering problem. As mentioned already, apart from the standard geometry-related singularities, extra image singularities related to the field exciting the scatterer (including, also, the field scattered back from neighboring scatterers) may exist as well. Unfortunately, this would imply the need for varying representation schemes adapted each time to the scattering scenario that the scatterer gets involved in. This constitutes an undesired complication.

4.3 Solution: A new representation of the fields based on multipolar sources distributed across the topological skeleton of the scatterer

In this section, we provide a general solution for the representation of the scattered fields that provides a path to overcome the problem of the Rayleigh Hypothesis while transcending such considerations of the analytic properties of the fields discussed in the previous section. Importantly, our method shall provide an all-around representation to represent the fields radiated by a scatterer of *arbitrary geometry*, being involved in an *arbitrary scattering scenario*. To achieve this, we will begin with the most general representation of the scattered fields given by Eq. (4.5), and we will apply the technique of employing expansions of the fields with respect to translated coordinate systems, in such a way that introduces the method of discrete sources distributed across the topological skeleton of the scatterer.

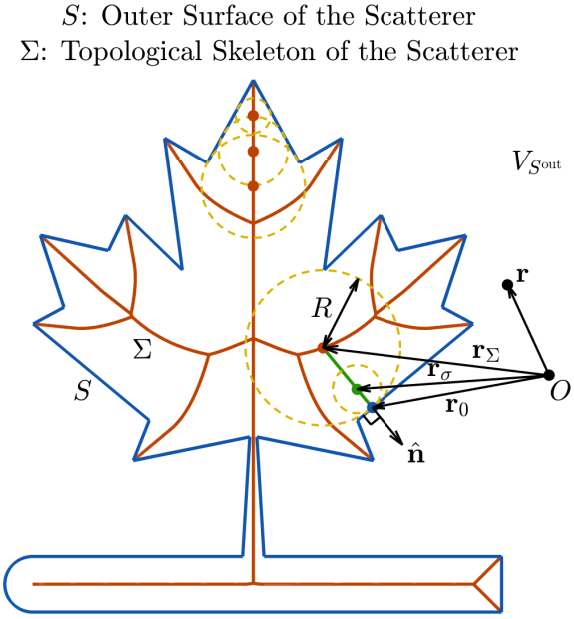

Figure 4.2: Illustration of the geometry of the problem (in 2D) with the scatterer bounded by S and its topological skeleton Σ. Adapted from Ref. [A5].

Working on Eq. (4.5), our first step is to consider the following change of reference frame for the DGF, which consists of a shift of the origin of the multipolar sources by a displacement $\mathbf{r}_\sigma(\mathbf{r}_0)$ that depends on each $\mathbf{r}_0$ point of the surface of the object S:

$$\overleftrightarrow{\mathbf{G}}(\mathbf{r},\mathbf{r}_0;k) \;=\; \overleftrightarrow{\mathbf{G}}(\mathbf{r}-\mathbf{r}_\sigma(\mathbf{r}_0),\mathbf{r}_0-\mathbf{r}_\sigma(\mathbf{r}_0);k), \tag{4.10}$$

where:

$$\mathbf{r}_\sigma(\mathbf{r}_0) \;=\; \mathbf{r}_0-\hat{\mathbf{n}}(\mathbf{r}_0)R(\mathbf{r}_0)\sigma(\mathbf{r}_0), \tag{4.11}$$

with $R(\mathbf{r}_0)$ being the radius of the largest circle (sphere in 3D) that can be inscribed inside S, without intersecting it, and tangentially to point $\mathbf{r}_0$ (see Fig. 4.2). $\sigma(\mathbf{r}_0)$ is some function that takes values within the range [0,1]. After introducing such a change of reference frame, we additionally make exclusively use of the second branch of the expansion of the DGF of Eq. (2.160) in terms of cylindrical waves (for 2D scatterers, translationally invariant along the z-axis), or the second branch of the expansion of the DGF of Eq. (2.161) in terms of spherical waves (for 3D scatterers). Finally, as a result, we arrive to representations of the scattered field valid everywhere inside the physical domain $V_{S^{\rm out}}$. For 2D scatterers the representation reads as:

$$\mathbf{E}^{\rm sca}(\mathbf{r},\omega) \;\equiv\; \sum_{\alpha,\mu_z}\int_{-\infty}^{+\infty}\mathrm{d}k_z\int_C \mathrm{d}\mathbf{r}_0\,\mathcal{A}^{\rm sca}_{\alpha,\mu_z}(\mathbf{r}_0;k_z,\omega)\mathbf{F}^{(3)}_{\alpha,\mu_z}(\mathbf{r}-\mathbf{r}_\sigma(\mathbf{r}_0);k_z,k), \quad \text{for} \quad \mathbf{r}\in V_{S^{\rm out}}, \tag{4.12}$$

with C being the contour of the cross-section of the scatterer in the $z=0$ plane, and the complex amplitudes are given by:

$$\begin{aligned}\mathcal{A}^{\rm sca}_{\alpha,\mu_z}(\mathbf{r}_0;k_z,\omega) \;=\; & \frac{\mathrm{i}}{8\pi}(-1)^{\mu_z}\int_{-\infty}^{+\infty}\mathrm{d}z_0\;\times \\ & \Big[\mathbf{F}^{(1)}_{\alpha,-\mu_z}(\mathbf{r}_0+z_0\hat{\mathbf{z}}-\mathbf{r}_\sigma(\mathbf{r}_0);-k_z,k)\cdot[\hat{\mathbf{n}}\times\nabla\times\mathbf{E}^{\rm sca}(\mathbf{r}_0+z_0\hat{\mathbf{z}},\omega)] \\ & +k\,\mathbf{F}^{(1)}_{\beta,-\mu_z}(\mathbf{r}_0+z_0\hat{\mathbf{z}}-\mathbf{r}_\sigma(\mathbf{r}_0);-k_z,k)\cdot[\hat{\mathbf{n}}\times\mathbf{E}^{\rm sca}(\mathbf{r}_0+z_0\hat{\mathbf{z}},\omega)]\Big].\end{aligned} \tag{4.13}$$

For 3D scatterers the expansion reads as:

$$\mathbf{E}^{\rm sca}(\mathbf{r},\omega) \;\equiv\; \sum_{\alpha,\mu_z\nu}\int_S \mathrm{d}^2\mathbf{r}_0\,\mathcal{A}^{\rm sca}_{\alpha,\mu_z\nu}(\mathbf{r}_0;\omega)\mathbf{F}^{(3)}_{\alpha,\mu_z\nu}(\mathbf{r}-\mathbf{r}_\sigma(\mathbf{r}_0);k), \quad \text{for} \quad \mathbf{r}\in V_{S^{\rm out}}, \tag{4.14}$$

and the complex amplitudes are given by:

$$\begin{aligned}\mathcal{A}^{\rm sca}_{\alpha,\mu_z\nu}(\mathbf{r}_0;\omega) \;=\; & \mathrm{i}k(-1)^{\mu_z}\Big[\mathbf{F}^{(1)}_{\alpha,-\mu_z\nu}(\mathbf{r}_0-\mathbf{r}_\sigma(\mathbf{r}_0);k)\cdot[\hat{\mathbf{n}}\times\nabla\times\mathbf{E}^{\rm sca}(\mathbf{r}_0,\omega)] \\ & +k\,\mathbf{F}^{(1)}_{\beta,-\mu_z\nu}(\mathbf{r}_0-\mathbf{r}_\sigma(\mathbf{r}_0);k)\cdot[\hat{\mathbf{n}}\times\mathbf{E}^{\rm sca}(\mathbf{r}_0,\omega)]\Big].\end{aligned} \tag{4.15}$$

Note the translation of the origins of the VCHs and VSHs in the above equations. We ended up with a representation scheme of the scattered field in terms of a distribution of multipolar sources over a closed surface inside the scatterer. Importantly, note that the position of each such elementary source is determined according to Eq. (4.11) relevant to the position of a point $\mathbf{r}_0$ on the surface S of the scatterer (see Fig. 4.2 and Eqs. (4.12, 4.14)). Furthermore, the amplitude of each such elementary source of the representation is directly specified by the tangential electric and magnetic scattered fields at the same point $\mathbf{r}_0$ on the scatterer's surface S (see Eqs. (4.13, 4.15)). However, even though we assign them such specific values here, it is important to note that those amplitudes are generally not unique. This can be easily deduced from the fact that the left-hand side of Eq. (4.3) vanishes for $\mathbf{r} \in V_{S^{\text{out}}}$, and, therefore, its right-hand side can be added to the right-hand side of Eq. (4.5). This would alter arbitrarily the surface currents there, and, therefore, the corresponding amplitudes of the representations. Any tangential field distribution that belongs to a standing wave whose continuation inside $V_{S^{\text{in}}}$ does not possess any singularity generates a vanishing field inside $V_{S^{\text{out}}}$ once propagated there through the Stratton-Chu formula of Eq. (4.5).

In this way, we have finally reached a representation of the scattered field that is valid everywhere inside the physical domain $V_{S^{\text{out}}}$. To do this, we employed a representation for the individual radiation of each surface current $[\hat{\mathbf{n}} \times \mathbf{E}^{\text{sca}}(\mathbf{r}_0, \omega)], [\hat{\mathbf{n}} \times \nabla \times \mathbf{E}^{\text{sca}}(\mathbf{r}_0, \omega)]$ at each point $\mathbf{r}_0$ that is valid everywhere in $V_{S^{\text{out}}}$. This was achieved by placing the center of the expansion of the DGF, that acts on those particular surface currents, somewhere on top of a linear segment inside the scatterer (see the green linear segment in Fig. 4.2) that constitutes the locus of the centers of all circles (spheres in 3D) that are tangent on S at $\mathbf{r}_0$, and that do not intersect S at any other point. Once such centers of expansion are chosen, the series expansion of the second branch of the employed DGFs in Eqs. (4.7, 4.8) is valid everywhere in $|\mathbf{r} - \mathbf{r}_\sigma| > |\mathbf{r}_0 - \mathbf{r}_\sigma|$, and, therefore, everywhere in $V_{S^{\text{out}}}$. In this way, we manage to hide at the interior of the scatterer the surfaces where the branches of Eqs. (4.7, 4.8) lie for each individual surface current, $|\mathbf{r} - \mathbf{r}_\sigma| = |\mathbf{r}_0 - \mathbf{r}_\sigma|$ (see the yellow dashed circles in Fig. 4.2). And, as a result, we get a representation of $\mathbf{E}^{\text{sca}}(\mathbf{r}, \omega)$ that is valid everywhere in $V_{S^{\text{out}}}$. As long as the representation of the radiation of each surface current is valid everywhere in $V_{S^{\text{out}}}$, the collective radiation emanating from all those surface currents, i.e., the representation that we employ for the scattered field in Eqs. (4.12, 4.14), shall be valid as well.

Actually, Eqs. (4.12, 4.14) correspond to a family of representations of the scattered field. Specifically, we have a different representation with multipolar sources distributed over different surfaces inside the scatterer corresponding to each function $\sigma(\mathbf{r}_0)$. In the limiting case that $\sigma(\mathbf{r}_0) = 0, \forall\, \mathbf{r}_0$, we have the sources distributed exactly across the surface of the scatterer S. This case corresponds to representations used in classical surface integral methods [283]. The major disadvantage here is that the kernel has singularities located exactly across the surface S, which typically results in a poor convergence of the fields' representation when the observation point $\mathbf{r}$ approaches S, i.e., in the vicinity of the scatterer. Nevertheless, we can push the singularities of the kernel further inside the scatterer by letting $\sigma(\mathbf{r}_0)$ take non-zero values. Specifically, taking the other limiting case of $\sigma(\mathbf{r}_0) = 1, \forall\, \mathbf{r}_0$, we reach a representation that is based on multipolar sources distributed across the surface Σ, which is defined as: $\mathbf{r}_\Sigma(\mathbf{r}_0) = \mathbf{r}_\sigma(\mathbf{r}_0)|_{\sigma(\mathbf{r}_0)=1, \forall\, \mathbf{r}_0}$. This zero-volume-enclosing surface, Σ, is by definition the *topological skeleton* of the scatterer (see Fig. 4.2).

The topological skeleton of an object is also known as its medial axis. It is defined as the locus of the centers of circles (spheres in 3D) that are tangent to its outer surface at two or more points, where all such circles (spheres in 3D) are contained inside the object

[284]. The topological skeleton of an object was first introduced by Blum in 1967 as a tool for biological shape recognition [285]. The medial axis, together with the associated radius function of the maximally inscribed circles (spheres in 3D), which we denote as $R(\mathbf{r}_0)$, is known as the medial axis transform (MAT) of the object. The MAT is a complete shape descriptor, i.e., we can use it to reconstruct the shape of the original object. Therefore, in that sense, it constitutes a compressed way to encode the shape of the object. Apart from medical imaging applications, the topological skeleton has found a wide variety of applications in computer graphics, animation, visualization, digital inspection, computer design, pattern recognition, robotics, collision detection, etc., where a compact shape representation supporting shape analysis and synthesis is important [284]. Let us note, that the "skeletonization" of an object is a quite mature field of research, and several methods exist to calculate the topological skeleton of a given object, with Voronoi diagrams usually playing a central role in that regard [286–288].

From the physical point of view, let us note the following regarding the introduced topological-skeleton-based representation of the scattered fields. On the one hand, we can claim that it constitutes an optimal representation since it provides the locus of the most compact support of multipolar sources that is able to overcome the problem of the Rayleigh Hypothesis for an arbitrary scattering scenario involving the considered scatterer. We would like to emphasize that, even though the topological skeleton does not necessarily pass through the singularities of the analytic continuation of the scattered fields, yet it provides a representation of the scattered field that is valid everywhere in $V_{S^{\text{out}}}$. In fact, assuming the *a priori* knowledge of the analytic properties of the scattered fields, then the most optimal and compact representation that does not suffer from the problem of the Rayleigh Hypothesis, would, instead, be the one based on a distribution of multipolar sources across the topological skeleton of the surface S', that is enclosed by S, and that encloses all the singularities of the analytic continuation of the fields inside the scatterer. However, we want to avoid such considerations since the resulting representations cannot be generalized to an arbitrary scattering scenario involving the considered scatterer. On the other hand, by placing the multipolar sources on the topological skeleton Σ, we also managed to move the singularities of the representation of the scattered field as far away from the surface of the scatterer S as possible. In that sense, this is the optimal placement of the distribution of the sources among all cases of different $\sigma(\mathbf{r}_0)$, guaranteeing better convergent properties of the near-fields. However, as it can be seen in Fig. 4.2, the topological skeleton Σ touches the surface of the scatterer S at its sharp edges. Note that such points always host singularities. However, this is not the case for a smooth surface S.

It is important to note that not all parts of the topological skeleton are equally significant. On the one hand, there may be significant small parts of the topological skeleton that are responsible for the radiation of a big part of the surface currents. Take, for example, a sphere whose topological skeleton is a single point at its center. In Lorenz-Mie theory, that point hosts the origin of a multipolar series of radiating VSHs that validly represents the scattered fields all over the physical domain $V_{S^{\text{out}}}$. On the other hand, it can frequenctly be the case that large parts of the topological skeleton correspond to only a minor part of the radiating surface currents. In such a case, "pruning" such insignificant parts of the topological skeleton can lead to a more compact representation of the fields. Nevertheless, this comes at the cost of sacrificing the guaranteed access to a valid representation of the fields at a small enough region of the physical domain in the vicinity of the scatterer.

Equations (4.12, 4.14) constitute an infinite-dimensional representation of the scattered fields allowing us to transcend the problem of the Rayleigh Hypothesis. However, for practical purposes, it is required to render those representations finite-dimensional. Therefore, we need to replace the integrals in Eqs. (4.12, 4.14) with finite sums. This process leads to the discretization of the topological skeleton Σ, which is substituted by a set of N points

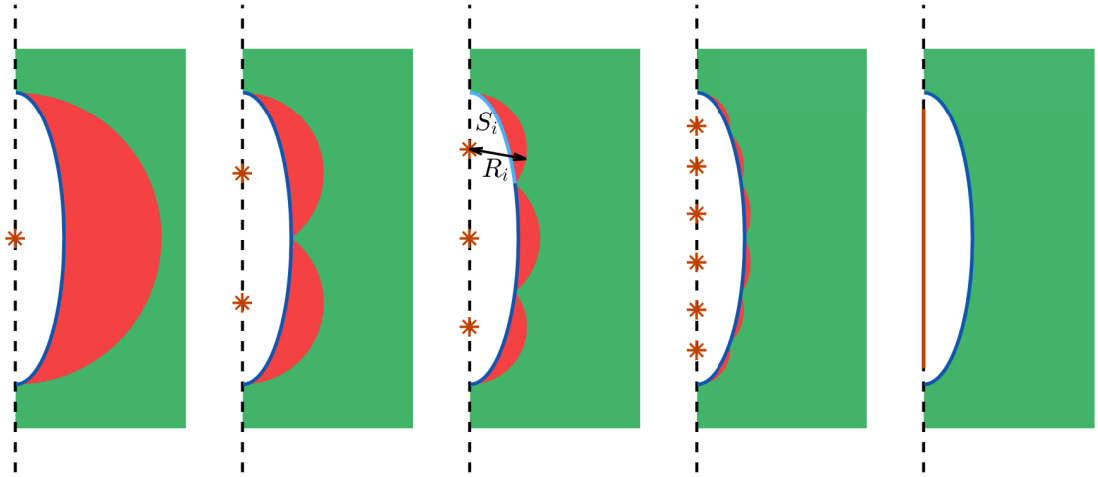

Figure 4.3: The effect of the discretization of the topological skeleton of a prolate spheroid on the region of validity of the representation (green region). Adapted from Ref. [A5].

(located at $\mathbf{r}_i$) that act as centers of multipolar expansions for the field that is radiated by the surface currents distributed over a surface S_i, that is part of $S = \sum_{i=1}^{N} S_i$ (see Fig.4.3). Specifically, for finite-dimensional representations of the scattered field based on those of Eqs. (4.12, 4.14), we can get the following expansion in terms of series of VCHs for 2D scatterers:

$$\mathbf{E}^{\mathrm{sca}}(\mathbf{r},\omega) \equiv \sum_{i=1}^{N}\sum_{\alpha,\mu_z}\int_{-\infty}^{+\infty} \mathrm{d}k_z \mathcal{A}^{\mathrm{sca}}_{\alpha,\mu_z,i}(k_z,\omega)\mathbf{F}^{(3)}_{\alpha,\mu_z}(\mathbf{r}-\mathbf{r}_i;k_z,k), \quad \text{for} \quad \sqrt{(x-x_i)^2+(y-y_i)^2} > R_i, \ \forall\, i, \tag{4.16}$$

with $C = \sum_{i=1}^{N} C_i$ and with the complex amplitudes being given by:

$$\begin{aligned}\mathcal{A}^{\mathrm{sca}}_{\alpha,\mu_z,i}(k_z,\omega) = \frac{\mathrm{i}}{8\pi}(-1)^{\mu_z}\int_{-\infty}^{+\infty}\mathrm{d}z_0\int_{C_i}\mathrm{d}\mathbf{r}_0 \times \\ \Big[\mathbf{F}^{(1)}_{\alpha,-\mu_z}(\mathbf{r}_0+z_0\hat{\mathbf{z}}-\mathbf{r}_i;-k_z,k)\cdot[\hat{\mathbf{n}}\times\nabla\times\mathbf{E}^{\mathrm{sca}}(\mathbf{r}_0+z_0\hat{\mathbf{z}},\omega)] \\ +k\,\mathbf{F}^{(1)}_{\beta,-\mu_z}(\mathbf{r}_0+z_0\hat{\mathbf{z}}-\mathbf{r}_i;-k_z,k)\cdot[\hat{\mathbf{n}}\times\mathbf{E}^{\mathrm{sca}}(\mathbf{r}_0+z_0\hat{\mathbf{z}},\omega)]\Big],\end{aligned} \tag{4.17}$$

while for the case of 3D scatterers, we have the following expansion in terms of series of VSHs:

$$\mathbf{E}^{\mathrm{sca}}(\mathbf{r},\omega) \equiv \sum_{i=1}^{N}\sum_{\alpha,\mu_z\nu,i}\mathcal{A}^{\mathrm{sca}}_{\alpha,\mu_z\nu,i}(\omega)\mathbf{F}^{(3)}_{\alpha,\mu_z\nu}(\mathbf{r}-\mathbf{r}_i;k), \quad \text{for} \quad |\mathbf{r}-\mathbf{r}_i| > R_i, \ \forall\, i, \tag{4.18}$$

with the complex amplitudes being given by:

$$\mathcal{A}^{\text{sca}}_{\alpha,\mu_z\nu,i}(\omega) = \mathrm{i}k(-1)^{\mu_z}\int_{S_i}\mathrm{d}^2\mathbf{r}_0\left[\mathbf{F}^{(1)}_{\alpha,-\mu_z\nu}(\mathbf{r}_0-\mathbf{r}_i;k)\cdot[\hat{\mathbf{n}}\times\nabla\times\mathbf{E}^{\text{sca}}(\mathbf{r}_0,\omega)]\right.$$
$$\left.+k\,\mathbf{F}^{(1)}_{\beta,-\mu_z\nu}(\mathbf{r}_0-\mathbf{r}_i;k)\cdot[\hat{\mathbf{n}}\times\mathbf{E}^{\text{sca}}(\mathbf{r}_0,\omega)]\right]. \quad (4.19)$$

Note that the resulting Eqs. (4.16, 4.18) are only valid outside the union of circles (spheres in 3D) that are centered at $\mathbf{r}=\mathbf{r}_i$, have a radius of R_i, and contain inside them the surface current sources that are distributed over the surface S_i (highlighted with light blue color in Fig. 4.3) that is associated with the i-th center of multipolar expansion of the discretized topological skeleton at $\mathbf{r}_i$. In Fig. 4.3, we illustrate the effect of discretization of the topological skeleton of a prolate spheroid on the region of validity of the representation of the scattered fields. As we increase the dimensionality of the representation, i.e., as we increase the number of the multipolar centers of expansion, we unlock access to the near-fields closer and closer to the surface of the scatterer S. For example, already with six points only, we see that we have restricted the problematic near-field region (with red color in Fig. 4.3b) rather significantly. Note that the full topological skeleton of a prolate spheroid of semi-minor axis a and semi-major axis b (along z) is a linear segment connecting the points $(x,y,z)=(0,0,\pm(b^2-a^2)/b)$. Importantly, let us note that those two points are not the foci of the spheroid, which have been identified to be the singular points of the analytic continuation of the scattered fields inside a prolate spheroid [130, 131, 137, 138].

Finally, let us comment on three more aspects related with the topological-skeleton-based representations of the scattered field that we ended up with:

- The surface bounding the union of spheres defined by $|\mathbf{r}-\mathbf{r}_i|=R_i$ does not generally constitute a hard boundary for the region of validity of the representation of the scattered fields. Instead, the multipolar series at each center of expansion of the discretized topological skeleton are expected to converge everywhere outside the sphere defined by $|\mathbf{r}-\mathbf{r}_i|=R_i'$, with $R_i'\leq R_i$ being the radius of the smallest sphere that encloses all the singularities of the analytic continuation of the fields that are radiated by the surface current sources distributed across S_i.

- The region of validity of the finite-dimensional representation of the scattered fields that we introduced is not unique since the complex amplitudes are not unique. First, as we discussed before, the radiating surface current distribution generating the scattered field in $V_{S^{\text{out}}}$ is not unique (see Eq. (4.9)). Furthermore, an arbitrary and non-optimal assignment of the radiating surface currents to the N multipolar centers of expansion (which, let us consider fixed here), may still lead, on the one hand, to multipolar amplitudes that accurately represent the far-field, but, on the other hand, may obstruct the access to the near-fields, since, then, the surface bounding the union of spheres defined by $|\mathbf{r}-\mathbf{r}_i|=R_i$ gets modified.

- The maximum multipolar order of the sources placed at $\mathbf{r}=\mathbf{r}_i$ needed to accurately represent the fields emanating from the corresponding radiating surface currents distributed across S_i shall depend on the radius R_i (in fact on the optical distance kR_i). Points of the topological skeleton placed at a large optical distance from the surface of the scatterer S shall generally require a larger number of multipoles for their expansions compared to points closer to S.

  In Fig. 4.4, we demonstrate the number of multipoles needed to achieve convergence for the reconstruction of the fields radiated by a dipolar emitter in free space (denoted with $\mathbf{d}$). We study this multipolar convergence as a function of 1) the optical distance

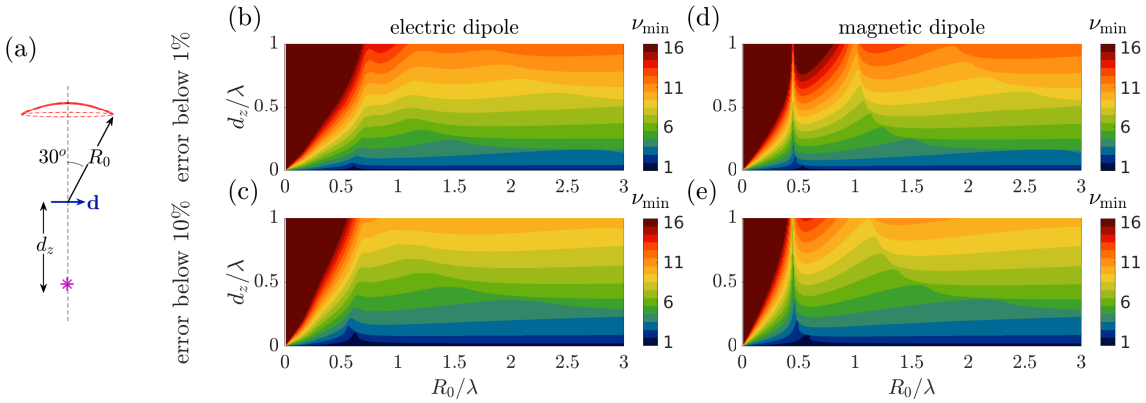

Figure 4.4: Study of the number of multipoles required to achieve convergence for the reconstruction of the fields radiated by a dipolar emitter in free space. a) The geometry of the problem. The magenta star indicates the position of the multipolar expansion. The blue vector indicates the position and orientation of the dipolar emitter. The red curve indicates the cross-section of a spherical cap over which we calculate the convergence of the representation of the radiated fields. b-e) Maps of the minimum multipolar order needed ($\nu_{\min}$) to achieve an average error below either 1% (b,d), or 10% (b,d), for the case of either an electric dipole (b,c) or a magnetic dipole (d,e) emitter. Adapted from Ref. [A5].

between the emitter and the observation point (R_0/λ), and 2) the optical distance between the emitter and a center of multipolar expansion (denoted with a magenta star) that is used to represent the radiation of the emitter (d_z/λ). Note that the fields radiated by the emitter have a singularity at its position, which can be thought of in analogy to the singularities of the analytic continuation of the fields that are radiated by the surface currents on S_i and that are represented by a multipolar expansion with respect to a center at $\mathbf{r}_i$. We observe that: 1) the larger the optical distance d_z/λ, the larger the number of multipoles needed for convergence, and 2) the larger the distance R_0/λ, the smaller the number of multipoles that are needed for convergence. Note that, for a fixed d_z/λ, after some "threshold" value of R_0/λ, as we move away from the singularity, i.e., as we move away from the near-field region of the radiated fields, the number of multipoles needed for convergence remains practically unchanged concerning R_0/λ.

In what follows, let us demonstrate the performance of the method of the topological skeleton numerically. Specifically, we are interested in studying how it practically deals with the problem of the Rayleigh Hypothesis, i.e., how well it provides an accurate representation of the near-field of a scatterer.

In our indicative example, we consider as a scatterer an axially symmetric object with a rather complex shape resembling that of a seahorse. In Fig. 4.5, the white-shaded region indicates the cross-section of such a scatterer along a meridian plane. The scatterer is embedded in free space and made of an isotropic, non-magnetic material with a refractive index of $n = 3.477$. Regarding the optical size of the considered scatterer, note that it is circumscribed by a sphere of radius half the wavelength of light in free space (λ). We consider the excitation of the scatterer by a monochromatic (with frequency ω_0), TE-polarized regular VSH of angular momentum along the z-axis, $\mu_z = 0$, and multipolar order, $\nu = 2$ (see Eq. (2.140) for its definition).

First, we perform a full-wave numerical simulation with a finite element solver JCM-suite [248] to calculate the electromagnetic response of the scatterer under such excitation.

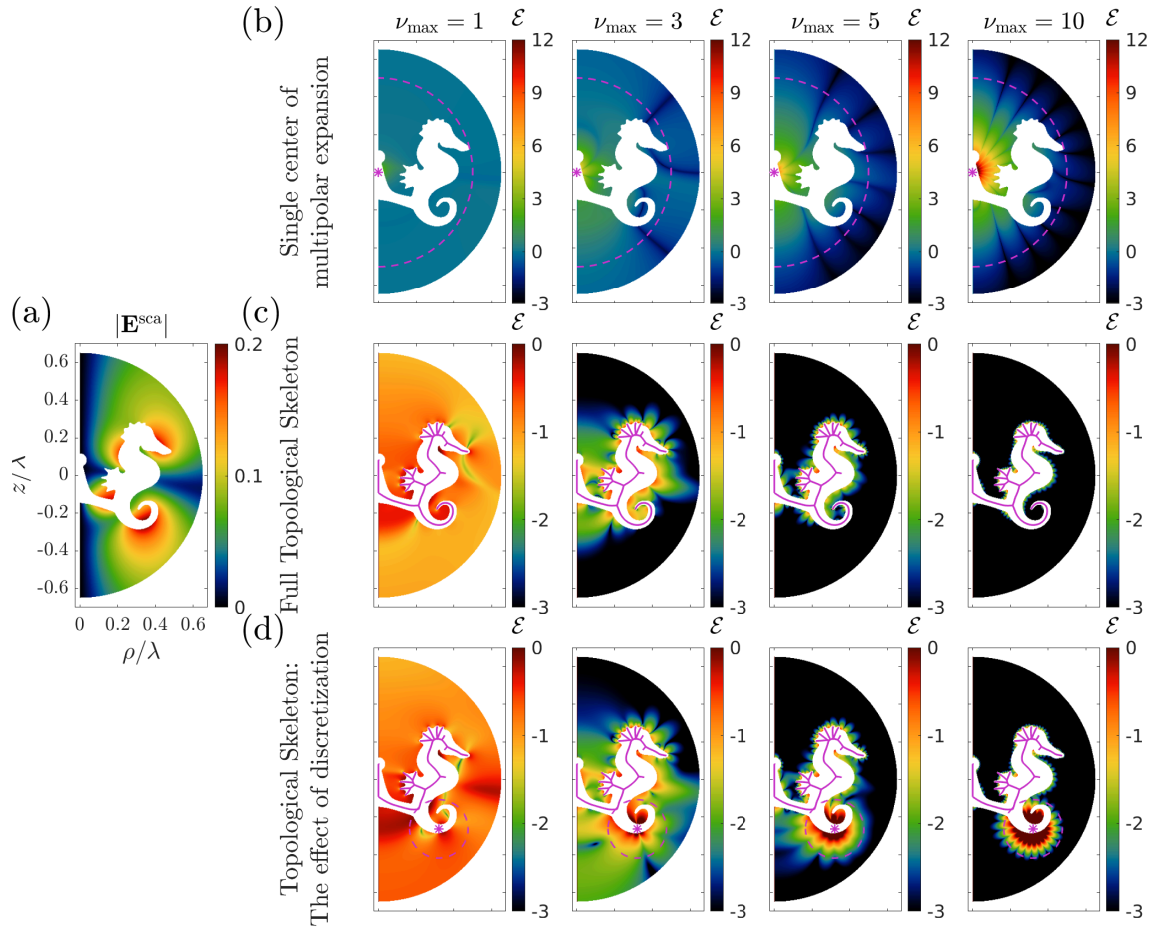

Figure 4.5: Numerical example with a comparison of the performance of different analytical representations of the scattered field, elucidating their relation with the problem of the Rayleigh Hypothesis. a) Plot of the norm of the scattered near-field of a sub-wavelength, axially symmetric seahorse (with its cross-section along a meridian plane being white-shaded) excited by a regular VSH, as it was calculated by a full-wave solver. Plots of the logarithmic relative error, $\mathcal{E}$, in the representation of the scattered near fields by: b) the conventional case of a single center of multipolar expansion of the fields (magenta star), c) a dense distribution of multipolar sources across the entire topological skeleton of the seahorse (magenta line), d) a dense distribution of multipolar sources across the topological skeleton of the seahorse with its tail being truncated and substituted by a single origin of multipolar expansion (magenta star) to represent the radiation of the tail specifically. The plots are given for different truncation orders, $\nu_{\max}$, of the infinite multipolar sums. The dashed magenta circles in (b) and (d) indicate the theoretical regions of validity of the representations. Adapted from Ref. [A5].

Note that, by exploiting the axial symmetry of both the geometry and the excitation, we performed the simulations in two dimensions, and, thus, we were able to reach an accuracy of the recorded near-fields up to at least the fourth significant digit. We used finite elements of size $\lambda/50$ and polynomial order 10. We recorded the scattered field within the near-field zone, inside a sphere of radius 0.65λ containing the scatterer. In Fig. 4.5a, we plot the norm of the scattered field, $|\mathbf{E}^{\mathrm{sca}}(\mathbf{r}, \omega_0)|$, as it was recorded from the full-wave simulation.

Next, we aim to study and compare how the problem of the Rayleigh Hypothesis is manifested in that particular example, once we employ different analytical representation schemes attempting to reconstruct the target scattered near-field that we got from the full-wave simulations. For this, we record the tangential field components at as many as 6000 points on the contour of the surface of the scatterer across a meridian plane, and we use them to get the complex amplitudes of the different analytical representations that we want to compare. To facilitate the comparisons, we establish the following logarithmic relative error metric:

$$\mathcal{E}(\mathbf{r},\omega_0) \quad = \quad \log_{10}\left[\frac{\left|\mathbf{E}^{\text{sca}}_{\text{analytical}}(\mathbf{r},\omega_0)-\mathbf{E}^{\text{sca}}_{\text{numerical}}(\mathbf{r},\omega_0)\right|}{\left|\mathbf{E}^{\text{sca}}_{\text{numerical}}(\mathbf{r},\omega_0)\right|}\right], \tag{4.20}$$

where $\mathbf{E}^{\text{sca}}_{\text{analytical}}(\mathbf{r},\omega_0)$ stands for the analytically reconstructed field based on the particular representation and $\mathbf{E}^{\text{sca}}_{\text{numerical}}(\mathbf{r},\omega_0)$ stands for the field that was calculated numerically from the full-wave solver.

The first case that we study is that of the conventional representation of the scattered field based on a single center of multipolar expansion at $\mathbf{r}=0$ (magenta star in Fig. 4.5b). Specifically, knowing the tangential scattered fields at the surface of the scatterer from the full-wave solver, we employ Eq. (4.19) to get the amplitudes of such a representation of the scattered field. As discussed already, this representation of the fields is *a priori* guaranteed to be valid only outside the minimal sphere that circumscribes the scatterer ($r>\max\{r_0\}$). To check this, we use the numerically calculated amplitudes to analytically reconstruct the near-fields by making use of Eq. (4.18), and, then, we calculate the log. relative error $\mathcal{E}(\mathbf{r})$ by comparing them against the numerical results. In Fig. 4.5b, we show color plots of $\mathcal{E}(\mathbf{r},\omega_0)$ for increasing multipolar order of truncation of the infinite series ($\nu_{\max}$). The dashed magenta line denotes the spherical shell of $r=\max\{r_0\}$, inside of which the Rayleigh Hypothesis is expected to be violated. Indeed, we observe that, for $\nu_{\max}=10$, we barely have any errors recorded in the dark blue region outside the magenta sphere, indicating a convergence of the series there. To be precise, small errors can be observed even a bit inside that sphere. As we discussed previously, the hard boundary of validity of such a representation is not the magenta sphere but a sphere of a generally smaller radius that circumscribes all the singularities of the analytic continuation of the scattered field inside the region of the scatterer.

Importantly, note that by increasing $\nu_{\max}$, on the one hand, we achieve better and better convergence of the series representation of the fields closer and closer to that spherical shell enclosing the singularities. But, on the other hand, we get a worse and worse divergence of the series representation of the fields in the physical domain contained inside the spherical shell that encloses the singularities. Such divergence of the fields in that region has already been observed in Ref. [130, 131]. In our exemplary case, whereas, for $\nu_{\max}=1$, we observe a relative error of an order of magnitude larger than the norm of the scattered near-field, for $\nu_{\max}=10$, a relative error of twelve orders of magnitude larger than the norm of the scattered near-field is to be observed.

Such large errors emanating from the divergence of such series representation of the fields in the near-field region of the scatterer, may at first suggest that the existing semi-analytical method of multiple light scattering, based on such conventional representations of the fields in terms of localized series of VSHs, would always become useless for modeling the near-field coupling between closely placed scatterers. In practice, this is seemingly not strictly the case, though. Quite surprisingly, in Ref. [131], it was demonstrated with counterexamples featuring near-field interactions between dimers of prolate spheroids, that sufficiently convergent results can be obtained in unexpected near-field regions when a very

large number (~ 40) of multipolar contributions is considered for the multi-scattering calculations (increasing the dimensionality of the problem dramatically, though). Note that, eventually, this additionally requires that the calculations are performed with quadruple-precision arithmetic to account for the interactions between multipoles of high order properly. Those results seem to suggest that the problem of the Rayleigh Hypothesis within the context of multi-scattering calculations is not intrinsic, i.e., associated with the inherently problematic analytic properties of the adopted representations of the fields. Instead, it appears to be a problem of numerical nature if we are always able to get convergent solutions for the general multi-scattering problem associated with an arbitrary geometric setup by ever increasing the multipolar truncation order and the arithmetic precision used for the calculations. However, on the one hand, whether this suggestion is true in its generality remains an interesting open question, and, on the other hand, even in such a case, it is evident that such problematic numerical issues stem from the analytic aspects of the problem. We would like to highlight that the topological skeleton method presented here provides representations of the scattered field that converge everywhere outside the scatterers for general geometries and that require only a reasonable number of multipoles.

In our second case study, we consider the newly introduced representation scheme for the scattered fields, which is based on a distribution of multipolar sources across the topological skeleton of the scatterer. First, we construct the topological skeleton of the axially symmetric seahorse based on a constrained Delaunay Triangulation method [288] (see the magenta solid line in Fig. 4.5c for a cross-section of the topological skeleton of the seahorse along a meridian plane). Then, we employ again Eq. (4.19) to get the amplitudes and use them to represent the scattered field in terms of radiating VSHs distributed over the topological skeleton of the seahorse with Eq. (4.18). Note that we densely discretize the meridian cross-section of the topological skeleton using $N = 6000$ points as well. That is to say that we assign each considered elementary radiating surface current to a distinct center of multipolar expansion. The integration over the azimuthal dimension of the skeleton is performed adaptively, resembling a perfectly fine discretization along the azimuthal dimension. In Fig. 4.5c, we plot again the calculated log. relative errors of the considered representation scheme for increasing multipolar order for the truncation of the series. We can observe that, by $\nu_{\max} = 10$, an accuracy of more than three significant digits is achieved almost all over the near-field region we monitor. Actually, already by $\nu_{\max} = 3$, we get an acceptable convergence of the series representation of the fields. We verify like this that the topological skeleton method can fully transcend the problem of the Rayleigh Hypothesis in our exemplary case. Let us highlight again that the closer the observation point to the surface of the scatterer, the larger the number of multipoles needed for an accurate representation of the fields. In other numerical examples not presented here, where the gradients of the scattered fields were stronger, indicating the presense of singularities of the analytic continuation of the fields closer to the surface of the scatterer, we observed a slower rate of convergence of the multipolar series expansion of the fields.

Next, in our last case study, we consider another representation scheme for the scattered fields with which we aim to study the discretization effects of the topological skeleton method. Specifically, as in the previous case, we begin with the full topological skeleton of the seahorse, but now we truncate its tail and employ a single center of multipolar expansion to represent the radiating fields emanating from the surface currents distributed across the tail of the seahorse. The magenta star in Fig. 4.5d denotes that introduced center of multipolar expansion. Let us highlight that, due to the axial symmetry, the star represents a ring of multipolar sources rather than a single multipolar center. Interestingly, note that the Discrete Sources Method, to facilitate the study of light scattering from axially symmetric and oblate objects, commonly employs multipolar sources with origins placed in the complex $z-$plane, and those sources actually constitute the image

of such a ring of sources in the real space [142]. Next, we use again Eq. (4.19) to get the amplitudes of our new representation. However, now, the dimensionality of the representation is reduced to $N = 4451$, as we truncated 1550 points belonging to the tail of the skeleton of the seahorse and substituted them with a single origin of expansion. What we expect is that this representation of the fields provides access to the near-fields everywhere outside a torus that is centered at the magenta star and that circumscribes the truncated tail of the seahorse. The dashed magenta circle in Fig. 4.5d indicates a cross-section of this torus along a meridian plane where we plot a map of the calculated log. relative errors $\mathcal{E}(\mathbf{r}, \omega_0)$ again. Indeed, we observe that such a representation still provides great accuracy of the reconstructed fields everywhere outside the aforementioned torus (actually, to be precise, everywhere outside the torus -of a bit smaller radius- that circumscribes the singularities of the analytic continuation of the fields radiated by the truncated tail of the seahorse). Hence, we can deduce that in practice the dimensionality of the topological-skeleton-based representation of the fields can be significantly reduced to a small enough number of centers of multipolar expansions by sacrificing the access of the representation to a small enough near-field region in the vicinity of the scatterer. For example, we saw in Fig. 4.3 that only six properly placed centers of multipolar expansion can be already enough to provide a good representation of the scattered near-fields by a prolate spheroid with an aspect ratio of three. Nevertheless, more complicated geometries generally require representations of higher dimensionality.

Finally, let us highlight the following two key observations regarding the number of multipoles needed in practice for sufficient convergence of the aforementioned multipolar series representations of the scattered field:

1. the smaller the optical distance between the observation point and the spherical (cylindrical in 2D) shell enclosing the singularities of the analytic continuation of the field represented by the particular multipolar center of expansion, and

2. the larger the optical distance between the multipolar center of expansion and the aforementioned singular shell, i.e., the larger the radius of the shell,

the more multipoles are needed for the convergence of the series representation of the field (see also Fig. 4.4 and the related discussion).

We would like to note that the above observations imply quite significant limitations for methods based on dipolar-only representations, such as e.g., in [57]. Such representations can only be practically applicable either for scatterers that are sufficiently optically small, or for distributions of dipolar sources that are placed at close enough optical distances from the surface of the scatterer (this would correspond, for example, to the non-optimal case of the representation of Eqs. (4.12, 4.14) with small values of $\sigma(\mathbf{r}_0)$). However, in the latter case, the dimensionality of the representation would typically be significantly increased, though, since it would generally require the spatial distribution of a significantly larger number of centers of expansion (although, with a fewer number of multipoles -6 for dipoles- at each center).

Furthermore, let us support the above-mentioned observations on the convergence of the infinite multipolar series of the representations of the scattered field with some additional exemplary numerical results.

In Fig. 4.6, we perform a statistical analysis of the convergence among several instances of 2D scatterers with varying geometry We illuminate them with monochromatic (of frequency ω_0) TE-polarized plane waves propagating along varying directions. Specifically, the angle of the illuminating plane waves is varied with a step of 5^o (for all non-trivial excitation angles with respect to the geometry of the scatterer). The scatterers are again considered to be inscribed inside a circle of radius half the free space wavelength. They

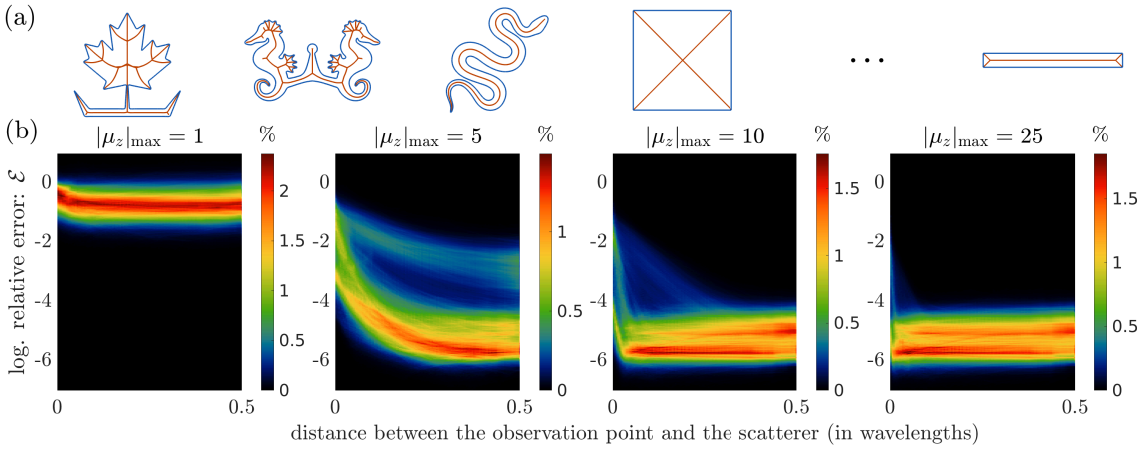

Figure 4.6: Statistical analysis of the convergence among several instances of 2D scatterers with varying geometry, illuminated by monochromatic, TE-polarized plane waves propagating along varying directions on the xy-plane: a) Illustration of the geometry of the considered 2D scatterers with blue color and their topological skeleton with red color. b) Plot of the statistics of the log. relative errors $\mathcal{E}(\mathbf{r}, \omega_0)$ recorded for the topological-skeleton-based representations, as a function of the distance between the observation point and the surface of the scatterer, and for varying truncation orders of the multipolar series ($|\mu_z|_{\max}$). Adapted from Ref. [A5].

are made of a material of refractive index $n = 3.477$ and embedded in free space. Eleven rectangular scatterers are considered with varying aspect ratios from one to ten. The surface and the topological skeleton of each scatterer are finely discretized using a large number of 12.000 points.

Specifically, we plot the statistics of the log. relative errors recorded for the topological-skeleton-based representations, as a function of the distance between the observation point and the surface of the scatterer. We observe that a smaller optical distance between the observation point and the scatterer generally requires a larger number of multipoles for sufficient convergence. As we highlighted above, we have a slower convergence rate for small distances between the observation point and the singularities of the analytic continuation of the scattered fields inside the scatterer. Furthermore, we would also like to highlight that the rate of such convergence varies significantly among our case studies. Note, for example, the different rates of convergence that we characteristically can observe, e.g., in the case of $|\mu_z|_{\max} = 5$, and, also, in comparison with the rest multipolar truncation orders. As we have already discussed, the convergence additionally depends on the distance between the multipolar center of expansion and the surface of the scatterer. For the cases of scatterers where such distance between the topological skeleton and the surface of the scatterer becomes large (like for rectangular scatterers of low aspect ratio), we observe a slower convergence rate, i.e., more multipoles are needed to accurately represent the near-fields.

Finally, in Fig. 4.7, we demonstrate the rate of convergence of the multipolar series for the case of a cylinder illuminated by a dipolar emitter placed in close proximity on top of it. Note that the emitter is known to induce an image singularity in the analytic continuation of the scattered fields of the cylinder at a small distance from its surface. Specifically, we study the case of a cylindrical disk with axial symmetry to the z-axis and with an aspect ratio of six, inscribed inside a sphere of radius one third of the free space wavelength λ, made of a material of refractive index $n = 3.477$ and embedded in free space. We excite it with a monochromatic (of frequency ω_0), z-oriented electric dipole

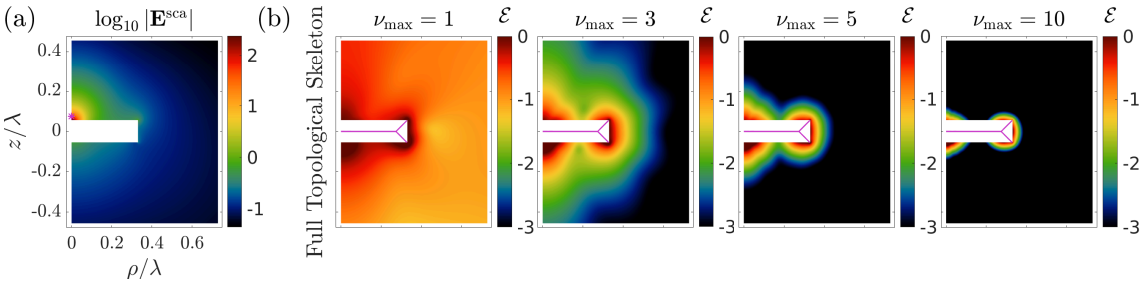

Figure 4.7: An exemplary study of the convergence of the topological-skeleton-based representation of a radiating field with a singularity located closely to the physical domain. Such is the case of the response of a cylindrical disk excited by a dipole emitter at close proximity (denoted with the magenta star in the figure). a) The logarithm of the norm of the scattered by the disk field upon such an excitation. b) Maps of the log. relative error $\mathcal{E}$ for the topological-skeleton-based representation of the fields for increasing truncation orders of the multipolar series. Adapted from Ref. [A5].

placed at a distance of $\lambda/50$ on top of the disk, which is illustrated with a magenta star in Fig. 4.7a. There, we plot the logarithm of the norm of the scattered by the disk field upon such an excitation. Indeed, we can observe the strong gradients of the field which are indicative of the presence of the image singularity in the analytic continuation of the fields inside the disk, at close proximity to the surface of the scatterer and the physical domain of the fields. In Fig. 4.7b, we plot maps of the log. relative error $\mathcal{E}(\mathbf{r}, \omega_0)$ for the topological-skeleton-based representation of the fields for increasing truncation orders of the multipolar series. The magenta line denotes the topological skeleton of the cylinder. Note that here we use 8.250 unevenly distributed (we considered a denser discretization at the region of strong gradients of the incident field) points for the fine discretization of both the surface of the cylinder and the topological skeleton over the meridian plane.

In this case, we observe a slower convergence rate of the multipolar series in the topological-skeleton-based representation of the scattered field. Although, theoretically, we can still achieve convergence all over the near-field region, we observe that a larger number of multipoles are needed for convergence, i.e., the convergence of the multipolar series in this case is poorer. That holds especially in the region close to the image singularity inside the disk, which locally induces strong gradients to the near-fields. Even though full convergence was achieved for the near fields in the case study of Fig. 4.5c already for a truncation of the multipolar series at $\nu_{max} = 10$, this is clearly not the case here. Radiating VSHs of higher multipolar orders, above $\nu_{max} = 10$, are needed to be added to the series in this case to achieve convergence of the near fields.

4.4 Construction of the distributed T-matrix assisted by topological-skeleton-based representations of the fields

In this section, we will introduce the distributed T-matrix of a scatterer, where we will employ a topological-skeleton-based representation of the incident and scattered fields. Such approach will lead us to a representation of the T-matrix of the scatterer that transcends the problem of the Rayleigh Hypothesis. We will describe a method that consists of four steps to calculate the distributed T-matrix of a scatterer with the help of a full-wave solver. The numerical simulations with the full-wave solver in this section have been performed in collaboration with M.Sc. Nanda Perdana.

Note that this section will focus on 3D scatterers, but, in analogy, an extension to

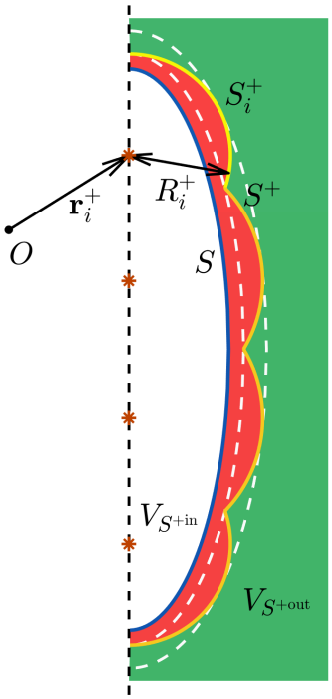

Figure 4.8: Illustration of the geometry of the problem.

2D scatterers is straightforward. Similarly as before, we consider an arbitrary stationary scatterer of arbitrary geometry bounded by a closed surface S (blue line in Fig. 4.8) and embedded inside a background medium that is homogeneous, isotropic and stationary, and is characterized by a wavenumber $k(\omega)$ and a wave-impedance $Z(\omega)$. Furthermore, we consider a surface S^+ (yellow line in Fig. 4.8) that: 1) *fully* encloses the scatterer in its interior, and, 2) is comprised by a union of spherical patches, S_i^+ (light yellow line in Fig. 4.8), that belong to N auxiliary spheres centered inside S at positions $\mathbf{r}_i^+$, with radii R_i^+, and with $S^+ = \sum_{i=1}^{N} S_i^+$. Moreover, the spherical patches are considered to have a minimum distance d_{min} and a maximum distance d_{max} from the surface of the scatterer S (points with minimum and maximum such distance from S are denoted with white dashed lines in Fig. 4.8). The surface S^+ divides the whole space into two regions: its interior, $V_{S^{+\text{in}}}$ (the white plus the red region in Fig. 4.8), and its exterior, $V_{S^{+\text{out}}}$ (the green region in Fig. 4.8). The centers of the auxiliary spheres $\mathbf{r}_i^+$ can be considered as a discretized version of the topological skeleton of the scatterer (for vanishing d_{min}), and, together with their respective radii R_i^+, they constitute a discretized version of the Medial Axis Transform of the scatterer (a compact shape descriptor of S). Finally, for a given surface S and for given d_{min}, d_{max} we consider an optimization process that determines $\mathbf{r}_i^+$, $\mathbf{R}_i^+$, while minimizing the number of the spheres N. In Fig. 4.8, we illustrate the geometry of the problem for the exemplary case of a scatterer of the shape of a rotationally symmetric prolate spheroid.

We will consider the surface S^+ to be the input/output surface/port of the scatterer (see also the discussion for scattering systems with zero genus topologically in Section 2.9). Specifically, we will solve the scattering problem of calculating the scattered field outside of S^+, i.e., in $V_{S^{+\text{out}}}$, once the incident field inside S^+, i.e., in $V_{S^{+\text{in}}}$, is known. We will consider that the incident field does not have any singularities inside S^+ and may only have such singularities in $V_{S^{+\text{out}}}$. On the other hand, the scattered field shall have singularities in its analytic continuation inside S. To solve this scattering problem we need to quantize the representations of the incident and scattered fields that are valid everywhere inside their respective physical domains.

Regarding the incident field, we can expand it into a series of regular VSHs with respect to the N multipolar centers of expansion at $\mathbf{r}_i^+$. However, such expansions shall generally only be valid, though, inside a sphere of radius R_i^+ that is only a part of $V_{S^{+\mathrm{in}}}$. This is because, generally, there may be singularities (e.g. from radiating emitters, or neighboring scatterers) anywhere outside of S^+. Hence we have:

$$\mathbf{E}^{\mathrm{inc}}(\mathbf{r},\omega) = \sum_{\nu\mu_z,\alpha} \mathcal{A}^{\mathrm{inc}}_{\alpha,\mu_z\nu,i}(\omega)\mathbf{F}^{(1)}_{\alpha,\mu_z\nu}(\mathbf{r}-\mathbf{r}_i^+;k), \quad \text{for } |\mathbf{r}-\mathbf{r}_i^+|<R_i^+, \tag{4.21}$$

with $\mathcal{A}^{\mathrm{inc}}_{\alpha,\mu_z\nu,i}(\omega)$ being some complex coefficients. However, we can get an expression for the incident field that is valid everywhere in $V_{S^{+\mathrm{in}}}$ by making use of the Stratton-Chu expression of Eq. (4.3) for the case of integration across the surface S^+. Additionally, making use of Eq. (4.21) to substitute the incident fields for the surface currents in the right-hand side of the equation across each part S_i^+ of S^+, and the first branch of Eq. (2.161) together with the translation: $\overleftrightarrow{\mathbf{G}}(\mathbf{r},\mathbf{r}_0;k)=\overleftrightarrow{\mathbf{G}}(\mathbf{r}-\mathbf{r}_i^+,\mathbf{r}_0-\mathbf{r}_i^+;k)$, for $\mathbf{r}_0\in S_i^+$, for the expansion of the DGF into a series of regular VSHs centered at $\mathbf{r}_i^+$ across each part S_i^+ of S^+, we readilly get the following quantized representation of the incident field that is valid everywhere inside S_i^+:

$$\mathbf{E}^{\mathrm{inc}}(\mathbf{r},\omega) = \sum_{i=1}^{N}\sum_{\nu\mu_z,\alpha} \mathcal{A}^{\mathrm{inc}}_{\alpha,\mu_z\nu,i}(\omega)\mathbf{E}^{\mathrm{inc}}_{\alpha,\mu_z\nu,i}(\mathbf{r},\omega), \quad \text{for } \mathbf{r}\in V_{S^{+\mathrm{in}}}, \tag{4.22}$$

where:

$$\mathbf{E}^{\mathrm{inc}}_{\alpha,\mu_z\nu,i}(\mathbf{r},\omega) = \int_{S_i^+} \mathrm{i}kZ\overleftrightarrow{\mathbf{G}}(\mathbf{r},\mathbf{r}_0;k)\cdot\mathbf{J}^{\mathrm{inc,e}}_{\alpha,\mu_z\nu,i}(\mathbf{r}_0,\omega) - \nabla\times\overleftrightarrow{\mathbf{G}}(\mathbf{r},\mathbf{r}_0;k)\cdot\mathbf{J}^{\mathrm{inc,m}}_{\alpha,\mu_z\nu,i}(\mathbf{r}_0,\omega)\mathrm{d}^2\mathbf{r}_0, \tag{4.23}$$

is the electric field radiated inside S^+ by the following electric and magnetic surface current sources distributed over S_i^+:

$$\begin{aligned}
\mathbf{J}^{\mathrm{inc,e}}_{\alpha,\mu_z\nu,i}(\mathbf{r}_0,\omega) &= \frac{\mathrm{i}}{Z}\left[\hat{\mathbf{n}}(\mathbf{r}_0)\times\mathbf{F}^{(1)}_{\beta,\mu_z\nu}(\mathbf{r}_0-\mathbf{r}_i^+;k)\right] \\
&= \frac{\mathrm{i}^{\delta_{\alpha\mathrm{N}}}}{Z} z^{(1)}_{\beta,\nu}(kR_i^+)\mathbf{f}_{\alpha,\mu_z\nu}(\hat{\mathbf{r}}_{0i}^+), \qquad (4.24)\\
\mathbf{J}^{\mathrm{inc,m}}_{\alpha,\mu_z\nu,i}(\mathbf{r}_0,\omega) &= \hat{\mathbf{n}}(\mathbf{r}_0)\times\mathbf{F}^{(1)}_{\alpha,\mu_z\nu}(\mathbf{r}_0-\mathbf{r}_i^+;k) \\
&= (-\mathrm{i})^{\delta_{\alpha\mathrm{N}}} z^{(1)}_{\alpha,\nu}(kR_i^+)\mathbf{f}_{\beta,\mu_z\nu}(\hat{\mathbf{r}}_{0i}^+), \qquad (4.25)
\end{aligned}$$

where $\beta\neq\alpha$. Here we introduce also the variables θ_{0i}^+, ϕ_{0i}^+ which are the polar and azimuthal angles that correspond to a coordinate system that is parallel to the global one and centered at $\mathbf{r}=\mathbf{r}_i^+$. The spherical unit vectors attached to this translated coordinate system will be denoted as $(\hat{\mathbf{r}}_{0i}^+,\hat{\boldsymbol{\theta}}_{0i}^+,\hat{\boldsymbol{\phi}}_{0i}^+)$. Note that those two angles, θ_{0i}^+, ϕ_{0i}^+, can be used to parametrize each spherical surface patch of S_i^+. $z^{(\iota)}_{\alpha,\nu}(x)$ are the generalized spherical Bessel functions and the functions $\mathbf{f}_{\alpha,\mu_z\nu}(\hat{\mathbf{r}}_{0i}^+)$ are given by Eqs. (2.142, 2.143) with respect to the aforementioned coordinate system. To get the final expressions of the above currents, we

made use of the definition of VSHs and the fact that the normal vector $\hat{\mathbf{n}}(\mathbf{r}_0)$ on S_i^+ is the radial one, with respect to that translated coordinate system.

On the other hand, regarding the scattered field, we can employ Eqs. (4.18, 4.19) from the previous section and expand it into a series of radiating VSHs with respect to the N multipolar centers of expansion at $\mathbf{r} = \mathbf{r}_i^+$. We obtain the following quantized representation of the scattered field that is valid everywhere outside of S_i^+:

$$\mathbf{E}^{\mathrm{sca}}(\mathbf{r},\omega) \equiv \sum_{i=1}^{N}\sum_{\alpha,\mu_z\nu,i}\mathcal{A}^{\mathrm{sca}}_{\alpha,\mu_z\nu,i}(\omega)\mathbf{F}^{(3)}_{\alpha,\mu_z\nu}(\mathbf{r}-\mathbf{r}_i^+;k), \quad \text{for} \quad \mathbf{r}\in V_{S^{+\mathrm{out}}}, \tag{4.26}$$

with the complex amplitudes being given by:

$$\begin{aligned}\mathcal{A}^{\mathrm{sca}}_{\alpha,\mu_z\nu,i}(\omega) = \mathrm{i}k^2(-1)^{\mu_z}\int_{S_i^+}\mathrm{d}^2\mathbf{r}_0\Big[&\mathrm{i}Z\mathbf{F}^{(1)}_{\alpha,-\mu_z\nu}(\mathbf{r}_0-\mathbf{r}_i^+;k)\cdot[\hat{\mathbf{n}}\times\mathbf{H}^{\mathrm{sca}}(\mathbf{r}_0,\omega)]\\ &+\mathbf{F}^{(1)}_{\beta,-\mu_z\nu}(\mathbf{r}_0-\mathbf{r}_i^+;k)\cdot[\hat{\mathbf{n}}\times\mathbf{E}^{\mathrm{sca}}(\mathbf{r}_0,\omega)]\Big].\end{aligned} \tag{4.27}$$

where $\mathbf{H}^{\mathrm{sca}}(\mathbf{r}_0,\omega)$ is the scattered magnetic field.

Finally, we can construct a distributed T-matrix, $\hat{\mathbf{T}}(\omega)$, to represent the scatterer by employing the attained quantized representations of the incident and scattered field and truncating the infinite multipolar sums in Eqs. (4.22, 4.26). Note that, also according to the relevant discussion in the previous section, the smaller the optical distance between the singularities of the incident field and the surface S_i^+ and the larger the optical distance between the center of multipolar expansion $\mathbf{r}_i^+$ and the surface S_i^+ (i.e., the larger the radius R_i^+ is), the larger the number of multipoles that needs to be taken into account for the $i-$th expansion center typically is. We can calculate the elements of the distributed T-matrix using a full-wave solver, where we excite the scatterer with the surface current distributions, $\left[\mathbf{J}^{\mathrm{inc,e}}_{\alpha',\mu_z'\nu',i'}(\mathbf{r}_0,\omega),\mathbf{J}^{\mathrm{inc,m}}_{\alpha',\mu_z'\nu',i'}(\mathbf{r}_0,\omega)\right]$, and then we record the corresponding scattered fields on S_i^+ (parametrized with respect to the angles $\theta_{0i}^+,\phi_{0i}^+$, instead of $\mathbf{r}_0$), $\left[\mathbf{E}^{\mathrm{sca}}_{\alpha',\mu_z'\nu',i'}(\theta_{0i}^+,\phi_{0i}^+,\omega),\mathbf{H}^{\mathrm{sca}}_{\alpha',\mu_z'\nu',i'}(\theta_{0i}^+,\phi_{0i}^+,\omega)\right]$, and we decompose them on the basis set that we constructed for the scattered fields using Eq. (4.27). Introducing the angular domains Θ_{0i}^+ and $\Phi_{0i}^+(\theta_{0i}^+)$ in the 2D space defined by the angles θ_{0i}^+, ϕ_{0i}^+, which characterize the spherical patches of S_i^+ once they are parametrized by those angles and substituting the definition of VSHs in Eq. (4.27), we get the following formula for the elements of the distributed T-matrix of the scatterer:

$$\begin{aligned}&\langle\alpha\,\mu_z\,\nu\,i\,\omega|\,\hat{\mathbf{T}}(\omega)\,|\alpha'\,\mu_z'\,\nu'\,i'\,\omega\rangle =\\ &\mathrm{i}^{2\mu_z+2+\delta_{\alpha\mathrm{N}}}\gamma_{-\mu_z\nu}(x_i^+)^2\int_{\Theta_{0i}^+}\sin\theta_{0i}^+\,\mathrm{d}\theta_{0i}^+\int_{\Phi_{0i}^+(\theta_{0i}^+)}\mathrm{d}\phi_{0i}^+\,e^{-\mathrm{i}\mu_z\phi_{0i}^+}\times\\ &\Big\{\big(\hat{\mathbf{x}}\cos\theta_{0i}^+\cos\phi_{0i}^+ + \hat{\mathbf{y}}\cos\theta_{0i}^+\sin\phi_{0i}^+ - \hat{\mathbf{z}}\sin\theta_{0i}^+\big)\cdot\\ &\Big[z^{(1)}_{\beta,\nu}(x_i^+)\tau^{(1+\delta_{\alpha\mathrm{N}})}_{-\mu_z\nu}(\theta_{0i}^+)\mathbf{E}^{\mathrm{sca}}_{\alpha',\mu_z'\nu',i'} - (-1)^{\delta_{\alpha\mathrm{N}}}z^{(1)}_{\alpha,\nu}(x_i^+)\tau^{(2-\delta_{\alpha\mathrm{N}})}_{-\mu_z\nu}(\theta_{0i}^+)Z\mathbf{H}^{\mathrm{sca}}_{\alpha',\mu_z'\nu',i'}\Big] +\\ &\big(-\mathrm{i}\hat{\mathbf{x}}\sin\phi_{0i}^+ + \mathrm{i}\hat{\mathbf{y}}\cos\phi_{0i}^+\big)\cdot\\ &\Big[z^{(1)}_{\beta,\nu}(x_i^+)\tau^{(2-\delta_{\alpha\mathrm{N}})}_{-\mu_z\nu}(\theta_{0i}^+)\mathbf{E}^{\mathrm{sca}}_{\alpha',\mu_z'\nu',i'} - (-1)^{\delta_{\alpha\mathrm{N}}}z^{(1)}_{\alpha,\nu}(x_i^+)\tau^{(1+\delta_{\alpha\mathrm{N}})}_{-\mu_z\nu}(\theta_{0i}^+)Z\mathbf{H}^{\mathrm{sca}}_{\alpha',\mu_z'\nu',i'}\Big]\Big\},\end{aligned} \tag{4.28}$$

where $x_i^+ = k(\omega)R_i^+$ and we omitted the arguments $(\theta_{0i}^+,\phi_{0i}^+,\omega)$ of the fields for brevity.

Like this, we can fill each column of the distributed T-matrix by performing a single simulation with a full-wave solver, where we illuminate the scatterer with the radiating surface currents that correspond to some particular multipole centered at one of the N centers of expansion and which are distributed over the corresponding spherical patches. After we record the corresponding scattered fields, we can calculate numerically the above integrals. Note that, inverting the system matrix of the full-wave solver (e.g. of the FEM solver in frequency domain), allows for the efficient calculation of the response of the scatterer upon multiple excitations, since then solving for different excitations simply becomes a matrix-vector multiplication.

Finally, by introducing the column vectors $\vec{\mathcal{A}}^{\rm inc}(\omega), \vec{\mathcal{A}}^{\rm sca}(\omega)$ containing the coefficients of the incident and the scattered fields, $\mathcal{A}^{\rm inc}_{\alpha,\mu_z\nu,i}(\omega), \mathcal{A}^{\rm sca}_{\alpha,\mu_z\nu,i}(\omega)$, we arrive at the following equation with the distributed T-matrix of the scatterer relating the coefficients of the incident field with the coefficients of the scattered field:

$$\vec{\mathcal{A}}^{\rm sca}(\omega) \;=\; \hat{\mathbf{T}}(\omega)\cdot\vec{\mathcal{A}}^{\rm inc}(\omega). \tag{4.29}$$

Let us now discuss another practical issue related with the above full-wave simulations for the calculation of the distributed T-matrix of the scatterer. The radiating currents $\left[\mathbf{J}^{\rm inc,e}_{\alpha',\mu'_z\nu',i'}(\mathbf{r}_0,\omega), \mathbf{J}^{\rm inc,m}_{\alpha',\mu'_z\nu',i'}(\mathbf{r}_0,\omega)\right]$ typically radiate fields with rather large gradients in their vicinity. Therefore, a very fine spatial discretization is needed in the vicinity of those surface current distributions in the full-wave solver. Moreover, the subtraction of the incident field from the total field to get the scattered field response over S^+ may not be numerically accurate for the same reason. Hence, it is typically more convenient to solve directly for the scattered field, instead of the total field, with the full-wave solver. This can be done by considering as a source the radiation of some effective extrinsic, volumetric, electric and magnetic polarization density inside the domain of the scatterer. Expressions for the latter can be derived by working as follows. First, let us write the Maxwell's equations that govern the incident and the total fields in our distributed T-matrix simulations described above:

$$\left(\begin{bmatrix}\mathbf{0} & \nabla\times\\ \nabla\times & \mathbf{0}\end{bmatrix} - \mathrm{i}\omega\begin{bmatrix}-\varepsilon(\omega)\mathbf{I} & \mathbf{0}\\ \mathbf{0} & \mu(\omega)\mathbf{I}\end{bmatrix}\right)\cdot\begin{bmatrix}\mathbf{E}^{\rm inc}_{\alpha',\mu'_z\nu',i'}\\ \mathbf{H}^{\rm inc}_{\alpha',\mu'_z\nu',i'}\end{bmatrix} \;=\; \begin{bmatrix}\mathbf{J}^{\rm inc,e}_{\alpha',\mu'_z\nu',i'}\\ -\mathbf{J}^{\rm inc,m}_{\alpha',\mu'_z\nu',i'}\end{bmatrix}\quad, \tag{4.30}$$

$$\left(\begin{bmatrix}\mathbf{0} & \nabla\times\\ \nabla\times & \mathbf{0}\end{bmatrix} - \mathrm{i}\omega\begin{bmatrix}\varepsilon_0\left[\mathbf{I}+\boldsymbol{\chi}_{\rm ee}(\mathbf{r},\omega)\right] & \sqrt{\varepsilon_0\mu_0}\boldsymbol{\chi}_{\rm em}(\mathbf{r},\omega)\\ \sqrt{\varepsilon_0\mu_0}\boldsymbol{\chi}_{\rm me}(\mathbf{r},\omega) & \mu_0\left[\mathbf{I}+\boldsymbol{\chi}_{\rm mm}(\mathbf{r},\omega)\right]\end{bmatrix}\right)\cdot\begin{bmatrix}\mathbf{E}^{\rm tot}_{\alpha',\mu'_z\nu',i'}\\ \mathbf{H}^{\rm tot}_{\alpha',\mu'_z\nu',i'}\end{bmatrix} = \begin{bmatrix}\mathbf{J}^{\rm inc,e}_{\alpha',\mu'_z\nu',i'}\\ -\mathbf{J}^{\rm inc,m}_{\alpha',\mu'_z\nu',i'}\end{bmatrix}\quad, \tag{4.31}$$

where $\varepsilon(\omega)$ and $\mu(\omega)$ are the dielectric permittivity and magnetic permeability of the background medium and $\boldsymbol{\chi}_{\rm ee}(\mathbf{r},\omega)$, $\boldsymbol{\chi}_{\rm em}(\mathbf{r},\omega)$, $\boldsymbol{\chi}_{\rm me}(\mathbf{r},\omega)$, $\boldsymbol{\chi}_{\rm mm}(\mathbf{r},\omega)$, are the susceptibility tensors that characterize the scatterer, which we consider to be local for simplicity. Subtracting the two equations above, results in the following Maxwell equations that the scattered fields obey:

$$\left(\begin{bmatrix}\mathbf{0} & \nabla\times\\ \nabla\times & \mathbf{0}\end{bmatrix} - \mathrm{i}\omega\begin{bmatrix}-\varepsilon_0\left[\mathbf{I}+\boldsymbol{\chi}_{\rm ee}(\mathbf{r},\omega)\right] & -\sqrt{\varepsilon_0\mu_0}\boldsymbol{\chi}_{\rm em}(\mathbf{r},\omega)\\ \sqrt{\varepsilon_0\mu_0}\boldsymbol{\chi}_{\rm me}(\mathbf{r},\omega) & \mu_0\left[\mathbf{I}+\boldsymbol{\chi}_{\rm mm}(\mathbf{r},\omega)\right]\end{bmatrix}\right)\cdot\begin{bmatrix}\mathbf{E}^{\rm sca}_{\alpha',\mu'_z\nu',i'}\\ \mathbf{H}^{\rm sca}_{\alpha',\mu'_z\nu',i'}\end{bmatrix} = \begin{bmatrix}-\mathrm{i}\omega\mathbf{P}^{\rm extr,e}_{\alpha',\mu'_z\nu',i'}\\ \mathrm{i}\omega\mathbf{P}^{\rm extr,m}_{\alpha',\mu'_z\nu',i'}\end{bmatrix}\quad, \tag{4.32}$$

with the effective extrinsic polarization densities induced inside the scatterer being given by the following equation:

$$\begin{bmatrix} \mathbf{P}^{\mathrm{extr,e}}_{\alpha',\mu_z'\nu',i'} \\ \mathbf{P}^{\mathrm{extr,m}}_{\alpha',\mu_z'\nu',i'} \end{bmatrix} = \begin{bmatrix} \varepsilon_0\left[\mathbf{I}+\boldsymbol{\chi}_{\mathrm{ee}}(\mathbf{r},\omega)\right]-\varepsilon(\omega)\mathbf{I} & \sqrt{\varepsilon_0\mu_0}\boldsymbol{\chi}_{\mathrm{em}}(\mathbf{r},\omega) \\ \sqrt{\varepsilon_0\mu_0}\boldsymbol{\chi}_{\mathrm{me}}(\mathbf{r},\omega) & \mu_0\left[\mathbf{I}+\boldsymbol{\chi}_{\mathrm{mm}}(\mathbf{r},\omega)\right]-\mu(\omega)\mathbf{I} \end{bmatrix} \cdot \begin{bmatrix} \mathbf{E}^{\mathrm{inc}}_{\alpha',\mu_z'\nu',i'} \\ \mathbf{H}^{\mathrm{inc}}_{\alpha',\mu_z'\nu',i'} \end{bmatrix}. \tag{4.33}$$

Note that the effective extrinsic polarization densities vanish outside the scatterer. They can be injected inside the simulation once the fields $\mathbf{E}^{\mathrm{inc}}_{\alpha',\mu_z'\nu',i'}$, $\mathbf{H}^{\mathrm{inc}}_{\alpha',\mu_z'\nu',i'}$ are known. The latter can be either calculated numerically with a full-wave solver that lets the currents $\mathbf{J}^{\mathrm{inc,e}}_{\alpha',\mu_z'\nu',i'}$, $\mathbf{J}^{\mathrm{inc,m}}_{\alpha',\mu_z'\nu',i'}$ propagate inside the background medium in the absence of the scatterer, or, alternatively, they can be retrieved semi-analytically by evaluating the integrals of Eq. (4.23). Specifically, substituting there the expressions of Eqs. (4.24, 4.25), as well as the expressions of the DGF and its curl (see Eqs. (8.55, 8.57) in [275]), we get the following equations that are suitable for semi-analytical evaluations:

$$\begin{aligned} \mathbf{E}^{\mathrm{inc}}_{\alpha,\mu_z\nu,i}(\mathbf{r},\omega) &= -(R_i^+)^2\gamma_{\mu_z\nu}e^{\mathrm{i}\mu_z\phi}\int_{\Theta^+_{0i}}\sin\theta^+_{0i}\,\mathrm{d}\theta^+_{0i}\times \\ &\quad\left\{k\,z^{(1)}_{\beta,\nu}(x_i^+)(-\mathrm{i})^{\delta_{\alpha\mathrm{M}}}\left[\sum_p \mathrm{i}^{\delta_{pp_\phi}}\tau^{(1+\Delta)}_{\mu_z\nu}(\theta^+_{0i})\mathbf{I}^{\mathrm{e}}_{p,\mu_z,i}(\mathbf{r},\omega;\theta^+_{0i})\right]+\right. \\ &\quad\left. z^{(1)}_{\alpha,\nu}(x_i^+)(-\mathrm{i})^{\delta_{\alpha\mathrm{N}}}\left[\sum_p \mathrm{i}^{\delta_{pp_\phi}}\tau^{(2-\Delta)}_{\mu_z\nu}(\theta^+_{0i})\mathbf{I}^{\mathrm{m}}_{p,\mu_z,i}(\mathbf{r},\omega;\theta^+_{0i})\right]\right\}, \end{aligned} \tag{4.34}$$

$$\begin{aligned} \mathbf{H}^{\mathrm{inc}}_{\alpha,\mu_z\nu,i}(\mathbf{r},\omega) &= -\frac{(R_i^+)^2}{\mathrm{i}Z}\gamma_{\mu_z\nu}e^{\mathrm{i}\mu_z\phi}\int_{\Theta^+_{0i}}\sin\theta^+_{0i}\,\mathrm{d}\theta^+_{0i}\times \\ &\quad\left\{z^{(1)}_{\beta,\nu}(x_i^+)(-\mathrm{i})^{\delta_{\alpha\mathrm{M}}}\left[\sum_p \mathrm{i}^{\delta_{pp_\phi}}\tau^{(1+\Delta)}_{\mu_z\nu}(\theta^+_{0i})\mathbf{I}^{\mathrm{m}}_{p,\mu_z,i}(\mathbf{r},\omega;\theta^+_{0i})\right]+\right. \\ &\quad\left. k\,z^{(1)}_{\alpha,\nu}(x_i^+)(-\mathrm{i})^{\delta_{\alpha\mathrm{N}}}\left[\sum_p \mathrm{i}^{\delta_{pp_\phi}}\tau^{(2-\Delta)}_{\mu_z\nu}(\theta^+_{0i})\mathbf{I}^{\mathrm{e}}_{p,\mu_z,i}(\mathbf{r},\omega;\theta^+_{0i})\right]\right\}, \end{aligned} \tag{4.35}$$

where p is an index taking the values $\{p_\theta, p_\phi\}$ and $\Delta = \delta_{\alpha\mathrm{M}}\delta_{pp_\phi} + \delta_{\alpha\mathrm{N}}\delta_{pp_\theta}$. Moreover, we have defined the following integrals (in the cylindrical coordinate system (ρ,ϕ,z)):

$$\begin{aligned} \mathbf{I}^{\mathrm{e}}_{p_\theta,\mu_z,i}(\mathbf{r},\omega;\theta^+_{0i}) &= e^{-\mathrm{i}\mu_z\phi}\int_{\Phi^+_{0i}(\theta^+_{0i})}\mathrm{d}\phi^+_{0i}\,e^{\mathrm{i}\mu_z\phi^+_{0i}}\overleftrightarrow{\mathbf{G}}(\mathbf{r}-\mathbf{r}_i^+,R_i^+\hat{\mathbf{r}}_i^+(\theta^+_{0i},\phi^+_{0i});k)\cdot\hat{\boldsymbol{\theta}}^+_{0i} = \\ &\quad\begin{bmatrix}\hat{\boldsymbol{\rho}}\\ \hat{\boldsymbol{\phi}}\\ \hat{\mathbf{z}}\end{bmatrix}^{\mathrm{T}}\cdot\int_{\Phi^+_{0i}(\theta^+_{0i})}\mathrm{d}\phi^+_{0i}\,e^{-\mathrm{i}\mu_z\Phi_0}\frac{e^{\mathrm{i}kR}}{4\pi R}\left\{\frac{k^2R^2+\mathrm{i}kR-1}{k^2R^2}\begin{bmatrix}\cos\theta^+_{0i}\cos\Phi_0\\ -\cos\theta^+_{0i}\sin\Phi_0\\ -\sin\theta^+_{0i}\end{bmatrix}+\right. \\ &\quad\frac{3-3\mathrm{i}kR-k^2R^2}{k^2R^4}\left[\cos\theta^+_{0i}[\rho\cos\Phi_0-\rho_i^+\cos(\Phi_0-\Phi)]-(z-z_i^+)\sin\theta_{0i}\right]\times \\ &\quad\left.\begin{bmatrix}\rho-\rho_i^+\cos\Phi-R_i^+\sin\theta^+_{0i}\cos\Phi_0\\ \rho_i^+\sin\Phi+R_i^+\sin\theta^+_{0i}\sin\Phi_0\\ z-z_i^+-R_i^+\cos\theta^+_{0i}\end{bmatrix}\right\}, \end{aligned} \tag{4.36}$$

$$\mathbf{I}^{\mathrm{e}}_{p_\phi,\mu_z,i}(\mathbf{r},\omega;\theta^+_{0i}) \;=\; e^{-\mathrm{i}\mu_z\phi}\int_{\Phi^+_{0i}(\theta^+_{0i})}\mathrm{d}\phi^+_{0i}\,e^{\mathrm{i}\mu_z\phi^+_{0i}}\overleftrightarrow{\mathbf{G}}(\mathbf{r}-\mathbf{r}^+_i,R^+_i\hat{\mathbf{r}}^+_i(\theta^+_{0i},\phi^+_{0i});k)\cdot\hat{\boldsymbol{\phi}}^+_{0i} \;=$$
$$\begin{bmatrix}\hat{\boldsymbol{\rho}}\\ \hat{\boldsymbol{\phi}}\\ \hat{\mathbf{z}}\end{bmatrix}^{\mathrm{T}}\cdot\int_{\Phi^+_{0i}(\theta^+_{0i})}\mathrm{d}\phi^+_{0i}\,e^{-\mathrm{i}\mu_z\Phi_0}\frac{e^{\mathrm{i}kR}}{4\pi R}\left\{\frac{k^2R^2+\mathrm{i}kR-1}{k^2R^2}\begin{bmatrix}\sin\Phi_0\\ \cos\Phi_0\\ 0\end{bmatrix}+\right.$$
$$\left.\frac{3-3\mathrm{i}kR-k^2R^2}{k^2R^4}\left[\rho\cos\Phi_0-\rho^+_i\cos(\Phi_0-\Phi)\right]\begin{bmatrix}\rho-\rho^+_i\cos\Phi-R^+_i\sin\theta^+_{0i}\cos\Phi_0\\ \rho^+_i\sin\Phi+R^+_i\sin\theta^+_{0i}\sin\Phi_0\\ z-z^+_i-R^+_i\cos\theta^+_{0i}\end{bmatrix}\right\}, \quad (4.37)$$

$$\mathbf{I}^{\mathrm{m}}_{p_\theta,\mu_z,i}(\mathbf{r},\omega;\theta^+_{0i}) \;=\; e^{-\mathrm{i}\mu_z\phi}\int_{\Phi^+_{0i}(\theta^+_{0i})}\mathrm{d}\phi^+_{0i}\,e^{\mathrm{i}\mu_z\phi^+_{0i}}\nabla\times\overleftrightarrow{\mathbf{G}}(\mathbf{r}-\mathbf{r}^+_i,R^+_i\hat{\mathbf{r}}^+_i(\theta^+_{0i},\phi^+_{0i});k)\cdot\hat{\boldsymbol{\theta}}^+_{0i} \;=$$
$$\begin{bmatrix}\hat{\boldsymbol{\rho}}\\ \hat{\boldsymbol{\phi}}\\ \hat{\mathbf{z}}\end{bmatrix}^{\mathrm{T}}\cdot\int_{\Phi^+_{0i}(\theta^+_{0i})}\mathrm{d}\theta^+_{0i}\mathrm{d}\phi^+_{0i}\,e^{-\mathrm{i}\mu_z\Phi_0}\frac{e^{\mathrm{i}kR}}{4\pi R}\times$$
$$\frac{\mathrm{i}kR-1}{R^2}\begin{bmatrix}(z-z^+_i)\cos\theta^+_{0i}\sin\Phi_0-\rho^+_i\sin\theta^+_{0i}\sin\Phi-R^+_i\sin\Phi_0\\ \rho\sin\theta^+_{0i}-\rho^+_i\sin\theta^+_{0i}\cos\Phi+(z-z^+_i)\cos\theta^+_{0i}\cos\Phi_0-R^+_i\cos\Phi_0\\ \rho^+_i\cos\theta^+_{0i}\sin(\Phi_0-\Phi)-\rho\cos\theta^+_{0i}\sin\Phi_0\end{bmatrix}, \quad (4.38)$$

$$\mathbf{I}^{\mathrm{m}}_{p_\phi,\mu_z,i}(\mathbf{r},\omega;\theta^+_{0i}) \;=\; e^{-\mathrm{i}\mu_z\phi}\int_{\Phi^+_{0i}(\theta^+_{0i})}\mathrm{d}\phi^+_{0i}\,e^{\mathrm{i}\mu_z\phi^+_{0i}}\nabla\times\overleftrightarrow{\mathbf{G}}(\mathbf{r}-\mathbf{r}^+_i,R^+_i\hat{\mathbf{r}}^+_i(\theta^+_{0i},\phi^+_{0i});k)\cdot\hat{\boldsymbol{\phi}}^+_{0i} \;=$$
$$\begin{bmatrix}\hat{\boldsymbol{\rho}}\\ \hat{\boldsymbol{\phi}}\\ \hat{\mathbf{z}}\end{bmatrix}^{\mathrm{T}}\cdot\int_{\Phi^+_{0i}(\theta^+_{0i})}\mathrm{d}\theta^+_{0i}\mathrm{d}\phi^+_{0i}\,e^{-\mathrm{i}\mu_z\Phi_0}\frac{e^{\mathrm{i}kR}}{4\pi R}\times$$
$$\frac{\mathrm{i}kR-1}{R^2}\begin{bmatrix}-\cos\Phi_0\left[z-z^+_i-R^+_i\cos\theta^+_{0i}\right]\\ \sin\Phi_0\left[z-z^+_i-R^+_i\cos\theta^+_{0i}\right]\\ \rho\cos\Phi_0-\rho^+_i\cos(\Phi_0-\Phi)-R^+_i\sin\theta^+_{0i}\end{bmatrix}, \quad (4.39)$$

where with $(\rho^+_i,\phi^+_i,z^+_i)$ we denoted the cylindrical coordinates of the $i-$th center of expansion located at $\mathbf{r}=\mathbf{r}^+_i$. Moreover, we defined the following quantities: $\Phi_0=\phi-\phi^+_{0i}$, $\Phi=\phi-\phi^+_i$, $Q=\sin\theta^+_{0i}[\rho\cos\Phi_0-\rho^+_i\cos(\Phi_0-\Phi)]+(z-z^+_i)\cos\theta^+_{0i}$, and $R=|\mathbf{r}-\mathbf{r}^+_i-R^+_i\hat{\mathbf{r}}^+_i(\theta^+_{0i},\phi^+_{0i})|=\sqrt{\rho^2+(\rho^+_i)^2+(z-z^+_i)^2+(R^+_i)^2-2R^+_iQ-2\rho\rho^+_i\cos\Phi}$. We would like to note that for small values of R, i.e., for small optical distances between the scatterer and the auxiliary surface S^+, the convergence of the above integrals may become slow. This is the reason why we introduced a minimum distance $d_{\min}$ between S and S^+ in the first place (see Fig. 4.8). In our exemplary study of a prolate spheroid (which we will discuss in what follows) we implemented both methods of evaluating the fields $\mathbf{E}^{\mathrm{inc}}_{\alpha',\mu'_z\nu',i'}$, $\mathbf{H}^{\mathrm{inc}}_{\alpha',\mu'_z\nu',i'}$ (semi-analytically and fully numerically) and we got equally good results with roughly equal speed. However, that only involved the simulation of a scatterer in two dimensions because of its rotational symmetry. Moreover, in this case, the evaluation of the integrals in Eqs. (4.36-4.39) can be easily performed analytically for the same reason.

Let us present now an example of the above described calculations of the distributed T-matrix of a scatterer. The numerical simulations below have been performed with the finite element method in frequency domain provided by COMSOL Multiphysics [261]. We consider a prolate spheroid with an aspect ratio of six, made of a non-magnetic material with a refractive index of 3.477. The scatterer is embedded in free space and its minor

axis is ten times smaller than the free space wavelength λ. First of all we calculate the discretized topological skeleton of such a scatterer by asking $d_{\min}$ to be at least 1% and $d_{\max}$ to be at most 2% of the free space wavelength. We end up with sixteen centers of multipolar expansions that are distributed along the rotational symmetry axis (z-axis) and in a symmetric way with respect to $z = 0$. Note that the placement of those centers of multipolar expansions is such that it abides to the spatial symmetries of the scatterer. Placing the multipoles along the symmetry axis facilitates the construction of eigenstates of the fields with well-defined angular momentum along the symmetry axis, whereas the symmetric placement of the centers with respect to the $z = 0$ axis could facilitate the construction of eigenstates of the fields with even and odd mirror symmetry with respect to the $z = 0$ plane (e.g., if the multipoles are taken into symmetric couples of zero and π phase difference, respectively).

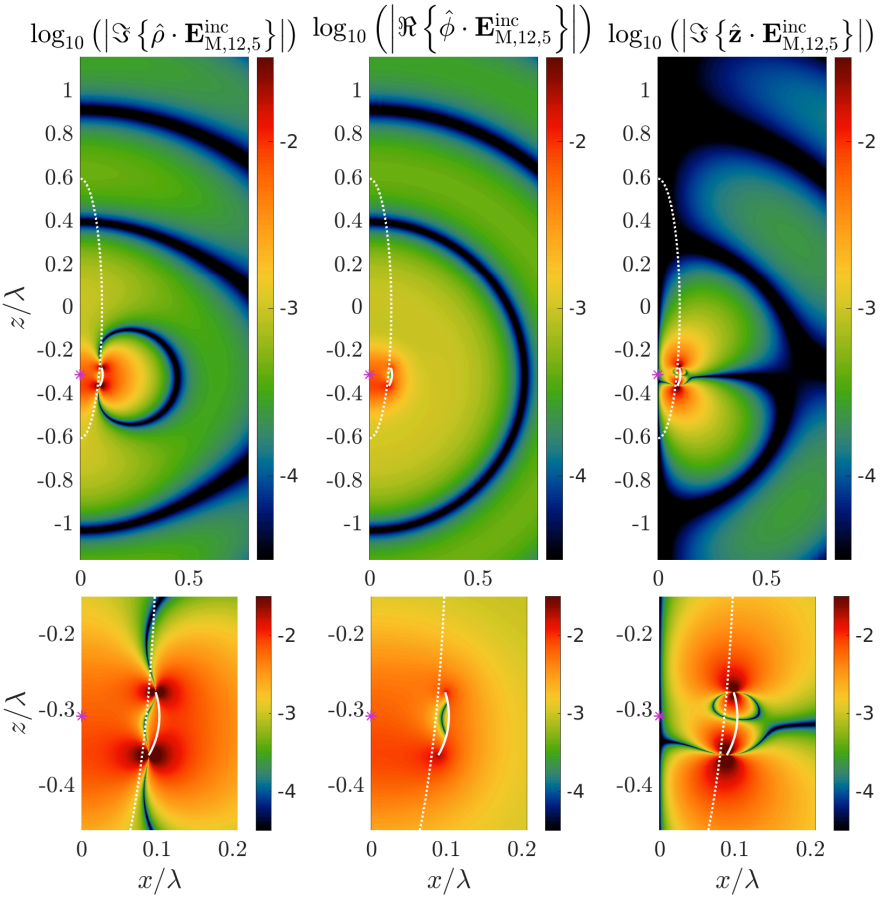

Figure 4.9: First step of the calculation of the distributed T-matrix of a prolate spheroid: Calculation of fields radiated in free space by the surface currents of Eqs. (4.24, 4.25) that are distributed across the spherical zone S_i^+ (white solid line). Specifically, we are interested in the fields inside the scatterer, i.e., inside the surface S (denoted with a white dotted line), so that, in the second step of our calculations, we plug them in Eq. (4.33) to compute the extrinsic polarization densities, which will constitute the effective sources for the scattered field calculations in the third step.

Once we have calculated the discretized topological skeleton of the scatterer, we start constructing its distributed T-matrix, column by column. The procedure for the calculation of each column is split in *four steps*. First of all, each column of the T-matrix corresponds to the excitation of the scatterer by some particular surface current distribu-

tion $\mathbf{J}^{\mathrm{inc,e}}_{\alpha',\mu'_z\nu',i'}$, $\mathbf{J}^{\mathrm{inc,m}}_{\alpha',\mu'_z\nu',i'}$ given by Eqs. (4.24, 4.25), distributed across a spherical zone S_i^+. In Fig. 4.9, we plot in logarithmic scale a cross-section (at the $\phi = 0$ meridian plane) of the (rotationally symmetric) fields radiated by those currents in free space for the case of $\mu'_z = 1$, $\nu' = 2$ and for the $i' = 5$-th multipolar site (denoted with a magenta star in the figure and located at $z_i^+ \simeq -0.307\lambda$). The spherical zone S_i^+ (of radius $R_i^+ \simeq 0.103\lambda$ and of polar-angular span between $\theta_{0i}^+ \simeq 72.25^o$ and $\theta_{0i}^+ \simeq 120.32^o$) that hosts the radiating currents is plotted with a white solid curve, whereas the surface of the scatterer S is plotted with a white dotted curve. Note the large field gradients in the vicinity of the current distribution. Here, we are interested to record those radiating fields, $\mathbf{E}^{\mathrm{inc}}_{\alpha',\mu'_z\nu',i'}$, $\mathbf{H}^{\mathrm{inc}}_{\alpha',\mu'_z\nu',i'}$, inside the volume of the scatterer, i.e., inside the white dotted surface S. The non-zero separation distance $d_{\min}$ helps to avoid recording nearly-singular fields inside S, which constitutes, numerically, a handicap. The computation of those radiating fields in free space, inside S, constitutes the first step of our calculations. It can be performed with either full-wave simulations (e.g., with a FEM, frequency domain solver). or semi-analytically by computing the integrals of Eqs. (4.34, 4.35).

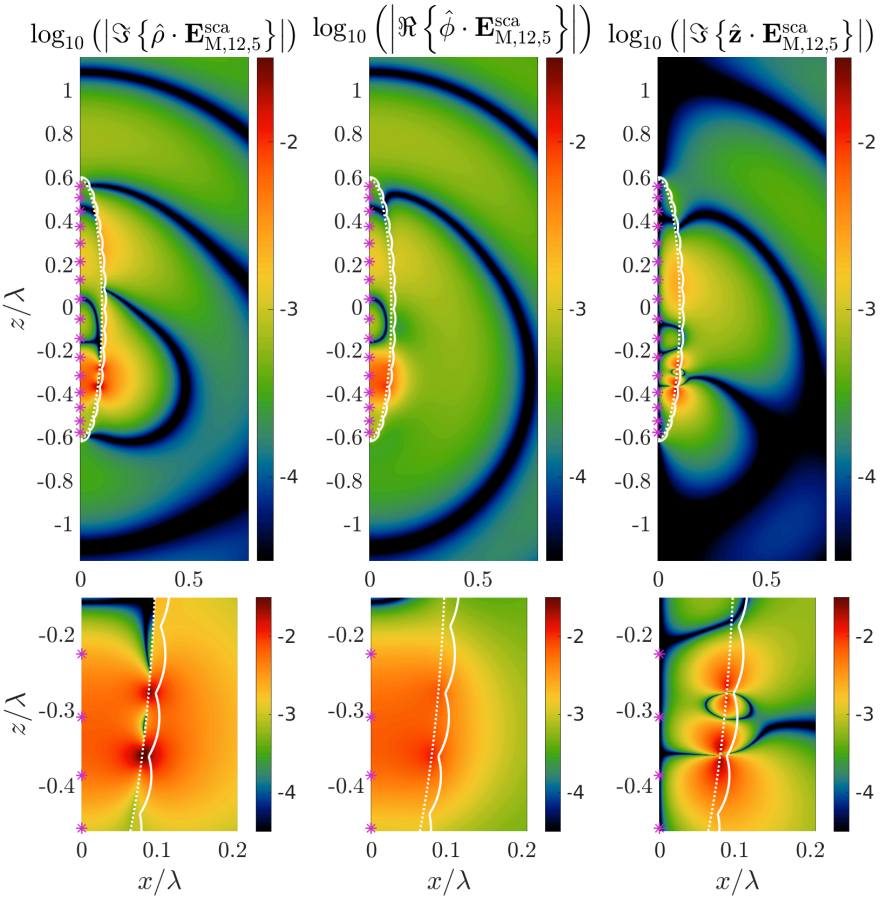

Figure 4.10: Third step of the calculation of the distributed T-matrix of a prolate spheroid: Solving the Maxwell equations of Eq. (4.32) (with a full-wave solver) for the excitation that corresponds to the surface-currents radiation of Fig. 4.9. The discretized topological skeleton of the scatterer is denoted with magenta stars, the surface of the scatterer S is plotted with a white dotted curve and the auxiliary input/output surface S^+ is plotted with a white solid curve. In the last (fourth) step of the calculations, we will record the scattered fields on S^+ and evaluate the elements of a column of the distributed T-matrix of the scatterer by making use of Eq. (4.28).

In the second step of our distributed T-matrix calculations, we plug the computed radiated fields, $\mathbf{E}^{\mathrm{inc}}_{\alpha',\mu'_z\nu',i'}$, $\mathbf{H}^{\mathrm{inc}}_{\alpha',\mu'_z\nu',i'}$, from the first step inside Eq. (4.33) to compute the extrinsic polarization densities $\mathbf{P}^{\mathrm{extr,e}}_{\alpha',\mu'_z\nu',i'}$, $\mathbf{P}^{\mathrm{extr,m}}_{\alpha',\mu'_z\nu',i'}$, which will act as sources for the scattered field calculations in the third step that will follow (see Eq. (4.32)).

Next, in the third step of our distributed T-matrix calculations, we perform a simulation with a full-wave solver to solve the Maxwell equations of Eq. (4.32). In Fig. 4.10, we plot the solution that we got for the excitation that corresponds to the surface-currents radiation of Fig. 4.9. The discretized topological skeleton of the scatterer with the sixteen multipolar sites are illustrated with magenta stars.

Finally, in the last step, we want to decompose the scattered-field response upon the quantized multipolar basis set that we constructed for the representation of an arbitrary scattered field (see Eq. (4.26)). Performing this projection of the recorded scattered fields on that Hilbert space of, essentially constitutes the calculation of the elements of the correspoding column of the distributed T-matrix of the scatterer. This is done by recording the scattered fields on each segment S_i^+ of the auxiliary input/output surface S^+ (denoted with a white solid curve in Fig. 4.10), and then by making use of Eq. (4.28), which involves the evaluation of projection integrals for each segment S_i^+.

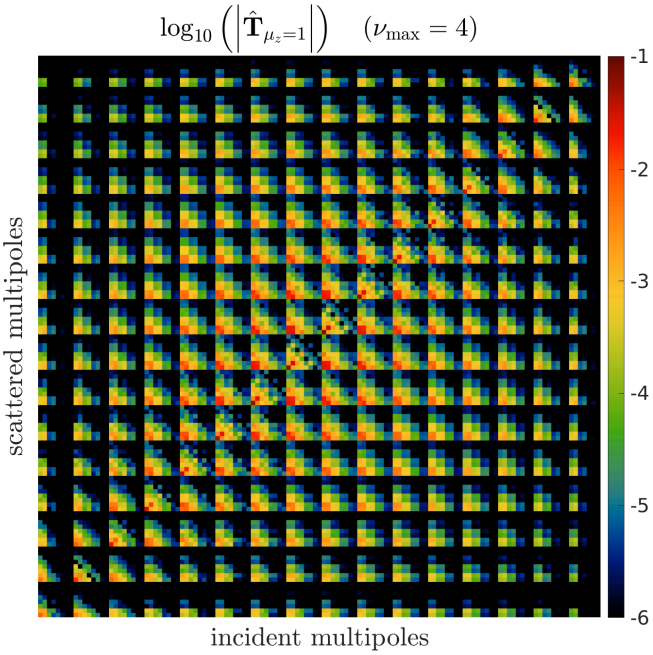

Figure 4.11: Plot of the elements (in logarithmic scale) of the distributed T-matrix of the prolate spheroid for $\mu_z = 1$ and for $\nu_{\max} = 4$. The separation of the matrix into 16×16 blocks, corresponding to interactions among the different multipolar sites of the topological skeleton can be observed. The diagonal blocks correspond to "local" interactions and the off-diagonal blocks correspond to "non-local" interactions. Moreover, each such block contains the specific interaction among the 8 considered multipoles (4 TE + 4 TM) in ascending multipolar order.

Consequently, repeating those four steps that we just described for all considered excitations, we can calculate entirely the distributed T-matrix of the scatterer column by column. Note that, in our exemplary case of the prolate spheroid, the distributed T-matrix, due to the rotational symmetry of the scatterer (with which the representations of the fields that we constructed abide, as we discussed already), is block-diagonal with respect to the angular momentum along the z-axis (μ_z), i.e., the axis of symmetry. In Fig. 4.11, we

plot the calculated norm (in logarithmic scale) of the elements of the $\mu_z = 1$ block of the distributed T-matrix of our exemplary scatterer, for a truncation of the multipolar series at $\nu_{\max} = 4$. Note that, the particular block is further separated into 16×16 sub-blocks, which correspond to the interactions among the 16 multipolar sites of our discretized topological skeleton of the prolate spheroid. The diagonal blocks correspond to "local" interactions, whereas the off-diagonal blocks correspond to "non-local" interactions. Furthermore, each of those sub-blocks contains multipolar interactions among the 8 considered multipoles (4 TE + 4 TM, for $\nu_{\max} = 4$). The sub-blocks are ordered with ascending $z-$coordinate of the center of expansion z_i^+ and the multipoles within each sub-block are ordered in ascending multipolar order (with alternating TE, TM multipoles).

In Fig. 4.11, we can observe that the strength of the multipolar transitions diminishes rapidly with increasing multipolar order. This is because the radii R_i^+ of the surface patches S_i^+ are optically quite small and, therefore, only the lowest multipolar orders are enough to represent the propagating part of the respective radiation, with the higher multi-polar orders contributing only to the representation of the evanescent near-fields. Moreover, we can observe that the multipolar transitions between multipoles that are located closer to the $z = 0$ plane are generally stronger, whereas the multipolar transitions between multipoles that are located near the tips of the prolate spheroid are generally weaker by orders of magnitude.

Next, having calculated the T-matrix of the exemplary scatterer, let us also demonstrate a practical example of how it can be used to model the response of the scatterer upon some arbitrary illuminating field. Specifically, let us consider the simple case of the excitation of the scatterer by a monochromatic (of frequency ω_0), circularly polarized plane wave propagating along the positive $z-$direction:

$$\mathbf{E}^{\text{inc}}(\mathbf{r}, \omega_0) \quad = \quad \left(\hat{\boldsymbol{\rho}} + \mathrm{i}\hat{\boldsymbol{\phi}} \right) e^{\mathrm{i}(\omega_0 z/c_0 + \phi)}. \tag{4.40}$$

Note that the above illumination constitutes a field of well-defined helicity and angular momentum $\lambda = \mu_z = 1$. Therefore, only the $\mu_z = 1$ block of the distributed T-matrix of the rotationally symmetric scatterer is receiving an input in this case. Specifically, the expansion of the incident field of Eq. (4.40) into the representation of Eq. (4.21) is done by using Eq. (2.152), resulting in the following amplitudes:

$$\mathcal{A}^{\text{inc}}_{\alpha,\mu_z\nu,i}(\omega_0) \quad = \quad \delta_{\mu_z 1}\, 4\pi\gamma_{-1\nu}\mathrm{i}^{\nu+1} e^{\mathrm{i}\omega_0 z_i^+/c_0}. \tag{4.41}$$

Note that it is possible to calculate those complex coefficients for arbitrarilly complex excitations, and, once we have the distributed T-matrix of the scatterer, getting its scattering response (represented by the scattered field coefficients) becomes a simple matter of vector-matrix multiplication (see Eq. (4.29)).

In Fig. 4.12a, we plot the scattered field upon such excitation, as it was recorded by a full-wave solver, and in Fig. 4.12b, we plot the logarithmic relative error $\mathcal{E}(\mathbf{r}, \omega_0)$, defined in Eq. (4.20), to compare the numerical results with the semi-analytical results obtained with the distributed T-matrix method, i.e., after making use of Eqs. (4.41, 4.29) (together with the spatial representations of the radiating VSHs from Section 2.6) into Eq. (4.26) to reconstruct the scattered fields. We observe an excellent agreement between the two results. Even for a low-dimensional representation of $\nu_{\max} = 4$ and $N = 16$ points in the discretized topological skeleton, we were able to transcend the problem of the Rayleigh Hypothesis and push the boundaries of validity of the reconstructed fields rather close to the surface of the scatterer S. Note that, at the limit of $\nu_{\max} \to \infty$ a fully convergent

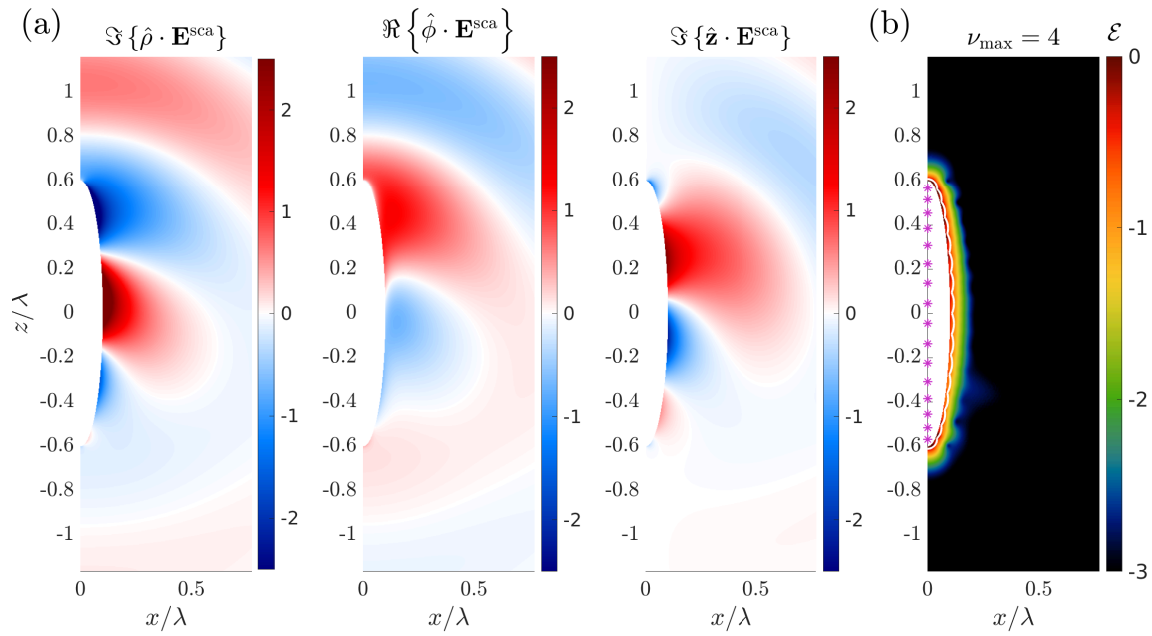

Figure 4.12: Exemplary comparison of the T-matrix method with a full-wave solver for the case of an illumination of the prolate spheroid by a circularly polarized plane wave propagating along the positive z-axis: a) The scattered fields as they were calculated by the full-wave solver. b) Map of the logarithmic relative error, $\mathcal{E}$, between the scattered fields obtained by the full-wave solver and the ones obtained by the distributed T-matrix method.

representation of the fields is expected to be obtained everywhere outside the auxiliary input/output surface S^+ (denoted by a white solid curve in the figure).

Thus, in Fig. 4.13, we demonstrate the rate of convergence of the series expansion of the near-fields in our exemplary case. Specifically, we plot maps of the logarithmic relative errors $\mathcal{E}(\mathbf{r},\omega_0)$ for five cases of $\nu_{\max}=\{2,4,8,16,24\}$. We observe that, whereas the convergence of the multipolar series is quite fast for intermediate (even relatively small) distances between the observation point and the scatterer, this is not the case as we approach rather close to the auxiliary surface S^+. There, the evanescent fields are stronger and the convergence of the multipolar series becomes quite slow, i.e., a large number of multipoles are needed for an accurate representation of the fields.

Finally, let us note that, even though the auxiliary input/output surface S^+ in our analysis above was considered to be the union of segments of spherical surfaces S_i^+, this shall not strictly be the case. This choice was made because it somehow simplifies the theoretical analysis that we presented above. However, proceeding in a similar way, the formulas in this section can be generalized for the general case of the auxiliary surface S^+ being an arbitrary surface fully enclosing the scatterer (and its bounding surface S). This approach may be more convenient depending on the actual implementation of the algorithm. Nevertheless, such generalized auxiliary surfaces S^+ again need to be somehow properly divided into N parts S_i^+, with each part being associated with a particular center of expansion in the discretized topological skeleton of the scatterer. Specifically, each S_i^+ shall contain those parts of S^+ that are closer to the $i-$th center of expansion (whose positions also need to be optimized). Note, though, that, even though the auxiliary surface is not selected to be a union of spherical segments, the region of validity of a representation of the scattered fields in terms of such a discretized distribution of multipolar sources inside the scatterer shall, still, always be bounded by such a union of spherical segments enclosing

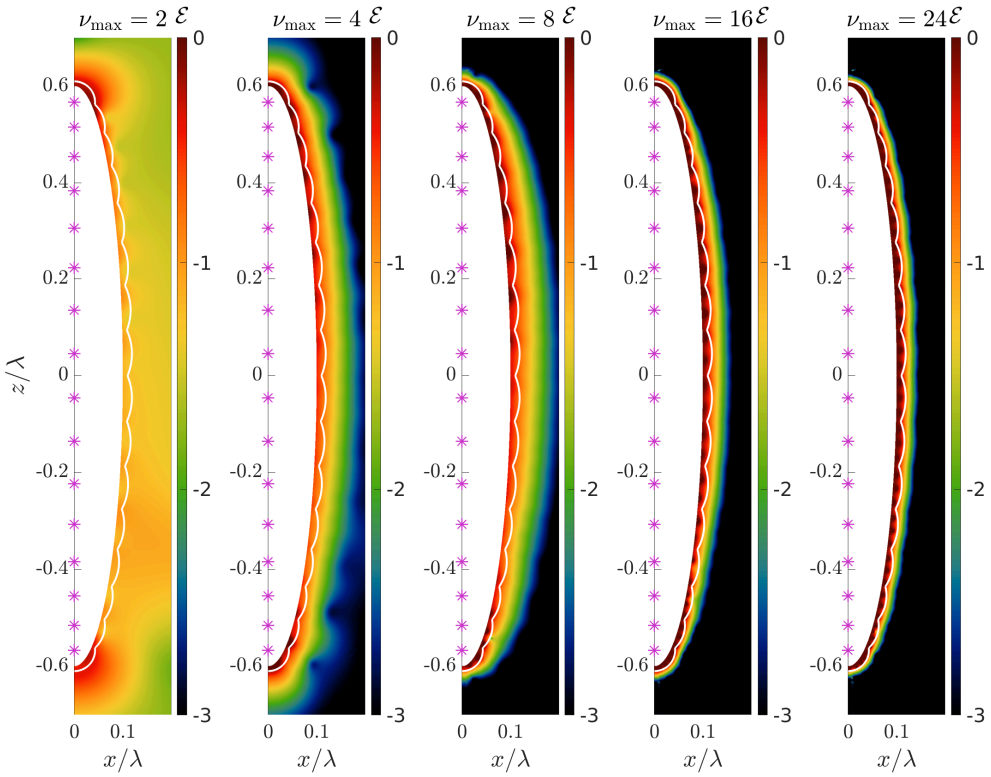

Figure 4.13: Illustration of the rate of convergence of the series expansion of the near-fields at the close vicinity of the prolate spheroid. At the limit of $\nu_{\max} \to \infty$ we expect a full convergence of the series everywhere outside the auxiliary input/output surface S^+ (denoted by a white solid curve). Note that a conventional representation of the fields in terms of a localized series of VSHs located at the center of the spheroid is not valid inside the sphere passing from the two foci of the spheroid.

the scatterer. Finally, note that the process of discretized skeletonization of scatterers of arbitrary geometry can be performed with such methods as the ones presented, e.g., in Ref. [289, 290] (see for example the first figure of Ref. [289], which can be adjusted from the physics point of view to generate discretized topological skeletons of scatterers of arbitrary geometry with varying $d_{\max}$). For the simple case of prolate spheroids that we demonstrated in this section, this we could simply do this discretized skeletonization semi-analytically.

4.5 Generalizing multiple light scattering calculations for the case of distributed T-matrices

In this section, we will briefly discuss the generalization of the conventional multiple light scattering method (see Section 5.9 in Ref. [257]) for the case of distributed T-matrices, which transcend the problem of the Rayleigh Hypothesis and are, therefore, suitable for an arbitrary multiple light scattering scenario, even if it involves strong near-field coupling phenomena. There, the modeling of the multi-scattering problem with the conventional T-matrix would typically fail due to the complications that arise from the Rayleigh Hypothesis.

Here we consider the case of light interaction with N_s stationary scatterers of arbitrary shape that do not touch each other. The scatterers are embedded inside a stationary,

homogeneous, and isotropic medium characterized by some wavenumber $k(\omega)$ and wave-impedance $Z(\omega)$. As long as the scatterers do not touch each other, there exists some distributed T-matrix of large enough dimensionality that overcomes the problem of the Rayleigh Hypothesis in that it allows to model the near-field coupling between neighboring scatterers.

In what follows, we will denote with $\hat{\mathbf{T}}_j$ the distributed T-matrix of the $j-$th scatterer, and, as a convention, we will consider that the multipoles of the representations of each distributed T-matrix are always with well-defined angular momentum with respect to the $+\hat{\mathbf{z}}-$axis of the global coordinate system, i.e., they are all commonly oriented. As we will see, the requirement of such common orientation facilitates the translation of the scattered fields by using the translation addition theorem of VSHs, without applying an extra rotation of the fields. Moreover, for each scatterer, we consider a local coordinate system attached specifically to it. The local coordinate system is parallel to the global coordinate system. The origin of the local coordinate system of the $j-$th scatterer is located at $\mathbf{r} = \mathbf{r}_{O_j}$. $\mathbf{r}_{O_j}$ can be an arbitrarily selected point, but, as we will see in the following, choosing it to be the center of the minimal sphere circumscribing the scatterer will provide minimal auxiliary local representations of the fields, which will assist their efficient translation. Furthermore, we consider that the $i-$th center of multipolar expansions of the topological skeleton of the $j-$th scatterer is located at $\mathbf{r} = \mathbf{r}_{j,i}$ and the number of those centers are N_j. Generally, we consider that the multipolar series for the $i-$th center of expansion of the $j-$th scatterer are truncated at $\nu_{\max,j,i}$ and, therefore, the dimensionality of each distributed T-matrix, $\hat{\mathbf{T}}_j$, is $D_j = 2\sum_{i=1}^{N_j} \nu_{\max,j,i}(\nu_{\max,j,i}+2)$.

Before moving to the multi-scattering calculations, let us note that, quite frequently in multi-scattering phenomena, we have the case that the scatterers are randomly oriented. A strength of the T-matrix method is that we can analytically obtain the T-matrix of a rotated version of a given scatterer based on the known T-matrix of the non-rotated scatterer. For example, let us consider a first scatterer with a distributed T-matrix $\hat{\mathbf{T}}_j$. The T-matrix of a scatterer that is a rotated version of the first scatterer, and is specifically obtained by rotating the first scatterer with a $z-y-z$ rotation through the Euler angles $(\alpha_\mathrm{r}, \beta_\mathrm{r}, \gamma_\mathrm{r})$ with respect to the scatterer's initial local coordinate system, is given by:

$$\hat{\mathbf{T}}_j^{\mathrm{rot}} = \hat{\mathbf{D}}(\alpha_\mathrm{r}, \beta_\mathrm{r}, \gamma_\mathrm{r}) \cdot \hat{\mathbf{T}}_j \cdot \hat{\mathbf{D}}(-\gamma_\mathrm{r}, -\beta_\mathrm{r}, -\alpha_\mathrm{r}), \tag{4.42}$$

where the square rotation matrix $\hat{\mathbf{D}}(\alpha_\mathrm{r}, \beta_\mathrm{r}, \gamma_\mathrm{r})$ is associated with the Wigner-D matrix (see Appendices B,C of Ref. [257]). Its elements are given by:

$$\begin{aligned}\langle \alpha\, \mu_z\, \nu\, i|\, \hat{\mathbf{D}}(\alpha_\mathrm{r}, \beta_\mathrm{r}, \gamma_\mathrm{r})\, |\alpha'\, \mu'_z\, \nu'\, i'\rangle &= \delta_{\alpha\alpha'}\delta_{\nu\nu'}\delta_{ii'} \\ &\times\ e^{-\mathrm{i}(\mu'_z\gamma_\mathrm{r}+\mu_z\alpha_\mathrm{r})}\frac{(-1)^{(\mu'_z+\mu_z)\cdot\delta_{\mu'_z<\mu_z}}}{2^{\frac{f+g}{2}}}\left[\frac{h!(f+g+h)!}{(f+h)!(g+h)!}\right]^{\frac{1}{2}} \\ &\times\ (1-\cos\beta_\mathrm{r})^{\frac{f}{2}}(1+\cos\beta_\mathrm{r})^{\frac{g}{2}}P_h^{(f,g)}(\cos\beta_\mathrm{r}),\end{aligned} \tag{4.43}$$

where $f = |\mu_z - \mu'_z|$, $g = |\mu_z + \mu'_z|$, $h = \nu - \frac{1}{2}(f+g)$, and $P_h^{(f,g)}(x)$ is the Jacobi polynomial of degree h. Importantly, note that the distributed T-matrices $\hat{\mathbf{T}}_j^{\mathrm{rot}}$ and $\hat{\mathbf{T}}_j$, have their multipoles quantized with respect to the same orientation, i.e., that of the $+\hat{\mathbf{z}}-$axis of the global coordinate system. They also have the same local coordinate system centered at $\mathbf{r} = \mathbf{r}_{O_j}$. However, note that the locations of the centers of multipolar expansions of their discretized topological skeletons differ. Specifically, the centers of expansion corresponding to $\hat{\mathbf{T}}_j^{\mathrm{rot}}$ are given by:

$$\mathbf{r}_{j,i}^{\mathrm{rot}} = \mathbf{r}_{O_j} + \mathbf{R}(\alpha_{\mathrm{r}}, \beta_{\mathrm{r}}, \gamma_{\mathrm{r}}) \cdot (\mathbf{r}_{j,i} - \mathbf{r}_{O,j}) \,, \tag{4.44}$$

where $\mathbf{R}(\alpha_{\mathrm{r}}, \beta_{\mathrm{r}}, \gamma_{\mathrm{r}})$ is a 3×3 matrix that rotates vectors through the Euler angles $\alpha_{\mathrm{r}}, \beta_{\mathrm{r}}, \gamma_{\mathrm{r}}$ following a $z-y-z$ rotation.

Next, we can move on establishing the multi-scattering problem in the framework of the distributed T-matrix of the scatterers. First, let us consider some arbitrary background field illuminating the aggregate of scatterers. The external illumination is expanded into a series of regular VSHs with respect to each center of expansion. Following the vector notation introduced in Eq. (4.29), we consider the vector $\vec{\mathcal{A}}_j^{\mathrm{inc},0}$ containing the complex coefficients representing the incident field with respect to the Hilbert space of the $j-$th scatterer (see Eq. (4.22)).

The cardinal point of the multi-scattering calculations is the fact that the effective incident field perceived by each scatterer is equal to the background incident field plus the scattered fields of all the rest of the scatterers, both represented with respect to the Hilbert space of the incident fields of that particular scatterer, i.e., as a series of regular VSHs attached to the centers of expansion of the discretized topological skeleton of that particular scatterer. Expressing the above sentence into a mathematical formula, gives us the following equation:

$$\vec{\mathcal{A}}_j^{\mathrm{sca}} = \hat{\mathbf{T}}_j \cdot \left(\vec{\mathcal{A}}_j^{\mathrm{inc},0} + \sum_{j' \neq j} \vec{\mathcal{A}}_j^{\mathrm{inc,j'}} \right), \tag{4.45}$$

with $\vec{\mathcal{A}}_j^{\mathrm{sca}}$ being the vector containing the complex coefficients representing the scattered field of the $j-$th scatterer with respect to its own Hilbert space and $\vec{\mathcal{A}}_j^{\mathrm{inc,j'}}$ is a vector containing the complex coefficients representing the scattered field of the $j'-$th scatterer with respect to the Hilbert space of the incident fields of the $j-$th scatterer. The above equation is the master equation of the multi-scattering problem. What is left so that we can solve the multi-scattering problem, is to relate the vectors $\vec{\mathcal{A}}_{j'}^{\mathrm{sca}}$ with the vectors $\vec{\mathcal{A}}_j^{\mathrm{inc,j'}}$. This is done by introducing a generalized translation matrix $\hat{\boldsymbol{\mathcal{T}}}_{j' \to j}$ that transforms between the two:

$$\vec{\mathcal{A}}_j^{\mathrm{inc,j'}} = \hat{\boldsymbol{\mathcal{T}}}_{j' \to j} \cdot \vec{\mathcal{A}}_{j'}^{\mathrm{sca}}. \tag{4.46}$$

We define those generalized translation matrices as:

$$\hat{\boldsymbol{\mathcal{T}}}_{j' \to j} = \begin{cases} \hat{\boldsymbol{\mathcal{T}}}_{j' \to j}^{\mathrm{nl} \to \mathrm{nl}}, & \text{for} \quad \left| \mathbf{r}_{O_j} - \mathbf{r}_{O_{j'}} \right| \leq R_j^{\mathrm{circ}} + R_{j'}^{\mathrm{circ}}, \\ \hat{\boldsymbol{\mathcal{T}}}_{j}^{\mathrm{l} \to \mathrm{nl}} \cdot \hat{\boldsymbol{\mathcal{T}}}_{j' \to j}^{\mathrm{l} \to \mathrm{l}} \cdot \hat{\boldsymbol{\mathcal{T}}}_{j'}^{\mathrm{nl} \to \mathrm{l}}, & \text{for} \quad \left| \mathbf{r}_{O_j} - \mathbf{r}_{O_{j'}} \right| > R_j^{\mathrm{circ}} + R_{j'}^{\mathrm{circ}}, \end{cases} \tag{4.47}$$

where with R_j^{circ} we denote the minimal radius of the sphere that is centered at $\mathbf{r} = \mathbf{r}_{O_j}$ and that circumscribes the spherical scatterer. That is to say that the two branches of the above equation correspond to the cases where those circumscribing spheres intersect or do not intersect each other. The first branch is applicable to the second case as well, but, as we will discuss in what follows, the evaluation of the matrix with the second branch is typically

quite more efficient. Let us first define the new translation matrices that we introduced in the two branches of the above equation. Note that the superscripts "nl" and "l" in those matrices refer to "non-local" and "local" representations of the respective scattered fields. "Non-local" corresponds to representations with multiple centers of multipolar expansions, as is the case with the distributed T-matrices, whereas "local" corresponds to representations with a single center of multipolar expansions, as is the case with the conventional T-matrices.

The matrix $\hat{\boldsymbol{\mathcal{T}}}^{\mathrm{nl}\to\mathrm{nl}}_{j'\to j}$ in the first branch, which corresponds to the case of overlapping circumscribing spheres, translates directly the non-locally represented scattered fields from the $j'-$th scatterer to the non-locally represented incident fields of the $j-$th scattering by simply making use of the translation addition theorem for VSHs. Specifically, we have:

$$\langle \alpha\, \mu_z\, \nu\, i|\, \hat{\boldsymbol{\mathcal{T}}}^{\mathrm{nl}\to\mathrm{nl}}_{j'\to j}\, |\alpha'\, \mu'_z\, \nu'\, i'\rangle \;=\; \mathrm{T}^{\alpha,\mu_z\nu;(3)}_{\alpha',\mu'_z\nu'}(\mathbf{r}_{j,i}-\mathbf{r}_{j',i'};k). \tag{4.48}$$

On the other hand, in the second branch, when the circumscribing spheres do not overlap, we perform the translation in three steps. With the first matrix $\hat{\boldsymbol{\mathcal{T}}}^{\mathrm{nl}\to\mathrm{l}}_{j'}$ we translate the non-locally represented radiating fields of the $j'-$th scatterer to a local representation of the radiating fields of the same scatterer. Next, with the second matrix $\hat{\boldsymbol{\mathcal{T}}}^{\mathrm{l}\to\mathrm{l}}_{j'\to j}$ we translate the locally represented radiating fields of the $j'-$th scatterer to a local representation of the incident fields of the $j-$th scatterer. Finally, with the last matrix $\hat{\boldsymbol{\mathcal{T}}}^{\mathrm{l}\to\mathrm{nl}}_{j}$ we translate the locally represented incident fields of the $j-$th scatterer to a non-local representation of the incident fields of the same scatterer. Note that this three-step approach in the second branch shall typically be quite more efficient than that of the first branch, because the matrix $\hat{\boldsymbol{\mathcal{T}}}^{\mathrm{l}\to\mathrm{l}}_{j'\to j}$ typically has significantly smaller dimensions than the matrix $\hat{\boldsymbol{\mathcal{T}}}^{\mathrm{nl}\to\mathrm{nl}}_{j'\to j}$. The dimensionality of non-local representations of the fields is typically quite larger than the local one. Hence, we only need to calculate the matrices $\hat{\boldsymbol{\mathcal{T}}}^{\mathrm{nl}\to\mathrm{l}}_{j'}$, $\hat{\boldsymbol{\mathcal{T}}}^{\mathrm{l}\to\mathrm{nl}}_{j}$ once for each scatterer, and then only calculate the small matrices $\hat{\boldsymbol{\mathcal{T}}}^{\mathrm{l}\to\mathrm{l}}_{j'\to j}$ for each pair of interacting scatterers. Due to the problem of the Rayleigh Hypothesis, we are not allowed to do this for the case of the first branch where the circumscribing spheres of the two interacting scatterers overlap. The rest three matrices of the second branch are defined as follows:

$$\langle \alpha\, \mu_z\, \nu|\, \hat{\boldsymbol{\mathcal{T}}}^{\mathrm{nl}\to\mathrm{l}}_{j'}\, |\alpha'\, \mu'_z\, \nu'\, i'\rangle \;=\; \mathrm{T}^{\alpha,\mu_z\nu;(1)}_{\alpha',\mu'_z\nu'}(\mathbf{r}_{O_{j'}}-\mathbf{r}_{j',i'};k), \tag{4.49}$$

$$\langle \alpha\, \mu_z\, \nu|\, \hat{\boldsymbol{\mathcal{T}}}^{\mathrm{l}\to\mathrm{l}}_{j'\to j}\, |\alpha'\, \mu'_z\, \nu'\rangle \;=\; \mathrm{T}^{\alpha,\mu_z\nu;(3)}_{\alpha',\mu'_z\nu'}(\mathbf{r}_{O_j}-\mathbf{r}_{O_{j'}};k), \tag{4.50}$$

$$\langle \alpha\, \mu_z\, \nu\, i|\, \hat{\boldsymbol{\mathcal{T}}}^{\mathrm{l}\to\mathrm{nl}}_{j}\, |\alpha'\, \mu'_z\, \nu'\rangle \;=\; \mathrm{T}^{\alpha,\mu_z\nu;(1)}_{\alpha',\mu'_z\nu'}(\mathbf{r}_{j,i}-\mathbf{r}_{O_{j'}};k), \tag{4.51}$$

with the translation coefficients of the translation addition theorem for VSHs being defined as (see Appendix C of Ref. [257] or Eq. (71) in Ref. [291]):

$$\mathrm{T}^{\alpha,\mu_z\nu;(\iota)}_{\alpha',\mu'_z\nu'}(\mathbf{r};k) \;=\; \mathrm{i}^{\nu-\nu'+2\mu_z+2}\sqrt{(2\nu+1)(2\nu'+1)}\; e^{\mathrm{i}(\mu'_z-\mu_z)\phi} \sum_{w=[|\nu-\nu'|+1-\delta_{\alpha\alpha'},2]}^{\nu+\nu'-1+\delta_{\alpha\alpha'}} \mathrm{i}^{w}\times$$
$$\sqrt{\frac{(w-\mu'_z+\mu_z)!}{(w+\mu'_z-\mu_z)!}}\, C^{\nu,\nu',w}_{-\mu_z,\mu'_z,\mu'_z-\mu_z}\, C^{\nu,\nu',w}_{-1,1,0}\; z^{(\iota)}_{\mathrm{M},w}(kr)\, P^{\mu'_z-\mu_z}_{w}(\cos\theta) \tag{4.52}$$

where (r,θ,ϕ) are the spherical coordinates of the vector $\mathbf{r}$ and $C^{j_1,j_2,J}_{m_1,m_2,m_1+m_2}$ are the Clebsch-Gordan coefficients. The last two functions are the generalized spherical Bessel

functions and the associated legendre functions that we have already defined before. Note that the summation over w is conducted with a step interval of 2.

Finally, by substituting Eq. (4.46) to the master equation 4.45 and repeating this for all scatterers, we readily get a linear system of equations with unknowns $\vec{\mathcal{A}}_j^{\mathrm{sca}}$ and knowns $\vec{\mathcal{A}}_j^{\mathrm{inc},0}$ whose solution reads as follows:

$$\begin{bmatrix} \vec{\mathcal{A}}_1^{\mathrm{sca}} \\ \vec{\mathcal{A}}_2^{\mathrm{sca}} \\ \vdots \\ \vec{\mathcal{A}}_{N_\mathrm{s}}^{\mathrm{sca}} \end{bmatrix} = \begin{bmatrix} \hat{\mathbf{I}} & -\hat{\mathbf{T}}_1 \cdot \hat{\boldsymbol{\mathcal{T}}}_{2\to 1} & \cdots & -\hat{\mathbf{T}}_1 \cdot \hat{\boldsymbol{\mathcal{T}}}_{N_\mathrm{s}\to 1} \\ -\hat{\mathbf{T}}_2 \cdot \hat{\boldsymbol{\mathcal{T}}}_{1\to 2} & \hat{\mathbf{I}} & \cdots & -\hat{\mathbf{T}}_2 \cdot \hat{\boldsymbol{\mathcal{T}}}_{N_\mathrm{s}\to 2} \\ \vdots & \vdots & \ddots & \vdots \\ -\hat{\mathbf{T}}_{N_\mathrm{s}} \cdot \hat{\boldsymbol{\mathcal{T}}}_{1\to N_\mathrm{s}} & -\hat{\mathbf{T}}_{N_\mathrm{s}} \cdot \hat{\boldsymbol{\mathcal{T}}}_{2\to N_\mathrm{s}} & \cdots & \hat{\mathbf{I}} \end{bmatrix}^{-1} \cdot \begin{bmatrix} \hat{\mathbf{T}}_1 \cdot \vec{\mathcal{A}}_1^{\mathrm{inc},0} \\ \hat{\mathbf{T}}_2 \cdot \vec{\mathcal{A}}_2^{\mathrm{inc},0} \\ \vdots \\ \hat{\mathbf{T}}_{N_\mathrm{s}} \cdot \vec{\mathcal{A}}_{N_\mathrm{s}}^{\mathrm{inc},0} \end{bmatrix} \tag{4.53}$$

Let us present now a simple, yet illustrative, numerical example of the above discussed multiple scattering calculations within the introduced framework of the distributed T-matrix formalism. Our aim here is to illustrate the fundamental advantages of the latter formalism in comparison with the traditional T-matrix representations based on series of localized VSHs. To that end, we consider the simple case of multiple scattering between a dimer of prolate ellipsoids at close proximity to each other, excited by a dipolar emitter placed at the center of the small gap between them. Specifically, the two ellipsoids are considered to be identical to that of the numerical example of the previous section, where their distributed T-matrix has been already calculated. They are embedded in free space, their major axis is parallel to the z-axis of the global coordinate system and their centers are located at the positions with coordinates $(x, y, z) = (\pm\lambda/20, 0, 0)$, i.e., the gap between them is considered to be 10% of the free space wavelength. At the center of the gap of the dimer, i.e., at the origin of the global coordinate system, we place a magnetic dipole moment of unitary strength that is directed towards the $+\hat{\mathbf{y}}$ direction and excites electromagnetically the dimer.

The representation of the field radiated by dipolar emitters in terms of localized series of radiating VSHs is given by Eq. (5.13) and by making use of the translation matrix of Eq. (4.50) we can calculate the vectors with the amplitudes of the incident field, $\vec{\mathcal{A}}_j^{\mathrm{inc},0}$. Then we can use those to solve the linear system of equations of Eq. (4.53) that governs the multiple scattering phenomena taking place.

It is instructive to note that it is numerically beneficial to exploit the symmetries of the system before solving it. Specifically, our system belongs to the $\mathrm{D}_{2\mathrm{h}}$ point group, which has 8 irreducible representations characterized by the 8 different combinations of even and odd mirror symmetries with respect to the yOz, xOz and xOy mirror symmetry planes. That is to say, we can use a proper unitary matrix to perform a symmetry transformation to the system of equations of Eq. (4.53) and bring it to a block diagonal form, with 8 blocks, each one corresponding to one of the irreducible representations of the $\mathrm{D}_{2\mathrm{h}}$ point group. This is simply done by considering the mirror symmetries of the VSHs, for which the reader can refer to Eqs. (5.26-5.28). Furthermore, our excitation with the $\hat{\mathbf{y}}$-polarized magnetic dipole, having an odd mirror symmetry with respect to the yOz and xOy planes and an even mirror symmetry with respect to the xOz plane, purely belongs to the $\mathrm{B}_{2\mathrm{g}}$ irreducible representation of the point group. Therefore, the dimensionality of the system of equations to be solved for our considered scenario can be effectively 8-fold reduced, which also provides us faster with numerically more stable and accurate results.

In Fig. 4.14, we perform a comparison between the scattered near fields, as they are obtained by full wave simulations with a finite element solver and by our semi-analytical multiple scattering method. The three rows of the figure correspond to cross sections of the xOz, yOz and xOy planes respectively. Due to the symmetries of the solutions, we

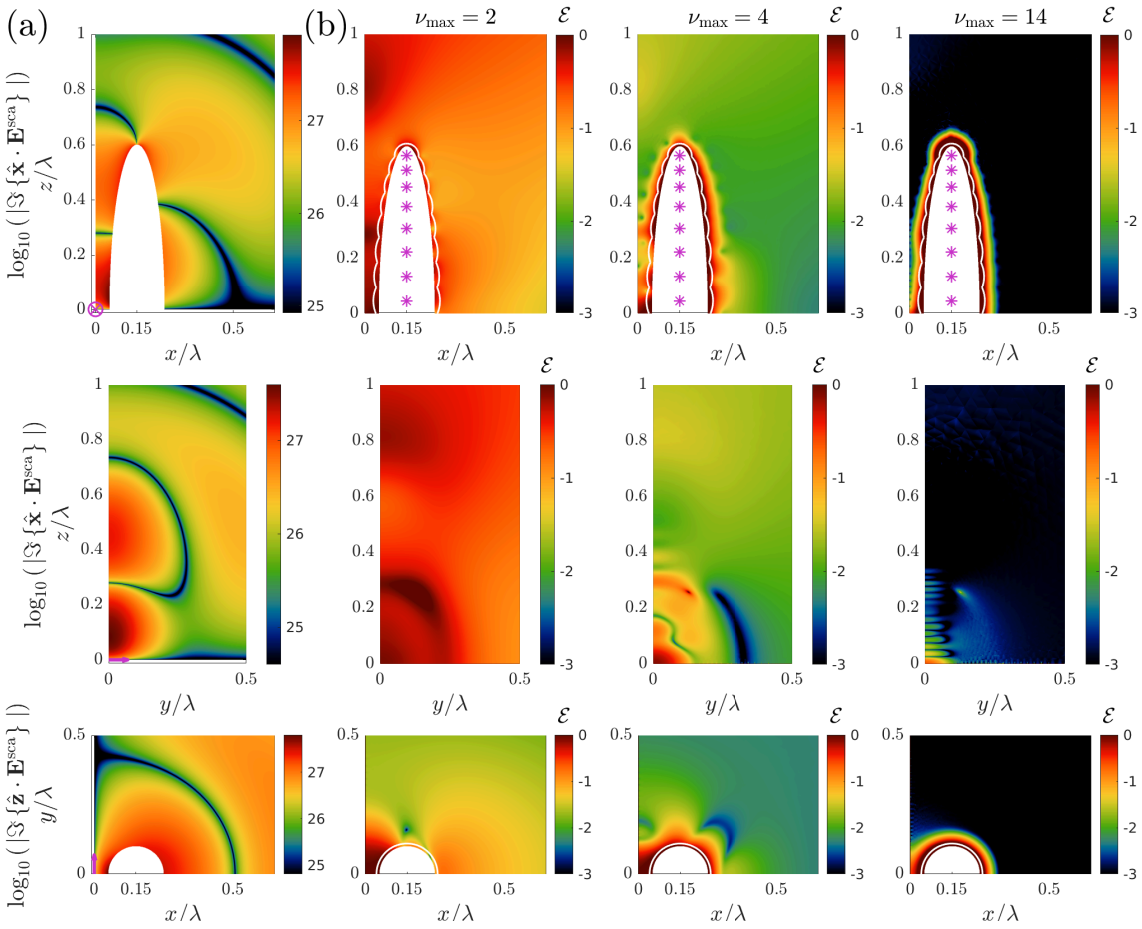

Figure 4.14: Exemplary comparison of the distributed T-matrix method with a full-wave solver for the case of an illumination of a dimer of prolate spheroids by a $\hat{\mathbf{y}}$-polarized magnetic dipole emitter placed at the center of the gap of the dimer, at the origin of the global coordinate system: a) The scattered fields, as they were calculated by the full-wave solver. b) Maps of the logarithmic relative error, $\mathcal{E}$, between the scattered fields obtained by the full-wave solver and the ones obtained by the distributed T-matrix method for three different values of $\nu_{\max}$. Due to the existing symmetries, the plots focus only on the first quadrant of the xOz, yOz and xOy planes.

only plot them for simplicity over the first quadrant of the planes. The first column of the figure, i.e., Fig. 4.14a, corresponds to the reference scattered field as it was calculated by the full wave solver. The magenta vectors symbolize the magnetic dipole emitter exciting the dimer of ellipsoids.

In Fig. 4.14b, we plot the logarithmic relative error, $\mathcal{E}$ (see Eq. (4.20)), between the semi-analytical and the numerical solutions for three different multipolar orders of truncation: $\nu_{\max} = \{2, 4, 14\}$. For the case of $\nu_{\max}$=2 we clearly observe that more multipolar terms are needed to accurately solve the considered multiple scattering problem, as the relative error of the near fields remains mainly above 10%. On the other hand, we see that a truncation multipolar order of $\nu_{\max}$=4 is already enough to mostly give decently accurate results with around 1%-3% of relative error in the near fields. However, there are still regions, especially inside the gap of the dimer that hosts strong near fields, where quite significant errors appear. Finally, for $\nu_{\max}$=14, we can see that the solution has fully converged almost everywhere and the near fields are represented with accuracy well below the 1% of relative error even inside the problematic region of the narrow gap.

It is important to note that the narrower the gap and the closer the emitter approaches the scatterers, the higher is the number of multipoles that are needed in the representations to get a convergent solution of the near fields. However, as long as the singularity of the incident field of the emitter as well as the singularities of the analytic continuation of the scattered fields of the neighboring scatterer do not intrude inside the S^+ closed surface that encloses each scatterer (which in the figure is denoted by a white line), we always expect to eventually have a convergent solution as the multipolar order of truncation, and therefore also the dimensionality of the system, gets increased.

Hence, evidently, the distributed T-matrix method is proven to be rather useful in the efficient semi-analytical treatment of problems related to, e.g., Purcell effect calculations for nanoantennas comprised by oligomers of non-spherical particles [292–295], or, generally, calculations of the optical response of complex multi-scattering systems comprised of aggregates of non-spherical particles [56, 57, 296].

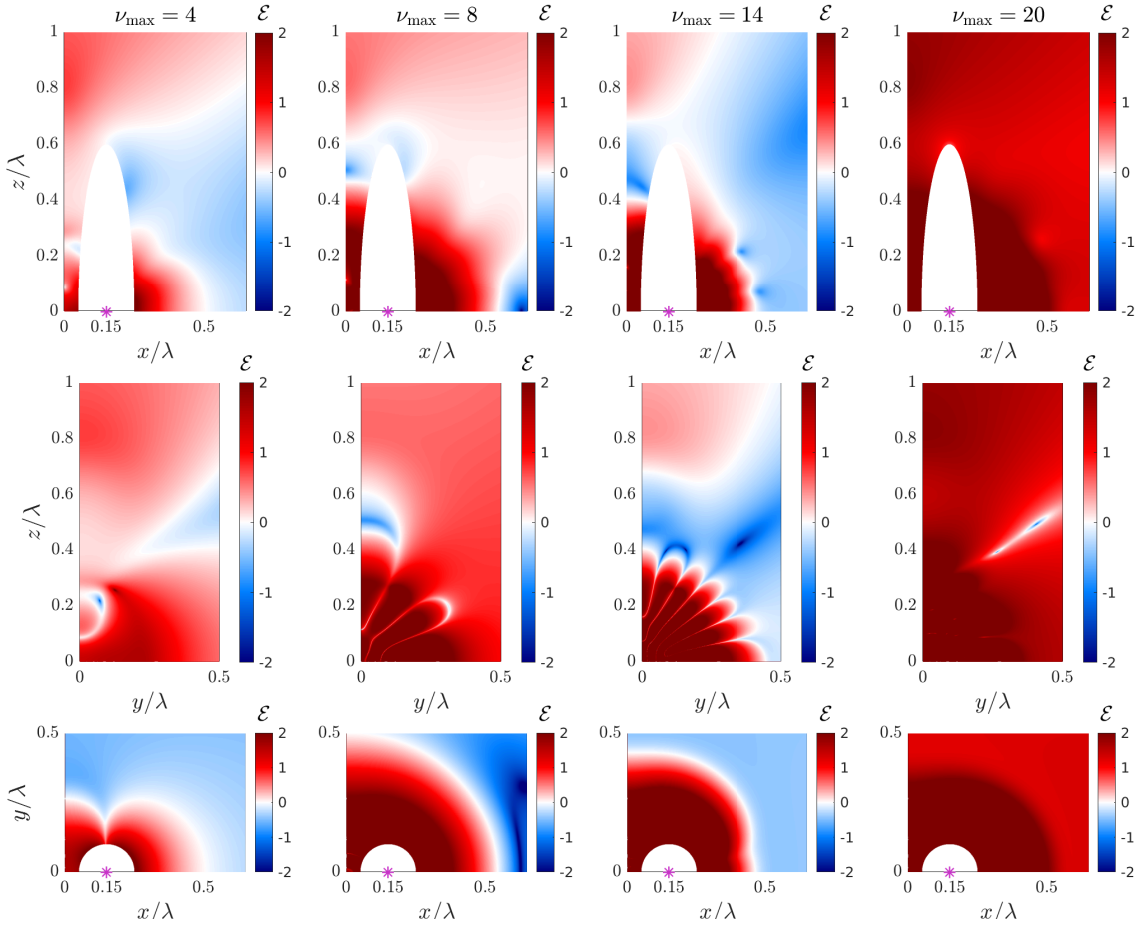

Figure 4.15: Same as Fig. 4.14b, but for the case where the semi-analytical T-matrix calculations are performed with the traditional formalism that is based on localized multipoles at the center of the scatterers (denoted with magenta stars). In contrast to Fig. 4.14, this figure demonstrates the failure of the traditional method to provide convergent results in such a multiple scattering scenario, due to the topology of the singularities of the involved fields (and their analytic continuation).

Next, we want to discuss the fundamental advantages of formulating the T-matrix method in its distributed sources variation that we introduced in this chapter, when it comes to the modeling of such complex multiple scattering phenomena like the ones that we consider as an example in this section. To that end, considering the same multiple

scattering example as before, in Fig. 4.15 we perform the same comparison as we did in Fig. 4.14b, plotting maps of the logarithmic relative errors of the near fields, but now for the case of ordinary T-matrix calculations where the fields are represented by localized series of VSHs at the center of each scatterer (denoted by magenta stars in the figure). We provide such maps for four different multipolar orders of truncation: $\nu_{\max} = \{4, 8, 14, 20\}$. Note that, by making use of the translation matrix given by Eq. (4.49), it is straightforward to obtain the ordinary T-matrix of the ellipsoids from their already previously calculated distributed T-matrix.

It can be observed that for increasing $\nu_{\max}$ the series representation of the scattered fields fails to converge and we do not get stable results. In fact, quite the contrary happens: we get errors that are orders of magnitude larger than the actual scattered fields, and after $\nu_{\max}$=20 the series even diverge everywhere. Note that the problem appears to be an incorrect evaluation of the multipolar scattering amplitudes and is not related with the particular representation of the scattered fields, since the latter, as long as the multipolar scattering amplitudes are accurately calculated, should still provide correct fields at the exterior of the spheres circumscribing the singularities of the analytic continuation of the scattered fields, even if it fails to do so at their interior. We clearly do not observe such a behavior for increasing $\nu_{\max}$ in Fig. 4.15.

The problem here seems to be that the effective incident field for each scatterer, i.e., the background field of the emitter together with the scattered field from the neighboring scatterer, is characterized by the presence of singularities within the sphere that circumscribes the scatterer. The field radiated by the emitter induces a singularity at the origin of the global coordinate system, whereas there are also further singularities in the analytic continuation of the scattered field of the neighboring scatterer in its interior. Apart of the well-known singularities at the foci of the ellipsoids, there exist also other image-singularities induced by the presence of the emitter and the neighboring scatterer at the vicinity of the ellipsoids [138]. Therefore, as a result, the effective incident field for each scatterer cannot be expanded into a convergent series of localized regular VSHs that is valid everywhere inside the circumscribing sphere of each scatterer, which renders the ordinary T-matrix formulation unable to solve the multiple scattering problem.

As we already discussed and demonstrated before, the distributed T-matrix formulation provides an efficient solution to such problems. Note that, quite bizarrely, it has been suggested in Ref. [131] that a recipe to overcome such problems with ordinary T-matrix multiple scattering calculations is to employ numerically expensive quarduple precision and use a rather large multipolar order of truncation. Other such alternative attempts for solutions involve those presented in Refs. [276–279].

Before closing this section, let us also discuss the case of multiple scattering phenomena within an infinite lattice (either 1D or 2D or 3D) [59]. Specifically, let us consider the previous aggregate of $N_{\rm s}$ scatterers comprising a unit cell of such an arbitrary infinite lattice of some discrete translational symmetry in space. The master equation of the multi-scattering system in this case reads as follows:

$$\vec{\mathcal{A}}_{j,u}^{\rm sca} \;=\; \hat{\mathbf{T}}_j \cdot \left(\vec{\mathcal{A}}_{j,u}^{\rm inc,0} + \sum_{\substack{j',u' \\ (j',u')\neq(j,u)}} \vec{\mathcal{A}}_{j,u}^{\rm inc,j',u'} \right), \tag{4.54}$$

where we introduced a further index u to refer to the $u-$th unit cell of the lattice. Next, in analogy to Eq. (4.46), we write

$$\vec{\mathcal{A}}_{j,u}^{\rm inc,j',u'} \;=\; \hat{\boldsymbol{\mathcal{T}}}_{j',u'\rightarrow j,u} \cdot \vec{\mathcal{A}}_{j',u'}^{\rm sca} \;. \tag{4.55}$$

Furthermore, since our system possesses some discrete translation symmetry in space it is instructive to introduce a spatial Floquet frequency vector $\mathbf{K}$ spanning the first Brillouin zone of the reciprocal lattice. Thus, if we further consider that we excite the lattice with some field of well-defined $\mathbf{K}$, $\vec{\mathcal{A}}^{\mathrm{inc},0}_{j,u}(\mathbf{K})$ (for which we have the symmetry $\vec{\mathcal{A}}^{\mathrm{inc},0}_{j,u'}(\mathbf{K}) = e^{\mathrm{i}\mathbf{K}\cdot\mathbf{R}_{u,u'}}\vec{\mathcal{A}}^{\mathrm{inc},0}_{j,u}(\mathbf{K})$), we additionally have that:

$$\vec{\mathcal{A}}^{\mathrm{sca}}_{j',u'}(\mathbf{K}) \;=\; e^{\mathrm{i}\mathbf{K}\cdot\mathbf{R}_{u,u'}}\vec{\mathcal{A}}^{\mathrm{sca}}_{j',u}(\mathbf{K}) \;, \tag{4.56}$$

where the vectors $\mathbf{R}_{u,u'}$ span the Bravais lattice for some fixed, arbitrary u and varying u'. Combining the above equations, and defining the following generalized lattice-sum translation matrices:

$$\hat{\boldsymbol{\mathcal{T}}}^{\mathrm{lattice}}_{j'\to j}(\mathbf{K}) \;=\; \begin{cases} \sum\limits_{u'\neq u} e^{\mathrm{i}\mathbf{K}\cdot\mathbf{R}_{u,u'}}\hat{\boldsymbol{\mathcal{T}}}_{j',u'\to j,u}, & \text{for} \quad j'=j, \\ \sum\limits_{u'} e^{\mathrm{i}\mathbf{K}\cdot\mathbf{R}_{u,u'}}\hat{\boldsymbol{\mathcal{T}}}_{j',u'\to j,u}, & \text{for} \quad j'\neq j, \end{cases} \;, \tag{4.57}$$

we finally get the following solution for the linear system of equations:

$$\begin{bmatrix} \vec{\mathcal{A}}^{\mathrm{sca}}_{1,u}(\mathbf{K}) \\ \vec{\mathcal{A}}^{\mathrm{sca}}_{2,u}(\mathbf{K}) \\ \vdots \\ \vec{\mathcal{A}}^{\mathrm{sca}}_{N_\mathrm{s},u}(\mathbf{K}) \end{bmatrix} = \begin{bmatrix} \hat{\mathbf{I}} - \hat{\mathbf{T}}_1\cdot\hat{\boldsymbol{\mathcal{T}}}^{\mathrm{lattice}}_{1\to 1}(\mathbf{K}) & -\hat{\mathbf{T}}_1\cdot\hat{\boldsymbol{\mathcal{T}}}^{\mathrm{lattice}}_{2\to 1}(\mathbf{K}) & \cdots & -\hat{\mathbf{T}}_1\cdot\hat{\boldsymbol{\mathcal{T}}}^{\mathrm{lattice}}_{N_\mathrm{s}\to 1}(\mathbf{K}) \\ -\hat{\mathbf{T}}_2\cdot\hat{\boldsymbol{\mathcal{T}}}^{\mathrm{lattice}}_{1\to 2}(\mathbf{K}) & \hat{\mathbf{I}} - \hat{\mathbf{T}}_2\cdot\hat{\boldsymbol{\mathcal{T}}}^{\mathrm{lattice}}_{2\to 2}(\mathbf{K}) & \cdots & -\hat{\mathbf{T}}_2\cdot\hat{\boldsymbol{\mathcal{T}}}^{\mathrm{lattice}}_{N_\mathrm{s}\to 2}(\mathbf{K}) \\ \vdots & \vdots & \ddots & \vdots \\ -\hat{\mathbf{T}}_{N_\mathrm{s}}\cdot\hat{\boldsymbol{\mathcal{T}}}^{\mathrm{lattice}}_{1\to N_\mathrm{s}}(\mathbf{K}) & -\hat{\mathbf{T}}_{N_\mathrm{s}}\cdot\hat{\boldsymbol{\mathcal{T}}}^{\mathrm{lattice}}_{2\to N_\mathrm{s}}(\mathbf{K}) & \cdots & \hat{\mathbf{I}} - \hat{\mathbf{T}}_{N_\mathrm{s}}\cdot\hat{\boldsymbol{\mathcal{T}}}^{\mathrm{lattice}}_{N_\mathrm{s}\to N_\mathrm{s}}(\mathbf{K}) \end{bmatrix}^{-1} \cdot \begin{bmatrix} \hat{\mathbf{T}}_1\cdot\vec{\mathcal{A}}^{\mathrm{inc},0}_{1,u}(\mathbf{K}) \\ \hat{\mathbf{T}}_2\cdot\vec{\mathcal{A}}^{\mathrm{inc},0}_{2,u}(\mathbf{K}) \\ \vdots \\ \hat{\mathbf{T}}_{N_\mathrm{s}}\cdot\vec{\mathcal{A}}^{\mathrm{inc},0}_{N_\mathrm{s},u}(\mathbf{K}) \end{bmatrix}. \tag{4.58}$$

Similarly as before, we have the following definition of the new translation matrices:

$$\hat{\boldsymbol{\mathcal{T}}}_{j',u'\to j,u} \;=\; \begin{cases} \hat{\boldsymbol{\mathcal{T}}}^{\mathrm{nl}\to\mathrm{nl}}_{j',u'\to j,u}, & \text{for} \quad \left|\mathbf{r}_{O_{j,u}} - \mathbf{r}_{O_{j',u}} - \mathbf{R}_{u,u'}\right| \leq R^{\mathrm{circ}}_j + R^{\mathrm{circ}}_{j'}, \\ \hat{\boldsymbol{\mathcal{T}}}^{\mathrm{l}\to\mathrm{nl}}_{j}\cdot\hat{\boldsymbol{\mathcal{T}}}^{\mathrm{l}\to\mathrm{l}}_{j',u'\to j,u}\cdot\hat{\boldsymbol{\mathcal{T}}}^{\mathrm{nl}\to\mathrm{l}}_{j'}, & \text{for} \quad \left|\mathbf{r}_{O_{j,u}} - \mathbf{r}_{O_{j',u}} - \mathbf{R}_{u,u'}\right| > R^{\mathrm{circ}}_j + R^{\mathrm{circ}}_{j'}, \end{cases} \tag{4.59}$$

with $\mathbf{r}_{O_{j,u}}$ denoting the origin of the local coordinate system of the $j-$th scatterer at the $u-$th unit cell of the lattice. Moreover, we define the following matrices:

$$\langle \alpha\,\mu_z\,\nu\,i|\,\hat{\boldsymbol{\mathcal{T}}}^{\mathrm{nl}\to\mathrm{nl}}_{j',u'\to j,u}\,|\alpha'\,\mu'_z\,\nu'\,i'\rangle \;=\; \mathrm{T}^{\alpha,\mu_z\nu;(3)}_{\alpha',\mu'_z\nu'}(\mathbf{r}_{j,i} - \mathbf{r}_{j',i'} - \mathbf{R}_{u,u'}; k), \tag{4.60}$$

$$\langle \alpha\,\mu_z\,\nu|\,\hat{\boldsymbol{\mathcal{T}}}^{\mathrm{l}\to\mathrm{l}}_{j',u'\to j,u}\,|\alpha'\,\mu'_z\,\nu'\rangle \;=\; \mathrm{T}^{\alpha,\mu_z\nu;(3)}_{\alpha',\mu'_z\nu'}(\mathbf{r}_{O_{j,u}} - \mathbf{r}_{O_{j',u'}} - \mathbf{R}_{u,u'}; k), \tag{4.61}$$

Finally, what is left, is to sketch a strategy for the efficient calculation of the infinite lattice sums in Eq. (4.57). This can be done by working in the following way: Let us split

the infinite sums in two parts. Specifically, let us consider that $u' = u'_{\mathrm{nl}} + u'_{\mathrm{l}}$, where, on the one hand, u'_{nl} spans all the u' for which a non-local interaction scheme is required, i.e., for which the first branch of Eq. (4.59) is picked, and, on the other hand, u'_{l} spans all the u' for which a local interaction scheme is preferred, i.e., for which the second branch of Eq. (4.59) is picked. Then Eq. (4.57) can take the following form:

$$\hat{\boldsymbol{\mathcal{T}}}^{\mathrm{lattice}}_{j'\to j}(\mathbf{K}) = \begin{cases} \left[\sum\limits_{u'_{\mathrm{nl}}\neq u} e^{\mathrm{i}\mathbf{K}\cdot\mathbf{R}_{u,u'_{\mathrm{nl}}}}\hat{\boldsymbol{\mathcal{T}}}_{j',u'_{\mathrm{nl}}\to j,u}\right] + \left[\sum\limits_{u'_{\mathrm{l}}\neq u} e^{\mathrm{i}\mathbf{K}\cdot\mathbf{R}_{u,u'_{\mathrm{l}}}}\hat{\boldsymbol{\mathcal{T}}}_{j',u'_{\mathrm{l}}\to j,u}\right], & \text{for} \quad j'=j, \\ \left[\sum\limits_{u'_{\mathrm{nl}}} e^{\mathrm{i}\mathbf{K}\cdot\mathbf{R}_{u,u'_{\mathrm{nl}}}}\hat{\boldsymbol{\mathcal{T}}}_{j',u'_{\mathrm{nl}}\to j,u}\right] + \left[\sum\limits_{u'_{\mathrm{l}}} e^{\mathrm{i}\mathbf{K}\cdot\mathbf{R}_{u,u'_{\mathrm{l}}}}\hat{\boldsymbol{\mathcal{T}}}_{j',u'_{\mathrm{l}}\to j,u}\right], & \text{for} \quad j'\neq j, \end{cases} \tag{4.62}$$

where the first of the two sums, i.e., the non-local ones, shall only contain a few terms and can be evaluated directly using the first branch of Eq. (4.59) together with Eq. (4.60). The second local sums are the ones that are infinite, but with some missing lattice terms, though. We can compensate for them, by adding and subtracting the missing non-local lattice terms to result in trully infinite sums. We proceed as follows by susbstituting with the second branch of Eq. (4.59):

$$\begin{aligned} \begin{bmatrix} \sum\limits_{u'_{\mathrm{l}}\neq u} e^{\mathrm{i}\mathbf{K}\cdot\mathbf{R}_{u,u'_{\mathrm{l}}}}\hat{\boldsymbol{\mathcal{T}}}_{j',u'_{\mathrm{l}}\to j,u} \\ \sum\limits_{u'_{\mathrm{l}}} e^{\mathrm{i}\mathbf{K}\cdot\mathbf{R}_{u,u'_{\mathrm{l}}}}\hat{\boldsymbol{\mathcal{T}}}_{j',u'_{\mathrm{l}}\to j,u} \end{bmatrix} &= \begin{bmatrix} \hat{\boldsymbol{\mathcal{T}}}^{\mathrm{l}\to\mathrm{nl}}_{j}\cdot\left(\sum\limits_{u'\neq u} e^{\mathrm{i}\mathbf{K}\cdot\mathbf{R}_{u,u'}}\hat{\boldsymbol{\mathcal{T}}}^{\mathrm{l}\to\mathrm{l}}_{j',u'\to j,u}\right)\cdot\hat{\boldsymbol{\mathcal{T}}}^{\mathrm{nl}\to\mathrm{l}}_{j'} \\ \hat{\boldsymbol{\mathcal{T}}}^{\mathrm{l}\to\mathrm{nl}}_{j}\cdot\left(\sum\limits_{u'} e^{\mathrm{i}\mathbf{K}\cdot\mathbf{R}_{u,u'}}\hat{\boldsymbol{\mathcal{T}}}^{\mathrm{l}\to\mathrm{l}}_{j',u'\to j,u}\right)\cdot\hat{\boldsymbol{\mathcal{T}}}^{\mathrm{nl}\to\mathrm{l}}_{j'} \end{bmatrix} \\ &- \begin{bmatrix} \hat{\boldsymbol{\mathcal{T}}}^{\mathrm{l}\to\mathrm{nl}}_{j}\cdot\left(\sum\limits_{u'_{\mathrm{nl}}\neq u} e^{\mathrm{i}\mathbf{K}\cdot\mathbf{R}_{u,u'_{\mathrm{nl}}}}\hat{\boldsymbol{\mathcal{T}}}^{\mathrm{l}\to\mathrm{l}}_{j',u'_{\mathrm{nl}}\to j,u}\right)\cdot\hat{\boldsymbol{\mathcal{T}}}^{\mathrm{nl}\to\mathrm{l}}_{j'} \\ \hat{\boldsymbol{\mathcal{T}}}^{\mathrm{l}\to\mathrm{nl}}_{j}\cdot\left(\sum\limits_{u'_{\mathrm{nl}}} e^{\mathrm{i}\mathbf{K}\cdot\mathbf{R}_{u,u'_{\mathrm{nl}}}}\hat{\boldsymbol{\mathcal{T}}}^{\mathrm{l}\to\mathrm{l}}_{j',u'_{\mathrm{nl}}\to j,u}\right)\cdot\hat{\boldsymbol{\mathcal{T}}}^{\mathrm{nl}\to\mathrm{l}}_{j'} \end{bmatrix}. \end{aligned} \tag{4.63}$$

Note that now the lattice sums are taking place inside the parenthesis and involve the local-to-local translation matrices. The second term that sums over u'_{nl} again typically contains a small number of terms and can be straightforwardly calculated by making use of Eq. (4.61). The first term with the infinite lattice sums over u' can be efficiently calculated by employing the Ewald summation method. In Ref. [297], the Ewald summations for such infinite lattice sums of spherical harmonics has been evaluated for arbitrary multipolar lattices. Moreover, in this work, generalized Ewald summation formulas are provided also for the case of lattice sums for arbitrarily displaced sites of summation, which corresponds to the case of $j' \neq j$ in our analysis.

Finally, before closing this section, let us emphasize that special care needs to be taken so that the auxiliary local representations of the fields, which we have introduced to facilitate the translations of the fields in this section, shall have large enough dimensionality (always with respect to the optical size of the circumscribing sphere of their respective scatterer), so that the calculated translation matrices are accurately represented.

5 — On the directional coupling of emitters into waveguides: the symmetries of the system's T-matrix and the role of the transverse angular momentum

5.1 Introduction

In this chapter, we study the directional coupling of chiral emitters into nearby waveguides, and we probe whether such a setup can be used for chiral sensing. First, in the second section, we introduce a representation of chiral emissions in terms of helical radiating VSHs. We specifically discuss the common case of dipolar emitters and do their mapping on our considered basis for the emissions. In the third section, we construct the T-matrix of the considered nanophotonic system and introduce as an observable the directionality of the coupling of the emitted light to the waveguide. Furthermore, we present our numerical results on directionality from an exemplary system. Our results on directionality are characterized by some symmetries with respect to the eigenvalues of the emissions, and, in the fourth section, we conduct a symmetry analysis of the T-matrix of the system to unveil its implications on the symmetries that we observe in the observed directionalities of our numerical experiments. The role of the transverse angular momentum of the emissions is studied in the last section. There, we identify a strong connection between the transverse angular momentum and the directionality of the evanescent part of the transverse angular spectrum responsible for the coupling of the emissions to the waveguide. Finally, we also discuss under this prism the coupling efficiency of the emissions, and we conduct a couple of extra numerical experiments with more challenging systems to check (quite successfully) the robustness of the observed phenomena of directional coupling.

5.2 A Hilbert space for chiral emissions

In this section, we introduce a Hilbert space to expand the electromagnetic radiation from general localized emitters. Specifically, since we are also interested to study the chirality of the emissions, we will introduce an appropriate basis of well-defined helicity. Finally, we will focus our discussion on dipolar emissions, which are prevalent for emitters of small optical size.

Let us consider localized emitters embedded inside an infinite, stationary, local, homogeneous, and isotropic medium characterized by a wavenumber $k(\omega)$, wave-impedance $Z(\omega)$, dielectric permittivity $\varepsilon(\omega)$, and magnetic permeability $\mu(\omega)$. The radiated electromagnetic field from such localized emitters needs obeys the Silver-Müller radiation condition at the infinite spherical surface originating at the location of the emitter. Therefore, a basis set of transverse, outgoing spherical waves is appropriate to expand their emitted electromagnetic field. As discussed in Section 2.7, the chirality of light is imprinted on its helicity, in a sense that two enantiomers of chiral emissions have opposite helicities. Hence,

a basis of radiating VSHs with well-defined helicity is appropriate to study phenomena based on the chirality of the emitted light. Those helical VSHs, are eigenstates of the helicity operator $\hat{\mathbf{\Lambda}}$ (defined in Eq. (2.162)) with eigenvalues $\lambda = \pm 1$ and are defined with respect to the TE, TM VSHs of well-defined parity (see Eqs. (2.140, 2.141, 2.184)):

$$|\lambda\,\mu_z\,\nu\,k\rangle^{(3)} \;=\; \frac{|\mathrm{M}\,\mu_z\,\nu\,k\rangle^{(3)} + \lambda\,|\mathrm{N}\,\mu_z\,\nu\,k\rangle^{(3)}}{\sqrt{2}}. \tag{5.1}$$

The real-space representation of the helical VSHs is given by substituting the expressions of Eqs. (2.140, 2.141) in the above equation and reads as:

$$\begin{aligned} |\lambda\,\mu_z\,\nu\,k\rangle^{(3)} &\equiv \mathbf{F}^{(3)}_{\lambda,\mu_z\nu}(\mathbf{r};k) \\ &= \frac{\lambda}{\sqrt{2}}\nu(\nu+1)\frac{\psi^{(3)}_{\mu_z\nu}(\mathbf{r};k)}{kr}\hat{\mathbf{r}} + \frac{\mathrm{i}}{2}\sum_{\lambda'=\pm1} z^{(3)}_{\lambda\lambda',\nu}(kr)\mathbf{f}_{\lambda',\mu_z\nu}(\hat{\mathbf{r}}), \end{aligned} \tag{5.2}$$

where we have defined the following quantities:

$$\mathbf{f}_{\lambda,\mu_z\nu}(\hat{\mathbf{r}}) \;=\; \frac{\mathbf{f}_{\mathrm{M},\mu_z\nu}(\hat{\mathbf{r}}) + \lambda\mathbf{f}_{\mathrm{N},\mu_z\nu}(\hat{\mathbf{r}})}{\sqrt{2}} = \mathrm{i}^{\nu-1}S_{\lambda,\mu_z\nu}(\theta,\phi)\;\hat{\mathbf{e}}_\lambda(\hat{\mathbf{r}}), \tag{5.3}$$

$$S_{\lambda,\mu_z\nu}(\theta,\phi) \;=\; \mathrm{i}^{1-\nu}\gamma_{\mu_z\nu}\tau^{(\lambda)}_{\mu_z\nu}(\theta)e^{\mathrm{i}\mu\phi}, \tag{5.4}$$

$$\tau^{(\lambda)}_{\mu_z\nu}(\theta) \;=\; -\tau^{(2)}_{\mu_z\nu}(\theta) - \lambda\tau^{(1)}_{\mu_z\nu}(\theta), \tag{5.5}$$

$$z^{(3)}_{\lambda\lambda',\nu}(x) \;=\; z^{(3)}_{\mathrm{M},\nu}(x) + \mathrm{i}\lambda\lambda' z^{(3)}_{\mathrm{N},\nu}(x), \tag{5.6}$$

where $\hat{\mathbf{e}}_\lambda(\hat{\mathbf{r}})$ is given by Eq. (2.186). The remaining quantities are defined in Section 2.6. Based on the result of Eq. (3.66) and the above definition, we also have the following far-field approximation of the radiating helical VSHs:

$$\left[\mathbf{F}^{(3)}_{\lambda,\mu_z\nu}(\mathbf{r};k)\right]_{kr\to\infty} \;=\; (-\mathrm{i})^\nu\;\mathbf{f}_{\lambda,\mu_z\nu}(\hat{\mathbf{r}})\;\frac{e^{\mathrm{i}kr}}{kr}. \tag{5.7}$$

Moreover, based on Eq. (2.155) and the above definition, the angular spectrum representations of the helical VSHs in terms of circularly polarized plane waves, $|\lambda\,\theta_{\hat{\mathbf{k}}}\,\phi_{\hat{\mathbf{k}}}\,k\rangle$ (defined in Eq. (2.185)), reads as follows:

$$|\lambda\,\mu_z\,\nu\,k\rangle^{(3)} \;=\; \frac{1}{2\pi}\int_0^{2\pi}\mathrm{d}\phi_{\hat{\mathbf{k}}}\int_{C^\pm}\sin\theta_{\hat{\mathbf{k}}}\mathrm{d}\theta_{\hat{\mathbf{k}}}\;S_{\lambda,\mu_z\nu}(\theta_{\hat{\mathbf{k}}},\phi_{\hat{\mathbf{k}}})\,|\lambda\,\theta_{\hat{\mathbf{k}}}\,\phi_{\hat{\mathbf{k}}}\,k\rangle\,, \quad \text{for } \mathrm{z}\gtrless 0, \tag{5.8}$$

where we need to take into account also evanescent waves by integrating over a contour on the complex polar-angle-of-propagation plane with $C^+ = [0, \frac{\pi}{2} - \mathrm{i}\infty]$ and $C^- = [\frac{\pi}{2} + \mathrm{i}\infty, \pi]$.

Finally, a general expression for the electric field radiated by such localized emitters takes the following form in abstract Dirac notation:

$$\mathbf{E}^{\mathrm{emit}} \;=\; \int_{-\infty}^{+\infty}\mathrm{d}\omega\sum_{\nu\mu_z,\lambda}\mathcal{A}^{\mathrm{emit}}_{\lambda,\mu_z\nu}(\omega)\,|\lambda\,\mu_z\,\nu\,k\rangle^{(3)}\,, \tag{5.9}$$

where $\mathcal{A}^{\text{emit}}_{\lambda,\mu_z\nu}(\omega)$ are some complex amplitudes. We can think of an emitter (in the zero-th order Born approximation of its interaction with its environment) as a localized external current distribution in space. The decomposition of its emitted field in a series of radiating VSHs can be done by expanding the DGF that acts on the current distribution in a series of such VSHs (see Eqs. (2.161, 2.158). From there, we can observe that the amplitudes of this expansion of the emitted fields will be given as the inner product between the localized current distribution and the regular VSHs. The spherical Bessel functions inside the regular VSHs vanish at the limit of small argument $kr \to 0$ with a rate of $(kr)^\nu$, with ν being the multipolar order. Therefore, optically small emitters whose current distribution is confined inside an optically small region shall predominantly exhibit dipolar emissions. Higher order multipolar emissions generally become more pronounced in amplitude as the optical size of the emitter grows and is able to "see" the local gradients of the field that excites the emitter. Therefore, although the engineering of mesoscopic quantum dots with higher order multipolar transitions of considerable strength is, e.g., possible [175, 298–300], let us specifically study further the case of the most common dipolar emissions.

The electric field emitted by an electric dipole emitter, $\mathbf{p}_\text{e}$, placed at the origin of the coordinate system is given by (see Eqs. (2.158, 2.169, 2.170):

$$\mathbf{E}^{\text{emit}}_{\mathbf{p}_\text{e}}(\mathbf{r},\omega) \;=\; \frac{k^2}{\varepsilon}\int_{\mathbb{R}^3} \overleftrightarrow{\mathbf{G}}(\mathbf{r},\mathbf{r}';k)\cdot\mathbf{p}_\text{e}\delta(\mathbf{r}')\mathrm{d}^3\mathbf{r}', \tag{5.10}$$

while the electric field emitted by a magnetic dipole emitter, $\mathbf{p}_\text{m}$, placed at the origin of the coordinate system is given by:

$$\mathbf{E}^{\text{emit}}_{\mathbf{p}_\text{m}}(\mathbf{r},\omega) \;=\; \frac{\mathrm{i}kZ}{\mu}\nabla\times\int_{\mathbb{R}^3} \overleftrightarrow{\mathbf{G}}(\mathbf{r},\mathbf{r}';k)\cdot\mathbf{p}_\text{m}\delta(\mathbf{r}')\mathrm{d}^3\mathbf{r}'. \tag{5.11}$$

Moreover, making use of Eqs. (2.161, 2.129, 5.1) and, also, of the following property of the regular VSHs:

$$\mathbf{F}^{(1)}_{\alpha,\mu_z\nu}(\mathbf{r}=0;k) \;=\; \delta_{\alpha\text{N}}\delta_{\nu 1}\frac{\hat{\mathbf{u}}_{\mu_z}}{\sqrt{6\pi}}, \qquad \text{with}: \quad \begin{bmatrix}\hat{\mathbf{u}}_{+1}\\ \hat{\mathbf{u}}_0\\ \hat{\mathbf{u}}_{-1}\end{bmatrix} = \begin{bmatrix}\frac{-1}{\sqrt{2}} & \frac{-\mathrm{i}}{\sqrt{2}} & 0\\ 0 & 0 & 1\\ \frac{+1}{\sqrt{2}} & \frac{-\mathrm{i}}{\sqrt{2}} & 0\end{bmatrix}\begin{bmatrix}\hat{\mathbf{x}}\\ \hat{\mathbf{y}}\\ \hat{\mathbf{z}}\end{bmatrix}, \tag{5.12}$$

we finally get the following relation between the fields radiated by dipoles and the helical VSHs:

$$\begin{bmatrix} \frac{\sqrt{6\pi\varepsilon}}{\mathrm{i}k^3}\,|\mathbf{E}^{\mathrm{emit}}_{\mathbf{p}_\mathrm{e}=\hat{\mathbf{x}}}\rangle \\ \frac{\sqrt{6\pi\varepsilon}}{\mathrm{i}k^3}\,|\mathbf{E}^{\mathrm{emit}}_{\mathbf{p}_\mathrm{e}=\hat{\mathbf{y}}}\rangle \\ \frac{\sqrt{6\pi\varepsilon}}{\mathrm{i}k^3}\,|\mathbf{E}^{\mathrm{emit}}_{\mathbf{p}_\mathrm{e}=\hat{\mathbf{z}}}\rangle \\ -\frac{\sqrt{6\pi\mu}}{k^3 Z}\,|\mathbf{E}^{\mathrm{emit}}_{\mathbf{p}_\mathrm{m}=\hat{\mathbf{x}}}\rangle \\ -\frac{\sqrt{6\pi\mu}}{k^3 Z}\,|\mathbf{E}^{\mathrm{emit}}_{\mathbf{p}_\mathrm{m}=\hat{\mathbf{y}}}\rangle \\ -\frac{\sqrt{6\pi\mu}}{k^3 Z}\,|\mathbf{E}^{\mathrm{emit}}_{\mathbf{p}_\mathrm{m}=\hat{\mathbf{z}}}\rangle \end{bmatrix} \equiv \begin{bmatrix} -1/\sqrt{2} & 0 & 1/\sqrt{2} & 0 & 0 & 0 \\ \mathrm{i}/\sqrt{2} & 0 & \mathrm{i}/\sqrt{2} & 0 & 0 & 0 \\ 0 & 1 & 0 & 0 & 0 & 0 \\ 0 & 0 & 0 & -1/\sqrt{2} & 0 & 1/\sqrt{2} \\ 0 & 0 & 0 & \mathrm{i}/\sqrt{2} & 0 & \mathrm{i}/\sqrt{2} \\ 0 & 0 & 0 & 0 & 1 & 0 \end{bmatrix} \cdot \begin{bmatrix} |\mathrm{N}\ +1\,1\,k\rangle^{(3)} \\ |\mathrm{N}\ \ 0\,1\,k\rangle^{(3)} \\ |\mathrm{N}\ -1\,1\,k\rangle^{(3)} \\ |\mathrm{M}\ +1\,1\,k\rangle^{(3)} \\ |\mathrm{M}\ \ 0\,1\,k\rangle^{(3)} \\ |\mathrm{M}\ -1\,1\,k\rangle^{(3)} \end{bmatrix} \tag{5.13}$$

$$= \begin{bmatrix} -1/2 & 0 & 1/2 & 1/2 & 0 & -1/2 \\ \mathrm{i}/2 & 0 & \mathrm{i}/2 & -\mathrm{i}/2 & 0 & -\mathrm{i}/2 \\ 0 & 1/\sqrt{2} & 0 & 0 & -1/\sqrt{2} & 0 \\ -1/2 & 0 & 1/2 & -1/2 & 0 & 1/2 \\ \mathrm{i}/2 & 0 & \mathrm{i}/2 & \mathrm{i}/2 & 0 & \mathrm{i}/2 \\ 0 & 1/\sqrt{2} & 0 & 0 & 1/\sqrt{2} & 0 \end{bmatrix} \cdot \begin{bmatrix} |{+1}\ +1\,1\,k\rangle^{(3)} \\ |{+1}\ \ 0\,1\,k\rangle^{(3)} \\ |{+1}\ -1\,1\,k\rangle^{(3)} \\ |{-1}\ +1\,1\,k\rangle^{(3)} \\ |{-1}\ \ 0\,1\,k\rangle^{(3)} \\ |{-1}\ -1\,1\,k\rangle^{(3)} \end{bmatrix}. \tag{5.14}$$

Conversely, inverting the last formula gives the following relation:

$$\begin{bmatrix} |{+1}\ +1\,1\,k\rangle^{(3)} \\ |{+1}\ \ 0\,1\,k\rangle^{(3)} \\ |{+1}\ -1\,1\,k\rangle^{(3)} \\ |{-1}\ +1\,1\,k\rangle^{(3)} \\ |{-1}\ \ 0\,1\,k\rangle^{(3)} \\ |{-1}\ -1\,1\,k\rangle^{(3)} \end{bmatrix} = \begin{bmatrix} -1/2 & -\mathrm{i}/2 & 0 & -1/2 & -\mathrm{i}/2 & 0 \\ 0 & 0 & 1/\sqrt{2} & 0 & 0 & 1/\sqrt{2} \\ 1/2 & -\mathrm{i}/2 & 0 & 1/2 & -\mathrm{i}/2 & 0 \\ 1/2 & \mathrm{i}/2 & 0 & -1/2 & -\mathrm{i}/2 & 0 \\ 0 & 0 & -1/\sqrt{2} & 0 & 0 & 1/\sqrt{2} \\ -1/2 & \mathrm{i}/2 & 0 & 1/2 & -\mathrm{i}/2 & 0 \end{bmatrix} \cdot \begin{bmatrix} \frac{\sqrt{6\pi\varepsilon}}{\mathrm{i}k^3}\,|\mathbf{E}^{\mathrm{emit}}_{\mathbf{p}_\mathrm{e}=\hat{\mathbf{x}}}\rangle \\ \frac{\sqrt{6\pi\varepsilon}}{\mathrm{i}k^3}\,|\mathbf{E}^{\mathrm{emit}}_{\mathbf{p}_\mathrm{e}=\hat{\mathbf{y}}}\rangle \\ \frac{\sqrt{6\pi\varepsilon}}{\mathrm{i}k^3}\,|\mathbf{E}^{\mathrm{emit}}_{\mathbf{p}_\mathrm{e}=\hat{\mathbf{z}}}\rangle \\ -\frac{\sqrt{6\pi\mu}}{k^3 Z}\,|\mathbf{E}^{\mathrm{emit}}_{\mathbf{p}_\mathrm{m}=\hat{\mathbf{x}}}\rangle \\ -\frac{\sqrt{6\pi\mu}}{k^3 Z}\,|\mathbf{E}^{\mathrm{emit}}_{\mathbf{p}_\mathrm{m}=\hat{\mathbf{y}}}\rangle \\ -\frac{\sqrt{6\pi\mu}}{k^3 Z}\,|\mathbf{E}^{\mathrm{emit}}_{\mathbf{p}_\mathrm{m}=\hat{\mathbf{z}}}\rangle \end{bmatrix}, \tag{5.15}$$

which can be rewritten in the following compact form:

$$|\lambda\,\mu_z\,1\,k\rangle^{(3)} \;=\; \lambda\frac{\sqrt{6\pi}}{\mathrm{i}k^3}\,|\mathbf{E}^{\mathrm{emit}}_{\mathbf{p}_\lambda=\hat{\mathbf{u}}_{\mu_z}}\rangle\,, \tag{5.16}$$

where $|\mathbf{E}^{\mathrm{emit}}_{\mathbf{p}_\lambda=\hat{\mathbf{u}}_{\mu_z}}\rangle$ represents the radiation from the helical dipole sources $\mathbf{p}_\lambda = \hat{\mathbf{u}}_{\mu_z}$, assuming vanishing radiation from emitters of opposite helicity: $\mathbf{p}_{-\lambda} = 0$ (see Eq. (2.168) for their definition with respect to electric and magnetic dipole sources). Finally, we can observe that the dipolar helical VSHs represent the radiation from spinning (with respect to the quantization z-axis, i.e., in the xOy plane) helical dipole moments (located at the origin of the coordinate system) of helicity λ and angular momentum μ_z. We would like to highlight the fact that the chiral and rotational properties of the dipoles are distinct: the former are characterized by the helicity λ, whereas the latter are characterized by the angular momentum μ_z.

5.3 The T-matrix of the nanophotonic system of an emitter coupled to a waveguide and its directionality

In this section, we will introduce a T-matrix characterizing the nanophotonic system of an emitter placed in close vicinity to a waveguide. The introduced T-matrix allows us

to study the directionality of the coupling of the light radiated by the emitter to the counterpropagating guided modes of the waveguide. We will also present results from full-wave simulations where we study the directionality in such an exemplary nanophotonic system.

Let us consider a single localized emitter embedded inside a medium like the one considered for the analysis of the previous section. Furthermore, let us consider the presence of some arbitrary (stationary) waveguide that is translationally invariant with respect to the x-axis of the coordinate system, i.e., whose optical axis coincides with the x-axis of the coordinate system. The waveguide is considered to have no material losses. Furthermore, to simplify the considered system, we assume a zero-th order Born approximation for the interaction between the emitter and waveguide. That is to say that we consider that the emitter does not interact at all with the field back-scattered from the waveguide. Thus, we consider the emitter as a black box out of which the light emissions emanate and couple to the waveguide, while the waveguide does not experience at all the emitter in the embedding medium.

To construct the T-matrix of our system, we specify the incident and the scattered fields that we will consider as the input and output of the T-matrix. Then, by constructing a finite Hilbert space for the representation of those fields, we end up with a particular representation of the T-matrix. In our case, the incident field is considered to be the light radiated by the emitter in an infinite embedding medium in the absence of the waveguide. Its representation is given by Eq. (5.9). This representation is valid everywhere outside the sphere that circumscribes the localized emitter. On the other hand, the scattered field is considered to be monitored at the planes $x = \pm X$, with $kX >> 1$. That is to say that we essentially monitor solely the field coupled to the bounded guided modes of the non-absorbing waveguide, since the incident field of the emitter vanishes there (at $x = \pm X$). Therefore, the scattered fields in the waveguide output can be represented with the following series (see Eq. (2.201) and the discussion in that section):

$$\mathbf{E}^{\text{guided}} \quad = \quad \int_{-\infty}^{+\infty} \mathrm{d}\omega \sum_{j=1}^{N_{\text{b}}(\omega)} \mathcal{A}_j^{\text{guided}}(\omega)\, |j\,\omega\rangle\,, \tag{5.17}$$

where $N_{\text{b}}(\omega)$ is the number of guided modes that the waveguide supports at some particular frequency, which we represent with the kets $|j\,\omega\rangle$ in abstract Dirac notation. $\mathcal{A}_j^{\text{guided}}(\omega)$ are complex coefficients.

As a result, by introducing vectors containing the complex coefficients representing the input and output fields inside their own Hilbert space, we construct a T-matrix representation of the system which reads as:

$$\vec{\mathcal{A}}^{\text{guided}}(\omega) \quad = \quad \hat{\mathbf{T}}(\mathbf{d},\omega) \cdot \vec{\mathcal{A}}^{\text{emit}}(\mathbf{d},\omega), \tag{5.18}$$

where the vector $\mathbf{d} = d_x\hat{\mathbf{x}} + d_y\hat{\mathbf{y}} + d_z\hat{\mathbf{z}}$ denotes the position of the emitter with respect to the global coordinate system. The elements of the T-matrix are denoted as $\langle j\,\omega|\,\hat{\mathbf{T}}(\mathbf{d},\omega)\,|\lambda\,\mu_z\,\nu\,k\rangle_{\mathbf{d}}^{(3)}$, where with the ket $|\lambda\,\mu_z\,\nu\,k\rangle_{\mathbf{d}}^{(3)}$ we denote an emitter located at $\mathbf{r} = \mathbf{d}$, and whose quantization axis is parallel to the z-axis of the global coordinate system.

Assuming that the modes of the waveguide are normalized to unit power flux (see Section 2.8), the total power coupled to all bounded modes propagating in the $\pm\hat{\mathbf{x}}$-direction (where we use the index $j^{\pm}$ to refer to all those modes), is then given by (see Eq. (2.206)):

$$C_{\pm\hat{\mathbf{x}}}(\mathbf{d},\omega) \;=\; \sum_{j=j^{\pm}} \left| \sum_{\nu\mu_z,\lambda} \mathcal{A}^{\text{emit}}_{\lambda,\mu_z\nu}(\mathbf{d},\omega)\, \langle j\,\omega|\, \hat{\mathbf{T}}(\mathbf{d},\omega)\, |\lambda\,\mu_z\,\nu\,k\rangle^{(3)}_{\mathbf{d}} \right|^2 . \tag{5.19}$$

The (logarithmic) directionality of the emitted light that was coupled to the waveguide is then defined as:

$$D(\mathbf{d},\omega) \;=\; \log_{10}\left[C_{+\hat{\mathbf{x}}}(\mathbf{d},\omega)/C_{-\hat{\mathbf{x}}}(\mathbf{d},\omega)\right], \tag{5.20}$$

where a positive(negative) value means a preferential coupling direction towards the positive(negative) $\hat{\mathbf{x}}$-direction. The norm of the value specifies the degree of directionality in orders of magnitude. Finally, defining the quantity $C_{\pm\hat{\mathbf{x}};\lambda,\mu_z\nu}(\mathbf{d},\omega)$ as the coupling power $C_{\pm\hat{\mathbf{x}}}(\mathbf{d},\omega)$ for the particular emission case $\mathcal{A}^{\text{emit}}_{\lambda',\mu'_z\nu'}(\mathbf{d},\omega) = \delta_{\lambda\lambda'}\delta_{\mu_z\mu'_z}\delta_{\nu\nu'}$ allows us to define directionality with respect to a single column of the T-matrix of the system:

$$D_{\lambda,\mu_z\nu}(\mathbf{d},\omega) \;=\; \log_{10}\left[C_{+\hat{\mathbf{x}};\lambda,\mu_z\nu}(\mathbf{d},\omega)/C_{-\hat{\mathbf{x}};\lambda,\mu_z\nu}(\mathbf{d},\omega)\right] \tag{5.21}$$

$$\;=\; \log_{10}\left[\frac{\sum_{j=j^+}\left|\langle j\,\omega|\,\hat{\mathbf{T}}(\mathbf{d},\omega)\,|\lambda\,\mu_z\,\nu\,k\rangle^{(3)}_{\mathbf{d}}\right|^2}{\sum_{j=j^-}\left|\langle j\,\omega|\,\hat{\mathbf{T}}(\mathbf{d},\omega)\,|\lambda\,\mu_z\,\nu\,k\rangle^{(3)}_{\mathbf{d}}\right|^2}\right]. \tag{5.22}$$

Investigating the latter quantity for an exemplary waveguide system will be the main task of the rest of this chapter.

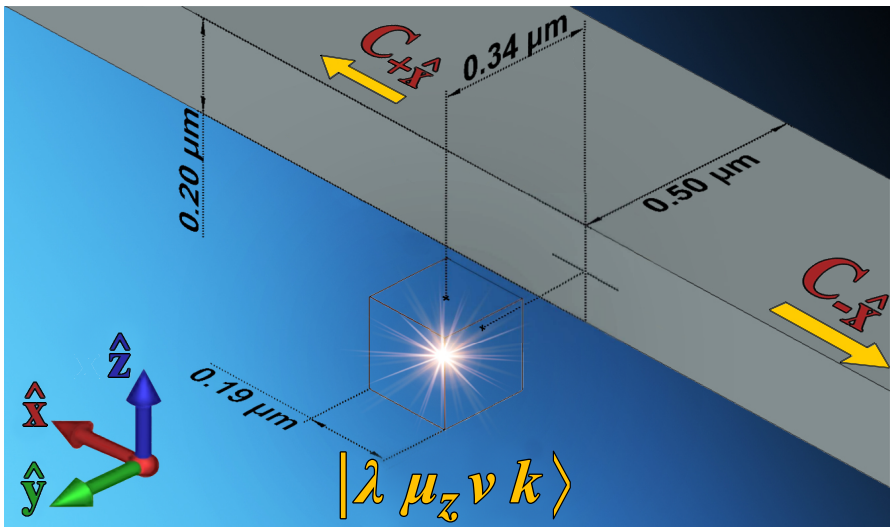

Figure 5.1: Illustration of the geometry of the problem. A multipolar emitter of well-defined hellicity and transverse angular momentum coupling light to the waveguide. The illustration was drawn by Maria Labrianidou. Adapted with permission from Ref. [A4] © John Wiley and Sons.

For this purpose, we perform numerical experiments with a full-wave solver. Specifically, we consider the case of a rectangular silicon waveguide embedded in free space, whose optical axis coincides with the x-axis of the global coordinate system. Its refractive index is considered to be fixed at the value of 3.477 across the whole spectrum of our

study. Its height is 200 nm and its width is 500 nm. The waveguide is invariant under reflections across the xOy and yOz planes. The geometry of the system is illustrated in Fig. 5.1. There, a multipolar emitter of well-defined helicity λ and transverse angular momentum μ_z is placed at a position (d_x, d_y, d_z)=(0 nm, 590 nm, 0 nm). We call this angular momentum transverse, since its quantization axis is perpendicular to the median plane of the waveguide xOy.

Furthermore, we use the surface equivalence principle to inject the radiated fields of the emitter inside the simulation domain (see Eq. (4.5)). Specifically, we use an auxiliary square box of dimension 190 nm centered at the position of the emitter (see Fig. 5.1), and we print on it an auxiliary surface current distribution with the emitted tangential electric and magnetic emitted fields. According to Eq. (4.5), the radiation of the auxiliary current distribution on the box reproduces the emitted field everywhere outside the auxiliary box. We use CST MWS to perform the full-wave simulations in time domain and such a type of excitation is supported there as a "nearfield source". We perform time-domain numerical simulations over a frequency window of 40 THz centered at around $f_0 = 193.4$ THz. The central frequency corresponds to a vacuum wavelength of $\lambda_0 = 1550$ nm, and the frequency span to a wavelength range between 1404 and 1729 nm. Specifically, we excite the system with a Gaussian pulse that has a standard deviation of 58.56 THz. The auxiliary surface current distributions are calculated for 41 frequencies (i.e., every 1 THz within the spectral window of interest) and imported in CST MWS using the NFS nearfield scan data exchange format. For practical purposes, the waveguide can be considered single-mode across the entire frequency band since the second mode is rather weakly guided there. The propagation constant of the guided mode at the central frequency is $\beta = 2.26\,k$. Considering a single-mode waveguide simplifies our studies. Note, also, that the waveguide ports recording the power coupled to each mode are placed at a relatively large distance from the emitter, specifically at the planes $x = \pm 6000$ nm.

Finally, let us highlight that free space radiation cannot couple to the guided mode. In fact, the coupling of the emissions to the guided modes is mediated solely through the evanescent part of the radiating fields characterized by $|k_x| = \beta > k$. Therefore, to have a considerable coupling efficiency, the waveguide needs to be placed at the near-field region of the emitter, where the respective evanescent fields are still strong. Furthermore, for the same reason, picking a fine mesh of the auxiliary box is crucial. A mesh step of $0.02\lambda_0$ was chosen, which allows us to correctly model fast varying evanescent fields with a spatial periodicity of even below $0.2\lambda_0$. Note also, that CST MWS adopts an opposite time convention compared to ours and therefore the auxiliary currents need to be conjugated prior to the injection in the full-wave solver. The injected tangential electric fields are calculated through Eq. (5.1) and their respective magnetic fields, being fields of pure helicity λ, are simply proportional to the electric fields: $\mathbf{H}_\lambda^{\text{emit}} = \lambda \mathbf{E}_\lambda^{\text{emit}}/\mathrm{i}Z$, which is a relation that simply comes from the vanishing Riemann-Silberstein vector of opposite helicity (see Eq. (2.167)).

Next, we perform 30 such numerical simulations by exciting the considered system each time with one of the 30 different radiating helical VSHs, $|\nu\,\mu_z\,\lambda\rangle$, up to the octupolar order ($\nu = 3$). We use the full-wave simulations to measure the directionality of the T-matrix of the system, i.e., the quantity defined in Eq. (5.22). In Fig. 5.2, we plot the results of our simulations in a way that suppresses their spectral dimension. Such a compact representation of our results facilitates the appreciation of their main qualitative characteristics. Specifically, we generate a statistical distribution of the recorded directionality across the entire considered frequency spectrum in the measurements, and we plot the probability distribution to measure some directionality within the considered spectrum, for each multipolar emitter (see insets of Fig. 5.2). Those probability distributions are encoded with a color and illustrated. We use the red color to refer to results from multipolar emitters of

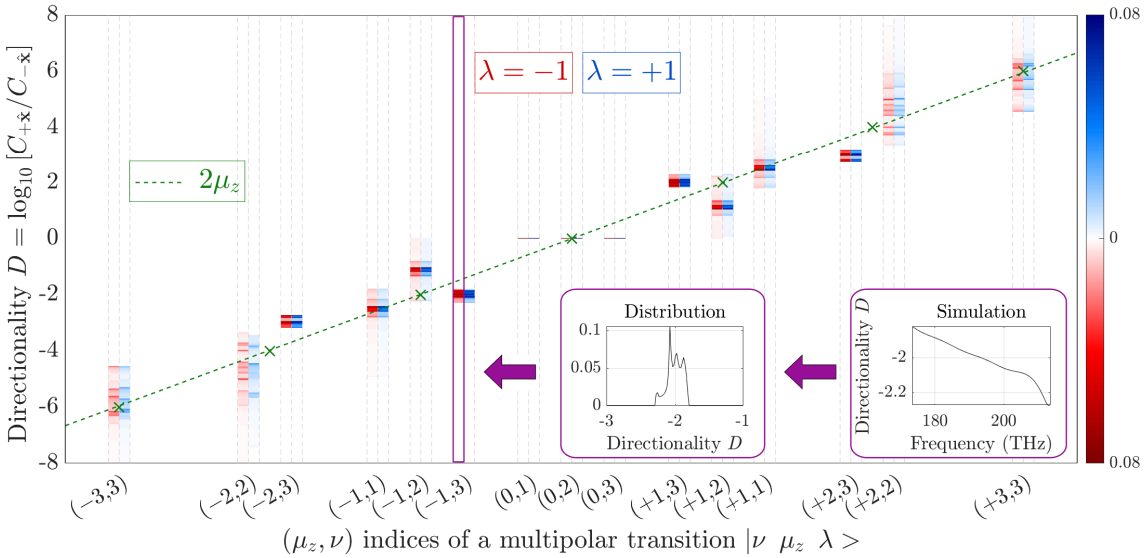

Figure 5.2: For each illuminating $|\nu\,\mu_z\,\lambda\rangle$, the graph shows the histogram of the logarithmic directionality of the coupling of the considered emitter into the waveguide. Each histogram is the distribution of the directionality obtained from a wideband numerical simulation (see inset). A more(less) intense color corresponds to a more(less) frequent occurrence of a particular directionality value in the frequency-dependent simulation results. Adapted with permission from Ref. [A4] © John Wiley and Sons.

negative helicity, and we use the blue color to refer to the results from multipolar emitters of positive helicity. The intensity of the color encodes the probability of occurence of some particular directionality in our measurements. Qualitatively, three main features are observed in Fig. 5.2.

- First of all, we observe a strong dependence of directionality D on the transverse angular momentum μ_z, which seems to approximately follow the green dashed line in Fig. 5.2 corresponding to $2\mu_z$. The sign of μ_z appears to fix the preferential coupling direction and, in a linear scale, the degree of directionality appears to grow approximately as $10^{2|\mu_z|}$. This exponential growth of directionality with respect to the transverse angular momentum is rather remarkable.

- Emissions of the same multipolar order ν and opposite transverse angular momentum μ_z appear to produce opposite values of directionality D. Moreover, the emissions of zero angular momentum μ_z demonstrate zero directionality.

- Emissions with the same multipolar content (μ_z, ν) but opposite helicity λ appear to produce the same values of directionality D. Note that there are only minor discrepancies occuring for large $|\mu_z|$ just because of the low signal-to-noise ratio in the non-preferred direction of the coupling of light. Importantly, this result strongly suggests that the considered nanophotonic device is inappropriate for the sensing of the chirality of the emitted light.

In what follows, we will study in further detail those three points. Specifically, we will shed light on the first point by studying the transverse angular spectrum of the radiated light from the multipolar emitters. For the other two points, we will study the reflections that the spatial symmetries of the system have on its T-matrix and the directionality of the coupled light.

5.4 A symmetry analysis of the T-matrix of the system

In this section, we will study the effect that the spatial symmetries of the system have on the measured directionalities of the near-field coupling of light radiated by the emitters into the waveguide. Specifically, we want to study what are the implications of the waveguide possessing some vertical mirror symmetry plane characterized by the eigenvalue $\sigma_{\mathrm{v}} = \pm 1$ (see Section 2.8).

To do this, we focus on the impact that such mirror symmetries of the waveguide have on the considered T-matrix of the system. This essentially requires to study the mirror transformation symmetries of the input and output eigenstates of the T-matrix of the system. Specifically, if we use the simplified kets $|\pm\hat{\mathbf{x}}\rangle$ to refer to the two counterpropagating modes of the single-mode waveguide (i.e., where the indices j^+ and j^- refer to a single mode), we get the following mirror transformations for the modes of a waveguide with mirror symmetries with respect to the yOz, xOz and xOy planes (like the one illustrated in Fig. 5.2):

$$\mathbf{M}_x \,|\pm\hat{\mathbf{x}}\rangle = |\mp\hat{\mathbf{x}}\rangle\,, \tag{5.23}$$

$$\mathbf{M}_y \,|\pm\hat{\mathbf{x}}\rangle = \sigma_y \,|\pm\hat{\mathbf{x}}\rangle\,, \tag{5.24}$$

$$\mathbf{M}_z \,|\pm\hat{\mathbf{x}}\rangle = \sigma_z \,|\pm\hat{\mathbf{x}}\rangle\,, \tag{5.25}$$

where $\mathbf{M}_x$, $\mathbf{M}_y$, and $\mathbf{M}_z$ denote the mirror symmetry transformation operators along the respective axes, and the eigenvalues σ_y, σ_z take the values ± 1 depending on the symmetries of the guided modes. For example, the fundamental mode of the waveguide in Fig. 5.2 is $y-$polarized and is characterized by $\sigma_y = -1$ and $\sigma_z = +1$. Regarding the mirror symmetry transformations of the emitted field, the following properties can be derived from the definition of the helical VSHs in Eq. (5.2):

$$\mathbf{M}_x \,|\lambda\,\mu_z\,\nu\,k\rangle_{\mathbf{d}}^{(3)} = -\,|-\lambda\,-\mu_z\,\nu\,k\rangle_{\bar{\mathbf{d}}_x}^{(3)}\,, \tag{5.26}$$

$$\mathbf{M}_y \,|\lambda\,\mu_z\,\nu\,k\rangle_{\mathbf{d}}^{(3)} = (-1)^{\mu_z+1}\,|-\lambda\,-\mu_z\,\nu\,k\rangle_{\bar{\mathbf{d}}_y}^{(3)}\,, \tag{5.27}$$

$$\mathbf{M}_z \,|\lambda\,\mu_z\,\nu\,k\rangle_{\mathbf{d}}^{(3)} = (-1)^{\mu_z+\nu+1}\,|-\lambda\,\mu_z\,\nu\,k\rangle_{\bar{\mathbf{d}}_z}^{(3)}\,, \tag{5.28}$$

where, e.g., with $\bar{\mathbf{d}}_x$ we denote the mirror symmetric point of $\mathbf{d}$ with respect to the xOz plane, located at $(-d_x, d_y, d_z)$. In view of the above symmetries, we would like to highlight two more general remarks: 1) a mirror symmetry transformation of a helical VSH with respect to an arbitrary plane flips its helicity, and 2) a mirror symmetry transformation of a helical VSH with respect to an arbitrary plane containing the quantization axis flips the sign of the angular momentum, whereas, if the reflection is done with respect to a plane that is perpendicular to the quantization axis, the sign of the angular momentum is maintained. Based on those remarks, we can extrapolate the above discussed symmetries for emitters with a quantization axis parallel to the z-axis to the general case of an arbitrarily selected quantization axis. For example, we will also discuss later the symmetry implications if a vertical angular momentum quantization axis is selected. The vertical quantization axis is defined as an axis that is on the median plane of the waveguide and parallel both to the optical axis of the waveguide and the quantization axis of the transverse angular momentum.

Furthermore, let us note that for a waveguide that is geometrically invariant with respect to the $\mathbf{M}_x$ mirror symmetry operator, we have the following symmetry for its T-matrix:

$$\mathbf{M}_x^\dagger \cdot \hat{\mathbf{T}}(\mathbf{d},\omega) \cdot \mathbf{M}_x = \hat{\mathbf{T}}(\bar{\mathbf{d}}_x,\omega), \tag{5.29}$$

and similarly for the other two mirror symmetry transformations.

Finally, the symmetries of Eqs. (5.23-5.29) together with the definitions of Eqs. (5.19-5.22) give the following regularities:

- For a single-mode waveguide that is invariant with respect to $\mathbf{M}_x$ we get the following symmetries:

$$C_{\pm\hat{\mathbf{x}};\lambda,\mu_z\nu}(\mathbf{d},\omega) = C_{\mp\hat{\mathbf{x}};-\lambda,-\mu_z\nu}(\bar{\mathbf{d}}_x,\omega), \tag{5.30}$$
$$D_{\lambda,\mu_z\nu}(\mathbf{d},\omega) = -D_{-\lambda,-\mu_z\nu}(\bar{\mathbf{d}}_x,\omega). \tag{5.31}$$

- For a single-mode waveguide that is invariant with respect to $\mathbf{M}_y$ we get the following symmetries:

$$C_{\pm\hat{\mathbf{x}};\lambda,\mu_z\nu}(\mathbf{d},\omega) = C_{\pm\hat{\mathbf{x}};-\lambda,-\mu_z\nu}(\bar{\mathbf{d}}_y,\omega), \tag{5.32}$$
$$D_{\lambda,\mu_z\nu}(\mathbf{d},\omega) = D_{-\lambda,-\mu_z\nu}(\bar{\mathbf{d}}_y,\omega). \tag{5.33}$$

- For a single-mode waveguide that is invariant with respect to $\mathbf{M}_z$ we get the following symmetries:

$$C_{\pm\hat{\mathbf{x}};\lambda,\mu_z\nu}(\mathbf{d},\omega) = C_{\pm\hat{\mathbf{x}};-\lambda,\mu_z\nu}(\bar{\mathbf{d}}_z,\omega), \tag{5.34}$$
$$D_{\lambda,\mu_z\nu}(\mathbf{d},\omega) = D_{-\lambda,\mu_z\nu}(\bar{\mathbf{d}}_z,\omega). \tag{5.35}$$

Moreover, let us note that, for a single-mode waveguide that is translationally invariant with respect to the x-axis, we also have the following symmetry for arbitrary displacement x_0:

$$C_{\pm\hat{\mathbf{x}};\lambda,\mu_z\nu}(\mathbf{d},\omega) = C_{\pm\hat{\mathbf{x}};\lambda,\mu_z\nu}(\mathbf{d}+x_0\hat{x},\omega), \tag{5.36}$$
$$D_{\lambda,\mu_z\nu}(\mathbf{d},\omega) = D_{\lambda,\mu_z\nu}(\mathbf{d}+x_0\hat{x},\omega). \tag{5.37}$$

Note that general selection rules for symmetry-prohibited and symmetry-allowed couplings of multipolar emissions to waveguides can also be derived from the above symmetry relations (see Ref. [A4]). The reflection symmetries of the emissions shall be identical to the reflection symmetries of the guided mode so that we can have symmetry-allowed coupling between the two. In other words, that is to say that the emissions need to transform in the same way as the guided mode with respect to the symmetry transformations that characterize the irreducible representation of the point symmetry group that the guided mode belongs to.

First of all, based on the above symmetries discussion, let us illustrate in Fig. 5.3 the transformations of a) the transverse angular momentum, b) the vertical angular momentum, and c) the helicity of a (displaced with respect to the median plane) emitter with respect to the $\mathbf{M}_x$, $\mathbf{M}_z$, and $\mathbf{M}_x\mathbf{M}_z$ reflection symmetries that the waveguide supposedly supports. In the leftmost panel of each subfigure, we consider an arbitrarily positioned multipolar emitter and we *assume* some particular preferential directionality towards the positive x-axis for some *assumed* eigenvalues of the initial emitter. In the next panels of the figure, we illustrate how the assumed directionality, position, helicity, and angular momentum of the initial emitter get transformed under the $\mathbf{M}_x$, $\mathbf{M}_z$, and $\mathbf{M}_x\mathbf{M}_z$ reflection symmetries. Note that the initial emitter can either have a well-defined transverse or well-defined vertical angular momentum.

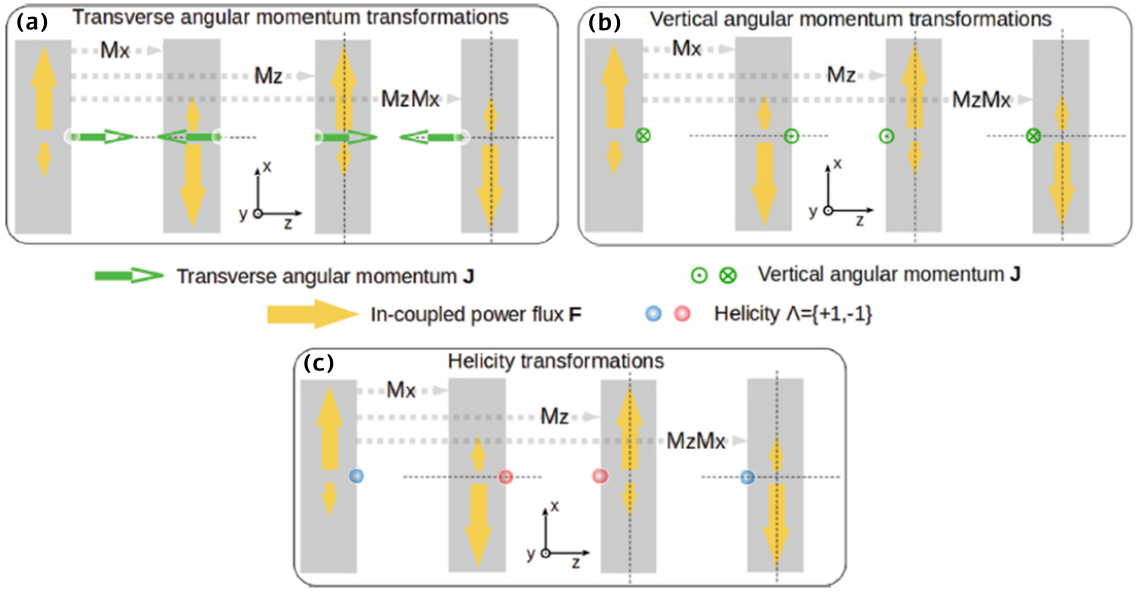

Figure 5.3: Illustration of the transformations of: a) the transverse angular momentum, b) the vertical angular momentum, and c) the helicity of a (displaced with respect to the median plane) emitter with respect to various reflection symmetries. The illustration was drawn by Dr. Ivan Fernandez-Corbaton. Adapted with permission from Ref. [A4] © John Wiley and Sons.

From this figure, we observe that the sign of directionality is not able to lock with either the sign of the vertical angular momentum or the sign of the helicity of the emitter for arbitrary displacement of the emitter with respect to the $z-$direction. On the other hand, it is important to note that the transverse angular momentum allows for that possibility based on our symmetry analysis.

Next, let us discuss in view of the above remarks the symmetries that we observed in the results of Fig. 5.2 that were referring to the coupling of multipolar emissions emanating from emitters with well-defined helicity and transverse angular momentum μ_z, located in the median plane xOy, with a waveguide that supported both the $\mathbf{M}_x$ and $\mathbf{M}_z$ reflection symmetries.

First, from Eq. (5.35), we get that: for emitters placed on the median plane and the waveguide supporting the $\mathbf{M}_z$ reflection symmetry, two emitters of the same eigenvalues (μ_z, ν, k) and opposite helicity λ have the same directionality.

Second, from Eqs. (5.31 and 5.37), we get that: for emitters placed on the median plane and the waveguide supporting the $\mathbf{M}_x$ reflection symmetry, two emitters of the same eigenvalues (ν, k) and opposite helicity and transverse angular momentum (λ, μ_z) have the opposite directionality.

Finally, combining the last two remarks together, we also get that: for emitters placed on the median plane and the waveguide supporting both the $\mathbf{M}_x$ and $\mathbf{M}_z$ reflection symmetries, two emitters of the same eigenvalues (λ, ν, k) and transverse angular momentum (λ, μ_z) have the opposite directionality. This regularity, for the case of $\mu_z = 0$ implies, also, that the directionality becomes zero.

The above regularities are to be clearly observed in Fig. 5.4, where we plot the spectra of the directionalities that we recorded in the simulations of Fig. 5.2 for the specific cases of $\mu_z = 0$ and $\mu_z = 1$. Note that for emissions of $\mu_z = 0$, we indeed observe practically zero directionality (we only record some background numerical noise). Furthermore, in Fig. 5.4, we, also, clearly see the rest of the discussed symmetries obeyed all across the recorded spectrum. Multipoles of opposite μ_z do produce exactly opposite directionalities

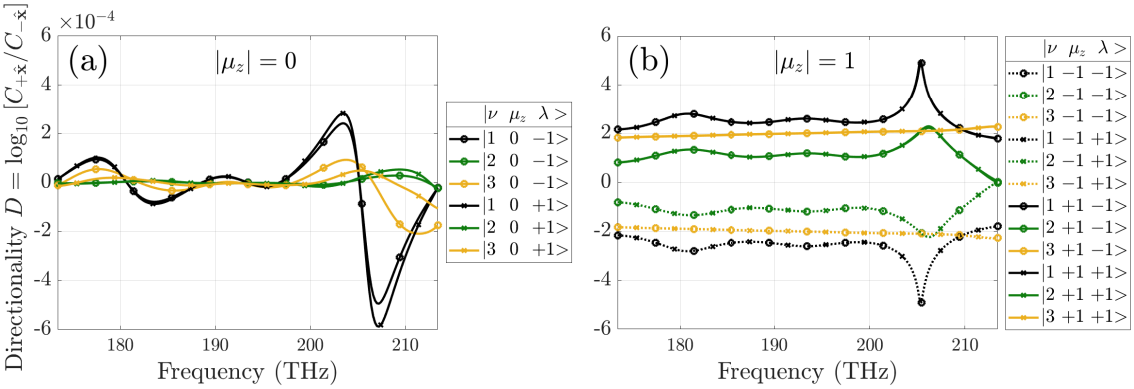

Figure 5.4: Directionality D with respect to frequency for the coupling of multipolar emissions with well-defined transverse angular momentum $\mu_z = 0$ in (a) and $\mu_z = 1$ in (b) from emitters located in the median plane xOy. Please note the different vertical scales in (a) and (b). Adapted with permission from Ref. [A4] © John Wiley and Sons.

and multipoles of opposite λ do produce identical directionalities.

5.5 The directionality of the evanescent part of the transverse angular spectrum of multipolar emissions: the special role of the transverse angular momentum

In the previous section, we identified that the sign of the transverse angular momentum μ_z is allowed from a symmetry perspective to follow the sign of directionality. But what, e.g., determines the preferential coupling direction in the leftmost panels of Fig. 5.3 in the first place? How can we justify the roughly $2\mu_z$ dependence of directionality that we recorded in our measurements in Fig. 5.2? Those are the questions that we will attempt to answer in this section. We will do this by searching for the origins of the recorded directionality in the intrinsic properties of the emissions themselves.

Specifically, since the waveguide is considered translationally invariant concerning the x-axis, we must decompose the multipolar emissions into another set of modes of well-defined linear momentum along the x-axis, k_x. We can then search for the origins of directionality in the emitted spectrum for such modes with opposite such linear momenta whose absolute value is equal to the propagation constant of the guided mode, i.e., with $k_x = \pm\beta$. We could do this, by expanding the helical radiating VSHs either into an angular spectrum of plane waves propagating inside the half-space that is transverse to its quantization axis and contains the waveguide (i.e., the $y < 590$ nm half-space, e.g., in Fig. 5.1), or into a series of cylindrical waves, i.e., regular VCHs, quantized along the optical axis of the waveguide. Here, we will opt for the first of the two approaches as it is simpler. The second representation of the emitted fields in terms of such regular VCHs, could, e.g., be obtained by appropriately propagating each plane wave of the representation of the first approach till the optical axis of the waveguide. Then we apply the transformation between plane and cylindrical waves given in Eq. (2.148).

We start our technical analysis from Eq. (5.8). There, we have an angular spectrum representation of radiating helical VSHs of well-defined transverse angular momentum μ_z located at the origin of the coordinate system. That angular spectrum, though, is only valid for the $z \gtrless 0$ half-spaces, whereas we are interested in an expression valid for the $y < 0$ half-space. After some algebraic manipulations, in the supplementary material of Ref. [A4], we derive the following transverse angular spectrum representation of the helical

multipoles:

$$|\lambda\,\mu_z\,\nu\,k\rangle^{(3)} \equiv \frac{1}{2\pi}\iint_{-\infty]}^{+\infty}\frac{\mathrm{d}k_x\mathrm{d}k_z}{-kk_y}\,S_{\lambda,\mu_z\nu}(\theta_{\hat{\mathbf{k}}},\phi_{\hat{\mathbf{k}}})\hat{\mathbf{e}}_\lambda(\hat{\mathbf{k}})e^{\mathrm{i}k\hat{\mathbf{k}}\cdot\mathbf{r}}, \qquad \text{for} \quad \mathrm{y}<0, \quad (5.38)$$

where $k_y=-\sqrt{k^2-k_x^2-k_z^2}$ and the dependence of $\theta_{\hat{\mathbf{k}}}$, $\phi_{\hat{\mathbf{k}}}$, and $\hat{\mathbf{k}}$ on k_x,k_z,k is given by Eqs. (2.135-2.137). Note that complex angles of propagation are used to refer to the evanescent part of the spectrum when k_y becomes imaginary. The unit vector of the circular polarization of the helical plane waves, $\hat{\mathbf{e}}_\lambda(\hat{\mathbf{k}})$, is given by Eq. (2.187). It is important to highlight that, apart from the norm of the unit vector of the propagation direction $\hat{\mathbf{k}}$, also the norm of $\hat{\mathbf{e}}_\lambda(\hat{\mathbf{k}})$ is not unitary for evanescent waves. Specifically, we have:

$$\left|\hat{\mathbf{e}}_\lambda(\hat{\mathbf{k}})\right| = \cosh\left(\mathrm{Im}\left\{\theta_{\hat{\mathbf{k}}}\right\}\right)\cosh\left(\mathrm{Im}\left\{\phi_{\hat{\mathbf{k}}}\right\}\right)+\lambda\cos\left(\mathrm{Re}\left\{\theta_{\hat{\mathbf{k}}}\right\}\right)\sinh\left(\mathrm{Im}\left\{\phi_{\hat{\mathbf{k}}}\right\}\right). \quad (5.39)$$

Furthermore, for complex angles, the polarization vectors of opposite helicity stop being orthogonal in the usual sense: $\hat{\mathbf{e}}_\lambda(\hat{\mathbf{k}})\cdot\hat{\mathbf{e}}^*_{\lambda'}(\hat{\mathbf{k}})\neq\delta_{\lambda\lambda'}$. Instead, we have the following orthogonality property, which is valid for complex angles of propagation as well: $\hat{\mathbf{e}}_\lambda(\hat{\mathbf{k}})\cdot\hat{\mathbf{e}}_{-\lambda'}(\hat{\mathbf{k}})=-\delta_{\lambda\lambda'}$. Let us also note two symmetry properties of the polarization vector that are specifically relevant to the case of the transverse angular spectrum that we study:

$$|\hat{\mathbf{e}}_\lambda(k_x,k_z)| = |\hat{\mathbf{e}}_{-\lambda}(-k_x,k_z)|, \quad (5.40)$$
$$|\hat{\mathbf{e}}_\lambda(k_x,k_z)| = |\hat{\mathbf{e}}_{-\lambda}(k_x,-k_z)|. \quad (5.41)$$

Equation (5.40) follows because $\theta_{\hat{\mathbf{k}}}$ does not depend on k_x, and, also, $\mathrm{Im}\left\{\phi_{\hat{\mathbf{k}}}(k_x,k_z)\right\}=-\mathrm{Im}\left\{\phi_{\hat{\mathbf{k}}}(-k_x,k_z)\right\}=\ln\left|\sqrt{k_x^2+k_y^2}\right|-\ln|k_x+\mathrm{i}\,k_y|$. Moreover, Eq. (5.41) follows because $\theta_{\hat{\mathbf{k}}}(k_x,k_z)=\pi-\theta_{\hat{\mathbf{k}}}(k_x,-k_z)$ and $\phi_{\hat{\mathbf{k}}}(k_x,k_z)=\phi_{\hat{\mathbf{k}}}(k_x,-k_z)$.

With Eq. (5.38) at hand, let us now study the directionality of the transverse angular spectrum of the emissions. We have already discussed that only evanescent waves of the transverse angular spectrum of the emissions with $k_x=\pm\beta$ couple to the two counter-propagating modes of the waveguide. Note that although evanescent plane waves do not carry power along the direction of their decay (towards the negative y-axis in our case), they can carry power along some direction perpendicular to their decay axis. By making use of Eq. (5.38) and after some straightforward algebra, we can show that the power flux density (norm of the real part of the Poynting vector) that the evanescent plane waves of the transverse angular spectrum carry is equal to $\left|S_{\lambda,\mu_z\nu}(\hat{\mathbf{k}})\hat{\mathbf{e}}_\lambda(\hat{\mathbf{k}})\right|^2/2Z$. Therefore, let us define the logarithm of the ratio of power flux densities below as the directionality of the emitted angular spectrum that is coupled to the two counterpropagating modes of the waveguide:

$$R_{\lambda,\mu_z\nu}(k_z)=\log_{10}\left[\frac{|S_{\lambda,\mu_z\nu}(k_x=+\beta,k_z)\hat{\mathbf{e}}_\lambda(k_x=+\beta,k_z)|^2}{|S_{\lambda,\mu_z\nu}(k_x=-\beta,k_z)\hat{\mathbf{e}}_\lambda(k_x=-\beta,k_z)|^2}\right]. \quad (5.42)$$

We now use Eqs. (5.4, 2.137, 2.136, 5.39, 5.40) to decompose Eq. (5.42) into two terms:

$$\begin{aligned} R_{\lambda,\mu_z\nu}(k_z) &= 2\log_{10}\left[\left|\frac{e^{\mathrm{i}\mu_z\phi_{\hat{\mathbf{k}}}(k_x=+\beta,k_z)}}{e^{\mathrm{i}\mu_z\phi_{\hat{\mathbf{k}}}(k_x=-\beta,k_z)}}\right|\frac{|\hat{\mathbf{e}}_\lambda(k_x=+\beta,k_z)|}{|\hat{\mathbf{e}}_\lambda(k_x=-\beta,k_z)|}\right] \\ &= 2\mu_z\log_{10}\left[\left|\frac{e^{\mathrm{i}\phi_{\hat{\mathbf{k}}}(k_x=+\beta,k_z)}}{e^{\mathrm{i}\phi_{\hat{\mathbf{k}}}(k_x=-\beta,k_z)}}\right|\right] + 2\lambda\log_{10}\left[\frac{|\hat{\mathbf{e}}_+(k_x=+\beta,k_z)|}{|\hat{\mathbf{e}}_+(k_x=-\beta,k_z)|}\right] \\ &= 2\mu_z\, f(k_z) + 2\lambda g(k_z), \end{aligned} \tag{5.43}$$

where we have defined the following quantities:

$$f(k_z) = \log_{10}\left[\left|\frac{e^{\mathrm{i}\phi_{\hat{\mathbf{k}}}(k_x=+\beta,k_z)}}{e^{\mathrm{i}\phi_{\hat{\mathbf{k}}}(k_x=-\beta,k_z)}}\right|\right] = \log_{10}\left[\left|\frac{\frac{\beta}{k}-\mathrm{i}\sqrt{1-\left(\frac{\beta}{k}\right)^2-\left(\frac{k_z}{k}\right)^2}}{\frac{\beta}{k}+\mathrm{i}\sqrt{1-\left(\frac{\beta}{k}\right)^2-\left(\frac{k_z}{k}\right)^2}}\right|\right], \tag{5.44}$$

$$g(k_z) = \log_{10}\left[\frac{|\hat{\mathbf{e}}_{+1}(k_x=+\beta,k_z)|}{|\hat{\mathbf{e}}_{+1}(k_x=-\beta,k_z)|}\right]. \tag{5.45}$$

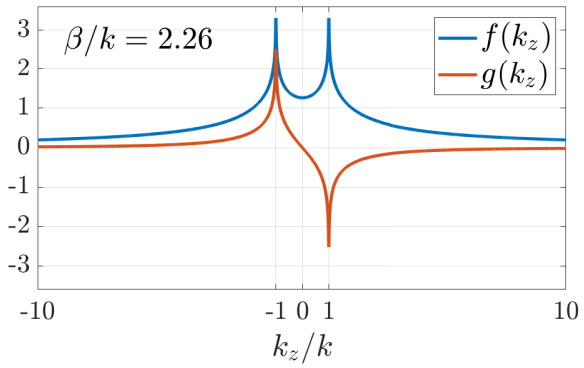

Figure 5.5: Plot of the functions $f(k_z), g(k_z)$ for $\beta/k = 2.26$. Adapted with permission from Ref. [A4] © John Wiley and Sons.

We observe that the quantity $R_{\lambda,\mu_z\nu}$ is the sum of two terms: one that is proportional to the transverse angular momentum μ_z and another one that is proportional to the helicity λ. Apart from the fact that both are functions of k_z, there is something to say about the weighting functions of those two terms. On the one hand, we have that $f(k_z)$, the weighting function of the $2\mu_z$-dependent term, is always positive since $\beta > k$. Moreover, it has an even symmetry $f(k_z) = f(-k_z)$. On the other hand, in view of Eqs. (5.40, 5.41), $g(k_z)$, the weighting function of the 2λ-dependent term, is a function with odd symmetry: $g(k_z) = -g(-k_z)$. Note that both functions have singularities at $|k_z| = k$ and approach zero in the limit of $|k_z| \to \infty$. In Fig. 5.5, we plot the two functions for the case of $\beta/k = 2.26$, which is the propagation constant of the guided mode of the waveguide that we considered in our full-wave simulations of Fig. 5.2, at the central excitation frequency f_0.

Furthermore, it can be shown that the inequality $f(k_z) \geq |g(k_z)| \geq 0$ always holds. This has as a consequence the following: *For non-zero μ_z, the sign of $R_{\lambda,\mu_z\nu}(k_z)$ solely depends on the sign of the transverse angular momentum μ_z, for all k_z.* Additionally, $R_{\lambda,\mu_z\nu}(k_z)$ does not depend on the multipolar order ν, and it has the symmetry property of $R_{\lambda,\mu_z\nu}(k_z) = R_{-\lambda,\mu_z j}(-k_z)$.

Let us now argue that the $2\mu_z$-dependent term in Eq (5.43) constitutes the origin of the dominant exponential dependence of the directionality D on μ_z that we observed in our measurements in Fig. 5.2. For this, we employ the following representation of the power coupled in the two modes in terms of the transverse angular spectrum of the multipolar emissions:

$$C_{\pm\hat{\mathbf{x}};\lambda,\mu_z\nu}(\mathbf{d}=0,\omega) \;=\; \left|\int_{-\infty}^{+\infty}\frac{\mathrm{d}k_z}{2\pi k k_y}S_{\lambda,\mu_z\nu}(\hat{\mathbf{k}}_\pm)|\hat{\mathbf{e}}_\lambda(\hat{\mathbf{k}}_\pm)|\,\langle\pm\hat{\mathrm{x}}|\,\hat{\mathbf{T}}(\mathbf{d}=0,\omega)\,|\lambda\,\mathbf{k}_\pm\rangle\right|^2, \quad (5.46)$$

where we represent the normalized plane waves $\hat{\mathbf{e}}_\lambda(\hat{\mathbf{k}})/|\hat{\mathbf{e}}_\lambda(\hat{\mathbf{k}})|e^{\mathrm{i}\mathbf{k}\cdot\mathbf{r}}$ with the kets $|\lambda\,\mathbf{k}_\pm\rangle$, and we also define $\mathbf{k}_\pm(k_z)=\pm\beta\hat{\mathbf{x}}-\sqrt{k^2-\beta^2-k_z^2}\hat{\mathbf{y}}+k_z\hat{\mathbf{z}}$. One can see from the above equation that the directionality D defined by Eq. (5.21) will be a function of coherent sums over k_z of the contributions of all the evanescent components of the multipolar spectrum with $k_x=\pm\beta$. Note that the cross-section of the waveguide, the multipolar order, and the distance between the emitter and the waveguide will how the different k_z-components will be combined. However, even though the directionality D is not directly related to the directionality of the emitted transverse angular spectrum, $R_{\lambda,\mu_z\nu}$, using the last line of Eq. (5.43), we can see whet the expected trends for it look like. As long as there is a large asymmetry between the amplitudes of the plane waves that couple to the two modes, a similar asymmetry is expected to the final amplitudes of the guided modes after the T-matrix-mediated transitions occur. This indirect relation between the two quantities can be seen by comparing Eqs. (5.42, 5.46).

Nevertheless, we should note that there is a family of waveguide geometries where the directionality D is directly related to $R_{\lambda,\mu_z\nu}$. This is the case where we have an arbitrary infinite planar waveguide that is parallel to the quantization axis of the emissions. Then, due to the additional translation invariance of such a waveguide along z, the directionality of the coupling of an emitter along its x-axis is given by: $D_{\lambda,\mu_z\nu}(\mathbf{d},\omega)=R_{\lambda,\mu_z\nu}(k_z=0)=2\mu_z\,f(k_z=0)$. Thus, in such a case, the directionality of the coupling of the emitted light depends exactly in a proportional way on the transverse angular momentum μ_z of the emitter. Moreover, it is independent of helicity λ, the multipolar order ν, and the distance between the emitter and the planar waveguide. Apart from its exponential μ_z-dependence, it only depends on the wavenumber k and the propagation constant β of the planar waveguide.

Next, let us plot the normalized amplitudes of the transverse angular spectrum of the emitters for better insights. In view of Eq. (5.38), let us define those amplitudes as:

$$S^{\hat{\mathbf{e}}}_{\lambda,\mu_z\nu}(k_x,k_z) \;=\; \frac{-k}{2\pi k_y}\,S_{\lambda,\mu_z\nu}(\theta_{\hat{\mathbf{k}}},\phi_{\hat{\mathbf{k}}})\left|\hat{\mathbf{e}}_\lambda(\hat{\mathbf{k}})\right|. \quad (5.47)$$

We plot those quantities in logarithmic scale in the first columns of Figs. 5.6-5.8. The three figures are for the dipolar ($\nu=1$), quadrupolar ($\nu=2$), and octupolar ($\nu=3$) emissions respectively. Note that the radial coordinate of the plot stands for $\log_{10}\left[\sqrt{k_x^2+k_z^2}/k\right]$, taking values from -1 to 1. The positive values correspond to the evanescent part of the angular spectrum and the negative values to the propagating part of the angular spectrum. The angular coordinate of the plot stands for the angle $\mathrm{atan2}(k_z,k_x)$, i.e., an angle of zero degrees corresponds to plane waves with positive k_x and zero k_z values. We only plot the emissions of positive helicity and non-negative transverse angular momentum. The transverse angular spectra of all the rest of the omitted cases of emissions up to the

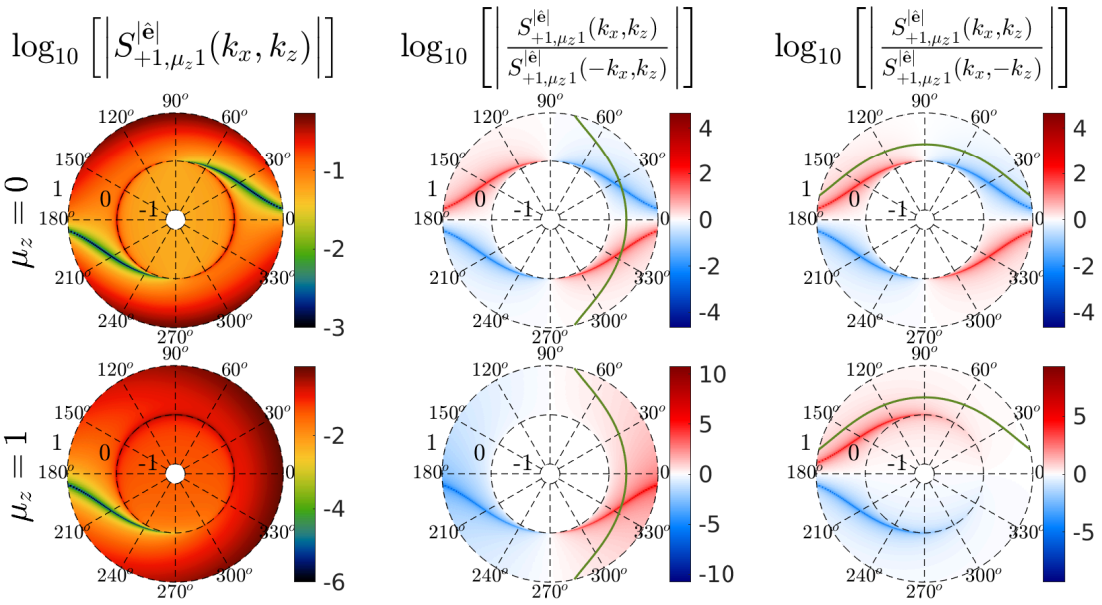

Figure 5.6: Polar plots of the dipolar transverse angular spectrum for the various cases of μ_z (first column). The radial coordinate of the plot stands for $\log_{10}\left[\sqrt{k_x^2+k_z^2}/k\right]$, whereas the angular coordinate of the plot stands for the angle $\mathrm{atan2}(k_z,k_x)$. In the middle column, we plot the directionality of the transverse angular spectrum of the first column. The green line highlights the values of the quantity $0.5R_{\lambda,\mu_z\nu}(k_z)$ for the case of $k_x=\beta=2.26k$. The third column is equivalent to the second one, but for the case that is relevant for a waveguide whose optical axis coincides with the quantization axis of the emitters, i.e., for the case of a longitudinal angular momentum.

octupolar order can be deduced from the presented ones by properly applying the mirror symmetry transformations of Eqs. (5.26-5.28).

In the middle column of Figs. 5.6-5.8, we plot the logarithmic directionality of the transverse angular spectrum of the emissions with respect to the x-axis. The plots indicate the relative asymmetry of the transverse angular spectra of the first column for opposite values of k_x. With a green line, we highlight the positions in the angular spectrum where $k_x=\beta=2.26\,k$, which is the propagation constant of the considered waveguide in Fig. 5.2. Along this line, the plotted quantity in the middle columns coincides with $0.5R_{\lambda,\mu_z\nu}(k_z)$. As we discussed already, the directionalities recorded along the green line indirectly reflect on the measured directionalities D measured in Fig. 5.2. Indeed, we observe that all along the green lines, for all cases of positive λ, μ_z, the measured directionality of the transverse angular spectrum is positive, indicating a preferential coupling direction along $+\hat{\mathbf{x}}$. For the cases of $\mu_z=0$ we observe an antisymmetric directionality with respect to k_z. With our symmetry analysis previously, we explained that D vanishes for multipolar emitters placed at the median plane of a waveguide that supports the $\mathbf{M}_z$ reflection symmetry. Furthermore, let us emphasize the quasi-linear increasing magnitude of the directionality of the transverse angular spectrum with increasing $|\mu_z|$. This provides extra justification for the measured results in Fig. 5.2.

Furthermore, let us note that for particular values of k_z along the green highlighted lines, we have large peaks of the directionality of the transverse angular spectrum. This is due to occurring deeps in the respective amplitudes of the spectrum that is relevant for the coupling with the mode propagating along the non-preferential direction. However, those large directionality values there shall not normally dominate the final value of measured

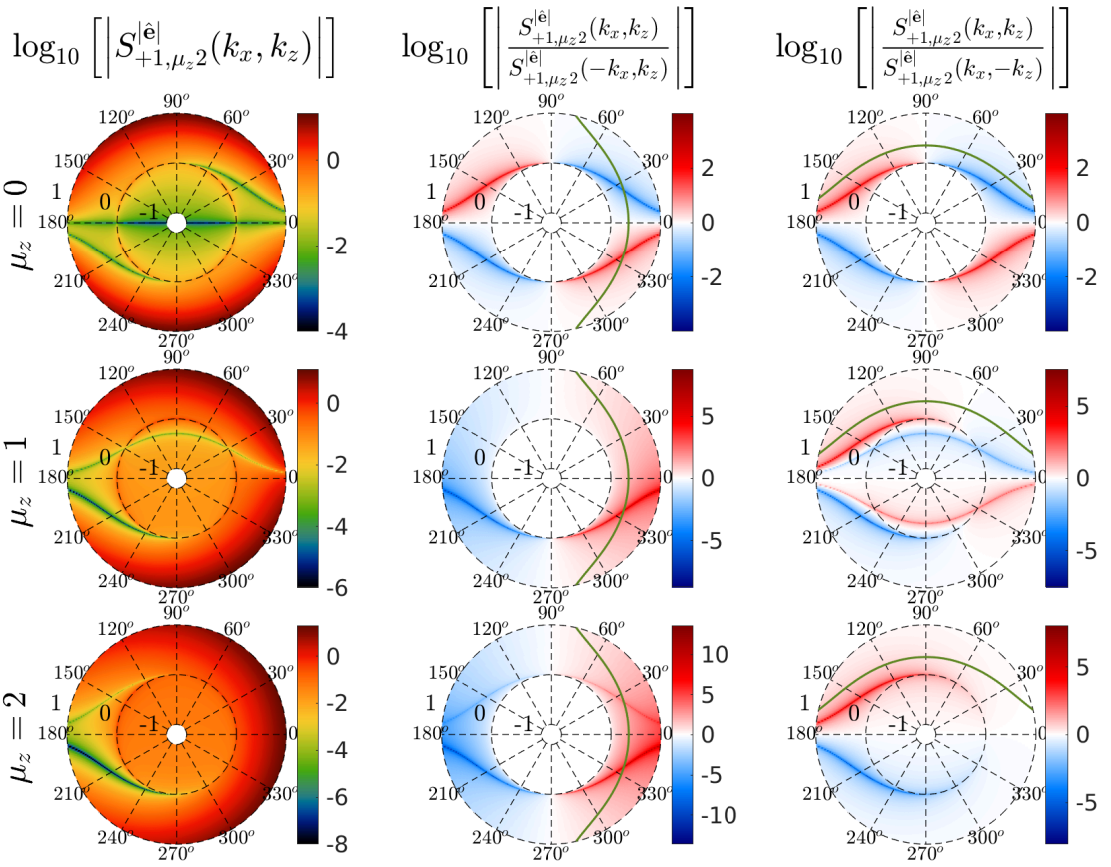

Figure 5.7: Same as Fig. 5.6 but for quadrupolar emissions.

D. First of all, the evanescent waves with large values of k_z experience a greater decay until they reach the waveguide, and, therefore, depending also on the optical distance between the emitter and the waveguide, they may finally have a rather minor contribution to the coupled light to the waveguide. But, apart from this, the directionality D, being a result of a coherent superposition of the contributions of all relevant k_z components of the transverse angular spectrum, shall merely be determined, not by the minima in the transverse angular spectra that correspond to the power coupled to the non-preferential direction, but, rather, by the maxima there.

Finally, in the last column of Figs. 5.6-5.8, similarly to the middle column, we plot the logarithmic directionality of the same transverse angular momentum spectra. Still, now we present the asymmetry of the spectra for opposite values of k_z. Those plots shall be indicative for the directionality D of the coupled emissions to a waveguide whose optical axis coincides with the quantization axis of the emitters, i.e., for the case of a longitudinal angular momentum. Here, we highlight again with a green curve the positions in the angular spectrum where $k_z = \beta = 2.26\,k$, which is the propagation constant of the considered waveguide in Fig. 5.2. In this case, the situation with the directionality is not as clear as previously. We generally have the green line passing through both red and blue regions, which makes it hard to predict the final impact of the directionality of the angular spectrum on D. However, as μ_z increases and approaches the value of ν, we can observe that the green line overlaps better and better with the red region of the directionality of the angular spectrum. For $\mu_z = \nu$, the green line crosses solely a red region. However, the degrees of directionalities that we observe in the spectra in this case of the longitudinal angular momentum are weaker than the ones that we observed before for the case of the transverse angular momenta in the middle columns of the figure.

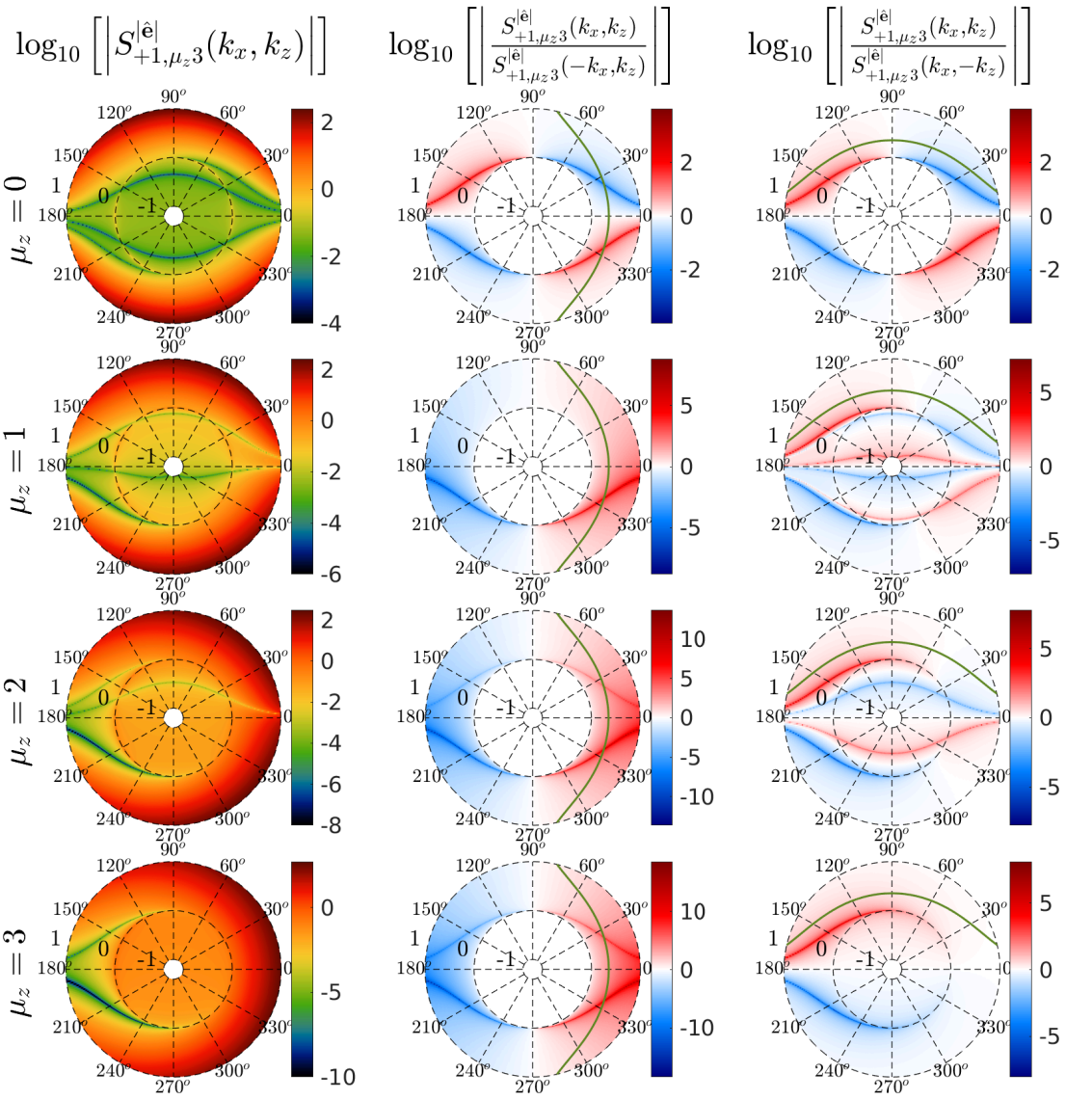

Figure 5.8: Same as Fig. 5.6 but for octupolar emissions.

Furthermore, there is another difference between the two cases. On the one hand, the directionality of the spectra for the case of the transverse angular momenta increases the larger the propagation constant of the guided mode is, i.e., the stronger the guidance of the mode is, and the deeper the evanescence of the coupled emitted fields is, the larger the directionality of the angular spectra is. On the other hand, the situation is opposite for the case of longitudinal angular momenta: the directionality of the angular spectra that couples to weakly guided modes in stronger.

Importantly, we would like to highlight that the longitudinal angular momentum could be used to sense chiral emissions. Once we select the longitudinal angular momentum, e.g., with an external bias of a static magnetic field, and, also, select, e.g., by exploiting the Zeeman splitting effect, a longitudinal angular momentum of a particular sign and of a magnitude that is equal to the multipolar order of the chiral multipolar emissions that we want to sense, then the last column of Figs. 5.6-5.8, together with the reflection symmetries of the emissions, propose that the directionality of the coupling of the emitted light shall be locked with the helicity of the emissions. The chiral sensing setup also requires a waveguide that supports a weakly guided mode of propagation constant almost equal to the wavenumber of free space.

Let us note that an emitter with well-known directional radiation properties of its propagating angular spectrum belongs to this family of emitters with well-defined longitudinal angular momentum. A $z-$oriented Huygens' dipole emitter is known to exhibit zero-backscattering in the $-\hat{\mathbf{z}}$ direction. It can be shown that it constitutes a superposition of the helical emissions of $|\lambda\,\mu_z\,\nu\,k\rangle^{(3)} = |{+1}\;{+1}\;1\,k\rangle^{(3)}$ and $|\lambda\,\mu_z\,\nu\,k\rangle^{(3)} = |{-1}\;{-1}\;1\,k\rangle^{(3)}$. The Huygens' dipole has been identified recently also for its near-field directional coupling with waveguide modes [301]. Its transverse angular spectrum is shown in Fig. 5.6. Note that its constitutive elements, $|{+1}\;{+1}\;1\,k\rangle^{(3)}$ and $|{-1}\;{-1}\;1\,k\rangle^{(3)}$, are mirror symmetric with respect to $\mathbf{M}_x$.

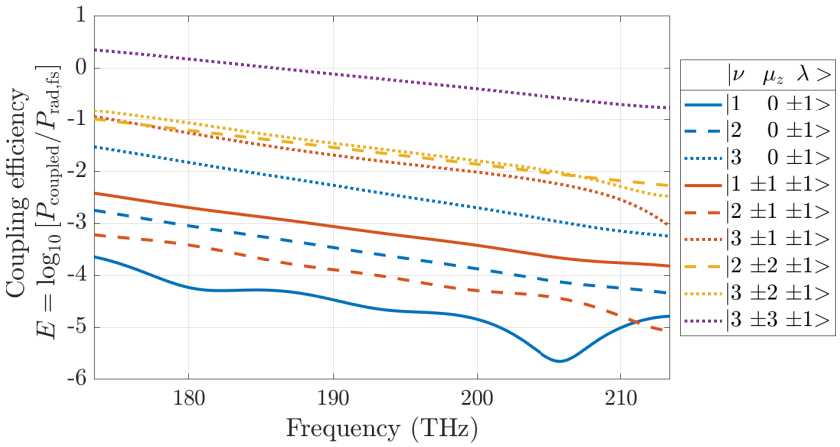

Figure 5.9: Plot of the coupling efficiencies of the multipolar transitions into the waveguide for the cases that are studied in Fig. 5.2.Adapted with permission from Ref. [A4] © John Wiley and Sons.

Finally, we would like to highlight another feature we observe in the first columns of Figs. 5.6-5.8. Generally, an increase in the strength of the evanescent part of the transverse angular spectrum is observed for increasing transverse angular momentum μ_z. Indeed, we can also verify this trend by plotting in Fig. 5.9 the coupling efficiencies of the multipolar transitions into the waveguide for the cases that we studied in Fig. 5.2. The coupling efficiency is defined as the logarithm of the ratio of the total power coupled to the two counterpropagating modes of the waveguide versus the total power radiated by the emitter in free space, i.e., in the absence of the waveguide. This observation is rather important since it can potentially make such higher-order multipolar transitions relevant when it comes to their detection by the waveguiding system, while, otherwise, they usually are relatively weakly excited by emitters in comparison to the more efficient usual dipolar transitions characterizing emitters of small optical size. Another thing to be observed in Fig. 5.9 is the diminishing trend of the coupling efficiency with increasing frequency. This can be explained by the fact that for large distances, the optical distance between the emitter and the waveguide becomes larger. Therefore, the deeply evanescent fields decay significantly when they arrive at the waveguide. As a result, only a part of the evanescent spectrum with small k_z values couples efficiently to the waveguide. Moreover, at higher frequencies, the propagation constant of the guided mode busually gets larger (with respect to the free space wavenumber). This also argues for a stronger decay of the part of the emitted fields involved into the coupling with the guided modes. A smaller distance between the emitter and the waveguide should generally shift all those curves up in higher values of coupling efficiencies. Finally, let us also note the interesting feature where we observe a spontaneous emission rate enhancement effect for the octupolar transitions with $|\mu_z| = 3$ at the lowest recorded frequencies.

Let us close this section by exploring the cases of a few other systems to examine how

robust this phenomenon of the linear dependence of the directionality on the transverse angular momentum of the emissions is. The intuition that we gain from the previous theoretical analysis tells us that the phenomenon of this directionality, being predominantly a result of the directional properties of the evanescent part of the emissions themselves, shall not be drastically affected by the particular configuration of the waveguide system (if we assume a fixed propagation constant β).

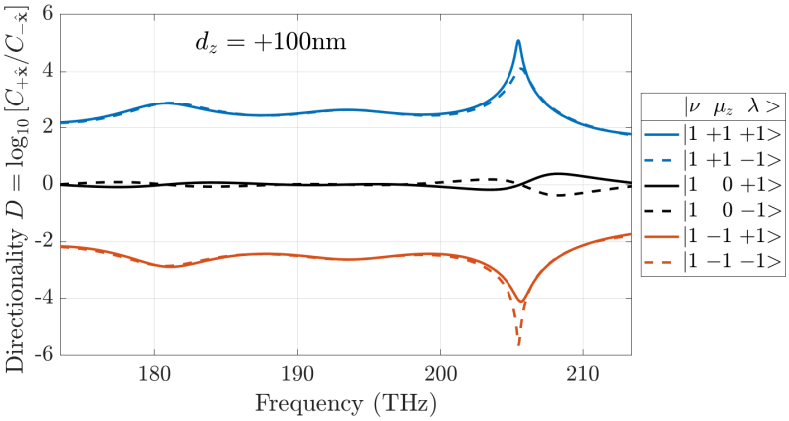

Figure 5.10: Directionality D with respect to frequency for the coupling of dipolar emissions from emitters that are displaced with a d_z=+100 nm from the xOy median plane. Adapted with permission from Ref. [A4] © John Wiley and Sons.

So, first, let us examine what happens with a simple perturbation of the initially considered system once we introduce a displacement of the emitter from the median plane at a distance of $d_z = 100$ nm. In Fig. 5.10, we plot the spectra of the measured directionality D for such a case. Comparing Fig. 5.10 with Fig. 5.4, we can observe that the directionalities of opposite helicities are no longer identical. Specifically, now we only have the symmetry that the directionalities of opposite helicity and opposite transverse angular momentum are opposite. This is a direct consequence of the $\mathbf{M}_x$ reflection symmetry of the system (see Eqs. (5.31, 5.37)). The $\mathbf{M}_z$ reflection symmetry now only relates the emissions between emitters with opposite displacement from the median plane along the z-axis. As a result, symmetries also do not give vanishing directionalities ideally for the cases of $\mu_z = 0$ anymore, which was the case in Fig. 5.4. However, apart from the breaking of those symmetries due to the displacement, the general trends of the recorded signals do remain the same. The signals of directionality that we record for $\mu_z = 0$ are nearly zero, whereas the signals that we record for $\mu_z = \pm 1$ vary around the values of ± 2, similarly to those of Fig. 5.4 where the emitters were not displaced. Hence, we deduce that the displacement of the emitters only has a minor effect on the observed phenomenon. A random placement of multiple such emitters on top of the waveguide shall, therefore, facilitate the up-scaling of the signal strengths of the coupled light without compromising the coupling directionality. Moreover, a superradiant scaling cannot be ruled out [302, 303]

Next, we consider the case of the emitters being placed inside a host medium, which is frequently the case in common experimental setups. Specifically, we consider the geometry presented in the inset of Fig. 5.11. We consider a rectangular layer of glass with a non-dispersive refractive index of 1.444 and a thickness of w=200 nm and a height of h=500 nm, as the embedding medium of the emitter. The emitter is placed at a quarter of the extent of the waveguide, i.e., at a distance of h/4 from its edge. The glass layer is placed on top of a rectangular silicon layer of the same dimensions. The refractive index of silicon is also considered non-dispersive and takes the value of 3.477. Like in our initial case, we excite the system with the same multipolar emitters (up to the octupolar order) and record

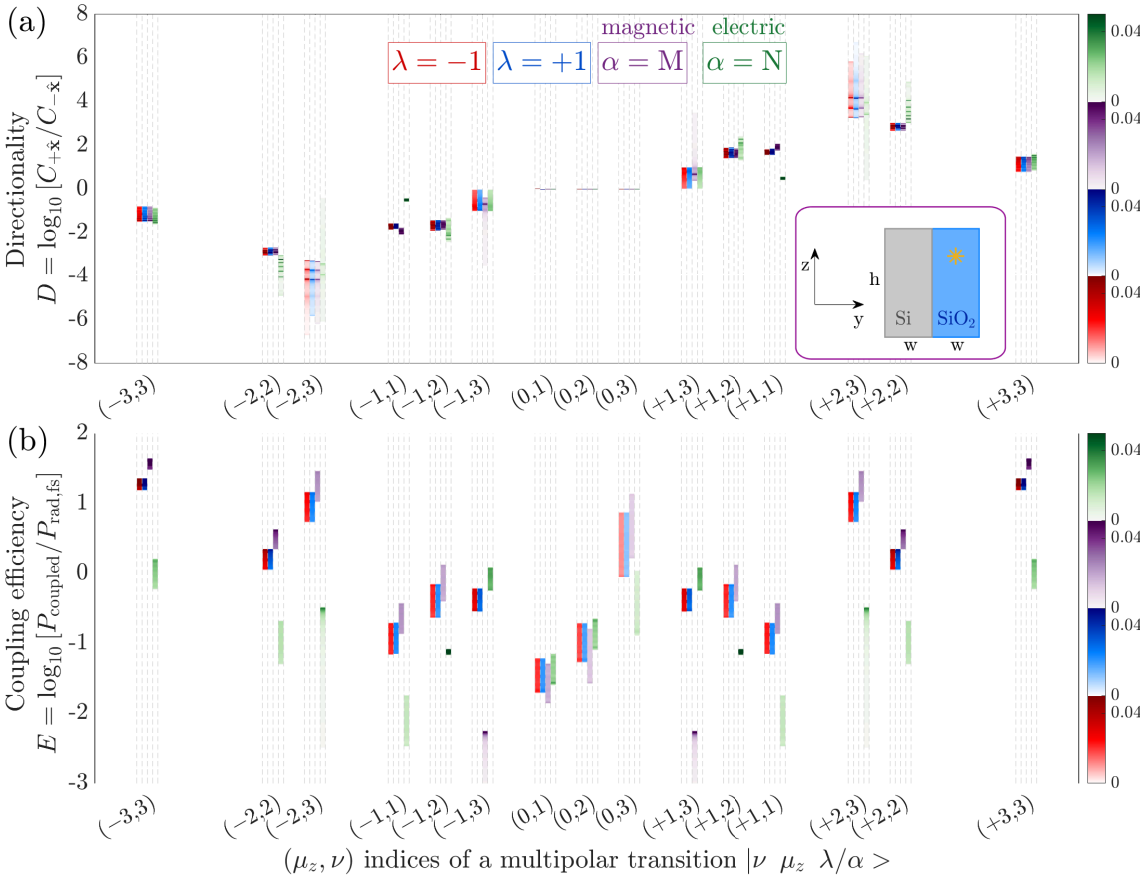

Figure 5.11: The case of emitters embedded in a glass layer on top of the waveguide: (a) Plot of the directionality for helical and electric/magnetic emissions with well-defined transverse angular momentum along the z-axis for the geometry in the inset, where w=200 nm and h=500 nm. The position of the emitter is marked by the yellow star, placed at the middle of the extent of the glass slab and at a qarter of its extent. (b) Plots of the corresponding coupling efficiencieds. Adapted with permission from Ref. [A4] © John Wiley and Sons.

the signals of directionality D across the same broadband spectrum of 40 THz bandwidth centered at 193.4 THz. This time apart of the helical emitters, we also excite with emitters of electric (TM) and magnetic (TE) types, to check whether they demonstrate a different behavior. So, in total, we excite with 30+30=60 emitters this time. This waveguide supports two modes with quite strong dispersion. The fundamental mode is characterized by a propagation constant that spans between a value of $\beta = 2.047k$ at the low frequencies and a value of $\beta = 2.468k$ at the high frequencies. The second mode is weakly guided at the interface of the two layers and is mostly localized inside the glass. Its propagation constant varies from $\beta = 1.12k$ at low frequencies till $\beta = 1.524k$ at high frequencies. Similarly as in Fig. 5.2, we plot our results of the recorded directionalities D in Fig. 5.11a and of the recorded coupling efficiencies (concerning the fundamental mode only) in Fig. 5.11b.

We, indeed, observe a quite similar behavior for both helical and electric/magnetic emitters (which are a perfect mix of helical emitters - see Eq. (5.1)). Furthermore, for $|\mu_z| \leq 2$, the directionality D exhibits, roughly, a linear dependence on μ_z with a slope similar to the slope observed in Fig. 5.2. However, the directionality of the $|\mu_z| = 3$ emissions breaks such linear dependence. We attribute this deviation to the initial multipolar emission reflecting off the air–glass interfaces, which shall be a secondary scattering process

that gives rise to other multipolar components. In Fig. 5.11b, we show the corresponding coupling efficiencies, which, for most cases, grow significantly as $|\mu_z|$ increases. The same thing we observed previously in Fig. 5.9. Moreover, we record again positive coupling efficiencies for several multipolar emissions. This implies that the waveguide mode collects more power than the emitter would radiate in the absence of the waveguide to an infinite homogeneous medium of the same material as the one where the emitter is embedded. That such coupling efficiency can be larger than one due to evanescent couplings was analytically shown for dipole emitters near a planar interface [304]. Furthermore, a related recent experimental observation was reported in Ref. [305].

Finally, it is important to mention that our observations here correspond to the case of the first fundamental guided mode of the waveguide. The effective refractive index of this mode is greater than the refractive index of the medium where we placed the emitter. For most parts of the spectrum, this is not the case for the second weakly guided mode that the waveguide supports. For that second mode, we observed much reduced directionalities and coupling efficiencies. We attribute this effect to the fact that the coupling of emitters inside the waveguide, for the case of a refractive index of the embedding medium that is larger than the effective refractive index of the guided mode, is not directly mediated by evanescent fields. As we discussed before, the evanescent fields of the emitters are mainly responsible for such prominent directionality features dependent on the transverse angular momentum of the emission. Therefore, we conclude that it is paramount to place the emitters inside a low-index medium to observe such phenomena.

6 — Conclusions

The presented thesis discussed ways to generalize the T-matrix method to address some contemporary needs for the modeling and analysis of nanophotonic systems. Specifically, we present three cases of **generalized T-matrices** that can enrich the toolkit of semi-analytical methods to model and study linear nanophotonic systems. In what follows, let us briefly highlight the key conclusion points from each chapter of this thesis and provide an outlook.

In the second chapter, we developed and discussed casual and stable models for linear time-varying bulk media. Our material models accounted also for temporal dispersion. However, on the one hand, those models were phenomenological, and, on the other hand, we adopted some assumptions (e.g., regarding the meromorphicity of the response function of the medium in frequency domain) that led to simplified models. Having in mind the complex physical processes that take place in practice in such (e.g., all-optically) time-modulated media at the microscopic level, one wonders about the actual complexity of the response function of such media. Unfortunately, so far there are not many experimental results against which such phenomenological models can be systematically tested and tuned properly. Moreover, testing the phenomenological models against quantum models that grasp in greater detail, from first principles, the underlying dynamics that take place at the microscopic level is also something essential that is missing. In fact, it even seems not clearly justified yet from the experiments whether the observed phenomenological modulation of the material properties of the media is really a linear phenomenon and is, therefore, able to be described by such response functions like the ones that we considered. If such is the case, then, assuming the all-optical modulations experimental setup, a variation of the intensity of the probe, for a given pump, i.e., for a given modulation of the medium, should not alter the measured material properties. Moreover, most experiments, so far, theoretically interpret their measured results with simple non-dispersive models, even though dispersion in the Epsilon-Near-Zero spectral regime of the measured media shall be rather prominent. To conclude, significant scientific efforts, both from a theory and experiment point of view, are still required to better understand and finely tune our material models for time-modulated media in optical frequencies.

Furthermore, the discussion on energy and photon number conservation in time-varying systems highlighted that, generally, time-varying media break the conservation of both. Actually, such systems generally behave as active, i.e., they can generate energy. Quite peculiarly, our discussion also showcased the emerging role of pseudo-photons, which are considered to have negative energies for negative frequencies. The deeper understanding of the physics surrounding the notion of pseudo-photons in time-varying media is of fundamental importance.

Besides this, we have discussed how time-varying systems generally break reciprocity. However, our generalization of the definition of reciprocity for time-varying systems was done from above, i.e., the definition was done from the macroscopic level, from which we later deduced the respective material properties of a reciprocal medium. However, for stationary media, the Onsager-Casimir reciprocal relations from statistical physics at the microscopic level are those that finally give the macroscopic definition of electromagnetic reciprocity. Therefore, the generalization of the Onsager-Casimir reciprocal relations

for time-varying systems from a microscopic level is missing to support our macroscopic definitions of reciprocity.

In the third chapter, we developed a T-matrix-based **Floquet-Mie theory** to semi-analytically solve the problem of light scattering from arbitrary time-modulated spherical scatterers. We observed that a prominent characteristic of such a time-varying scattering system is that of inelastic scattering of light at different frequencies from the incident one. Identifying methods with full-wave simulations to generalize the calculation of such T-matrices for non-spherical scatterers is important. While spherical scatterers are rather useful to efficiently probe fundamental physical phenomena, for practical applications usually the consideration of non-spherical scatterers is required. Here, the most significant impediment probably is the rather inefficient way that the existing full-wave solvers simulate time-varying systems.

Moreover, we have demonstrated phenomena of parametric oscillations in time-varying spheres, mediated by parametric Mie resonances. A deeper understanding of the multipolar eigenmode analysis of such systems is required. Besides this, the stability of such time-varying systems, i.e., the regime where the poles of the system move to the upper-half complex Floquet frequency space, is not yet systematically studied.

Furthermore, we have also discussed the breaking of reciprocity in time-modulated scatterers under the prism of their T-matrix. Designing nanophotonic systems that break reciprocity in the synthetic spectral dimension and implement conventional non-reciprocal operations, such as those of the isolators or circulators, is an interesting research direction that can reveal the unexplored potential of time-varying nanophotonic systems, providing, even, useful applications.

In the fourth chapter, we presented the **topological skeleton method**, which we employed to revise the conventional T-matrix of scatterers so that we transcend the problem of the Rayleigh Hypothesis. The newly introduced **distributed T-matrix** formalism allows for the accurate near-field coupling between scatterers at close proximity. We demonstrated and implemented with an FEM solver the calculation of the distributed T-matrix of an ellipsoid. A generalization of the calculations for scatterers of arbitrary geometry, without rotational symmetry, is quite straightforward once the topological skeleton and the necessary construction and division of the auxiliary surface of the scatterer are available. However, an efficient algorithm, tailored to the needs of our physical problem needs to be developed to address the topological skeleton calculations of 3D scatterers of arbitrary geometry. Such an algorithm needs to accept as inputs by the user the minimum and maximum distance between the auxiliary surface and the surface of the scatterer, as well as some measure of desired accuracy that can be used for the multipolar truncation of the infinite representations. Under these requirements, the algorithm should provide an optimized finite topological-skeleton-based representation of minimized dimensionality.

Additionally, we derived the extension of the conventional theoretical formulation of multi-scattering interactions to account for the newly introduced distributed T-matrices. The implementation of the respective necessary algorithmic extensions in existing T-matrix-based computational packages that perform multi-scattering calculations is further required. Note that the transformation between a distributed-T-matrix-based representation of a system of aggregated scatterers and its S-matrix representation that is suitable for the coupling of the aggregate with planar layer interfaces is rather straightforward. However, what is really interesting, is to probe for opportunities for the even further generalization of the distributed T-matrix formalism, to account for scatterers placed on top of substrates. This case requires special treatment since the abstracted individual scatterers cannot be considered any more to be embedded inside a homogeneous background medium for the calculation of their individual T-matrices.

Finally, in the fifth chapter, we presented a generalized T-matrix approach to analyze

phenomena of **directional coupling of emitted light into waveguides**. To probe the role of the chirality of the emissions regarding the directionality of the couplings, we employed a basis set of helical spherical waves to expand the emissions at the input of the T-matrix. However, we found out that the directionality of the emissions has only a minor dependence on the handedness of the emissions. We discussed **the prominent role of the transverse angular momentum** of the emissions that predominantly dictates the directionality of the couplings: its sign specifies the preferred direction of coupling and its absolute value dictates the degree of directionality in orders of magnitude. We identified the origins of that directionality by studying the evanescent part of the angular spectrum of the emissions, which also demonstrates a strong transverse-angular-momentum-dependent directionality. Additionally, we checked the robustness of the observed directional effects by considering a couple of other cases of more complicated waveguiding systems compared to the original.

Furthermore, we studied the role of two other quantization axes: the vertical and the longitudinal one. Performing a symmetry analysis of the T-matrix of the system, we found that the vertical angular momentum does not exhibit the same directionality characteristics and that it is position dependent. On the other hand, we were able to identify a chiral directional coupling mechanism for the case where there is a synergy between the helicity and the longitudinal angular momentum of the emissions. For emissions whose multipolar order is equal to the absolute value of the longitudinal angular momentum and locking the sign of the helicity of the emissions to that of the longitudinal angular momentum, e.g., by exploiting the Zeeman splitting effect, we can achieve a directional resolution of the handedness of the emissions. Note that, in this case, the directional effect is more pronounced for weakly guided modes.

Regarding potential future extensions of our study on directional coupling of emissions to waveguides, we identify two main research directions. First, in our studies we assumed a zero-th order Born approximation, i.e., we neglected higher order interactions between the emitter and the waveguide. Moreover, the interaction of the emitter with other emitters that potentially can also be present, was neglected as well. However, in several cases such interactions may have rather strong impact on the observed directionality and fully distort the regularities that we observed in our studies. Note, for example, that interesting synergetic effects among emitters, leading to superradiant collective coupled emissions have been reported in the literature. On the other hand, in our studies, to simplify our analysis, we have been generally exciting the waveguiding systems with single helical multipoles of our constructed Hilbert space. However, in many cases, we cannot generally predict from our studies the resulting directionality from an arbitrary coherent superposition of such multipolar emissions. Investigating the potential of designing such superimposed multipolar configurations of emissions for achieving optimal directionalities, tailored to the particular waveguide system, is another interesting research direction.

Bibliography

[A1] G. Ptitcyn *et al.*, "Floquet–mie theory for time-varying dispersive spheres," *Laser & Photonics Reviews*, vol. 17, no. 3, p. 2 100 683, 2023. DOI: https://doi.org/10.1002/lpor.202100683. eprint: https://onlinelibrary.wiley.com/doi/pdf/10.1002/lpor.202100683. [Online]. Available: https://onlinelibrary.wiley.com/doi/abs/10.1002/lpor.202100683.

[A2] P. Garg, A. G. Lamprianidis, D. Beutel, T. Karamanos, B. Verfürth, and C. Rockstuhl, "Modeling four-dimensional metamaterials: A t-matrix approach to describe time-varying metasurfaces," *Optics Express*, vol. 30, no. 25, pp. 45 832–45 847, Dec. 2022. DOI: 10.1364/OE.476035. [Online]. Available: https://opg.optica.org/oe/abstract.cfm?URI=oe-30-25-45832.

[A3] V. Asadchy *et al.*, "Parametric mie resonances and directional amplification in time-modulated scatterers," *Physical Review Applied*, vol. 18, no. 5, p. 054 065, 2022.

[A4] A. G. Lamprianidis, X. Zambrana-Puyalto, C. Rockstuhl, and I. Fernandez-Corbaton, "Directional coupling of emitters into waveguides: A symmetry perspective," *Laser & Photonics Reviews*, vol. 16, no. 1, p. 2 000 516, 2022. DOI: https://doi.org/10.1002/lpor.202000516. eprint: https://onlinelibrary.wiley.com/doi/pdf/10.1002/lpor.202000516. [Online]. Available: https://onlinelibrary.wiley.com/doi/abs/10.1002/lpor.202000516.

[A5] A. G. Lamprianidis, C. Rockstuhl, and I. Fernandez-Corbaton, "Transcending the rayleigh hypothesis with multipolar sources distributed across the topological skeleton of a scatterer," *Journal of Quantitative Spectroscopy and Radiative Transfer*, vol. 296, p. 108 455, 2023, ISSN: 0022-4073. DOI: https://doi.org/10.1016/j.jqsrt.2022.108455. [Online]. Available: https://www.sciencedirect.com/science/article/pii/S0022407322003909.

[1] H. Hertz, *Electric waves: being researches on the propagation of electric action with finite velocity through space*. Dover Publications, 1893.

[2] G. Marconi, "Wireless telegraphic communication," *Nobel Lecture*, vol. 11, pp. 198–222, 1909.

[3] G. Mie, "Beiträge zur optik trüber medien, speziell kolloidaler metallösungen," *Annalen der Physik*, vol. 330, no. 3, pp. 377–445, 1908. DOI: https://doi.org/10.1002/andp.19083300302. eprint: https://onlinelibrary.wiley.com/doi/pdf/10.1002/andp.19083300302. [Online]. Available: https://onlinelibrary.wiley.com/doi/abs/10.1002/andp.19083300302.

[4] P. Lilienfeld, "Gustav mie: The person," *Applied Optics*, vol. 30, no. 33, pp. 4696–4698, Nov. 1991. DOI: 10.1364/AO.30.004696. [Online]. Available: https://opg.optica.org/ao/abstract.cfm?URI=ao-30-33-4696.

[5] W. Hergert and T. Wriedt, *The Mie theory: basics and applications*. Springer, 2012, vol. 169.

[6] *Political guidelines of the commission 2019-2024*, 2019. [Online]. Available: https://commission.europa.eu/strategy-and-policy/priorities-2019-2024_en.

[7] M. L. Brongersma, Y. Cui, and S. Fan, "Light management for photovoltaics using high-index nanostructures," *Nature materials*, vol. 13, no. 5, pp. 451–460, 2014.

[8] H. A. Atwater and A. Polman, "Plasmonics for improved photovoltaic devices," *Nature materials*, vol. 9, no. 3, pp. 205–213, 2010.

[9] U. W. Paetzold *et al.*, "Disorder improves nanophotonic light trapping in thin-film solar cells," *Applied physics letters*, vol. 104, no. 13, p. 131 102, 2014.

[10] R. H. Siddique *et al.*, "Bioinspired phase-separated disordered nanostructures for thin photovoltaic absorbers," *Science advances*, vol. 3, no. 10, e1700232, 2017.

[11] Y. J. Donie *et al.*, "Light trapping in thin film silicon solar cells via phase separated disordered nanopillars," *Nanoscale*, vol. 10, no. 14, pp. 6651–6659, 2018.

[12] S. Makarov *et al.*, "Halide-perovskite resonant nanophotonics," *Advanced optical materials*, vol. 7, no. 1, p. 1 800 784, 2019.

[13] Y. Wang *et al.*, "Diffraction-grated perovskite induced highly efficient solar cells through nanophotonic light trapping," *Advanced Energy Materials*, vol. 8, no. 12, p. 1 702 960, 2018.

[14] K. Vynck, M. Burresi, F. Riboli, and D. S. Wiersma, "Photon management in two-dimensional disordered media," *Nature Materials*, vol. 11, no. 12, pp. 1017–1022, Dec. 2012, ISSN: 1476-4660. DOI: 10.1038/nmat3442. [Online]. Available: https://doi.org/10.1038/nmat3442.

[15] E. Agrell *et al.*, "Roadmap of optical communications," *Journal of Optics*, vol. 18, no. 6, p. 063 002, May 2016. DOI: 10.1088/2040-8978/18/6/063002. [Online]. Available: https://dx.doi.org/10.1088/2040-8978/18/6/063002.

[16] A. Mansour, R. Mesleh, and M. Abaza, "New challenges in wireless and free space optical communications," *Optics and Lasers in Engineering*, vol. 89, pp. 95–108, 2017, 3DIM-DS 2015: Optical Image Processing in the context of 3D Imaging, Metrology, and Data Security, ISSN: 0143-8166. DOI: https://doi.org/10.1016/j.optlaseng.2016.03.027. [Online]. Available: https://www.sciencedirect.com/science/article/pii/S0143816616300252.

[17] H. Kaushal, V. Jain, and S. Kar, *Free space optical communication*. Springer, 2017.

[18] H. Kaushal and G. Kaddoum, "Optical communication in space: Challenges and mitigation techniques," *IEEE Communications Surveys & Tutorials*, vol. 19, no. 1, pp. 57–96, 2017. DOI: 10.1109/COMST.2016.2603518.

[19] D. M. Cornwell, "Nasa's optical communications program for 2017 and beyond," in *2017 IEEE International Conference on Space Optical Systems and Applications (ICSOS)*, 2017, pp. 10–14. DOI: 10.1109/ICSOS.2017.8357203.

[20] S. Zhu, X. Chen, X. Liu, G. Zhang, and P. Tian, "Recent progress in and perspectives of underwater wireless optical communication," *Progress in Quantum Electronics*, vol. 73, p. 100 274, 2020.

[21] Z. Zhu *et al.*, "Compensation-free high-dimensional free-space optical communication using turbulence-resilient vector beams," *Nature communications*, vol. 12, no. 1, p. 1666, 2021.

[22] J. Zhao *et al.*, "Programmable time-domain digital-coding metasurface for nonlinear harmonic manipulation and new wireless communication systems," *National Science Review*, vol. 6, no. 2, pp. 231–238, Nov. 2018, ISSN: 2095-5138. DOI: 10.1093/nsr/nwy135. eprint: https://academic.oup.com/nsr/article-pdf/6/2/231/38915351/nwy135.pdf. [Online]. Available: https://doi.org/10.1093/nsr/nwy135.

[23] P. Marin-Palomo *et al.*, "Microresonator-based solitons for massively parallel coherent optical communications," *Nature*, vol. 546, no. 7657, pp. 274–279, 2017.

[24] C. Miller, *Chip War: The Fight for the World's Most Critical Technology*. Simon and Schuster, 2022.

[25] H. J. Levinson, "High-na euv lithography: Current status and outlook for the future," *Japanese Journal of Applied Physics*, vol. 61, no. SD, SD0803, 2022.

[26] L. Wischmeier *et al.*, "High-NA EUV lithography optics becomes reality," in *Extreme Ultraviolet (EUV) Lithography XI*, N. M. Felix and A. Lio, Eds., International Society for Optics and Photonics, vol. 11323, SPIE, 2020, p. 1 132 308. DOI: 10.1117/12.2543308. [Online]. Available: https://doi.org/10.1117/12.2543308.

[27] H. Schneider *et al.*, "High-end EUV photomask repairs for 5nm technology and beyond," in *Photomask Technology 2020*, M. E. Preil, Ed., International Society for Optics and Photonics, vol. 11518, SPIE, 2020, p. 1 151 808. DOI: 10.1117/12.2572879. [Online]. Available: https://doi.org/10.1117/12.2572879.

[28] C. Lian, C. Vagionas, T. Alexoudi, N. Pleros, N. Youngblood, and C. Ríos, *Nanophotonics*, vol. 11, no. 17, pp. 3823–3854, 2022. DOI: doi:10.1515/nanoph-2022-0089. [Online]. Available: https://doi.org/10.1515/nanoph-2022-0089.

[29] S. V. Makarov *et al.*, "Light-induced tuning and reconfiguration of nanophotonic structures," *Laser & Photonics Reviews*, vol. 11, no. 5, p. 1 700 108, 2017. DOI: https://doi.org/10.1002/lpor.201700108. eprint: https://onlinelibrary.wiley.com/doi/pdf/10.1002/lpor.201700108. [Online]. Available: https://onlinelibrary.wiley.com/doi/abs/10.1002/lpor.201700108.

[30] Y. J. Donie *et al.*, "Planarized and compact light scattering layers based on disordered titania nanopillars for light extraction in organic light emitting diodes," *Advanced Optical Materials*, vol. 9, no. 14, p. 2 001 610, 2021.

[31] L. Zschiedrich, H. J. Greiner, S. Burger, and F. Schmidt, "Numerical analysis of nanostructures for enhanced light extraction from OLEDs," in *Light-Emitting Diodes: Materials, Devices, and Applications for Solid State Lighting XVII*, K. P. Streubel, H. Jeon, L.-W. Tu, and M. Strassburg, Eds., International Society for Optics and Photonics, vol. 8641, SPIE, 2013, 86410B. DOI: 10.1117/12.2001132. [Online]. Available: https://doi.org/10.1117/12.2001132.

[32] A. Vaskin, R. Kolkowski, A. F. Koenderink, and I. Staude, *Nanophotonics*, vol. 8, no. 7, pp. 1151–1198, 2019. DOI: doi:10.1515/nanoph-2019-0110. [Online]. Available: https://doi.org/10.1515/nanoph-2019-0110.

[33] N. Yu and F. Capasso, "Flat optics with designer metasurfaces," *Nature materials*, vol. 13, no. 2, pp. 139–150, 2014.

[34] S.-W. Moon, Y. Kim, G. Yoon, and J. Rho, "Recent progress on ultrathin metalenses for flat optics," *Iscience*, vol. 23, no. 12, p. 101 877, 2020.

[35] A. Tittl *et al.*, "Imaging-based molecular barcoding with pixelated dielectric metasurfaces," *Science*, vol. 360, no. 6393, pp. 1105–1109, 2018.

[36] S. Zhang *et al.*, *Nanophotonics*, vol. 10, no. 1, pp. 259–293, 2021. DOI: doi:10.1515/nanoph-2020-0373. [Online]. Available: https://doi.org/10.1515/nanoph-2020-0373.

[37] P. Scott, X. Garcia-Santiago, D. Beutel, C. Rockstuhl, M. Wegener, and I. Fernandez-Corbaton, "On enhanced sensing of chiral molecules in optical cavities," *Applied Physics Reviews*, vol. 7, no. 4, p. 041 413, 2020.

[38] J. Xavier, D. Yu, C. Jones, E. Zossimova, and F. Vollmer, *Nanophotonics*, vol. 10, no. 5, pp. 1387–1435, 2021. DOI: doi:10.1515/nanoph-2020-0593. [Online]. Available: https://doi.org/10.1515/nanoph-2020-0593.

[39] L. Huang, L. Xu, M. Woolley, and A. E. Miroshnichenko, "Trends in quantum nanophotonics," *Advanced Quantum Technologies*, vol. 3, no. 4, p. 1 900 126, 2020. DOI: https://doi.org/10.1002/qute.201900126. eprint: https://onlinelibrary.wiley.com/doi/pdf/10.1002/qute.201900126. [Online]. Available: https://onlinelibrary.wiley.com/doi/abs/10.1002/qute.201900126.

[40] A. S. Solntsev, G. S. Agarwal, and Y. S. Kivshar, "Metasurfaces for quantum photonics," *Nature Photonics*, vol. 15, no. 5, pp. 327–336, 2021.

[41] B. Gallinet, J. Butet, and O. J. Martin, "Numerical methods for nanophotonics: Standard problems and future challenges," *Laser & Photonics Reviews*, vol. 9, no. 6, pp. 577–603, 2015.

[42] H. Chung and O. D. Miller, "High-na achromatic metalenses by inverse design," *Optics Express*, vol. 28, no. 5, pp. 6945–6965, Mar. 2020. DOI: 10.1364/OE.385440. [Online]. Available: https://opg.optica.org/oe/abstract.cfm?URI=oe-28-5-6945.

[43] P.-I. Schneider, X. G. Santiago, C. Rockstuhl, and S. Burger, "Global optimization of complex optical structures using Bayesian optimization based on Gaussian processes," in *Digital Optical Technologies 2017*, B. C. Kress and P. Schelkens, Eds., International Society for Optics and Photonics, vol. 10335, SPIE, 2017, 103350O. DOI: 10.1117/12.2270609. [Online]. Available: https://doi.org/10.1117/12.2270609.

[44] S. Molesky, Z. Lin, A. Y. Piggott, W. Jin, J. Vucković, and A. W. Rodriguez, "Inverse design in nanophotonics," *Nature Photonics*, vol. 12, no. 11, pp. 659–670, 2018.

[45] Y. Augenstein and C. Rockstuhl, "Inverse design of nanophotonic devices with structural integrity," *ACS photonics*, vol. 7, no. 8, pp. 2190–2196, 2020.

[46] S. So, T. Badloe, J. Noh, J. Bravo-Abad, and J. Rho, *Nanophotonics*, vol. 9, no. 5, pp. 1041–1057, 2020. DOI: doi:10.1515/nanoph-2019-0474. [Online]. Available: https://doi.org/10.1515/nanoph-2019-0474.

[47] P. R. Wiecha, A. Arbouet, C. Girard, and O. L. Muskens, "Deep learning in nanophotonics: Inverse design and beyond," *Photon. Res.*, vol. 9, no. 5, B182–B200, May 2021. DOI: 10.1364/PRJ.415960. [Online]. Available: https://opg.optica.org/prj/abstract.cfm?URI=prj-9-5-B182.

[48] T. W. Hughes, M. Minkov, V. Liu, Z. Yu, and S. Fan, "Full wave simulation and optimization of large area metalens," in *OSA Optical Design and Fabrication 2021 (Flat Optics, Freeform, IODC, OFT)*, Optica Publishing Group, 2021, FTh3C.5. DOI: 10.1364/FLATOPTICS.2021.FTh3C.5. [Online]. Available: https://opg.optica.org/abstract.cfm?URI=FLATOPTICS-2021-FTh3C.5.

[49] Z. Bo, X. Zheng-hui, R. Wu, L. Wei-ming, and S. Xin-qing, "Accelerating fdtd algorithm using gpu computing," in *2011 IEEE International Conference on Microwave Technology & Computational Electromagnetics*, 2011, pp. 410–413. DOI: 10.1109/ICMTCE.2011.5915546.

[50] J. Lu and J. Vuckovic, *Fdtd-z : A systolic scheme for gpu-accelerated nanophotonic simulation.* [Online]. Available: https://gist.github.com/jlu-spins/0f3c5459bd4386150ae30b17f7c6a5e3.

[51] M. I. Mishchenko, G. Videen, V. A. Babenko, N. G. Khlebtsov, and T. Wriedt, "T-matrix theory of electromagnetic scattering by particles and its applications: A comprehensive reference database," *Journal of Quantitative Spectroscopy and Radiative Transfer*, vol. 88, no. 1-3, pp. 357–406, 2004.

[52] P. R. Wiecha, "Pygdm—a python toolkit for full-field electro-dynamical simulations and evolutionary optimization of nanostructures," *Computer Physics Communications*, vol. 233, pp. 167–192, 2018, ISSN: 0010-4655. DOI: https://doi.org/10.1016/j.cpc.2018.06.017. [Online]. Available: https://www.sciencedirect.com/science/article/pii/S001046551830225X.

[53] N. Stefanou, V. Yannopapas, and A. Modinos, "Multem 2: A new version of the program for transmission and band-structure calculations of photonic crystals," *Computer Physics Communications*, vol. 132, no. 1, pp. 189–196, 2000, ISSN: 0010-4655. DOI: https://doi.org/10.1016/S0010-4655(00)00131-4. [Online]. Available: https://www.sciencedirect.com/science/article/pii/S0010465500001314.

[54] A. Egel, L. Pattelli, G. Mazzamuto, D. S. Wiersma, and U. Lemmer, "Celes: Cuda-accelerated simulation of electromagnetic scattering by large ensembles of spheres," *Journal of Quantitative Spectroscopy and Radiative Transfer*, vol. 199, pp. 103–110, 2017.

[55] A. Egel, K. M. Czajkowski, D. Theobald, K. Ladutenko, A. S. Kuznetsov, and L. Pattelli, "Smuthi: A python package for the simulation of light scattering by multiple particles near or between planar interfaces," *Journal of Quantitative Spectroscopy and Radiative Transfer*, vol. 273, p. 107 846, 2021.

[56] D. Theobald *et al.*, "Simulation of light scattering in large, disordered nanostructures using a periodic t-matrix method," *Journal of Quantitative Spectroscopy and Radiative Transfer*, vol. 272, p. 107 802, 2021.

[57] M. Bertrand, A. Devilez, J.-P. Hugonin, P. Lalanne, and K. Vynck, "Global polarizability matrix method for efficient modeling of light scattering by dense ensembles of non-spherical particles in stratified media," *Journal of the Optical Society of America A*, vol. 37, no. 1, pp. 70–83, Jan. 2020. DOI: 10.1364/JOSAA.37.000070. [Online]. Available: http://opg.optica.org/josaa/abstract.cfm?URI=josaa-37-1-70.

[58] J. Skarda *et al.*, "Low-overhead distribution strategy for simulation and optimization of large-area metasurfaces," *npj Computational Materials*, vol. 8, no. 1, p. 78, Apr. 2022, ISSN: 2057-3960. DOI: 10.1038/s41524-022-00774-y. [Online]. Available: https://doi.org/10.1038/s41524-022-00774-y.

[59] D. Beutel, A. Groner, C. Rockstuhl, and I. Fernandez-Corbaton, "Efficient simulation of biperiodic, layered structures based on the t-matrix method," *Journal of the Optical Society of America B*, vol. 38, no. 6, pp. 1782–1791, Jun. 2021. DOI: 10.1364/JOSAB.419645. [Online]. Available: https://opg.optica.org/josab/abstract.cfm?URI=josab-38-6-1782.

[60] A. Rahimzadegan *et al.*, "A comprehensive multipolar theory for periodic metasurfaces," *Advanced Optical Materials*, vol. 10, no. 10, p. 2 102 059, 2022. DOI: https://doi.org/10.1002/adom.202102059. eprint: https://onlinelibrary.wiley.com/doi/pdf/10.1002/adom.202102059. [Online]. Available: https://onlinelibrary.wiley.com/doi/abs/10.1002/adom.202102059.

[61] M. Fruhnert, I. Fernandez-Corbaton, V. Yannopapas, and C. Rockstuhl, "Computing the t-matrix of a scattering object with multiple plane wave illuminations," *Beilstein journal of nanotechnology*, vol. 8, no. 1, pp. 614–626, 2017.

[62] G. Demésy, J.-C. Auger, and B. Stout, "Scattering matrix of arbitrarily shaped objects: Combining finite elements and vector partial waves," *Journal of the Optical Society of America A*, vol. 35, no. 8, pp. 1401–1409, 2018.

[63] B. Sun, L. Bi, P. Yang, M. Kahnert, and G. Kattawar, *Invariant Imbedding T-matrix method for light scattering by nonspherical and inhomogeneous particles*. Elsevier, 2019.

[64] T. Wriedt, "Using the t-matrix method for light scattering computations by non-axisymmetric particles: Superellipsoids and realistically shaped particles," *Particle & Particle Systems Characterization: Measurement and Description of Particle Properties and Behavior in Powders and Other Disperse Systems*, vol. 19, no. 4, pp. 256–268, 2002.

[65] A. Lakhtakia, V. K. Varadan, and V. V. Varadan, "Iterative extended boundary condition method for scattering by objects of high aspect ratios," *The Journal of the Acoustical Society of America*, vol. 76, no. 3, pp. 906–912, 1984.

[66] D. Beutel, A. Groner, C. Rockstuhl, and I. Fernandez-Corbaton, "Efficient simulation of biperiodic, layered structures based on the t-matrix method," *Journal of the Optical Society of America B*, vol. 38, no. 6, pp. 1782–1791, 2021.

[67] M. V. Zhelyeznyakov, A. Zhan, and A. Majumdar, "Design and optimization of ellipsoid scatterer-based metasurfaces via the inverse t-matrix method," *OSA Continuum*, vol. 3, no. 1, pp. 89–103, Jan. 2020. DOI: 10.1364/OSAC.376537. [Online]. Available: http://opg.optica.org/osac/abstract.cfm?URI=osac-3-1-89.

[68] H.-C. Lin, Z. Wang, and C. W. Hsu, "Fast multi-source nanophotonic simulations using augmented partial factorization," *Nature Computational Science*, vol. 2, no. 12, pp. 815–822, Dec. 2022, ISSN: 2662-8457. DOI: 10.1038/s43588-022-00370-6. [Online]. Available: https://doi.org/10.1038/s43588-022-00370-6.

[69] D. Rodrigo *et al.*, "Mid-infrared plasmonic biosensing with graphene," *Science*, vol. 349, no. 6244, pp. 165–168, 2015. DOI: 10.1126/science.aab2051. eprint: https://www.science.org/doi/pdf/10.1126/science.aab2051. [Online]. Available: https://www.science.org/doi/abs/10.1126/science.aab2051.

[70] M. M. Salary, S. Jafar-Zanjani, and H. Mosallaei, "Time-varying metamaterials based on graphene-wrapped microwires: Modeling and potential applications," *Physical Review B*, vol. 97, p. 115 421, 11 Mar. 2018. DOI: 10.1103/PhysRevB.97.115421. [Online]. Available: https://link.aps.org/doi/10.1103/PhysRevB.97.115421.

[71] M. Liu, D. A. Powell, Y. Zarate, and I. V. Shadrivov, "Huygens' metadevices for parametric waves," *Physical Review X*, vol. 8, p. 031 077, 3 Sep. 2018. DOI: 10.1103/PhysRevX.8.031077. [Online]. Available: https://link.aps.org/doi/10.1103/PhysRevX.8.031077.

[72] X. Wang, M. S. Mirmoosa, V. S. Asadchy, C. Rockstuhl, S. Fan, and S. A. Tretyakov, "Metasurface-based realization of photonic time crystals," *Science Advances*, vol. 9, no. 14, eadg7541, 2023. DOI: 10.1126/sciadv.adg7541. eprint: https://www.science.org/doi/pdf/10.1126/sciadv.adg7541. [Online]. Available: https://www.science.org/doi/abs/10.1126/sciadv.adg7541.

[73] D. Shrekenhamer, W.-C. Chen, and W. J. Padilla, "Liquid crystal tunable metamaterial absorber," *Physical Review Letters*, vol. 110, p. 177 403, 17 Apr. 2013. DOI: 10.1103/PhysRevLett.110.177403. [Online]. Available: https://link.aps.org/doi/10.1103/PhysRevLett.110.177403.

[74] J. Bohn *et al.*, "Active tuning of spontaneous emission by mie-resonant dielectric metasurfaces," *Nano Letters*, vol. 18, no. 6, pp. 3461–3465, Jun. 2018, ISSN: 1530-6984. DOI: 10.1021/acs.nanolett.8b00475. [Online]. Available: https://doi.org/10.1021/acs.nanolett.8b00475.

[75] K. Zangeneh Kamali *et al.*, "Reversible image contrast manipulation with thermally tunable dielectric metasurfaces," *Small*, vol. 15, no. 15, p. 1 805 142, 2019. DOI: https://doi.org/10.1002/smll.201805142. eprint: https://onlinelibrary.wiley.com/doi/pdf/10.1002/smll.201805142. [Online]. Available: https://onlinelibrary.wiley.com/doi/abs/10.1002/smll.201805142.

[76] I. A. D. Williamson, M. Minkov, A. Dutt, J. Wang, A. Y. Song, and S. Fan, "Integrated nonreciprocal photonic devices with dynamic modulation," *Proceedings of the IEEE*, vol. 108, no. 10, pp. 1759–1784, 2020. DOI: 10.1109/JPROC.2020.3023959.

[77] D. Wang *et al.*, "Switchable ultrathin quarter-wave plate in terahertz using active phase-change metasurface," *Scientific Reports*, vol. 5, no. 1, p. 15 020, Oct. 2015, ISSN: 2045-2322. DOI: 10.1038/srep15020. [Online]. Available: https://doi.org/10.1038/srep15020.

[78] M. Z. Alam, I. De Leon, and R. W. Boyd, "Large optical nonlinearity of indium tin oxide in its epsilon-near-zero region," *Science*, vol. 352, no. 6287, pp. 795–797, 2016.

[79] N. Kinsey, C. DeVault, J. Kim, M. Ferrera, V. M. Shalaev, and A. Boltasseva, "Epsilon-near-zero al-doped zno for ultrafast switching at telecom wavelengths," *Optica*, vol. 2, no. 7, pp. 616–622, Jul. 2015. DOI: 10.1364/OPTICA.2.000616. [Online]. Available: https://opg.optica.org/optica/abstract.cfm?URI=optica-2-7-616.

[80] M. Ferrera and E. G. Carnemolla, "Ultra-fast transient plasmonics using transparent conductive oxides," *Journal of Optics*, vol. 20, no. 2, p. 024 007, Jan. 2018. DOI: 10.1088/2040-8986/aa9d01. [Online]. Available: https://dx.doi.org/10.1088/2040-8986/aa9d01.

[81] J. B. Khurgin, "Expanding the photonic palette: Exploring high index materials," *ACS Photonics*, vol. 9, no. 3, pp. 743–751, Mar. 2022. DOI: 10.1021/acsphotonics.1c01834. [Online]. Available: https://doi.org/10.1021/acsphotonics.1c01834.

[82] E. Galiffi *et al.*, "Photonics of time-varying media," *Advanced Photonics*, vol. 4, no. 1, p. 014 002, 2022. DOI: 10.1117/1.AP.4.1.014002. [Online]. Available: https://doi.org/10.1117/1.AP.4.1.014002.

[83] R. Tirole *et al.*, "Double-slit time diffraction at optical frequencies," *Nature Physics*, pp. 1–4, 2023.

[84] M. R. Shcherbakov *et al.*, "Ultrafast all-optical tuning of direct-gap semiconductor metasurfaces," *Nature communications*, vol. 8, no. 1, pp. 1–6, 2017.

[85] M. R. Shcherbakov, K. Werner, Z. Fan, N. Talisa, E. Chowdhury, and G. Shvets, "Photon acceleration and tunable broadband harmonics generation in nonlinear time-dependent metasurfaces," *Nature Communications*, vol. 10, no. 1, p. 1345, Mar. 2019, ISSN: 2041-1723. DOI: 10.1038/s41467-019-09313-8. [Online]. Available: https://doi.org/10.1038/s41467-019-09313-8.

[86] N. Karl *et al.*, "Frequency conversion in a time-variant dielectric metasurface," *Nano Letters*, vol. 20, no. 10, pp. 7052–7058, Oct. 2020, ISSN: 1530-6984. DOI: 10.1021/acs.nanolett.0c02113. [Online]. Available: https://doi.org/10.1021/acs.nanolett.0c02113.

[87] N.-H. Shen *et al.*, "Optically implemented broadband blueshift switch in the terahertz regime," *Physical Review Letters*, vol. 106, p. 037 403, 3 Jan. 2011. DOI: 10.1103/PhysRevLett.106.037403. [Online]. Available: https://link.aps.org/doi/10.1103/PhysRevLett.106.037403.

[88] N. Engheta, "Metamaterials with high degrees of freedom: Space, time, and more," *Nanophotonics*, vol. 10, no. 1, pp. 639–642, Jan. 2021, ISSN: 2192-8614. DOI: 10.1515/nanoph-2020-0414.

[89] A. Dutt *et al.*, "Creating boundaries along a synthetic frequency dimension," *Nature Communications*, vol. 13, no. 1, p. 3377, Jun. 2022, ISSN: 2041-1723. DOI: 10.1038/s41467-022-31140-7. [Online]. Available: https://doi.org/10.1038/s41467-022-31140-7.

[90] Z. Yu and S. Fan, "Complete optical isolation created by indirect interband photonic transitions," *Nature Photonics*, vol. 3, no. 2, pp. 91–94, 2009.

[91] D. L. Sounas and A. Alù, "Angular-momentum-biased nanorings to realize magnetic-free integrated optical isolation," *ACS Photonics*, vol. 1, no. 3, pp. 198–204, 2014.

[92] Y. Shi, S. Han, and S. Fan, "Optical circulation and isolation based on indirect photonic transitions of guided resonance modes," *ACS Photonics*, vol. 4, no. 7, pp. 1639–1645, 2017.

[93] T. Dinc, M. Tymchenko, A. Nagulu, D. Sounas, A. Alù, and H. Krishnaswamy, "Synchronized conductivity modulation to realize broadband lossless magnetic-free non-reciprocity," *Nature Communications*, vol. 8, no. 1, p. 795, 2017.

[94] R. Fleury, D. Sounas, and A. Alù, "Non-reciprocal optical mirrors based on spatio-temporal acousto-optic modulation," *Journal of Optics*, vol. 20, no. 3, p. 034 007, 2018.

[95] S. Taravati, N. Chamanara, and C. Caloz, "Nonreciprocal electromagnetic scattering from a periodically space-time modulated slab and application to a quasisonic isolator," *Physical Review B*, vol. 96, no. 16, p. 165 144, 2017.

[96] X. Wang *et al.*, "Nonreciprocity in bianisotropic systems with uniform time modulation," *Physical Review Letters*, vol. 125, no. 26, p. 266 102, 2020.

[97] E. S. Cassedy and A. A. Oliner, "Dispersion relations in time-space periodic media: Part i—stable interactions," *Proceedings of the IEEE*, vol. 51, no. 10, pp. 1342–1359, 1963.

[98] M. M. Salary, S. Jafar-Zanjani, and H. Mosallaei, "Time-varying metamaterials based on graphene-wrapped microwires: Modeling and potential applications," *Physical Review B*, vol. 97, no. 11, p. 115 421, 2018.

[99] D. Ramaccia, D. L. Sounas, A. Alù, A. Toscano, and F. Bilotti, "Phase-induced frequency conversion and doppler effect with time-modulated metasurfaces," *IEEE Transactions on Antennas and Propagation*, vol. 68, no. 3, pp. 1607–1617, 2019.

[100] D. Holberg and K. Kunz, "Parametric properties of fields in a slab of time-varying permittivity," *IEEE Transactions on Antennas and Propagation*, vol. 14, no. 2, pp. 183–194, 1966.

[101] N. Wang, Z.-Q. Zhang, and C. T. Chan, "Photonic floquet media with a complex time-periodic permittivity," *Physical Review B*, vol. 98, no. 8, p. 085 142, 2018.

[102] T. T. Koutserimpas and R. Fleury, "Nonreciprocal gain in non-hermitian time-floquet systems," *Physical Review Letters*, vol. 120, no. 8, p. 087 401, 2018.

[103] F. Biancalana, A. Amann, A. V. Uskov, and E. P. O'Reilly, "Dynamics of light propagation in spatiotemporal dielectric structures," *Physical Review E*, vol. 75, no. 4, p. 046 607, Apr. 2007. DOI: 10.1103/PhysRevE.75.046607. [Online]. Available: https://link.aps.org/doi/10.1103/PhysRevE.75.046607 (visited on 12/03/2021).

[104] J. R. Zurita-Sánchez, P. Halevi, and J. C. Cervantes-Gonzalez, "Reflection and transmission of a wave incident on a slab with a time-periodic dielectric function $\varepsilon(t)$," *Physical Review A*, vol. 79, no. 5, p. 053 821, May 2009. DOI: 10.1103/PhysRevA.79.053821. [Online]. Available: https://link.aps.org/doi/10.1103/PhysRevA.79.053821 (visited on 12/03/2021).

[105] E. Lustig, Y. Sharabi, and M. Segev, "Topological aspects of photonic time crystals," *Optica*, vol. 5, no. 11, pp. 1390–1395, Nov. 2018, ISSN: 2334-2536. DOI: 10.1364/OPTICA.5.001390. [Online]. Available: https://www.osapublishing.org/optica/abstract.cfm?uri=optica-5-11-1390 (visited on 12/03/2021).

[106] J. Park and B. Min, "Spatiotemporal plane wave expansion method for arbitrary space–time periodic photonic media," *Optics Letters*, vol. 46, no. 3, pp. 484–487, Feb. 2021, ISSN: 1539-4794. DOI: 10.1364/OL.411622. [Online]. Available: https://www.osapublishing.org/ol/abstract.cfm?uri=ol-46-3-484 (visited on 12/03/2021).

[107] Y. Sharabi, E. Lustig, and M. Segev, "Disordered photonic time crystals," *Physical Review Letters*, vol. 126, no. 16, p. 163 902, 2021.

[108] M. Lyubarov, Y. Lumer, A. Dikopoltsev, E. Lustig, Y. Sharabi, and M. Segev, "Amplified emission and lasing in photonic time crystals," *Science*, vol. 377, no. 6604, pp. 425–428, 2022. DOI: 10.1126/science.abo3324. eprint: https://www.science.org/doi/pdf/10.1126/science.abo3324. [Online]. Available: https://www.science.org/doi/abs/10.1126/science.abo3324.

[109] Y. Sharabi, A. Dikopoltsev, E. Lustig, Y. Lumer, and M. Segev, "Spatiotemporal photonic crystals," *Optica*, vol. 9, no. 6, pp. 585–592, Jun. 2022. DOI: 10.1364/OPTICA.455672. [Online]. Available: https://opg.optica.org/optica/abstract.cfm?URI=optica-9-6-585.

[110] M. S. Mirmoosa, M. S. M. Mollaei, G. A. Ptitcyn, C. R. Simovski, and S. A. Tretyakov, "Time-varying plasmonic particles," in *2021 Fifteenth International Congress on Artificial Materials for Novel Wave Phenomena (Metamaterials)*, Sep. 2021, pp. 272–274. DOI: 10.1109/Metamaterials52332.2021.9577104.

[111] D. M. Solís and N. Engheta, "Functional analysis of the polarization response in linear time-varying media: A generalization of the Kramers-Kronig relations," *Physical Review B*, vol. 103, no. 14, p. 144 303, Apr. 2021. DOI: 10.1103/PhysRevB.103.144303.

[112] A. Mekawy, H. Li, Y. Radi, and A. Alù, "Parametric enhancement of radiation from electrically small antennas," *Physical Review Applied*, vol. 15, no. 5, p. 054 063, May 2021. DOI: 10.1103/PhysRevApplied.15.054063.

[113] M. S. Mirmoosa, T. T. Koutserimpas, G. A. Ptitcyn, S. A. Tretyakov, and R. Fleury, "Dipole polarizability of time-varying particles," *New Journal of Physics*, vol. 24, no. 6, p. 063 004, Jun. 2022, ISSN: 1367-2630. DOI: 10.1088/1367-2630/ac6b4c.

[114] I. Stefanou, P. A. Pantazopoulos, and N. Stefanou, "Light scattering by a spherical particle with a time-periodicrefractive index," *Journal of the Optical Society of America B*, vol. 38, no. 2, pp. 407–414, Feb. 2021. DOI: 10.1364/JOSAB.408559. [Online]. Available: http://josab.osa.org/abstract.cfm?URI=josab-38-2-407.

[115] L. Rayleigh, "On the dynamical theory of gratings," *Proceedings of the Royal Society of London. Series A, Containing Papers of a Mathematical and Physical Character*, vol. 79, no. 532, pp. 399–416, 1907, ISSN: 09501207. [Online]. Available: http://www.jstor.org/stable/92655 (visited on 05/09/2022).

[116] R. F. Millar, "On the rayleigh assumption in scattering by a periodic surface," *Mathematical Proceedings of the Cambridge Philosophical Society*, vol. 65, no. 3, pp. 773–791, 1969. DOI: 10.1017/S0305004100003613.

[117] A. G. Voronovich, "Rayleigh hypothesis," in *Light Scattering and Nanoscale Surface Roughness*, A. A. Maradudin, Ed. Boston, MA: Springer US, 2007, pp. 93–105, ISBN: 978-0-387-35659-4. DOI: 10.1007/978-0-387-35659-4_4. [Online]. Available: https://doi.org/10.1007/978-0-387-35659-4_4.

[118] H. Kalhor, "Numerical evaluation of rayleigh hypothesis for analyzing scattering from corrugated gratings–te polarization," *IEEE Transactions on Antennas and Propagation*, vol. 24, no. 6, pp. 884–889, 1976. DOI: 10.1109/TAP.1976.1141432.

[119] J. M. Soto-Crespo, M. Nieto-Vesperinas, and A. T. Friberg, "Scattering from slightly rough random surfaces: A detailed study on the validity of the small perturbation method," *Journal of the Optical Society of America A*, vol. 7, no. 7, pp. 1185–1201, Jul. 1990. DOI: 10.1364/JOSAA.7.001185. [Online]. Available: http://opg.optica.org/josaa/abstract.cfm?URI=josaa-7-7-1185.

[120] S. Christiansen and R. Kleinman, "On a misconception involving point collocation and the rayleigh hypothesis," *IEEE Transactions on Antennas and Propagation*, vol. 44, no. 10, pp. 1309–1316, 1996. DOI: 10.1109/8.537324.

[121] R. Zaridze, G. Bit-Babik, K. Tavzarashvili, D. Economou, and N. Uzunoglu, "Wave field singularity aspects in large-size scatterers and inverse problems," *IEEE Transactions on Antennas and Propagation*, vol. 50, no. 1, pp. 50–58, 2002. DOI: 10.1109/8.992561.

[122] T. Watanabe, Y. Choyal, K. Minami, and V. L. Granatstein, "Range of validity of the rayleigh hypothesis," *Physical Review E*, vol. 69, p. 056 606, 5 May 2004. DOI: 10.1103/PhysRevE.69.056606. [Online]. Available: https://link.aps.org/doi/10.1103/PhysRevE.69.056606.

[123] A. V. Tishchenko, "Numerical demonstration of the validity of the rayleigh hypothesis," *Optics Express*, vol. 17, no. 19, pp. 17 102–17 117, Sep. 2009. DOI: 10.1364/OE.17.017102. [Online]. Available: http://opg.optica.org/oe/abstract.cfm?URI=oe-17-19-17102.

[124] I. Petoev, V. Tabatadze, D. Kakulia, and R. Zaridze, "About scattered field's singularities and rayleigh hypothesis," in *2012 XVIIth International Seminar/Workshop on Direct and Inverse Problems of Electromagnetic and Acoustic Wave Theory - (DIPED)*, 2012, pp. 17–22.

[125] P. A. Martin, "Two-dimensional acoustic scattering, conformal mapping, and the rayleigh hypothesis," *The Journal of the Acoustical Society of America*, vol. 132, no. 4, pp. 2184–2188, 2012. DOI: 10.1121/1.4747004. eprint: https://doi.org/10.1121/1.4747004. [Online]. Available: https://doi.org/10.1121/1.4747004.

[126] T. Rother and M. Kahnert, "The rayleigh hypothesis," in *Electromagnetic Wave Scattering on Nonspherical Particles: Basic Methodology and Simulations*. Berlin, Heidelberg: Springer Berlin Heidelberg, 2014, pp. 171–201, ISBN: 978-3-642-36745-8. DOI: 10.1007/978-3-642-36745-8_6. [Online]. Available: https://doi.org/10.1007/978-3-642-36745-8_6.

[127] R. F. Millar, "The rayleigh hypothesis and a related least-squares solution to scattering problems for periodic surfaces and other scatterers," *Radio Science*, vol. 8, no. 8-9, pp. 785–796, 1973. DOI: https://doi.org/10.1029/RS008i008p00785. eprint: https://agupubs.onlinelibrary.wiley.com/doi/pdf/10.1029/RS008i008p00785. [Online]. Available: https://agupubs.onlinelibrary.wiley.com/doi/abs/10.1029/RS008i008p00785.

[128] A. A. Antonov and M. V. Gorkunov, "Corrugated silicon metasurface optimized within the rayleigh hypothesis for anomalous refraction at large angles," *Journal of the Optical Society of America B*, vol. 36, no. 8, pp. 2118–2125, Aug. 2019. DOI: 10.1364/JOSAB.36.002118. [Online]. Available: http://opg.optica.org/josab/abstract.cfm?URI=josab-36-8-2118.

[129] T. Rother and S. C. Hawkins, "Notes on rayleigh's hypothesis and the extended boundary condition method," *The Journal of the Acoustical Society of America*, vol. 149, no. 4, pp. 2179–2188, 2021. DOI: 10.1121/10.0003958. eprint: https://doi.org/10.1121/10.0003958. [Online]. Available: https://doi.org/10.1121/10.0003958.

[130] B. Auguié, W. R. C. Somerville, S. Roache, and E. C. L. Ru, "Numerical investigation of the rayleigh hypothesis for electromagnetic scattering by a particle," *Journal of Optics*, vol. 18, no. 7, p. 075 007, May 2016. DOI: 10.1088/2040-8978/18/7/075007. [Online]. Available: https://doi.org/10.1088%2F2040-8978%2F18%2F7%2F075007.

[131] D. Schebarchov, E. C. L. Ru, J. Grand, and B. Auguié, "Mind the gap: Testing the rayleigh hypothesis in t-matrix calculations with adjacent spheroids," *Optics Express*, vol. 27, no. 24, pp. 35 750–35 760, Nov. 2019. DOI: 10.1364/OE.27.035750. [Online]. Available: http://www.opticsexpress.org/abstract.cfm?URI=oe-27-24-35750.

[132] R. T.Bates, "Analytic constraints on electromagnetic field computations," *IEEE Transactions on Microwave Theory and Techniques*, vol. 23, no. 8, pp. 605–623, 1975. DOI: 10.1109/TMTT.1975.1128639.

[133] P. M. van den Berg and J. T. Fokkema, "The rayleigh hypothesis in the theory of reflection by a grating," *Journal of the Optical Society of America*, vol. 69, no. 1, pp. 27–31, Jan. 1979. DOI: 10.1364/JOSA.69.000027. [Online]. Available: http://www.osapublishing.org/abstract.cfm?URI=josa-69-1-27.

[134] P. M. van den Berg and J. T. Fokkema, "The rayleigh hypothesis in the theory of diffraction by a perturbation in a plane surface," *Radio Science*, vol. 15, no. 4, pp. 723–732, 1980. DOI: https://doi.org/10.1029/RS015i004p00723. eprint: https://agupubs.onlinelibrary.wiley.com/doi/pdf/10.1029/RS015i004p00723. [Online]. Available: https://agupubs.onlinelibrary.wiley.com/doi/abs/10.1029/RS015i004p00723.

[135] D. Maystre and M. Cadilhac, "Singularities of the continuation of fields and validity of rayleigh's hypothesis," *Journal of Mathematical Physics*, vol. 26, no. 9, pp. 2201–2204, 1985. DOI: 10.1063/1.526847. [Online]. Available: https://doi.org/10.1063/1.526847.

[136] M. Burrows, "Equivalence of the rayleigh solution and the extended-boundary-condition solution for scattering problems," English, *Electronics Letters*, vol. 5, 277–278(1), 12 Jun. 1969, ISSN: 0013-5194. [Online]. Available: https://digital-library.theiet.org/content/journals/10.1049/el_19690210.

[137] A. G. Kyurkchan, B. Y. Sternin, and V. E. Shatalov, "Singularities of continuation of wave fields," *Physics-Uspekhi*, vol. 39, no. 12, pp. 1221–1242, Dec. 1996. DOI: 10.1070/pu1996v039n12abeh000184. [Online]. Available: https://doi.org/10.1070%5C%2Fpu1996v039n12abeh000184.

[138] A. Kyurkchan and N. Smirnova, *Mathematical Modeling in Diffraction Theory: Based on A Priori Information on the Analytical Properties of the Solution*. Elsevier Science, 2015, ISBN: 9780128037485. [Online]. Available: https://books.google.de/books?id=gHy8BwAAQBAJ.

[139] S. Pulbere and T. Wriedt, "Light scattering by cylindrical fibers with high aspect ratio using the null-field method with discrete sources," *Particle & Particle Systems Characterization*, vol. 21, no. 3, pp. 213–218, 2004. DOI: https://doi.org/10.1002/ppsc.200400864. eprint: https://onlinelibrary.wiley.com/doi/pdf/10.1002/ppsc.200400864. [Online]. Available: https://onlinelibrary.wiley.com/doi/abs/10.1002/ppsc.200400864.

[140] T. Wriedt, "Review of the null-field method with discrete sources," *Journal of Quantitative Spectroscopy and Radiative Transfer*, vol. 106, no. 1, pp. 535–545, 2007, IX Conference on Electromagnetic and Light Scattering by Non-Spherical Particles, ISSN: 0022-4073. DOI: https://doi.org/10.1016/j.jqsrt.2007.01.043. [Online]. Available: http://www.sciencedirect.com/science/article/pii/S0022407307000532.

[141] A. Doicu, *Acoustic and Electromagnetic Scattering Analysis Using Discrete Sources*. 2000. DOI: 10.1016/B978-012219740-6/50000-9.

[142] A. Doicu, T. Wriedt, and Y. Eremin, *Light Scattering by Systems of Particles: Null-Field Method with Discrete Sources: Theory and Programs* (Springer Series in Optical Sciences). Springer Berlin Heidelberg, 2006, ISBN: 9783540336976. [Online]. Available: https://books.google.de/books?id=NXK7BQAAQBAJ.

[143] J. Eremin, N. Orlov, and V. Rozenberg, "Scattering by non-spherical particles," *Computer Physics Communications*, vol. 79, no. 2, pp. 201–214, 1994, ISSN: 0010-4655. DOI: https://doi.org/10.1016/0010-4655(94)90068-X. [Online]. Available: https://www.sciencedirect.com/science/article/pii/001046559490068X.

[144] E. Moreno, D. Erni, C. Hafner, and R. Vahldieck, "Multiple multipole method with automatic multipole setting applied to the simulation of surface plasmons in metallic nanostructures," *Journal of the Optical Society of America A*, vol. 19, no. 1, pp. 101–111, Jan. 2002. DOI: 10.1364/JOSAA.19.000101. [Online]. Available: http://josaa.osa.org/abstract.cfm?URI=josaa-19-1-101.

[145] R. Mitsch, C. Sayrin, B. Albrecht, P. Schneeweiss, and A. Rauschenbeutel, "Quantum state-controlled directional spontaneous emission of photons into a nanophotonic waveguide," *Nature Communications*, vol. 5, no. 1, Dec. 2014. DOI: 10.1038/ncomms6713. [Online]. Available: https://doi.org/10.1038/ncomms6713.

[146] I. Söllner *et al.*, "Deterministic photon–emitter coupling in chiral photonic circuits," *Nature Nanotechnology*, vol. 10, no. 9, pp. 775–778, 2015. DOI: 10.1038/nnano.2015.159.

[147] R. J. Coles *et al.*, "Chirality of nanophotonic waveguide with embedded quantum emitter for unidirectional spin transfer," *Nature Communications*, vol. 7, no. 1, p. 11 183, 2016, ISSN: 2041-1723. DOI: 10.1038/ncomms11183. [Online]. Available: https://doi.org/10.1038/ncomms11183.

[148] L. Scarpelli *et al.*, "99% beta factor and directional coupling of quantum dots to fast light in photonic crystal waveguides determined by spectral imaging," *Physical Review B*, vol. 100, p. 035 311, 3 Jul. 2019. DOI: 10.1103/PhysRevB.100.035311. [Online]. Available: https://link.aps.org/doi/10.1103/PhysRevB.100.035311.

[149] P. Mrowiński *et al.*, "Directional emission of a deterministically fabricated quantum dot–bragg reflection multimode waveguide system," *ACS Photonics*, vol. 6, no. 9, pp. 2231–2237, 2019. DOI: 10.1021/acsphotonics.9b00369. eprint: https://doi.org/10.1021/acsphotonics.9b00369. [Online]. Available: https://doi.org/10.1021/acsphotonics.9b00369.

[150] M. J. Mehrabad *et al.*, "Chiral topological photonics with an embedded quantum emitter," *Optica*, vol. 7, no. 12, pp. 1690–1696, Dec. 2020. DOI: 10.1364/OPTICA.393035. [Online]. Available: https://opg.optica.org/optica/abstract.cfm?URI=optica-7-12-1690.

[151] H. Siampour *et al.*, "Observation of large spontaneous emission rate enhancement of quantum dots in a broken-symmetry slow-light waveguide," *npj Quantum Information*, vol. 9, no. 1, p. 15, Feb. 2023, ISSN: 2056-6387. DOI: 10.1038/s41534-023-00686-9. [Online]. Available: https://doi.org/10.1038/s41534-023-00686-9.

[152] M. F. Picardi *et al.*, "Experimental demonstration of linear and spinning janus dipoles for polarisation- and wavelength-selective near-field coupling," *Light: Science & Applications*, vol. 8, no. 1, p. 52, Jun. 2019, ISSN: 2047-7538. DOI: 10.1038/s41377-019-0162-x. [Online]. Available: https://doi.org/10.1038/s41377-019-0162-x.

[153] L. Fang, H.-Z. Luo, X.-P. Cao, S. Zheng, X.-L. Cai, and J. Wang, "Ultra-directional high-efficiency chiral silicon photonic circuits," *Optica*, vol. 6, no. 1, pp. 61–66, Jan. 2019. DOI: 10.1364/OPTICA.6.000061.

[154] J. Petersen, J. Volz, and A. Rauschenbeutel, "Chiral nanophotonic waveguide interface based on spin-orbit interaction of light," *Science*, vol. 346, no. 6205, pp. 67–71, 2014. DOI: 10.1126/science.1257671.

[155] F. J. Rodriguez-Fortuno, I. Barber-Sanz, D. Puerto, A. Griol, and A. Martínez, "Resolving light handedness with an on-chip silicon microdisk," *ACS Photonics*, vol. 1, no. 9, pp. 762–767, 2014. DOI: 10.1021/ph500084b.

[156] F. Le Kien and A. Rauschenbeutel, "Anisotropy in scattering of light from an atom into the guided modes of a nanofiber," *Physical Review A*, vol. 90, no. 2, p. 023 805, 2014.

[157] M. F. Picardi, A. Manjavacas, A. V. Zayats, and F. J. Rodriguez-Fortuno, "Unidirectional evanescent-wave coupling from circularly polarized electric and magnetic dipoles: An angular spectrum approach," *Physical Review B*, vol. 95, p. 245 416, 24 Jun. 2017. DOI: 10.1103/PhysRevB.95.245416. [Online]. Available: https://link.aps.org/doi/10.1103/PhysRevB.95.245416.

[158] M. F. Picardi, A. V. Zayats, and F. J. Rodrguez-Fortuno, "Janus and huygens dipoles: Near-field directionality beyond spin-momentum locking," *Physical Review Letters*, vol. 120, p. 117 402, 11 Mar. 2018. DOI: 10.1103/PhysRevLett.120.117402. [Online]. Available: https://link.aps.org/doi/10.1103/PhysRevLett.120.117402.

[159] L. Wei and F. J. Rodriguez-Fortuno, "Momentum-space geometric structure of helical evanescent waves and its implications on near-field directionality," *Physical Review Applied*, vol. 13, p. 014 008, 1 Jan. 2020. DOI: 10.1103/PhysRevApplied.13.014008. [Online]. Available: https://link.aps.org/doi/10.1103/PhysRevApplied.13.014008.

[160] R. S. Savelev, D. F. Kornovan, V. V. Yaroshenko, and M. I. Petrov, "Analogue of the kerker effect for localized modes of discrete high-index dielectric nanowaveguides," *Journal of Applied Physics*, vol. 125, no. 12, p. 123 104, 2019. DOI: 10.1063/1.5087248. [Online]. Available: https://doi.org/10.1063/1.5087248.

[161] J. E. Vázquez-Lozano, A. Martinez, and F. J. Rodriguez-Fortuno, "Near-field directionality beyond the dipole approximation: Electric quadrupole and higher-order multipole angular spectra," *Physical Review Applied*, vol. 12, p. 024 065, 2 Aug. 2019. DOI: 10.1103/PhysRevApplied.12.024065. [Online]. Available: https://link.aps.org/doi/10.1103/PhysRevApplied.12.024065.

[162] A. Aiello, P. Banzer, M. Neugebauer, and G. Leuchs, "From transverse angular momentum to photonic wheels," *Nature Photonics*, vol. 9, no. 12, pp. 789–795, Dec. 2015, ISSN: 1749-4885. [Online]. Available: http://dx.doi.org/10.1038/nphoton.2015.203.

[163] K. Y. Bliokh, D. Smirnova, and F. Nori, "Quantum spin hall effect of light," *Science*, vol. 348, no. 6242, pp. 1448–1451, 2015. DOI: 10.1126/science.aaa9519.

[164] B. le Feber, N. Rotenberg, and L. Kuipers, "Nanophotonic control of circular dipole emission," *Nature Communications*, vol. 6, p. 6695, Apr. 2015. [Online]. Available: https://doi.org/10.1038/ncomms7695.

[165] K. Y. Bliokh, F. Rodriguez-Fortuno, F. Nori, and A. V. Zayats, "Spin-orbit interactions of light," *Nature Photonics*, vol. 9, no. 12, pp. 796–808, 2015. DOI: doi:10.1038/nphoton.2015.201.

[166] I. Fernandez-Corbaton, X. Zambrana-Puyalto, N. Bonod, and C. Rockstuhl, "Transverse multipolar light-matter couplings in evanescent waves," *Physical Review A*, vol. 94, Jun. 2016. DOI: 10.1103/PhysRevA.94.053822.

[167] A. Espinosa-Soria and A. Martinez, "Transverse spin and spin-orbit coupling in silicon waveguides," *IEEE Photonics Technology Letters*, vol. 28, no. 14, pp. 1561–1564, Jul. 2016. DOI: 10.1109/lpt.2016.2553841. [Online]. Available: https://doi.org/10.1109/lpt.2016.2553841.

[168] T. V. Mechelen and Z. Jacob, "Universal spin-momentum locking of evanescent waves," *Optica*, vol. 3, no. 2, p. 118, Jan. 2016. DOI: 10.1364/optica.3.000118. [Online]. Available: https://doi.org/10.1364/optica.3.000118.

[169] P. Lodahl *et al.*, "Chiral quantum optics," *Nature*, vol. 541, no. 7638, pp. 473–480, Jan. 2017, ISSN: 1476-4687. DOI: 10.1038/nature21037. [Online]. Available: https://doi.org/10.1038/nature21037.

[170] S. M. Barnett, M. Babiker, and M. J. Padgett, "Optical orbital angular momentum," *Philosophical Transactions of the Royal Society A: Mathematical, Physical and Engineering Sciences*, vol. 375, no. 2087, p. 20 150 444, 2017. DOI: 10.1098/rsta.2015.0444. [Online]. Available: https://royalsocietypublishing.org/doi/abs/10.1098/rsta.2015.0444.

[171] A. T. O'Neil, I. MacVicar, L. Allen, and M. J. Padgett, "Intrinsic and extrinsic nature of the orbital angular momentum of a light beam," *Physical Review Letters*, vol. 88, no. 5, p. 053 601, Jan. 2002. DOI: 10.1103/PhysRevLett.88.053601. [Online]. Available: http://link.aps.org/doi/10.1103/PhysRevLett.88.053601 (visited on 05/10/2013).

[172] M. Padgett and R. Bowman, "Tweezers with a twist," *Nature Photonics*, vol. 5, no. 6, pp. 343–348, Jun. 2011, ISSN: 1749-4885. DOI: 10.1038/nphoton.2011.81. (visited on 04/10/2013).

[173] R. P. Cameron, S. M. Barnett, and A. M. Yao, "Optical helicity, optical spin and related quantities in electromagnetic theory," *New Journal of Physics*, vol. 14, no. 5, p. 053 050, May 2012, ISSN: 1367-2630. DOI: 10.1088/1367-2630/14/5/053050. [Online]. Available: http://iopscience.iop.org/1367-2630/14/5/053050.

[174] S. Tojo, M. Hasuo, and T. Fujimoto, "Absorption enhancement of an electric quadrupole transition of cesium atoms in an evanescent field," *Physical Review Letters*, vol. 92, no. 5, p. 053 001, 2004.

[175] M. L. Andersen, S. Stobbe, A. S. Sorensen, and P. Lodahl, "Strongly modified plasmon–matter interaction with mesoscopic quantum emitters," *Nature Physics*, vol. 7, no. 3, pp. 215–218, Mar. 2011, ISSN: 1745-2481. DOI: 10.1038/nphys1870. [Online]. Available: https://doi.org/10.1038/nphys1870.

[176] C.-F. Cheng *et al.*, "Electric-quadrupole transition of h_2 determined to 10^{-9} precision," *Physical Review A*, vol. 85, p. 024 501, 2 Feb. 2012. DOI: 10.1103/PhysRevA.85.024501. [Online]. Available: https://link.aps.org/doi/10.1103/PhysRevA.85.024501.

[177] S. Karaveli and R. Zia, "Strong enhancement of magnetic dipole emission in a multilevel electronic system," *Optics Letters*, vol. 35, no. 20, pp. 3318–3320, Oct. 2010. DOI: 10.1364/OL.35.003318. [Online]. Available: http://ol.osa.org/abstract.cfm?URI=ol-35-20-3318.

[178] M. Kasperczyk, S. Person, D. Ananias, L. D. Carlos, and L. Novotny, "Excitation of magnetic dipole transitions at optical frequencies," *Physical Review Letters*, vol. 114, p. 163 903, 16 Apr. 2015. DOI: 10.1103/PhysRevLett.114.163903. [Online]. Available: https://link.aps.org/doi/10.1103/PhysRevLett.114.163903.

[179] A. Vaskin *et al.*, "Manipulation of magnetic dipole emission from eu3+ with mie-resonant dielectric metasurfaces," *Nano Letters*, vol. 19, no. 2, pp. 1015–1022, 2019. DOI: 10.1021/acs.nanolett.8b04268. [Online]. Available: https://doi.org/10.1021/acs.nanolett.8b04268.

[180] M. Sharnoff, "Validity conditions for the kramers-kronig relations," *American Journal of Physics*, vol. 32, no. 1, pp. 40–44, 1964. DOI: 10.1119/1.1970070. eprint: https://doi.org/10.1119/1.1970070. [Online]. Available: https://doi.org/10.1119/1.1970070.

[181] J. D. Jackson, *Classical electrodynamics*, 1999.

[182] V. Lucarini, J. Saarinen, K. Peiponen, and E. Vartiainen, *Kramers-Kronig Relations in Optical Materials Research* (Springer Series in Optical Sciences). Springer Berlin Heidelberg, 2005, ISBN: 9783540236733. [Online]. Available: https://books.google.de/books?id=U21PMIXyk7IC.

[183] H. S. Sehmi, W. Langbein, and E. A. Muljarov, "Optimizing the drude-lorentz model for material permittivity: Examples for semiconductors," in *2017 Progress In Electromagnetics Research Symposium - Spring (PIERS)*, 2017, pp. 994–1000. DOI: 10.1109/PIERS.2017.8261889.

[184] E. Kaxiras and J. D. Joannopoulos, *Quantum Theory of Materials*. Cambridge University Press, 2019. DOI: 10.1017/9781139030809.

[185] A. D. Yaghjian, "Internal energy, q-energy, poynting's theorem, and the stress dyadic in dispersive material," *IEEE Transactions on Antennas and Propagation*, vol. 55, no. 6, pp. 1495–1505, 2007. DOI: 10.1109/TAP.2007.897350.

[186] J. Pendry, "Photon number conservation in time dependent systems," *Optics Express*, vol. 31, no. 1, pp. 452–458, 2023.

[187] J. Pendry, E. Galiffi, and P. Huidobro, "Photon conservation in trans-luminal metamaterials," *Optica*, vol. 9, no. 7, pp. 724–730, 2022.

[188] S. A. R. Horsley and J. B. Pendry, "Time varying gratings model Hawking radiation," Feb. 2023. DOI: 10.48550/arXiv.2302.04066. [Online]. Available: https://preprints.opticaopen.org/articles/preprint/Time_varying_gratings_model_Hawking_radiation/22097141.

[189] V. H. Rumsey, "Reaction concept in electromagnetic theory," *Physical Review*, vol. 94, pp. 1483–1491, 6 Jun. 1954. DOI: 10.1103/PhysRev.94.1483. [Online]. Available: https://link.aps.org/doi/10.1103/PhysRev.94.1483.

[190] V. S. Asadchy, M. S. Mirmoosa, A. Díaz-Rubio, S. Fan, and S. A. Tretyakov, "Tutorial on electromagnetic nonreciprocity and its origins," *Proceedings of the IEEE*, vol. 108, no. 10, pp. 1684–1727, 2020. DOI: 10.1109/JPROC.2020.3012381.

[191] V. Agranovich and V. Ginzburg, *Crystal Optics with Spatial Dispersion, and Excitons* (Springer Series in Solid-State Sciences). Springer Berlin Heidelberg, 2013, ISBN: 9783662024065. [Online]. Available: https://books.google.de/books?id=18L-CAAAQBAJ.

[192] A. Serdyukov, I. Semchenko, S. Tretyakov, and A. Sihvola, *Electromagnetics of bi-anisotropic materials: Theory and applications*, English. Switzerland: Gordon and Breach Science Publishers, 2001.

[193] L. Onsager, "Reciprocal relations in irreversible processes. i.," *Physical Review*, vol. 37, pp. 405–426, 4 Feb. 1931. DOI: 10.1103/PhysRev.37.405. [Online]. Available: https://link.aps.org/doi/10.1103/PhysRev.37.405.

[194] H. Casimir, "Reciprocity theorems and irreversible processes," *Proceedings of the IEEE*, vol. 51, no. 11, pp. 1570–1573, 1963. DOI: 10.1109/PROC.1963.2627.

[195] L. Landau and E. Lifshitz, *Statistical Physics: Volume 5*. Elsevier Science, 2013, ISBN: 9780080570464. [Online]. Available: https://books.google.gr/books?id=VzgJN-XPTRsC.

[196] A. Lakhtakia and R. A. Depine, "On onsager relations and linear electromagnetic materials," *AEU - International Journal of Electronics and Communications*, vol. 59, no. 2, pp. 101–104, 2005, ISSN: 1434-8411. DOI: https://doi.org/10.1016/j.aeue.2005.01.008. [Online]. Available: https://www.sciencedirect.com/science/article/pii/S1434841105000129.

[197] D. L. Sounas and A. Alù, "Non-reciprocal electromagnetics in time-varying systems," in *2017 IEEE International Symposium on Antennas and Propagation, USNC/URSI National Radio Science Meeting*, 2017, pp. 439–440. DOI: 10.1109/APUSNCURSINRSM.2017.8072262.

[198] A. Shaltout, A. Kildishev, and V. Shalaev, "Time-varying metasurfaces and lorentz non-reciprocity," *Optical Materials Express*, vol. 5, no. 11, pp. 2459–2467, Nov. 2015. DOI: 10.1364/OME.5.002459. [Online]. Available: https://opg.optica.org/ome/abstract.cfm?URI=ome-5-11-2459.

[199] X. Guo, Y. Ding, Y. Duan, and X. Ni, "Nonreciprocal metasurface with space–time phase modulation," *Light: Science & Applications*, vol. 8, no. 1, p. 123, Dec. 2019, ISSN: 2047-7538. DOI: 10.1038/s41377-019-0225-z. [Online]. Available: https://doi.org/10.1038/s41377-019-0225-z.

[200] C. Caloz, A. Alù, S. Tretyakov, D. Sounas, K. Achouri, and Z.-L. Deck-Léger, "Electromagnetic nonreciprocity," *Physical Review Appled*, vol. 10, p. 047 001, 4 Oct. 2018. DOI: 10.1103/PhysRevApplied.10.047001. [Online]. Available: https://link.aps.org/doi/10.1103/PhysRevApplied.10.047001.

[201] J. Wang, J. F. Herrmann, J. D. Witmer, A. H. Safavi-Naeini, and S. Fan, "Photonic modal circulator using temporal refractive-index modulation with spatial inversion symmetry," *Physical Review Letters*, vol. 126, p. 193 901, 19 May 2021. DOI: 10.1103/PhysRevLett.126.193901. [Online]. Available: https://link.aps.org/doi/10.1103/PhysRevLett.126.193901.

[202] Z. Yu and S. Fan, "Complete optical isolation created by indirect interband photonic transitions," *Nature Photonics*, vol. 3, no. 2, pp. 91–94, Feb. 2009, ISSN: 1749-4893. DOI: 10.1038/nphoton.2008.273. [Online]. Available: https://doi.org/10.1038/nphoton.2008.273.

[203] K. Fang, Z. Yu, and S. Fan, "Photonic aharonov-bohm effect based on dynamic modulation," *Physical Review Letters*, vol. 108, p. 153 901, 15 Apr. 2012. DOI: 10.1103/PhysRevLett.108.153901. [Online]. Available: https://link.aps.org/doi/10.1103/PhysRevLett.108.153901.

[204] P. Morse and H. Feshbach, *Methods of theoretical physics* (International series in pure and applied physics). McGraw-Hill, 1953.

[205] W. Miller, *Symmetry and Separation of Variables* (Encyclopedia of Mathematics and its Applications). Cambridge University Press, 2012, ISBN: 9780521177399. [Online]. Available: https://books.google.de/books?id=ct6iSgAACAAJ.

[206] C. Tai, I. Antennas, P. Society, I. M. Theory, and T. Society, *Dyadic Green Functions in Electromagnetic Theory* (IEEE Press Publication Series). IEEE Press, 1994, ISBN: 9780780304499. [Online]. Available: https://books.google.de/books?id=wiNRAAAAMAAJ.

[207] I. Fernandez-Corbaton, "A conformally invariant derivation of average electromagnetic helicity," *Symmetry*, vol. 11, no. 11, 2019, ISSN: 2073-8994. DOI: 10.3390/sym11111427. [Online]. Available: https://www.mdpi.com/2073-8994/11/11/1427.

[208] I. Fernandez-Corbaton, M. Fruhnert, and C. Rockstuhl, "Dual and chiral objects for optical activity in general scattering directions," *ACS Photonics*, vol. 2, no. 3, pp. 376–384, Mar. 2015. DOI: 10.1021/ph500419a. [Online]. Available: https://doi.org/10.1021/ph500419a.

[209] F. Graf, J. Feis, X. Garcia-Santiago, M. Wegener, C. Rockstuhl, and I. Fernandez-Corbaton, "Achiral, helicity preserving, and resonant structures for enhanced sensing of chiral molecules," *ACS Photonics*, vol. 6, no. 2, pp. 482–491, Feb. 2019. DOI: 10.1021/acsphotonics.8b01454. [Online]. Available: https://doi.org/10.1021/acsphotonics.8b01454.

[210] J. Petersen, J. Volz, and A. Rauschenbeutel, "Chiral nanophotonic waveguide interface based on spin-orbit interaction of light," *Science*, vol. 346, no. 6205, pp. 67–71, 2014. DOI: 10.1126/science.1257671. eprint: https://www.science.org/doi/pdf/10.1126/science.1257671. [Online]. Available: https://www.science.org/doi/abs/10.1126/science.1257671.

[211] A. Lakhtakia, *Beltrami Fields in Chiral Media* (Series in Contemporary Chemical Physics). World Scientific, 1994, ISBN: 9789810214036. [Online]. Available: https://books.google.de/books?id=7ZJGn2Mq6yMC.

[212] Y. Tang and A. E. Cohen, "Optical chirality and its interaction with matter," *Physical Review Letters*, vol. 104, p. 163 901, 16 Apr. 2010. DOI: 10.1103/PhysRevLett.104.163901. [Online]. Available: https://link.aps.org/doi/10.1103/PhysRevLett.104.163901.

[213] L. V. Poulikakos *et al.*, "Optical chirality flux as a useful far-field probe of chiral near fields," *ACS Photonics*, vol. 3, no. 9, pp. 1619–1625, Sep. 2016. DOI: 10.1021/acsphotonics.6b00201. [Online]. Available: https://doi.org/10.1021/acsphotonics.6b00201.

[214] A. W. Snyder, J. D. Love, *et al.*, *Optical waveguide theory*. Chapman and hall London, 1983, vol. 175.

[215] R. Carminati and J. C. Schotland, *Principles of Scattering and Transport of Light*. Cambridge University Press, 2021. DOI: 10.1017/9781316544693.

[216] L. Zhang, F. Monticone, and O. D. Miller, *All electromagnetic scattering bodies are matrix-valued oscillators*, 2022. arXiv: 2211.04457 [physics.optics].

[217] K. Vynck *et al.*, *Light in correlated disordered media*, 2021. arXiv: 2106.13892 [physics.optics].

[218] C. Majorel *et al.*, *Nanophotonics*, vol. 11, no. 16, pp. 3663–3678, 2022. DOI: doi:10.1515/nanoph-2022-0308. [Online]. Available: https://doi.org/10.1515/nanoph-2022-0308.

[219] S. J. Rahi, T. Emig, N. Graham, R. L. Jaffe, and M. Kardar, "Scattering theory approach to electrodynamic casimir forces," *Physical Review D*, vol. 80, p. 085 021, 8 Oct. 2009. DOI: 10.1103/PhysRevD.80.085021. [Online]. Available: https://link.aps.org/doi/10.1103/PhysRevD.80.085021.

[220] P. Lalanne, W. Yan, K. Vynck, C. Sauvan, and J.-P. Hugonin, "Light interaction with photonic and plasmonic resonances," *Laser & Photonics Reviews*, vol. 12, no. 5, p. 1 700 113, 2018. DOI: https://doi.org/10.1002/lpor.201700113. eprint: https://onlinelibrary.wiley.com/doi/pdf/10.1002/lpor.201700113. [Online]. Available: https://onlinelibrary.wiley.com/doi/abs/10.1002/lpor.201700113.

[221] F. Alpeggiani, N. Parappurath, E. Verhagen, and L. Kuipers, "Quasinormal-mode expansion of the scattering matrix," *Physical Review X*, vol. 7, p. 021 035, 2 Jun. 2017. DOI: 10.1103/PhysRevX.7.021035. [Online]. Available: https://link.aps.org/doi/10.1103/PhysRevX.7.021035.

[222] T. Weiss and E. A. Muljarov, "How to calculate the pole expansion of the optical scattering matrix from the resonant states," *Physical Review B*, vol. 98, p. 085 433, 8 Aug. 2018. DOI: 10.1103/PhysRevB.98.085433. [Online]. Available: https://link.aps.org/doi/10.1103/PhysRevB.98.085433.

[223] M. Benzaouia, J. D. Joannopoulos, S. G. Johnson, and A. Karalis, "Quasi-normal mode theory of the scattering matrix, enforcing fundamental constraints for truncated expansions," *Physical Review Res.*, vol. 3, p. 033 228, 3 Sep. 2021. DOI: 10.1103/PhysRevResearch.3.033228. [Online]. Available: https://link.aps.org/doi/10.1103/PhysRevResearch.3.033228.

[224] I. B. Soltane, R. Colom, F. Dierick, B. Stout, and N. Bonod, "Multiple-Order Singularity Expansion Method," Feb. 2023. DOI: 10.48550/arXiv.2302.01988. [Online]. Available: https://preprints.opticaopen.org/articles/preprint/Multiple-Order_Singularity_Expansion_Method/22048484.

[225] C. Sauvan, "Quasinormal modes expansions for nanoresonators made of absorbing dielectric materials: Study of the role of static modes," *Optics Express*, vol. 29, no. 6, pp. 8268–8282, Mar. 2021. DOI: 10.1364/OE.417909. [Online]. Available: https://opg.optica.org/oe/abstract.cfm?URI=oe-29-6-8268.

[226] M. I. Abdelrahman and B. Gralak, "Completeness and divergence-free behavior of the quasi-normal modes using causality principle," *OSA Continuum*, vol. 1, no. 2, pp. 340–348, Oct. 2018. DOI: 10.1364/OSAC.1.000340. [Online]. Available: https://opg.optica.org/osac/abstract.cfm?URI=osac-1-2-340.

[227] M. B. Doost, W. Langbein, and E. A. Muljarov, "Resonant state expansion applied to two-dimensional open optical systems," *Physical Review A*, vol. 87, p. 043 827, 4 Apr. 2013. DOI: 10.1103/PhysRevA.87.043827. [Online]. Available: https://link.aps.org/doi/10.1103/PhysRevA.87.043827.

[228] M. B. Doost, W. Langbein, and E. A. Muljarov, "Resonant-state expansion applied to three-dimensional open optical systems," *Physical Review A*, vol. 90, p. 013 834, 1 Jul. 2014. DOI: 10.1103/PhysRevA.90.013834. [Online]. Available: https://link.aps.org/doi/10.1103/PhysRevA.90.013834.

[229] R. Colom, R. McPhedran, B. Stout, and N. Bonod, "Modal analysis of anapoles, internal fields, and fano resonances in dielectric particles," *Journal of the Optical Society of America B*, vol. 36, no. 8, pp. 2052–2061, Aug. 2019. DOI: 10.1364/JOSAB.36.002052. [Online]. Available: https://opg.optica.org/josab/abstract.cfm?URI=josab-36-8-2052.

[230] P. Lalanne, *Mode volume of electromagnetic resonators: Let us try giving credit where it is due*, 2020. arXiv: 2011.00218 [physics.optics].

[231] C. Sauvan, T. Wu, R. Zarouf, E. A. Muljarov, and P. Lalanne, "Normalization, orthogonality, and completeness of quasinormal modes of open systems: The case of electromagnetism," *Optics Express*, vol. 30, no. 5, pp. 6846–6885, Feb. 2022. DOI: 10.1364/OE.443656. [Online]. Available: https://opg.optica.org/oe/abstract.cfm?URI=oe-30-5-6846.

[232] P. Waterman, "Matrix formulation of electromagnetic scattering," *Proceedings of the IEEE*, vol. 53, no. 8, pp. 805–812, 1965. DOI: 10.1109/PROC.1965.4058.

[233] P. C. Waterman, "Symmetry, unitarity, and geometry in electromagnetic scattering," *Physical Review D*, vol. 3, pp. 825–839, 4 Feb. 1971. DOI: 10.1103/PhysRevD.3.825. [Online]. Available: https://link.aps.org/doi/10.1103/PhysRevD.3.825.

[234] P. C. Waterman, "New formulation of acoustic scattering," *The Journal of the Acoustical Society of America*, vol. 45, no. 6, pp. 1417–1429, 1969. DOI: 10.1121/1.1911619. eprint: https://doi.org/10.1121/1.1911619. [Online]. Available: https://doi.org/10.1121/1.1911619.

[235] M. I. Mishchenko, L. D. Travis, and D. W. Mackowski, "T-matrix method and its applications to electromagnetic scattering by particles: A current perspective," *Journal of Quantitative Spectroscopy and Radiative Transfer*, vol. 111, no. 11, pp. 1700–1703, 2010, 50 Years of JQSRT, ISSN: 0022-4073. DOI: https://doi.org/10.1016/j.jqsrt.2010.01.030. [Online]. Available: https://www.sciencedirect.com/science/article/pii/S0022407310000531.

[236] D. W. Mackowski and M. I. Mishchenko, "Calculation of the t matrix and the scattering matrix for ensembles of spheres," *Journal of the Optical Society of America A*, vol. 13, pp. 2266–2277, 1996. DOI: 10.1364/JOSAA.13.002266.

[237] L. Liu and M. I. Mishchenko, "Effects of aggregation on scattering and radiative properties of soot aerosols," *Journal of Geophysical Research: Atmospheres*, vol. 110, no. D11, 2005. DOI: https://doi.org/10.1029/2004JD005649. eprint: https://agupubs.onlinelibrary.wiley.com/doi/pdf/10.1029/2004JD005649. [Online]. Available: https://agupubs.onlinelibrary.wiley.com/doi/abs/10.1029/2004JD005649.

[238] P. Yang *et al.*, "Modeling of the scattering and radiative properties of nonspherical dust-like aerosols," *Journal of Aerosol Science*, vol. 38, no. 10, pp. 995–1014, 2007, ISSN: 0021-8502. DOI: https://doi.org/10.1016/j.jaerosci.2007.07.001. [Online]. Available: https://www.sciencedirect.com/science/article/pii/S0021850207001061.

[239] L. Pattelli, A. Egel, U. Lemmer, and D. S. Wiersma, "Role of packing density and spatial correlations in strongly scattering 3d systems," *Optica*, vol. 5, no. 9, pp. 1037–1045, 2018.

[240] D. A. B. Miller, "All linear optical devices are mode converters," *Optics Express*, vol. 20, no. 21, pp. 23 985–23 993, Oct. 2012. DOI: 10.1364/OE.20.023985. [Online]. Available: https://opg.optica.org/oe/abstract.cfm?URI=oe-20-21-23985.

[241] I. L. Rasskazov, P. S. Carney, and A. Moroz, "Stratify: A comprehensive and versatile matlab code for a multilayered sphere," *OSA Continuum*, vol. 3, no. 8, pp. 2290–2306, 2020.

[242] B. Stout, C. Andraud, S. Stout, and J. Lafait, "Absorption in multiple-scattering systems of coated spheres," *Journal of the Optical Society of America A*, vol. 20, no. 6, pp. 1050–1059, Jun. 2003. DOI: 10.1364/JOSAA.20.001050. [Online]. Available: https://opg.optica.org/josaa/abstract.cfm?URI=josaa-20-6-1050.

[243] M. P. Ioannidou and D. P. Chrissoulidis, "Electromagnetic-wave scattering by a sphere with multiple spherical inclusions," *Journal of the Optical Society of America A*, vol. 19, no. 3, pp. 505–512, 2002.

[244] A. FRESNEL, *Mémoire sur la loi des modifications que la réflexion imprime à la lumière polarisée (memoir on the law of the modifications that reflection impresses on polarized light)*, 1823.

[245] J. W. Goodman, *Introduction to Fourier optics*. Roberts and Company publishers, 2005.

[246] M. M. Bay, S. Vignolini, and K. Vynck, "Pyllama: A stable and versatile python toolkit for the electromagnetic modelling of multilayered anisotropic media," *Computer Physics Communications*, vol. 273, p. 108 256, 2022, ISSN: 0010-4655. DOI: https://doi.org/10.1016/j.cpc.2021.108256. [Online]. Available: https://www.sciencedirect.com/science/article/pii/S0010465521003684.

[247] M. Onishi, K. Crabtree, and R. A. Chipman, "Formulation of rigorous coupled-wave theory for gratings in bianisotropic media," *Journal of the Optical Society of America A*, vol. 28, no. 8, pp. 1747–1758, Aug. 2011. DOI: 10.1364/JOSAA.28.001747. [Online]. Available: https://opg.optica.org/josaa/abstract.cfm?URI=josaa-28-8-1747.

[248] S. Burger, L. Zschiedrich, J. Pomplun, and F. Schmidt, "Jcmsuite: An adaptive fem solver for precise simulations in nano-optics," in *Integrated Photonics and Nanophotonics Research and Applications*, Optica Publishing Group, 2008, ITuE4. DOI: 10.1364/IPNRA.2008.ITuE4. [Online]. Available: https://opg.optica.org/abstract.cfm?URI=IPNRA-2008-ITuE4.

[249] J. Lu and J. Vučković, "Nanophotonic computational design," *Optics Express*, vol. 21, no. 11, pp. 13 351–13 367, Jun. 2013. DOI: 10.1364/OE.21.013351. [Online]. Available: https://opg.optica.org/oe/abstract.cfm?URI=oe-21-11-13351.

[250] L. F. Frellsen, Y. Ding, O. Sigmund, and L. H. Frandsen, "Topology optimized mode multiplexing in silicon-on-insulator photonic wire waveguides," *Optics Express*, vol. 24, no. 15, pp. 16 866–16 873, Jul. 2016. DOI: 10.1364/OE.24.016866. [Online]. Available: https://opg.optica.org/oe/abstract.cfm?URI=oe-24-15-16866.

[251] Y. Shi, W. Shin, and S. Fan, "Multi-frequency finite-difference frequency-domain algorithm for active nanophotonic device simulations," *Optica*, vol. 3, no. 11, pp. 1256–1259, 2016.

[252] E. Lustig *et al.*, "Photonic time-crystals - fundamental concepts," *Optics Express*, vol. 31, no. 6, pp. 9165–9170, Mar. 2023. DOI: 10.1364/OE.479367. [Online]. Available: https://opg.optica.org/oe/abstract.cfm?URI=oe-31-6-9165.

[253] S. Saha *et al.*, "Photonic time crystals: A materials perspective," *Optics Express*, vol. 31, no. 5, pp. 8267–8273, Feb. 2023. DOI: 10.1364/OE.479257. [Online]. Available: https://opg.optica.org/oe/abstract.cfm?URI=oe-31-5-8267.

[254] J. R. Zurita-Sánchez, P. Halevi, and J. C. Cervantes-Gonzalez, "Reflection and transmission of a wave incident on a slab with a time-periodic dielectric function $\epsilon(t)$," *Physical Review A*, vol. 79, no. 5, p. 053 821, 2009.

[255] E. Lustig, Y. Sharabi, and M. Segev, "Topological aspects of photonic time crystals," *Optica*, vol. 5, no. 11, pp. 1390–1395, 2018.

[256] V. Pacheco-Peña and N. Engheta, *Nanophotonics*, vol. 9, no. 2, pp. 379–391, 2020. DOI: doi:10.1515/nanoph-2019-0305. [Online]. Available: https://doi.org/10.1515/nanoph-2019-0305.

[257] M. Mishchenko, M. Andrew A. Lacis, L. Travis, and A. Lacis, *Scattering, Absorption, and Emission of Light by Small Particles*. Cambridge University Press, 2002, ISBN: 9780521782524. [Online]. Available: https://books.google.de/books?id=i6r1YFyK%5C_g8C.

[258] A. P. Moneda and D. P. Chrissoulidis, "Dyadic green's function of a sphere with an eccentric spherical inclusion," *Journal of the Optical Society of America A*, vol. 24, no. 6, pp. 1695–1703, Jun. 2007. DOI: 10.1364/JOSAA.24.001695. [Online]. Available: http://josaa.osa.org/abstract.cfm?URI=josaa-24-6-1695.

[259] M. R. Shcherbakov *et al.*, "Time-variant metasurfaces enable tunable spectral bands of negative extinction," *Optica*, vol. 6, no. 11, pp. 1441–1442, 2019.

[260] H. Li, A. Mekawy, and A. Alù, "Beyond chu's limit with floquet impedance matching," *Physical Review Letters*, vol. 123, no. 16, p. 164 102, 2019.

[261] S. COMSOL AB Stockholm, *Comsol multiphysics® v. 5.4*. [Online]. Available: http://www.comsol.com/products/multiphysics/.

[262] Y. Zhou *et al.*, "Broadband frequency translation through time refraction in an epsilon-near-zero material," *Nature Communications*, vol. 11, no. 1, p. 2180, May 2020, ISSN: 2041-1723. DOI: 10.1038/s41467-020-15682-2. [Online]. Available: https://doi.org/10.1038/s41467-020-15682-2.

[263] M. Z. Alam, I. D. Leon, and R. W. Boyd, "Large optical nonlinearity of indium tin oxide in its epsilon-near-zero region," *Science*, vol. 352, no. 6287, pp. 795–797, 2016. DOI: 10.1126/science.aae0330. eprint: https://www.science.org/doi/pdf/10.1126/science.aae0330. [Online]. Available: https://www.science.org/doi/abs/10.1126/science.aae0330.

[264] R. N. S. Suryadharma, M. Fruhnert, C. Rockstuhl, and I. Fernandez-Corbaton, "Singular-value decomposition for electromagnetic-scattering analysis," *Physical Review A*, vol. 95, p. 053 834, 5 May 2017. DOI: 10.1103/PhysRevA.95.053834. [Online]. Available: https://link.aps.org/doi/10.1103/PhysRevA.95.053834.

[265] A. G. Lamprianidis and A. E. Miroshnichenko, "Excitation of nonradiating magnetic anapole states with azimuthally polarized vector beams," *Beilstein Journal of Nanotechnology*, vol. 9, pp. 1478–1490, 2018, ISSN: 2190-4286. DOI: 10.3762/bjnano.9.139.

[266] M. Faraday, "Xvii. on a peculiar class of acoustical figures; and on certain forms assumed by groups of particles upon vibrating elastic surfaces," *Philosophical transactions of the Royal Society of London*, no. 121, pp. 299–340, 1831.

[267] L. Rayleigh, "Xvii. on the maintenance of vibrations by forces of double frequency, and on the propagation of waves through a medium endowed with a periodic structure," *The London, Edinburgh, and Dublin Philosophical Magazine and Journal of Science*, vol. 24, no. 147, pp. 145–159, 1887.

[268] A. A. Post, G. De Groot, A. Daffertshofer, and P. J. Beek, "Pumping a playground swing," *Motor Control*, vol. 11, no. 2, pp. 136–150, 2007.

[269] H. Rabin, *Quantum Electronics: A Treatise* (Quantum electronics : a treatise. Volume I, Nonlinear optics τ. 1). Elsevier Science, 1975, ISBN: 9780323162425. [Online]. Available: https://books.google.de/books?id=bjWQhgOU8K0C.

[270] A. Yariv and W. Louisell, "5a2-theory of the optical parametric oscillator," *IEEE Journal of Quantum Electronics*, vol. 2, no. 9, pp. 418–424, 1966.

[271] M. Kerker, D.-S. Wang, and C. L. Giles, "Electromagnetic scattering by magnetic spheres," *Journal of the Optical Society of America*, vol. 73, no. 6, pp. 765–767, Jun. 1983. DOI: 10.1364/JOSA.73.000765. [Online]. Available: https://www.osapublishing.org/abstract.cfm?uri=josa-73-6-765 (visited on 05/10/2017).

[272] W. Liu and Y. S. Kivshar, "Generalized kerker effects in nanophotonics and meta-optics," *Optics Express*, vol. 26, no. 10, pp. 13 085–13 105, May 2018. DOI: 10.1364/OE.26.013085. [Online]. Available: https://opg.optica.org/oe/abstract.cfm?URI=oe-26-10-13085.

[273] A. Chen and F. Monticone, "Active scattering-cancellation cloaking: Broadband invisibility and stability constraints," *IEEE Transactions on Antennas and Propagation*, vol. 68, no. 3, pp. 1655–1664, 2020. DOI: 10.1109/TAP.2019.2948528.

[274] J. A. Stratton and L. J. Chu, "Diffraction theory of electromagnetic waves," *Physical Review*, vol. 56, pp. 99–107, 1 Jul. 1939. DOI: 10.1103/PhysRev.56.99. [Online]. Available: https://link.aps.org/doi/10.1103/PhysRev.56.99.

[275] L. Novotny and B. Hecht, *Principles of Nano-Optics*, 2nd ed. Cambridge University Press, 2012. DOI: 10.1017/CBO9780511794193.

[276] A. Egel, D. Theobald, Y. Donie, U. Lemmer, and G. Gomard, "Light scattering by oblate particles near planar interfaces: On the validity of the t-matrix approach," *Optics Express*, vol. 24, no. 22, pp. 25 154–25 168, Oct. 2016. DOI: 10.1364/OE.24.025154. [Online]. Available: http://www.opticsexpress.org/abstract.cfm?URI=oe-24-22-25154.

[277] D. Theobald, A. Egel, G. Gomard, and U. Lemmer, "Plane-wave coupling formalism for T-matrix simulations of light scattering by nonspherical particles," *Physical Review A*, vol. 96, p. 033 822, 3 Sep. 2017. DOI: 10.1103/PhysRevA.96.033822. [Online]. Available: https://link.aps.org/doi/10.1103/PhysRevA.96.033822.

[278] A. Egel, Y. Eremin, T. Wriedt, D. Theobald, U. Lemmer, and G. Gomard, "Extending the applicability of the t-matrix method to light scattering by flat particles on a substrate via truncation of sommerfeld integrals," *Journal of Quantitative Spectroscopy and Radiative Transfer*, vol. 202, pp. 279–285, 2017, ISSN: 0022-4073. DOI: https://doi.org/10.1016/j.jqsrt.2017.08.016. [Online]. Available: http://www.sciencedirect.com/science/article/pii/S0022407317305939.

[279] T. Martin, "T-matrix method for closely adjacent obstacles," *Journal of Quantitative Spectroscopy and Radiative Transfer*, vol. 234, pp. 40–46, 2019, ISSN: 0022-4073. DOI: https://doi.org/10.1016/j.jqsrt.2019.06.001. [Online]. Available: http://www.sciencedirect.com/science/article/pii/S002240731930278X.

[280] R. Zaridze, R. Jobava, G. Bit-Banik, D. Karkasbadze, D. Economou, and N. Uzunoglu, "The method of auxiliary sources and scattered field singularities (caustics)," *Journal of Electromagnetic Waves and Applications*, vol. 12, no. 11, pp. 1491–1507, 1998. DOI: 10.1163/156939398X00430. eprint: https://doi.org/10.1163/156939398X00430. [Online]. Available: https://doi.org/10.1163/156939398X00430.

[281] D. I. Kaklamani and H. T. Anastassiu, "Aspects of the method of auxiliary sources (mas) in computational electromagnetics," *IEEE Antennas and Propagation Magazine*, vol. 44, no. 3, pp. 48–64, 2002. DOI: 10.1109/MAP.2002.1028734.

[282] N. L. Tsitsas, G. P. Zouros, G. Fikioris, and Y. Leviatan, "On methods employing auxiliary sources for 2-d electromagnetic scattering by noncircular shapes," *IEEE Transactions on Antennas and Propagation*, vol. 66, no. 10, pp. 5443–5452, 2018. DOI: 10.1109/TAP.2018.2855963.

[283] A. M. Kern and O. J. F. Martin, "Surface integral formulation for 3d simulations of plasmonic and high permittivity nanostructures," *Journal of the Optical Society of America A*, vol. 26, no. 4, pp. 732–740, Apr. 2009. DOI: 10.1364/JOSAA.26.000732. [Online]. Available: http://josaa.osa.org/abstract.cfm?URI=josaa-26-4-732.

[284] P. Saha, G. Borgefors, and G. di Baja, *Skeletonization: Theory, Methods and Applications*. Elsevier Science, 2017, ISBN: 9780081012925. [Online]. Available: https://books.google.de/books?id=x7oIDgAAQBAJ.

[285] H. Blum, *A Transformation for Extracting New Descriptors of Shape*. M.I.T. Press, 1967. [Online]. Available: https://books.google.de/books?id=0Jl5zQEACAAJ.

[286] A. Tagliasacchi, T. Delame, M. Spagnuolo, N. Amenta, and A. Telea, "3d skeletons: A state-of-the-art report," *Computer Graphics Forum*, vol. 35, no. 2, pp. 573–597, 2016. DOI: https://doi.org/10.1111/cgf.12865. eprint: https://onlinelibrary.wiley.com/doi/pdf/10.1111/cgf.12865. [Online]. Available: https://onlinelibrary.wiley.com/doi/abs/10.1111/cgf.12865.

[287] F. Sun, Y. Choi, Y. Yu, and W. Wang, "Medial meshes – a compact and accurate representation of medial axis transform," *IEEE Transactions on Visualization and Computer Graphics*, vol. 22, pp. 1278–1290, 2016.

[288] J. J. Zou, H.-H. Chang, and H. Yan, "A new skeletonization algorithm based on constrained delaunay triangulation," in *ISSPA '99. Proceedings of the Fifth International Symposium on Signal Processing and its Applications (IEEE Cat. No.99EX359)*, vol. 2, 1999, 927–930 vol.2. DOI: 10.1109/ISSPA.1999.815823.

[289] G. Bradshaw and C. O'Sullivan, "Adaptive medial-axis approximation for sphere-tree construction," *ACM Transactions on Graphics*, vol. 23, no. 1, pp. 1–26, Jan. 2004, ISSN: 0730-0301. DOI: 10.1145/966131.966132. [Online]. Available: https://doi.org/10.1145/966131.966132.

[290] S. Stolpner, P. Kry, and K. Siddiqi, "Medial spheres for shape approximation," *IEEE Transactions on Pattern Analysis and Machine Intelligence*, vol. 34, no. 6, pp. 1234–1240, 2012. DOI: 10.1109/TPAMI.2011.254.

[291] D. W. Mackowski, "Exact solution for the scattering and absorption properties of sphere clusters on a plane surface," *Journal of Quantitative Spectroscopy and Radiative Transfer*, vol. 109, no. 5, pp. 770–788, 2008, ISSN: 0022-4073. DOI: https://doi.org/10.1016/j.jqsrt.2007.08.024. [Online]. Available: https://www.sciencedirect.com/science/article/pii/S0022407307002282.

[292] S. Bidault, M. Mivelle, and N. Bonod, "Dielectric nanoantennas to manipulate solid-state light emission," *Journal of Applied Physics*, vol. 126, no. 9, p. 094 104, Sep. 2019, ISSN: 0021-8979. DOI: 10.1063/1.5108641. eprint: https://pubs.aip.org/aip/jap/article-pdf/doi/10.1063/1.5108641/15232817/094104_1_online.pdf. [Online]. Available: https://doi.org/10.1063/1.5108641.

[293] A. Krasnok, M. Caldarola, N. Bonod, and A. Alú, "Spectroscopy and biosensing with optically resonant dielectric nanostructures," *Advanced Optical Materials*, vol. 6, no. 5, p. 1 701 094, 2018. DOI: https://doi.org/10.1002/adom.201701094. eprint: https://onlinelibrary.wiley.com/doi/pdf/10.1002/adom.201701094. [Online]. Available: https://onlinelibrary.wiley.com/doi/abs/10.1002/adom.201701094.

[294] B. Rolly, B. Stout, and N. Bonod, "Boosting the directivity of optical antennas with magnetic and electric dipolar resonant particles," *Opt. Express*, vol. 20, no. 18, pp. 20 376–20 386, Aug. 2012. DOI: 10.1364/OE.20.020376. [Online]. Available: https://opg.optica.org/oe/abstract.cfm?URI=oe-20-18-20376.

[295] D. Rocco, A. Lamprianidis, A. E. Miroshnichenko, and C. D. Angelis, "Giant electric and magnetic purcell factor in dielectric oligomers," *J. Opt. Soc. Am. B*, vol. 37, no. 9, pp. 2738–2744, Sep. 2020. DOI: 10.1364/JOSAB.399665. [Online]. Available: https://opg.optica.org/josab/abstract.cfm?URI=josab-37-9-2738.

[296] Z. Yu *et al.*, "Wavefront shaping: A versatile tool to conquer multiple scattering in multidisciplinary fields," *The Innovation*, vol. 3, no. 5, p. 100 292, 2022, ISSN: 2666-6758. DOI: https://doi.org/10.1016/j.xinn.2022.100292. [Online]. Available: https://www.sciencedirect.com/science/article/pii/S2666675822000881.

[297] D. Beutel, I. Fernandez-Corbaton, and C. Rockstuhl, "Unified lattice sums accommodating multiple sublattices for solutions of the helmholtz equation in two and three dimensions," *Physical Review A*, vol. 107, p. 013 508, 1 Jan. 2023. DOI: 10.1103/PhysRevA.107.013508. [Online]. Available: https://link.aps.org/doi/10.1103/PhysRevA.107.013508.

[298] P. Tighineanu, A. S. Sorensen, S. Stobbe, and P. Lodahl, "The mesoscopic nature of quantum dots in photon emission," in *Quantum Dots for Quantum Information Technologies*, P. Michler, Ed. Cham: Springer International Publishing, 2017, pp. 165–198, ISBN: 978-3-319-56378-7. DOI: 10.1007/978-3-319-56378-7_5. [Online]. Available: https://doi.org/10.1007/978-3-319-56378-7_5.

[299] J. R. Zurita-Sánchez and L. Novotny, "Multipolar interband absorption in a semiconductor quantum dot. i. electric quadrupole enhancement," *Journal of the Optical Society of America B*, vol. 19, no. 6, pp. 1355–1362, Jun. 2002. DOI: 10.1364/JOSAB.19.001355. [Online]. Available: https://opg.optica.org/josab/abstract.cfm?URI=josab-19-6-1355.

[300] S. Stobbe, P. T. Kristensen, J. E. Mortensen, J. M. Hvam, J. Mork, and P. Lodahl, "Spontaneous emission from large quantum dots in nanostructures: Exciton-photon interaction beyond the dipole approximation," *Physical Review B*, vol. 86, p. 085 304, 8 Aug. 2012. DOI: 10.1103/PhysRevB.86.085304. [Online]. Available: https://link.aps.org/doi/10.1103/PhysRevB.86.085304.

[301] M. F. Picardi, A. V. Zayats, and F. J. Rodriguez-Fortuno, "Janus and huygens dipoles: Near-field directionality beyond spin-momentum locking," *Physical Review Letters*, vol. 120, p. 117 402, 11 Mar. 2018. DOI: 10.1103/PhysRevLett.120.117402. [Online]. Available: https://link.aps.org/doi/10.1103/PhysRevLett.120.117402.

[302] D. F. Kornovan, M. I. Petrov, and I. V. Iorsh, "Transport and collective radiance in a basic quantum chiral optical model," *Physical Review B*, vol. 96, p. 115 162, 11 Sep. 2017. DOI: 10.1103/PhysRevB.96.115162. [Online]. Available: https://link.aps.org/doi/10.1103/PhysRevB.96.115162.

[303] R. Jones, G. Buonaiuto, B. Lang, I. Lesanovsky, and B. Olmos, "Collectively enhanced chiral photon emission from an atomic array near a nanofiber," *Physical Review Letters*, vol. 124, p. 093 601, 9 Mar. 2020. DOI: 10.1103/PhysRevLett.124.093601. [Online]. Available: https://link.aps.org/doi/10.1103/PhysRevLett.124.093601.

[304] W. Lukosz and R. E. Kunz, "Light emission by magnetic and electric dipoles close to a plane interface. i. total radiated power," *Journal of the Optical Society of America*, vol. 67, no. 12, pp. 1607–1615, Dec. 1977. DOI: 10.1364/JOSA.67.001607. [Online]. Available: https://opg.optica.org/abstract.cfm?URI=josa-67-12-1607.

[305] P. Kolchin *et al.*, "High purcell factor due to coupling of a single emitter to a dielectric slot waveguide," *Nano Letters*, vol. 15, no. 1, pp. 464–468, Jan. 2015, ISSN: 1530-6984. DOI: 10.1021/nl5037808. [Online]. Available: https://doi.org/10.1021/nl5037808.

Acknowledgements

To Martalycia,
for her love and patience.

There may be some moments, especially like this one when you are writing the last page of your dissertation, that scientific research seems to be a solitary venture in pursue of the great individual accomplishments. Fortunately, this is not really the case. Today's modern university has its historical origin at the medieval monastic schools, however, the production of scientific research is naturally becoming socialized, by necessity for its further development. And I have been a little witness of this beautiful, yet struggling, historical process.

Dear former and present colleagues and friends, I was so fortunate to work and, also, share precious personal moments with you. I have learned a lot from you and experienced a lot with you. I wish you all the best!

I would like to express my deepest gratitude to my supervisor, Carsten, and to the German citizens for providing me with the opportunity and the support to pursue my PhD studies here, in Karlsruhe.

Daß ihr hier sitzen könnt: So manche Schlacht
wurd drum gewagt. Ihr mögt sie gern vergessen.
Nur wißt: Hier haben andere schon gesessen.
Die saßen über Menschen dann. Gebt acht!

Was immer ihr erforscht einst und erfindet.
Euch wird nicht nützen, was ihr auch erkennt.
So es euch nicht zu klugem Kampf verbindet.
Und euch von allen Menschenfeinden trennt.

Vergeßt nicht: Mancher euresgleichen stritt.
Daß ihr hier sitzen könnt und nicht mehr sie.
Und nun vergrabt euch nicht und kämpfet mit.
Und lernt das Lernen und verlernt es nie.

Bertolt Brecht

"Sancho Pansa, der sich übrigens dessen nie gerühmt hat, gelang es im Laufe der Jahre, durch Beistellung einer Menge Ritter- und Räuberromane in den Abend- und Nachtstunden seinen Teufel, dem er später den Namen Don Quixote gab, derart von sich abzulenken, daß dieser dann haltlos die verrücktesten Taten aufführte, die aber mangels eines vorbestimmten Gegenstandes, der eben Sancho Pansa hätte sein sollen, niemandem schadeten. Sancho Pansa, ein freier Mann, folgte gleichmütig, vielleicht aus einem gewissen Verantwortlichkeitsgefühl, dem Don Quixote auf seinen Zügen und hatte davon eine große und nützliche Unterhaltung bis an sein Ende."

– Franz Kafka

Selbstständigkeitserklärung

Eidesstattliche Versicherung gemäß § 13 Absatz 2 Ziffer 3 der Promotionsordnung des Karlsruher Instituts für Technologie (KIT) für die KIT-Fakultät für Physik:

1. Bei der eingereichten Dissertation zu dem Thema "Generalized transition matrix methods for the analysis of linear nanophotonic systems" handelt es sich um meine eigenständig erbrachte Leistung.

2. Ich habe nur die angegebenen Quellen und Hilfsmittel benutzt und mich keiner unzulässigen Hilfe Dritter bedient. Insbesondere habe ich wörtlich oder sinngemäß aus anderen Werken übernommene Inhalte als solche kenntlich gemacht.

3. Die Arbeit oder Teile davon habe ich wie bislang nicht an einer Hochschule des In- oder Auslands als Bestandteil einer Prüfungs- oder Qualifikationsleistung vorgelegt.

4. Die Richtigkeit der vorstehenden Erklärungen bestätige ich.

5. Die Bedeutung der eidesstattlichen Versicherung und die strafrechtlichen Folgen einer unrichtigen oder unvollständigen eidesstattlichen Versicherung sind mir bekannt.

Ich versichere an Eides statt, dass ich nach bestem Wissen die reine Wahrheit erklärt und nichts verschwiegen habe.

Ort und Datum Unterschrift